Surface Integrity on Grinding of Gamma Titanium Aluminide Intermetallic Compounds

A Thesis
Presented to
The Academic Faculty

by

Gregorio Roberto Murtagian

In Partial Fulfillment
of the Requirements for the Degree
Doctor of Philosophy

G.W.Woodruff School of Mechanical Engineering
Georgia Institute of Technology
August 2004

Surface Integrity on Grinding of Gamma Titanium Aluminide Intermetallic Compounds

Approved by:

Professor Steven Danyluk, Committee Chair	Professor Ashok Saxena (UARK-ME)
Professor David McDowell (ME-MSE)	Professor Carlos Santamarina (CE)
Dr. Hugo Ernst (CINI-TENARIS)	Professor Thomas Kurfess (ME)

Date Approved: 3 August 2004

. . . to my parents Sergio and Vera, who taught me the value of hard work and the meaning of unconditional love

. . . to my beloved cheerleaders Verónica and Camila who fill my life with enjoyment

ACKNOWLEDGEMENTS

This thesis would have not been possible without the support and confidence of my advisor. My special thanks to Dr. S. Danyluk for accepting me as his student and giving me his confidence. I enjoyed a truly doctoral scholar experience under his guidance and support. I would like to thank the rest of the committee members, Dr. H. Ernst, Dr. D. McDowell, Dr. A. Saxena, Dr. C. Santamarina, and Dr. T. Kurfess for their time, and valuable comments to improve the quality of this work.

I would like to thank Dr. A. Sarce, Dr. A. Pignotti, and Dr. J. Garcia Velasco for their confidence and support to pursue this path. I also appreciate the financial support given by CINI-TENARIS.

I would like to thank Dr. P. McQuay and Dr. D. Lee from Howmet Castings for providing the TiAl slabs used for this work. Also, to Dr. B. Varghese from GE Superabrasives for providing the diamond abrasives, and to Dr. M. Dvoretsky from Noritake Abrasives for the manufacturing the wheels.

I appreciate the help provided by the ORNL HTML personnel, in particular Dr. T. Watkins, B. Kevin, Dr. E. Lara-Curzio, Dr. L. Riester, Dr. M. Ferber, and Dr. P. Blau.

I would like to thank D. Rogers, G. Payne, N. Moody, L. Teasley, S. Sheffield, V. Bortkevich, J. Witzel, S. Schulte, J. Donnell, and D. Osorno for their kindness and willingness to help.

I have enjoyed very interesting discussions with Dr. R. Hecker, Dr. P. Jones, M. Shenoy, J. Mayeur, Dr. R. McGinty, A. Caccialupi, B. Hagege, and many others that were very helpful for a better understanding of grinding and modeling.

I would like to thank all my office mates, in particular Inho Yoon, for his unconditional friendship and collaboration, and with whom I enjoyed fantastic jam sessions of chamber music. Finally, I appreciate the fun and entertainment I had playing soccer with the “burros”.

TABLE OF CONTENTS

LIST OF TABLES

LIST OF FIGURES

LIST OF ABBREVIATIONS AND SYMBOLS

ABBREVIATIONS

$2D$	Two dimensional
$3D$	Three dimensional
A	Constant
a	Value of depth of cut
A_b	Area of the split Hopkinson test bar
A_m	Mean area of exposed abrasive grits
A_s	Instantaneous area of the specimen
A_{ch}	Undeformed chip cross section
Ag	Angular abrasive grit shape
$ANOVA$	Analysis of variance
APB	Antiphase boundary
$at.\%$	Atomic percent
atm	Atomic mass
b	Workpiece/wheel contact width
b_c	Undeformed chip thickness
BA	Bearing area
BCC	Body centered cubic
Bk	Blocky abrasive grit shape

C_0 Split Hopkinson test bar Young's modulus

C_d Dynamic cumulative pdf of cutting edges density

C_f Grinding friction coefficient

C_s Static cumulative pdf of cutting edges density

CCT Continuous cooling transformation

CPS Counts per second

d_g^w Abrasive grit diameter at the grit depth of cut

D_f Dynamic indentation factor

d_s Wheel diameter

DAQ Data acquisition

DoC Wheel depth of cut

DOE Design of experiments

DOF Degree of freedom

E Young's modulus

E'_g Grinding specific energy

E^* Contact elastic modulus

E_b Split Hopkinson test bar Young's modulus

E_s Wheel's elastic modulus

E_w Workpiece elastic modulus

EDM Electric discharge machine

F F-statistics

f Materials friction coefficient

F'_N Grinding specific normal force

F'_T Grinding specific tangential force

F''_N Normal force per abrasive grit

F''_T Tangential force per abrasive grit

f_g Abrasive grit/workpiece friction coefficient

F_N Grinding normal force

f_s Strain gage constant

F_T Grinding tangential force

FCC Face centered cubic

FCT Face centered tetragonal

G_f Grain factor

G_h Abrasive grit shape

G_z Abrasive grit size

h Abrasive penetration

h_0 Depth of damage

H_g Grinding hardness

H_v Vickers hardness

h_{cr} Critical abrasive penetration

HCF High cycle fatigue

HCP Hexagonal closed packed

HIP Hot hydrostatic press

k Constant

K_g Equivalent grain spring constant

l_c Contact length

LA Wheel with large angular abrasives

LB Wheel with large blocky abrasives

LFS Lateral free surfaces

LHS Left hand side

m Flow exponent

MBG Metal bonded grit

N'_d Specific active number of cutting edges

$ORNL$ Oak Ridge National Laboratory

P'_w Grinding specific power

P_w Grinding power

PCF Plastic constraint factor

PD Plastic deformation

PDD Plastic Deformation Depth

pdf Probability distribution function

PE Plane strain

$PEEQ$ Equivalent plastic strain

PS Plane stress

R_a Surface average roughness

R_r Roughness related empirical constant

RHS Right hand side

rnd Random

RS Residual stress

RT Room temperature

SA Wheel with small angular abrasives

SB Wheel with small blocky abrasives

sd Standard deviation

SEM Scanning electron microscopy

$SMRR$ Specific material removal rate

t Time

V_e Strain gage applied voltage

V_R^g Strain gages reflected voltage signal

V_s Wheel peripheral speed

V_T^g Strain gages transmitted voltage signal

V_w Workpiece or table speed

W_f Wear factor

W_r Wheel wear

z Distance to the wheel surface

z^* Wheel engagement depth

SYMBOLS

α_g Grit attack angle

β Dimensionless constant determined by the indentation geometry

$\dot{\gamma}_0$ Reference shear rate

$\dot{\gamma}^{\alpha}$ Shear rate per slip system

δ dimensionless constant determined by the indenter geometry

ε'_{ij} Strain components in the laboratory reference system

ε_{ij} Strain components in the sample reference system

Θ One half detector angle or Bragg angle

θ_a Abrasive cone angle

λ X-ray wavelength

μ Linear absorption coefficient

ν Poisson's ratio

ν_s Wheel's Poisson's modulus

ν_w Workpiece Poisson's modulus

ϖ_s Angle of shadow

ρ Density

ρ_b Split Hopkinson test bar density

$\underset{\sim}{\sigma}^{pk(2)}$ Second Piola-Kirchhoff stress

σ_R Rayleigh pdf parameter

τ^{α} Resolved shear stress in each slip system

τ_{CRSS} Critical resolved shear stress

Φ Azimuthal or polar angle

χ Rocking angle

Ψ Tilt angle

Ω Incident angle

$\underset{\sim}{\Omega}$ Total spin tensor

$\underset{\sim}{\Omega}^e$ Elastic spin tensor

$\bar{}$ Intermediate configuration

$\breve{}$ Intermediate configuration

$\hat{}$ Corotational (with the continuum rotation) intermediate configuration

$\tilde{}$ Intermediate unstressed configuration

$C_{\theta,\rho}$ Elastic constant on generic polar direction

$\underset{\sim}{\underset{\sim}{C}}$ Fourth order stiffness tensor

$\underset{\sim}{C}^e$ Elastic right Cauchy-Green tensor

$\underset{\sim}{C}^p$ Plastic right Cauchy-Green tensor

$\underset{\sim}{D}$ Total symmetric part of the velocity deformation gradient tensor

$\underset{\sim}{D}^e$ Symmetric elastic part of the velocity deformation gradient tensor

$\underset{\sim}{D}^p$ Symmetric plastic part of the velocity deformation gradient tensor

$d_{\{hkl\}}$ Interplanar distance at the stressed condition for family of planes {hkl}

$d^0_{\{hkl\}}$ Interplanar distance at the unstressed condition for family of planes {hkl}

$\underset{\sim}{F}$ Total deformation gradient

$\underset{\sim}{F}^e$ Elastic deformation gradient

$\underset{\sim}{F}^p$ Plastic deformation gradient

g^α Drag stress per slip system

$h_{\alpha\beta}$ Hardening coefficients matrix

$I_{2\Theta}$ Intensity at the specified angle 2Θ

I_{peak} Intensity scaling parameter

$\underset{\sim}{L}$ Total velocity deformation gradient tensor

$\underset{\sim}{L}^e$ Elastic velocity deformation gradient tensor

$\underset{\sim}{L}^p$ Plastic velocity deformation gradient tensor

$\underset{\sim}{n}_0$ Unit vector normal to the slip plane

$\underset{\sim}{R}$ Continuum rotation tensor

$\underset{\sim}{R}^p$ Continuum plastic rotation tensor

$\underset{\sim}{U}$ Right stretch tensor

$\underset{\sim}{U}^p$ Plastic right stretch tensor

$\underset{\sim}{V}$ Left stretch tensor

$\underset{\sim}{n}$ Generic polar unit vector

$\underset{\sim}{s}_0$ Unit vector in the slip direction

$\underset{\sim}{W}$ Total skewsymmetric part of the velocity deformation gradient tensor

$\underset{\sim}{W}^e$ Skewsymmetric elastic part of the velocity deformation gradient tensor

$\underset{\sim}{W}^p$ Skewsymmetric plastic part of the velocity deformation gradient tensor

X Lagrangian, reference, undeformed, or initial configuration

x Eulerian, spatial, deformed, or current configuration

SUMMARY

Gamma-TiAl is an ordered intermetallic compound characterized by high strength to density ratio, good oxidation resistance, and good creep properties at elevated temperatures. However, it is intrinsically brittle at room temperature. This thesis investigates the potential for the use of grinding to process TiAl into useful shapes. Grinding is far from completely understood, and many aspects of the individual mechanical interactions of the abrasive grit with the material and their effect on surface integrity are unknown. The development of new synthetic diamond superabrasives in which shape and size can be controlled raises the question of the influence of those variables on the surface integrity.

The goal of this work is to better understand the fundamentals of the abrasive grit/material interaction in grinding operations. Experimental, analytical, and numerical work was done to characterize and predict the resultant deformation and surface integrity on ground lamellar gamma-TiAl.

Grinding tests were carried out, by analyzing the effects of grit size and shape, workpiece speed, wheel depth of cut, and wear on the subsurface plastic deformation depth (PDD). A practical method to assess the PDD is introduced based on the measurement of the lateral material flow by 3D non-contact surface profilometry. This method combines the quantitative capabilities of the microhardness measurement with the sensitivity of Nomarski microscopy. The scope and limitations of this technique are analyzed. Mechanical properties were obtained by quasi-static and split Hopkinson bar compression tests. Residual stress plots were obtained by x-ray, and surface roughness and cracking were evaluated.

The abrasive grit/material interaction was accounted by modeling the force per abrasive grit for different grinding conditions, and studying its correlation to the PDD. Numerical models of this interaction were used to analyze boundary conditions, and abrasive size effects on the PDD. An explicit 2D triple planar slip crystal plasticity model of single point scratching was used to analyze the effects of lamellae orientation, material anisotropy, and grain boundaries on the deformation.

CHAPTER I

INTRODUCTION

1.1 Historical Perspective

Grinding is one of the earliest shaping processes known to man. In the Neolithic Period (15000 to 5000 B.C.) it was used to shape stone tools. Grinding is based on the progressive abrasive wear of the workpiece by a number of hard grits embedded in a matrix. Mechanization of grinding had been developed by the middle of the 15^{th} century but the first grinding machine was not built until about 1830 (Woodbury, 1959). Early research on grinding was based on empirical knowledge but the need for precision and speed required by the 20^{th} century's industry provided the driving force for more specialized research in the area. During the 1970's and 1980's numerous phenomenological models were developed as shown in Shaw (1972), Hahn and Lindsay (1982a,b,c,d), and Malkin (1989). This trend faded for several reasons: basic industry needs were met, the work yielded only particular results, the models needed to be calibrated with extensive, time consuming and expensive tests, and during the last years cylindrical grinding has been replaced by hard turning. The research reported in this thesis re-examines grinding as a cost effective technique for shaping intermetallic compounds, and its implications for surface integrity. Intermetallic compounds refer to a phase type formed when atoms of two or more metals combine in relatively simple stoichiometric proportions to produce a crystal different in structure from the individual metals. The constituent elements have strong bonds, that typically include metallic, ionic or covalent types and are usually ordered in two or more sublattices, each with its own distinct population of atoms. Intermetallics have long-range order on their crystal structure below a critical temperature. Deviations from precise stoichiometry on one or both sides of the nominal ideal atomic ratios produces partial disorder. The relatively high activation energy for chemical diffusion in the ordered lattice causes high creep resistance at elevated temperatures. The ordered intermetallic structure is characterized by a high strength to density ratio, good oxidation resistance, and good creep properties at elevated temperatures. However, this intrinsically strong atomic bonding is often associated with brittleness at room temperature (Larsen

et al., 1996), making the shaping process critical to structural integrity. The interest in $\gamma - TiAl$ intermetallic compounds started in the 1950's motivated by its light weight and its potential for the kind of high temperature applications such as needed by the aeronautical industry (Kim, 1995; Dimiduk et al., 1992; Austin et al., 1997). Potential applications in combustion engines include valves, turbine wheels of exhaust gas turbochargers, connecting rods, and piston pins. The mass reduction leads to improved fuel economy and higher engine performance due to a considerable decrease of inertia and friction losses. Grinding of $\gamma - TiAl$ holds the promise of precision high performance components free of critical defects at minimum time and cost.

1.2 Gamma-TiAl

Intermetallic $TiAl$-based alloys are well suited for rotary and reciprocating components in engines under high thermal and mechanical load because of their high-temperature properties (Kim, 1989; Kim and Dimiduk, 1991; Clemens et al., 1999; Clemens and Kestler, 2000; Knippscheer and Frommeyer, 1999). These properties include low density ($\simeq 3.8 g/cm^3$), acceptable yield strength ($400 - 650 MPa$), high specific stiffness ($E/\rho \simeq 46 GPa\ cm^3/gm$), and good oxidation resistance and creep up to 700°C, at which limitations might arise from microstructural instabilities (Chatterjee et al., 2000) which degrade the creep properties, and from an insufficient oxidation resistance (Brady et al., 1996). From room temperature to $800°C$ the thermal expansion coefficient ranges from 11.5 $10^{-6} K^{-1}$ to 12.5 $10^{-6} K^{-1}$, while the thermal conductivity ranges from $19 W/m\ K$ to $43 W/m\ K$. These values exhibit sufficient thermal compatibility to other engine materials, such as steels or Ni-based alloys (Knippscheer and Frommeyer, 1999). These properties make $TiAl$ also appealing for applications as thin films for structural coatings (Kim et al., 2004).

1.2.1 Phase Diagram and Microstructure

Figure 1.1 shows the binary equilibrium phase diagram of Ti-Al (Kattner et al., 1992; Ohnuma et al., 2000). Most of the research has been focused on the Ti-(45-48)Al (at.%) composition, where balanced properties of fracture toughness, fatigue life, and tensile strength are achieved. At the binary composition of Ti-47Al the material begins to solidify partially in the two-phase region $L \rightarrow L + \beta$, β being a disordered BCC (body centered cubic) phase. The material then goes through a transformation $L + \beta \rightarrow L + \alpha$, in which α is a disordered HCP (hexagonal closed packed) phase.

During cooling it follows the solid-solid, diffusion controlled, eutectoid transformation $\alpha \rightarrow \alpha + \gamma$, where γ is an ordered FCT (face centered tetragonal) superlattice with the structure $L1_0$ (Strukturbericht symbol) or $tP2$ (Pearsons symbol). The final transformation is $\alpha + \gamma \rightarrow \alpha_2 + \gamma$; α_2 being an ordered HCP superlattice with $D0_{19}$ or $hP2$ structure. At the binary phase zone the α_2 phase is Ti_3Al ($L1_0$) while the γ is $TiAl$ ($D0_{19}$). The γ FCT unit cell is only slightly distorted ($c/a \simeq 1.02$) and consists of alternating planes of Ti and Al atoms in the [001] direction. From the phase diagram the proportion of γ phase is significantly greater than that of α_2 at Ti-47Al composition. Figure 1.2 represents the $TiAl$ and Ti_3Al crystal structures.

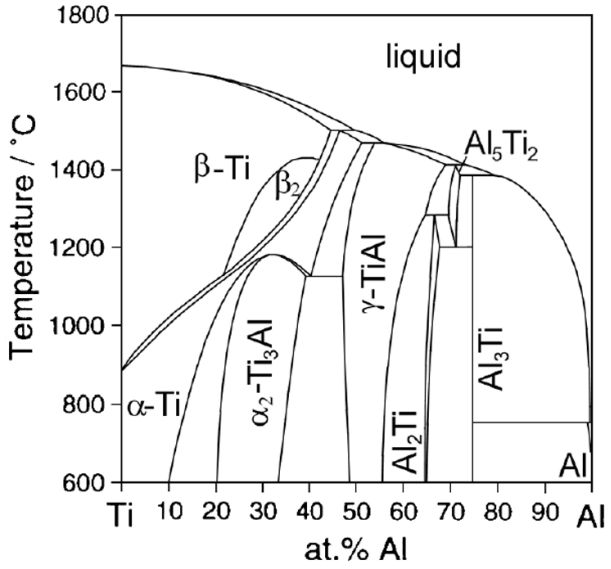

Figure 1.1: Equilibrium phase diagram of TiAl (Kattner et al., 1992; Ohnuma et al., 2000).

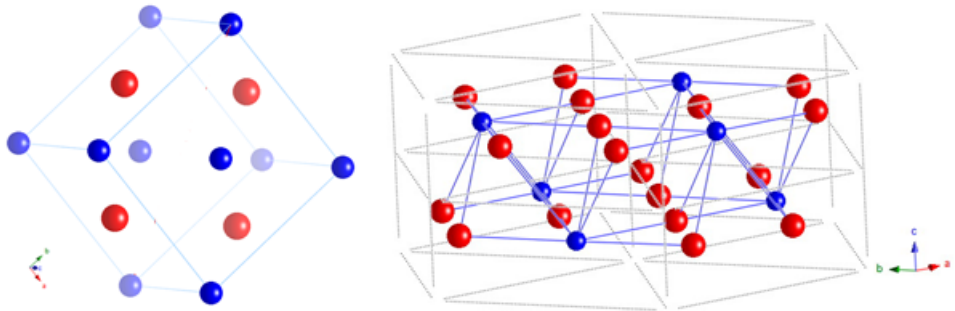

Figure 1.2: $TiAl$ (left) FCT-like structure and Ti_3Al (right) HCP-like structure. Ti atoms in red.

The lamellar structure is formed by nucleation and growth of γ plates (Yamabe et al., 1994) from

the α phase with little compositional adjustment, in which layers of α_2-γ are piled up with crystallographic alignment at the phases interface such that $\{111\}_\gamma||(0001)_{\alpha_2}$ and $[1\bar{1}1]_\gamma|| < 11\bar{2}0 >_{\alpha_2}$. However, the $[\bar{1}10]$ direction and the other two $[10\bar{1}]$, and $[0\bar{1}1]$ directions on (111) in the γ phase are not equivalent to each other because of the tetragonal $L1_0$ structure of the γ phase, while directions of $\langle 11\bar{2}0\rangle$ on the basal plane in the α_2 phase are all equivalent. Thus, when the γ phase precipitates from the α parent phase, the $L1_0$ structure can be formed in six orientation variants corresponding to the six possible orientations of the $[\bar{1}10]$ direction on the α phase along a reference $\langle 11\bar{2}0\rangle$ direction on the α_2 phase (Yamaguchi and Inui, 1993). Adjacents γ plates can be rotated by $60°n$ with $0 \leq n \leq 5$, and/or translated by 0, $1/2\langle 10\bar{1}]$, $1/6\langle 11\bar{2}]$ or $1/6\langle 1\bar{2}1]$ lattice vectors, with respect to the other γ plate (Yamaguchi et al., 2000). Domains of different variant types can coexist within each γ lamella (Feng et al., 1989; Inui et al., 1992b). Such domain boundaries as well as γ/γ lamellar boundaries are all γ/γ intervariant boundaries.

1.2.2 Thermal Treatment and Alloys

In the disordered-ordered transformation at high cooling rates a massive transformation occurs, and at slower cooling rates a lamellar transformation takes place as pointed out by Hono et al. (1996) and shown in Figure 1.3. A microstructural classification system has been proposed by Kim (1994), which defines four types of microstructure: near-gamma, duplex, nearly lamellar and fully lamellar. The Al-deficient $TiAl$ alloys can be subject to different heating/quenching/annealing cycles transforming to the γ, α, and α_2 single and multi-phase regions of the phase diagram to produce α_2-γ fully lamellar, equiaxed (with small amounts of α_2), and duplex equiaxed +lamellar $+\alpha_2$ microstructural morphologies (Yamabe et al., 1995; Zhang et al., 2000). Multiple heat treatments have also been used as a grain refining method (Cao et al., 2000). Generally, the influence of microstructure on mechanical properties of $\gamma - TiAl$-based alloys can be summarized as follows: coarse-grained fully lamellar microstructures exhibit relatively good fracture toughness and excellent creep resistance, but poor tensile ductility and strength especially at room temperature. Relatively fine-grained equiaxed primary annealed, near-gamma, duplex microstructures with only small amounts of lamellar colonies show low fracture toughness and creep resistance

but moderate tensile ductility and strength at room temperature and elevated temperatures (Marketz et al., 2003). Clemens and Kestler (2000) have shown that thermomechanical processing and heat treatments have a strong influence on the actual γ/α_2-volume fraction in $\gamma - TiAl$-based alloys. In thermodynamic equilibrium, the γ/α_2 volume fraction is controlled by the Al-content and additional alloying elements and is typically in the range of $0.05 - 0.2$ (Kim, 1989, 1994).

Several alloying elements are utilized to improve the mechanical and chemical properties of $TiAl$. The composition (in at.%) of conventional engineering $\gamma - TiAl$-based alloys can be summarized as follows (Marketz et al., 2003):

$$Ti_{45-52} - Al_{45-48} - X_{1-3} - Y_{2-5} - Z_{<1}$$

where

$$X = Cr,\ Mn,\ V; \quad Y = Nb,\ Ta,\ W,\ Mo; \quad Z = Si,\ B,\ C$$

The alloying elements marked with X, Y, and Z all affect more or less the position of the phase boundaries in the Ti-Al binary phase diagram (Kim, 1989; Kattner et al., 1992; Hall and Huang, 1991). The addition of Cr appears to reduce the τ_{CRSS} (critical resolved shear stress) for $1/2\langle 110]$ dislocation motion, while Mn and V appear to reduce the τ_{CRSS} for $1/2\langle 110]$ dislocations and the the stacking fault energy (Hao et al., 1999), and thus increase the ductility of the alloys at room temperature by increasing the propensity for mechanical twinning (Kawabata et al., 1989). The other elements are used to improve high temperature characteristics such as oxidation resistance (Nb, Shemet et al. 1999; Ta, Yamaguchi and Umakoshi 1990; Mo, Perez et al. 2000; Zr, Shemet et al. 1999), high temperature strength (Nb, Tetsui 2002), and creep resistance (Si, Noda et al. 1995; Viswanathan et al. 1999; W, Seo et al. 2001; C, Viswanathan et al. 1999). Boron is typically used as a grain refining agent. In alloys with a trace amount of Boron ($B \leq 0.03$at.%), the solute drag effect of Boron atoms appears to be the controlling factor on the lateral thickening of γ lamellae, resulting in fine lamellar spacing. In alloys containing a certain amount of Boron ($B \geq 0.1 - 0.2$at.%), the presence of fine boride particles reduces the undercooling required for lamellar formation and as a result, coarse lamellar spacing was observed (Zhang and Deevi, 2002). McQuay et al. (1999) have shown that the minimum creep rate is a decreasing function of the volume fraction of lamellar grains in near lamellar and duplex $Ti - 47Al - 2Nb - 2Mn$ with TiB_2 alloy.

Textures play a special role in the $\gamma - TiAl$ based intermetallic alloys. Under industrial conditions with relatively slow solidification the ingots have a dendritic growth in the direction of heat flow and a very strong local texture. The lamellae planes $\{111\}$ are aligned normal to the solidification direction and are parallel to the cylindrical surfaces of the ingots. Pores and microscopic shrinkage cavities within the as-cast material can be eliminated by an adequate hot isostatic pressing (HIP) process or thermomechanical treatment.

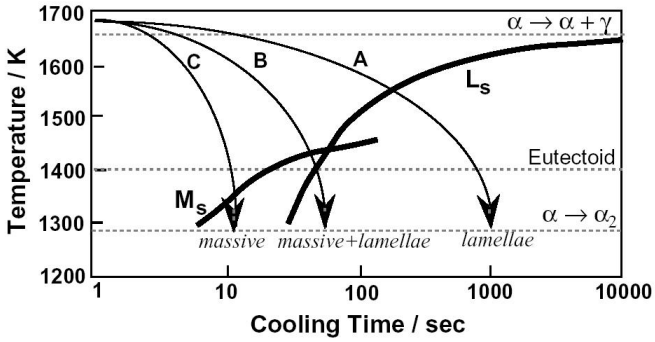

Figure 1.3: CCT curves showing the solid-solid transformation on Ti-48Al (Hono et al., 1996).

1.2.3 Deformation Mechanisms

The deformation modes of $\gamma - TiAl$-based alloys strongly depend on their microstructure, alloy composition and temperature. The single $\alpha_2 - Ti_3Al$ phase is more hard and brittle than the $\gamma - TiAl$ phase and it has a significant effect on the mechanical properties, deformation behavior and ductility of $\gamma - TiAl$ two phase alloys. It is well established (Inui et al., 1992a; Yamaguchi and Umakoshi, 1990; Appel and Wagner, 1998) that deformation of $\gamma - TiAl$ under most conditions occurs on $\{111\}$ planes by activation of ordinary dislocations with the Burgers vector $b = 1/2\langle 110\rangle$ and superdislocations with the Burgers vector $b = \langle 101\rangle$ and $b = \langle 11\bar{2}\rangle$, respectively. In addition mechanical twinning along $1/6\langle 11\bar{2}\rangle\{111\}$ occurs that does not alter the ordered $L1_0$ structure of the $\gamma - TiAl$. Figure 1.5 shows the potential slip and twinning systems of the $L1_0$ structure, in the schematic drawing of a three-layer sequence of atom stacking on the (111) plane. It can be seen from Fig. 1.5 that along the $\langle 110\rangle$-directions there is only one type of atom (either Ti or Al). This type of dislocation is called ordinary dislocation, and referred to as "easy slip". By contrast Ti-atoms and Al-atoms interchange in $\langle 011\rangle$-directions and, therefore, the so-called superdislocations

must activate in $\langle 011 \rangle$-directions which are dissociated into two $1/2\langle 101 \rangle$-dislocations separated by an APB (antiphase boundary). This is referred to as "hard slip". Additionally, the $L1_0$ structure can be twinned by the $\{111\}\langle 11\bar{2}]$ variants of the normal FCC twinning mode. As shown in Fig. 1.5, the Burgers vector $b_3 = 1/6[11\bar{2}]$ preserves the order of $\gamma - TiAl$ and this twinning mode is, therefore, called true twinning. Partial dislocations by Burgers vectors $b_1 = 1/6[\bar{2}11]$, and $b_2 = 1/6[1\bar{2}1]$, respectively, change the order of $\gamma - TiAl$ and these modes are called pseudo twinning. The relative contributions of the individual mechanisms to the deformation mainly depend on the aluminium concentration, the content of ternary elements and the deformation temperature (Appel and Wagner, 1998). In the $\alpha_2 - Ti_3Al$ phase the possible slip modes are $10\bar{1}0\langle 1\bar{2}10 \rangle$ prism slip; $(0001)\langle 1\bar{2}10 \rangle$ basal slip, and $\langle 11\bar{2}6 \rangle$ pyramidal slip with very different values of τ_{CRSS} (Umakoshi et al. (1993)).

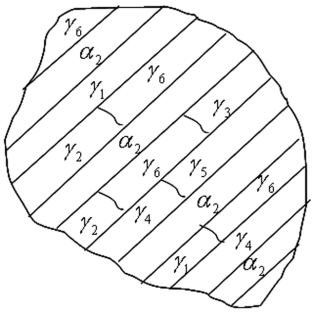

Figure 1.4: Lamellae colony showing the α_2 phase and different variants of γ phase.

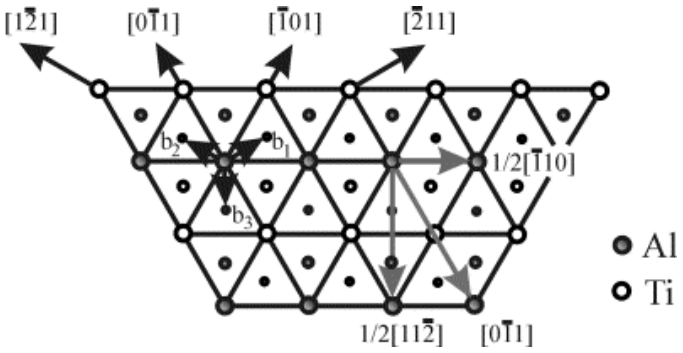

Figure 1.5: Potential slip and twinning systems of the $L1_0$ structure (Appel and Wagner, 1998).

1.3 Grinding

Grinding is a material removal process that is used to achieve fine surface finishes, tight geometric tolerances, and complex contours. Grinding is a multipoint machining process with a stochastic distribution of tool geometries like grain size, rake (attack) angle, etc., producing a distribution on process parameters such as grit force, grit depth of cut, among others. Due to the negative rake angle of the grinding wheel abrasive grits, the specific cutting energy (energy consumed to remove a unit volume of material) of this process is higher than in other machining processes like turning, milling, etc. (Wang and Subhash, 2002). Consequently the material is subjected to high plastic deformation and temperature gradients. There are four primary types of grinding according to the workpiece desired geometry: surface, cylindrical, internal, and centerless grinding (Tlusty, 1999). Although surface grinding is the focus of this research the results can be utilized for other grinding operations. Also, grinding can be categorized according to the DoC, as creep-feed grinding used for stock removal where the DoC is of the order of several millimeters; and finish grinding where DoC is of the order of a micron to several tens of microns as in the present work. Figure 1.6 shows a schematic of a surface grinding process. In this case, the wheel of diameter ds is rotating

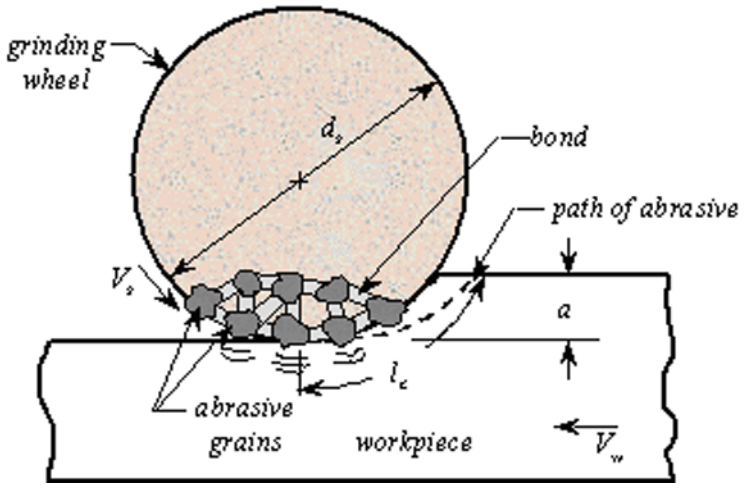

Figure 1.6: Schematics of grinding.

counterclockwise, while the workpiece is moving from right to left; the wheel peripheral speed V_s and the workpiece speed V_w are in opposite directions; this kinematic configuration is called upgrinding. The wheel DoC (a) is typically 10-50μm, but it should be noted that the penetration depth of single abrasive grits on the material is much smaller than this DoC. The wheel is in

contact with the workpiece along the contact length l_c, in a width b, perpendicular to the page and parallel to the axis of rotation. Conventional grinding uses Al_2O_3 (aluminum oxide), and SiC (silicon carbide), and with the industrial production of synthetic superabrasive particles, CBN (cubic boron nitride) and diamond have come into current use. These superabrasives are considerably harder than conventional abrasives allowing the machining of hard materials while presenting less wear. Figure 1.7 shows a simplified schematic of the input-output variables in grinding. The wheel topography is defined by the size, size distribution, shape, and concentration of the abrasive used along with the dressing tools and kinematics. During grinding, forces are applied to the abrasive grits which are embedded in a matrix. The elastic displacements of individual engaged grits are of the order of magnitude of the abrasive grit DoC, therefore, the knowledge of the wheel topography and the kinematic conditions are the base for modeling the chip geometry (Verkerk and Peters, 1977). With the consideration of the workpiece mechanical properties and cooling conditions, single grit forces can be obtained (Shaw, 1972). Output variables such as forces, power, temperature, geometry, surface integrity, and wheel wear are obtained. It has to be noted that most of the variables are stochastic in nature and strongly coupled, which complicates the understanding of grinding and is the main reason why the empirical knowledge of the process is far ahead of theoretical developments. As an example, wheel wear will affect wheel topography and all linked variables. The complexity of wear can be appreciated from the work of Meng and Ludema (1995); and Ludema (1996) where more than 300 equations were surveyed for modeling friction and wear and the reason of this diversity (and lack of fitness) were analyzed.

Abrasive grit size affects the amount of material that is involved in the deformation process. Wheel grit size varies typically from $40\mu m$ to $300\mu m$, but only a small fraction of an abrasive grit is actually interacting with the material. Typically the depth of cut of each grain is of the order of a few microns and the width of the groove left is of the order of tens of microns. One question that arises is if the same deformation mechanisms are acting with different grit sizes (Begley and Hutchinson, 1998), since at different grinding operation conditions the cutting specific energy depends of the DoC (Hwang et al., 1999; Wang and Subhash, 2002).

Numerous studies in machining have shown that different tool geometries (rake angle, nose radius, etc.) have a great influence on the machining forces and surface finishing (Briscoe et al.,

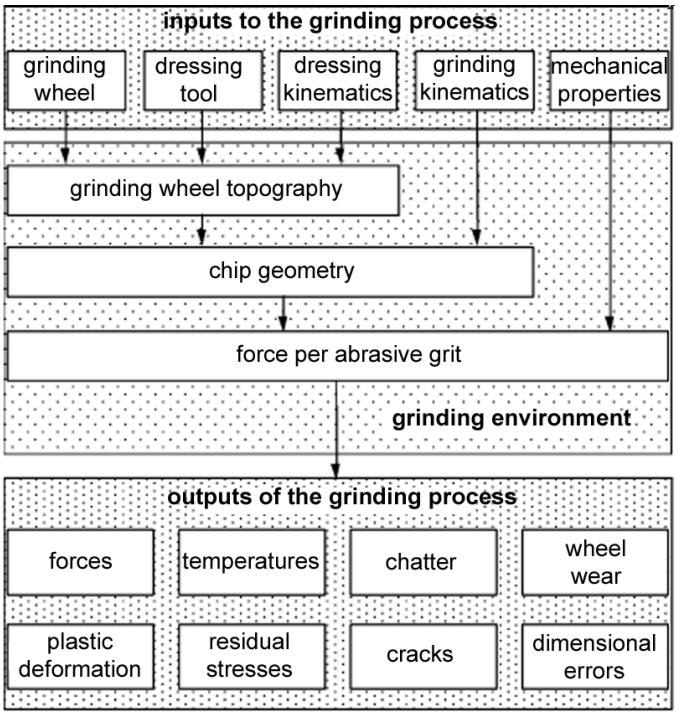

Figure 1.7: Input/output variables in grinding (modified from Chen et al., 2002).

1991; Tlusty, 1999) and it is well known (Hutchings, 1992; Williams, 1999) that given certain geometrical conditions there is a threshold of grit rake angle below which plowing occurs without material removal. There is not a precise definition of the grain shape to describe abrasive grits. Several factors are considered in defining the abrasive grit geometry as more "angular" or more "blocky". These factors take into account parameters like the area to perimeter ratio, deviation from a perfect sphere, and others not disclosed by manufacturers. It can be argued that blocky shaped grits will produce a greater hydrostatic stress state in the material compared with angular shapes. In several models the abrasive grit tip radius is considered spherical with the radius as a fraction of the grain size (Shaw, 1972), some other models simplify it as conical (Badger and Torrance, 2000).

Another consideration involves the material time-dependent behavior. At low deformation rates material deformation mechanisms are allowed to act and redistribution of deformation (and stresses) takes place, preventing localized plastic flow in specific shearing bands and/or planes of fracture with the consequent material removal. The deformation rate in high speed machining is in the range of $10^3 - 10^5 sec^{-1}$ (Subhash et al., 1999).

1.4 Effects of Machining on Gamma-TiAl

Machining processes can have an effect on the mechanical properties of the workpiece, in particular they can impact the high cycle fatigue (HCF) performance which is different from the one predicted using polished samples (Trail and Bowen, 1995; Bentley et al., 1999; Jones and Eylon, 1999; Sharman et al., 2001b; Novovic et al., 2004), and tensile properties (Schneibel et al., 1993; Darolia and Walston, 1996). These effects can be positive in incrementing the HCF life by leaving a surface layer with compressive residual stress (Balart et al., 2004) or recrystallized material of smaller grain size compared to the parent (Jones and Eylon, 1999); but detrimental effects are more often observed due to generation of cracks or tensile residual stress.

The high energy input during grinding creates a temperature gradient with the consequent thermal deformation gradient and the possibility of generating tensile residual stresses (Mahdi and Zhang, 1997), cracking (Eda et al., 1983), and dimensional instabilities (Kagiwada and Kanauchi, 1985). Also, the material thermomechanical history has to be considered. As grinding is a multipass process, subsurface material layers are subjected to thermal and mechanical deformation cycles. Also, it is important to consider that plastic deformation and damage are cumulative in the material where usually no healing processes take place during machining. Therefore low cycle fatigue may be the cause of fracture in some brittle intermetallic compounds or ceramics during grinding.

Residual stresses (RS) in grinding can originate from a contribution of thermomechanical effects that produce inhomogeneous deformation. Some causes are the scratching of abrasive grits, cumulative deformation leading to fracture, thermally-induced deformation, or due to phase transformations in which there is a volume change (Mahdi and Zhang, 1997). Grinding operating conditions can leave either compressive, in what was called "gentle grinding conditions" or tensile residual stresses in "abusive grinding conditions" as shown in Fig. 1.8 by the early work of Field (1972). During grinding thermal effects become important when material properties are sensitive to temperature, where phase transformations or thermal cracking may take place (Grum, 2001). Thermally activated mechanisms will be favored, with eventual changes of the material behavior (i.e. brittle/ductile transition, dislocation annihilation, etc). The compressive/tensile residual stress transition is due in part to thermal effects as shown by Balart et al. (2004), who have found that a material dependent critical surface temperature has to be reached to left tensile residual

stresses. Measurements of residual stress on $\gamma - TiAl$ by use of different techniques has been made by Kondoh et al. (1999), Richter and Hofmann (2002), and Bentley et al. (2001).

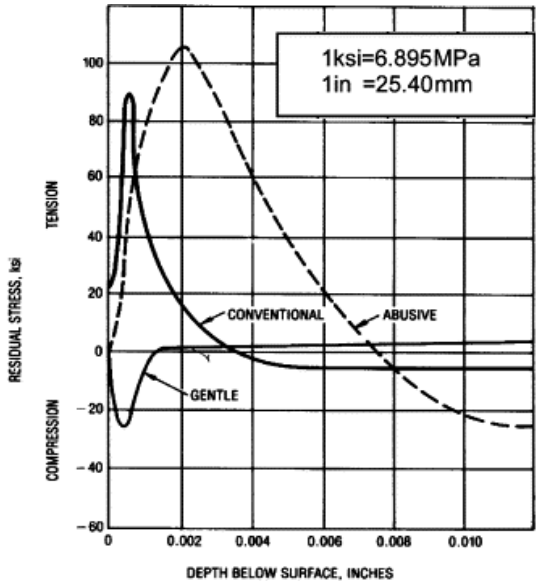

Figure 1.8: Residual stress for an AISI 4340 steel under different grinding conditions (Field, 1972).

1.5 Surface Integrity Evaluation

Surface integrity refers to studies of the changes of surface topography and geometry, and subsurface physical and chemical characteristics such as composition, microstructure, phases, residual stresses, hardness, cracking, and embrittlement among other effects due to machining or another surface generating operation. A review done by Field et al. (1972), and Brinksmeier (1989) describes some of the techniques to evaluate surface integrity such as optical and electronic microscopy, x-ray in both the diffraction and the fluorescent mode, ultrasound used in scanning acoustic microscopy to give information on the physical or even chemical nature of superficial layers, Raman spectroscopy for studying superficial structures, chemical composition and stresses in crystalline and amorphous materials, instrumented microindentation for evaluating mechanical material properties like hardness and Young's modulus, and photothermal microscopy for the non-destructive testing of the local thermal properties of materials among others. The work reported here is not only related to the evaluation of the plastic deformation depth, but also residual stress, cracking, and machined surface roughness as measures of surface integrity.

1.5.1 Plastic Deformation Depth Measurement

Measurement of hardness due to cold work in the subsurface is one of the most widespread methods for determining deformed zones. These measurements are usually represented as plots of hardness versus depth taking as a base line the bulk hardness such as shown in the work of Field et al. (1972); Bentley et al. (1999); Jones and Eylon (1999). The size of the hardened zone is of the order of tens to hundred of microns, and microhardness techniques need to be used in order to measure the hardness gradient. Some techniques are the micro-Vickers, Knoop, and Berkovich, whose description can be found somewhere else, for example in Newby (1989). Scratching is a derivation of the microhardness technique, and it consists of scratching the material with a given force and then measuring the scratched groove width as a function of distance to the edge. Simple models can be applied to determine the hardening (Liu et al., 2002). A disadvantage of this technique is the scatter that usually accompanies the results. This scatter is due to uncertainties in measurement of the indent diagonals, and in the case of $\gamma - TiAl$, its anisotropic mechanical behavior, and heterogeneity of properties between the α_2 and γ phases, that distorts the indent geometry. Another disadvantage is that microhardness cannot be measured close to deformed edges, not only because of lack of surrounding material, but also because the lack of surface planarity impairs indentation.

Optical microscopy is another technique to evaluate PDD (plastic deformation depth) and it is based on the observation of ridges at surfaces. It usually uses Nomarski illumination which is especially suited for the evaluation of surface quality and defects that otherwise with regular microscopy/SEM would not be visible (see Robinson and Bradbury, 1992). The Nomarski illumination method incorporates polarization and phase shift techniques that cause minute departures of the surface from a perfect plane to appear as different colors. All quantitative measurements are made by using a reticule in the optics objective. As with any observational technique the disadvantage is that it is subjective.

Xu and Jahanmir (1994) developed the bonded interface, or split specimen technique, to observe damage on machined ceramics using Nomarski microscopy. Damage was defined in their work as the presence of cracks, and/or twins, and/or slip bands. In their technique two polished surfaces of the (split) sample are glued together with cyanoacrylate (super glue), the specimen is machined and the two surfaces are separated and placed under the microscope.

Nelson (1997) utilized the bonded interface technique to observe the PDD on ground $TiAl$ samples and further implemented the use of a profilometer to evaluate the damaged zone by changes in the surface roughness. Under conditions of plastic deformation, twins/shear bands will produce some roughness on the polished surfaces of the sample. Razavi (2000), and later Stone (2003) had used the same technique for measuring PDD in their work. The disadvantage of this technique lies in the difficulty of surface sample preparation, and the resulting variable spacing of the glued interfaces in the sample and, between samples, that leads to a large variability of results due to variable mechanical constraint conditions.

CHAPTER II

PRESENT WORK

2.1 Motivation

Grinding of $\gamma - TiAl$ is far from completely understood, and many aspects of the individual mechanical interactions of the abrasive grit with the material and their effect on surface integrity are unknown.

Data on machinability, surface integrity, and fatigue performance of $\gamma - TiAl$-based alloys have been published by researchers at The University of Birmingham (Trail and Bowen, 1995; Bentley et al., 1999, 2001; Sharman et al., 2001a,b; Mantle and Aspinwall, 2001; Novovic et al., 2004). They have carried out hardness profiling, 2D surface roughness parameters determination, microscopy cracking evaluation, and in some cases residual stress measurements by using the hole drilling method and strain gages. All the experimental data were analyzed statistically with the operation parameters and their conclusions based on that analysis.

Jones (1997); Jones and Eylon (1999) have worked on the fatigue resistance of machined $TiAl$ at RT on samples with and without heat treatment after machining. After a comprehensive fractographic analysis and microstructure evaluation, they concluded that the fatigue life is affected by machining conditions and that at high temperatures the fatigue crack initiation site changes from surface to bulk. They have observed that a recrystallized zone of smaller grain size is formed on machined surfaces after they were heat treated at 750°C for 1hr. Surface integrity was evaluated with the Nomarski microscopy and hardness profiling. Machining parameters were not explicitly considered nor was a model proposed for the relation of these parameters with the observed behavior.

The work performed at The Georgia Institute of Technology by Nelson (1997); Razavi (2000); and Stone (2003) has been based on the use of the split-sample technique and 2D profilometry to measure subsurface damage, and the use of the model of Lawn and Wilshaw (1975) and Aurora et al. (1979) to relate the total grinding normal force with the damage. Even though the model of Lawn

and Wilshaw (1975) and Aurora et al. (1979) relates the indentation force, material hardness and indenter geometry to the PDD for a single indenter, Nelson (1997); Razavi (2000); and Stone (2003) related the total normal force in grinding with the PDD without considering the indentation process itself. Furthermore, the technique utilized for PDD determination was dependent on the user's experimental skills in sample preparation, selection of the site to measure the profile, and criteria to separate the deformed from the undeformed zone.

The individual mechanical interactions of the abrasive grit in grinding differs from material to material. Models for PDD prediction should account for the interaction of single abrasive grits with the material to have some physical insight of the process. This interaction is produced at the microscopic length scale, and material dependent deformation mechanisms at that scale level should be accounted for. In the present case those are individual lamellae colonies presenting elastic and viscoplastic anisotropy, grain boundaries and their effect on local deformation behavior that can yield to localized failures, and relative abrasive grit/lamellae size effects that will also influence strain localization and failure.

There is also the need to develop a validated and systematic experimental technique to obtain information which could be related to mechanical performance, in particular to HCF. As reported by Jones (1997); Jones and Eylon (1999), the technique of microhardness evaluation is not as sensitive as the Nomarski microscopy to define the PDD because of measurement uncertainties.

The development of new synthetic superabrasives in which shape and size can be controlled raises the question of the influence those variables may have on surface integrity since it can be argued that blocky shaped grits will produce a greater hydrostatic stress state than angular grits.

The progress on testing instrumentation, and specifically the advent of 3D non-contact surface profilometry (Forman, 1979) allows to perform quantitative evaluation of deformed surfaces. Vertical resolution of the order of nanometers can be easily achieved and the possibility of analyzing relatively large areas (of several mm^2) with resolution of the order of microns allows the study of quantitative deformation inhomogeneity i.e. due to grain size effects. The advance in numerical computer software along with computer power allows huge amounts of experimental data to be analyzed in a reasonable time.

The recent advances in crystal plasticity models of $\gamma - TiAl$, along with the improvement on

the kinematics of grinding modeling, present the opportunity to relate the macroscopic grinding variables to the individual grit forces and better understand the fundamentals of the interaction between individual abrasive grits and individual lamellar colonies.

2.2 Objective

To better understand the fundamentals of the abrasive grit/material interaction in grinding operations, and resultant deformation and surface integrity on lamellar $\gamma - TiAl$.

2.3 Methodology and Outline

The present work contains experimental, analytical, and numerical developments as shown in the overview of Fig. 2.1. In the experimental part of the work, Chapter 3 presents the chemical, microstructural and mechanical properties of the present alloy either found in the literature (elastic constants) or obtained through dynamic, and quasi-static compression tests and instrumented indentation. Chapter 4 presents the detailed experimental technique developed for the evaluation of the PDD based on the works of Xu and Jahanmir (1994); and Nelson (1997), with the range of applicability and limitations. Chapter 5 presents the grinding experimental methodology and statistical analysis of results, including PDD, surface parameters, and cracking. Appendix A completes the chapter with the table of the complete set of grinding experimental data. Chapter 6 presents the methodology utilized to measure and analyze RS on the surface and subsurface of selected ground samples, based on the work of Winholtz and Cohen (1988); Wagner et al. (1983); and Richter and Hofmann (2002), as well as the RS data analysis. Appendix B completes the chapter with the data obtained by analysis as well as experimental vs. analytical comparison plots of strain. Chapter 7 presents the modeling of the force per abrasive grit for different grinding conditions based on the work of Hecker (2002). The analysis of the correlation of this parameter with PDD is also presented. Chapter 8 presents the two numerical models used to simulate indentation and scratching of abrasive grits on the material. One model utilizes isotropic elastic-viscoplastic properties and it is utilized to obtain the difference in PDD under PE (plane strain) and PS (plane stress) conditions of indentation and relate the PDD measured at the sample free surface with the one at the material bulk. 3D scratching models were utilized to analyze the variation of PDD

with the applied normal force. An anisotropic elastic-viscoplastic crystal plasticity model based on the works of Kad et al. (1995); McGinty (2001); Dimiduk et al. (2001); and Brockman (2003) was further extended to analyze the effect of lamellar colony/indenter relative size, and lamellae orientation on plastic deformation.

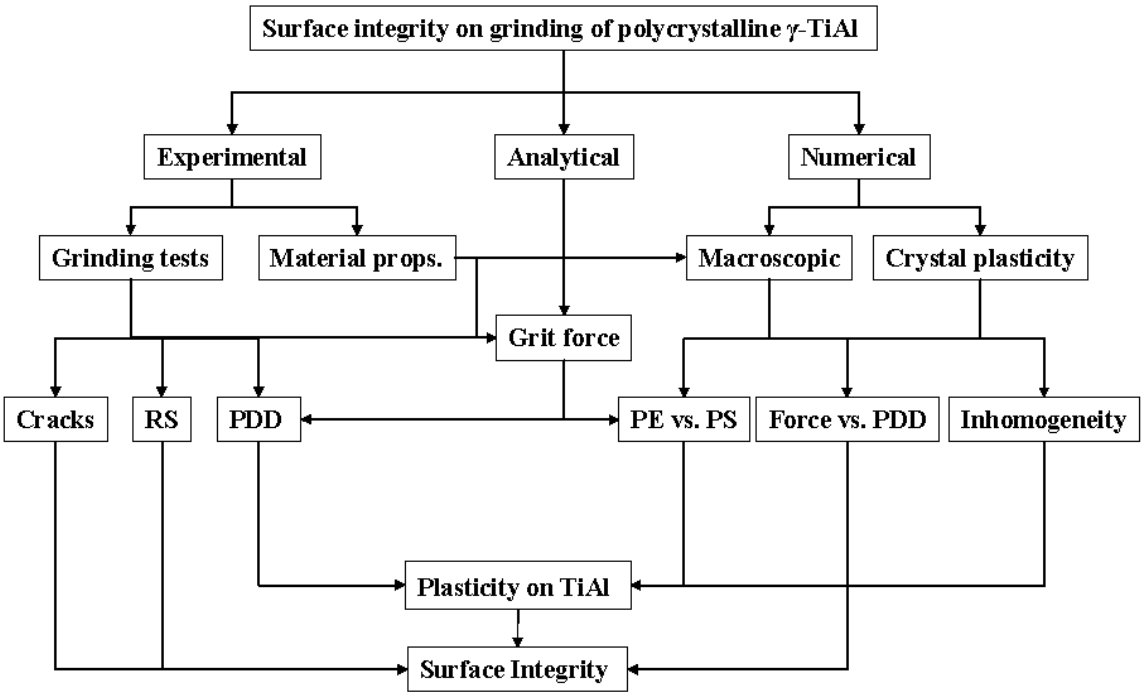

Figure 2.1: Thesis overview.

CHAPTER III

MATERIAL CHARACTERIZATION

This Chapter presents the metallurgical and mechanical material characterization section that was needed for input into the numerical models. Chemical composition and microstructure were analyzed, and the elastic constants of individual phases, and lamellae obtained from the literature. Dynamic and quasi-static compression tests as well as instrumented indentation tests were performed at RT.

3.1 Chemical Composition and Metallography

The alloy used for this research was Howmet's $47XD$ Titanium Aluminide with a composition of Ti-47Al-2Nb-2Mn-0.3B at. %, produced by induction skull melting into slabs of $25mm$ thickness. In order to reduce porosity and homogenize the microstructure, the slabs were HIPped at 1300°C at 165MPa for 4hs with a subsequent heat treatment at 1010°C for 50hs. Figure 3.1 shows the phase diagram of Ti-Al indicating the different phase crystal structure. $TiAl$-based alloys with slightly Al-deficient compositions exhibit γ/α_2 microstructures and often contain a considerable volume fraction of morphologically lamellar colonies as in the present case. The lamellar colonies consist of a majority of variants of γ-TiAl and α_2-Ti_3Al lamellae. The addition of Mn improves the RT ductility (Kawabata et al., 1989; Hao et al., 1999); the addition of Nb improves the oxidation resistance (Shemet et al., 1999), and high temperature strength (Tetsui, 2002), the addition of Boron is used for grain refinement (Zhang and Deevi, 2002), and improved creep resistance (McQuay et al., 1999). Figure 3.2 shows the microstructure of the material used where lamellae colonies of 250μm average size can be observed, while Fig. 3.3 shows a lamellae boundary, where the different orientation of adjacent colonies can be observed.

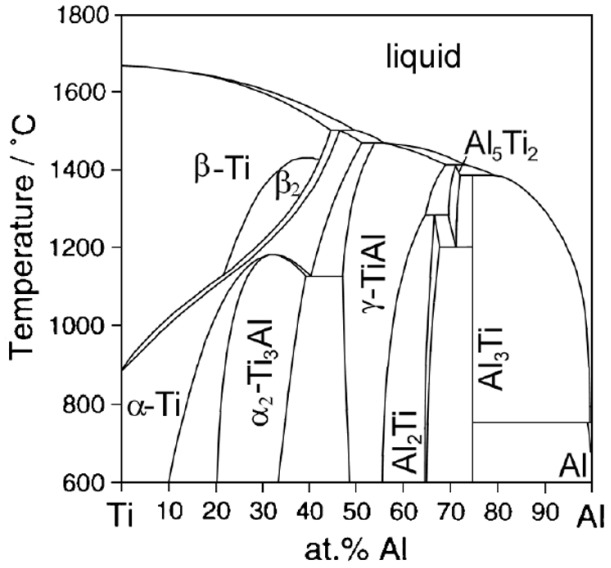

Figure 3.1: Equilibrium phase diagram of Ti-Al (Kattner et al., 1992; Ohnuma et al., 2000).

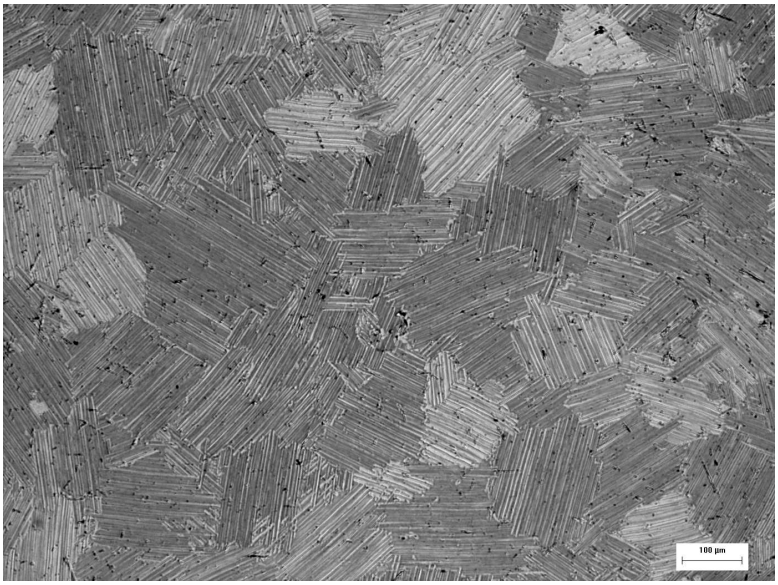

Figure 3.2: Microstructure of the utilized $TiAl$ showing lamellae colonies of 250μm average size.

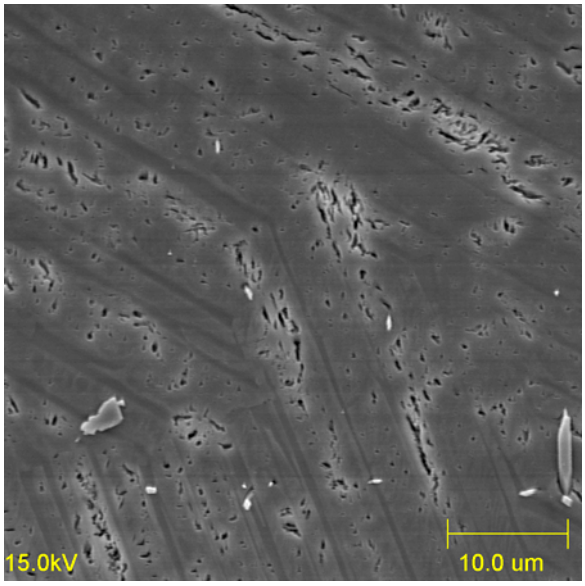

Figure 3.3: Microstructure of the utilized TiAl showing a lamellar colony boundary.

3.2 Elastic Constants

The studied alloy is a two phase lamellar structure, which is the result of phase transformations and ordering reactions occurring during solidification and cooling in which layers of α_2-γ are piled up with crystallographic alignment at the phases interface such that

$$\{111\}_\gamma||(0001)_{\alpha_2} \text{ and } [1\bar{1}1]_\gamma|| < 11\bar{2}0 >_{\alpha_2} \quad \text{(Yamabe et al., 1994)}$$

A laminate material is formed where the ratio of the two phases as well as the thickness of each layer will influence the overall elastic behavior of the colony. It is impractical to model the lamellae explicitly in a polycrystalline material since layer thickness is of the order of 10nm to a few microns. Therefore the effective elastic properties for the lamellar colonies calculated from the constituent properties have to be used. Yoo and Fu (1998) had determined the elastic properties of $\gamma - TiAl$ and $\alpha_2 - Ti_3Al$ phases. Frank et al. (2003) and Brockman (2003) had used these constants to find the effective elastic constants of lamellar colonies of different α_2 to γ ratios using the method proposed by Pagano (1974) developed for laminated orthotropic materials. The elastic constants for colonies with a ratio α_2-γ of 1:10, which is the one used in this work, as well as the constants for each constituent are presented in Table 3.1. For the $\gamma - TiAl$ with a $L1_0$ structure, directions 1, 2, and 3 correspond respectively to the [100], [010], and [001] crystal directions. In the case of

$\alpha_2 - Ti_3Al$ with a $D0_{19}$ structure the direction 1 corresponds to the crystal axis $[11\bar{2}0]$ and the 3 axis is parallel to [0001].

Table 3.1: Elastic constants.

		$\gamma - TiAl$			
$E_{11} =$	140GPa	$\nu_{12} =$	0.284	$G_{12} =$	78GPa
$E_{22} =$	140GPa	$\nu_{13} =$	0.298	$G_{13} =$	105GPa
$E_{33} =$	135GPa	$\nu_{23} =$	0.298	$G_{23} =$	105GPa
		$\alpha_2 - Ti_3Al$			
$E_{11} =$	125GPa	$\nu_{12} =$	0.454	$G_{12} =$	43GPa
$E_{22} =$	125GPa	$\nu_{13} =$	0.154	$G_{13} =$	62GPa
$E_{33} =$	191GPa	$\nu_{23} =$	0.154	$G_{23} =$	62GPa
		1:10 ratio $\alpha_2 - Ti_3Al : \gamma - TiAl$			
$E_{11} =$	187.0GPa	$\nu_{12} =$	0.284	$G_{12} =$	72.6GPa
$E_{22} =$	187.0GPa	$\nu_{13} =$	0.146	$G_{13} =$	66.9GPa
$E_{33} =$	218.9GPa	$\nu_{23} =$	0.146	$G_{23} =$	66.9GPa

Using the Voigt notation, where indices contract as $11 \rightarrow 1$, $22 \rightarrow 2$, $33 \rightarrow 3$, $12 \rightarrow 4$, $13 \rightarrow 5$, and $23 \rightarrow 6$, the fourth order stiffness tensor will be written as shown in Eq. 3.1 for general orthotropic material. The relation between the engineering elastic constants presented in Table 3.1 and the component of the stiffness matrix are given in Eq. 3.2 with the restrictions given by Eq. 3.3. In this case, the material presents transverse isotropy having the stiffness matrix with only 5 independent constants. In its principal direction this matrix is represented by Eq. 3.4. The spatial variation of the directional elastic constant $C_{\theta,\rho}$ is shown in Fig. 3.4, where θ, and ρ define the direction of the generic polar unit vector $\underset{\sim}{n}$ as shown in Eq. 3.5. Figure 3.5 represents the planar variation of the elastic constants for the [100][010] isotropic plane and the [100][001] plane.

$$\underset{\approx}{C} = \begin{bmatrix} C_{11} & C_{12} & C_{13} & 0 & 0 & 0 \\ C_{21} & C_{22} & C_{23} & 0 & 0 & 0 \\ C_{31} & C_{32} & C_{33} & 0 & 0 & 0 \\ 0 & 0 & 0 & C_{44} & 0 & 0 \\ 0 & 0 & 0 & 0 & C_{55} & 0 \\ 0 & 0 & 0 & 0 & 0 & C_{66} \end{bmatrix} \tag{3.1}$$

$$
\begin{aligned}
C_{11} &= E_1 \left(1 - \nu_{23}\nu_{32}\right) \Upsilon \\
C_{22} &= E_2 \left(1 - \nu_{13}\nu_{31}\right) \Upsilon \\
C_{33} &= E_3 \left(1 - \nu_{12}\nu_{21}\right) \Upsilon \\
C_{12} &= E_1 \left(\nu_{21} + \nu_{31}\nu_{23}\right) \Upsilon \\
C_{13} &= E_1 \left(\nu_{31} + \nu_{21}\nu_{32}\right) \Upsilon \\
C_{23} &= E_2 \left(\nu_{32} + \nu_{12}\nu_{31}\right) \Upsilon \\
C_{44} &= G_{12} \\
C_{55} &= G_{13} \\
C_{66} &= G_{23} \\
\Upsilon &= \frac{1}{1 - \nu_{12}\nu_{21} - \nu_{23}\nu_{32} - \nu_{31}\nu_{13} - 2\nu_{21}\nu_{32}\nu_{13}}
\end{aligned}
\tag{3.2}
$$

$$
\begin{aligned}
& C_{11},\ C_{22},\ C_{33},\ C_{44},\ C_{55},\ C_{66} > 0 \\
& |C_{12}| < (C_{11}C_{22})^{\frac{1}{2}} \\
& |C_{13}| < (C_{11}C_{33})^{\frac{1}{2}} \\
& |C_{23}| < (C_{22}C_{33})^{\frac{1}{2}} \\
& \det\left(\underset{\sim}{\underset{\sim}{C}}\right) > 0
\end{aligned}
\tag{3.3}
$$

$$
\underset{\sim}{\underset{\sim}{C}} = \begin{bmatrix}
211.6 & 66.0 & 40.6 & 0 & 0 & 0 \\
 & 211.6 & 40.6 & 0 & 0 & 0 \\
 & & 232.8 & 0 & 0 & 0 \\
 & & & 72.6 & 0 & 0 \\
 & Sym & & & 66.9 & 0 \\
 & & & & & 66.9
\end{bmatrix} [GPa] \tag{3.4}
$$

$$
C_{\theta,\rho} = \underset{\sim}{n}\ \underset{\sim}{n}\ \underset{\sim}{\underset{\sim}{C}}\ \underset{\sim}{n}\ \underset{\sim}{n} \tag{3.5}
$$

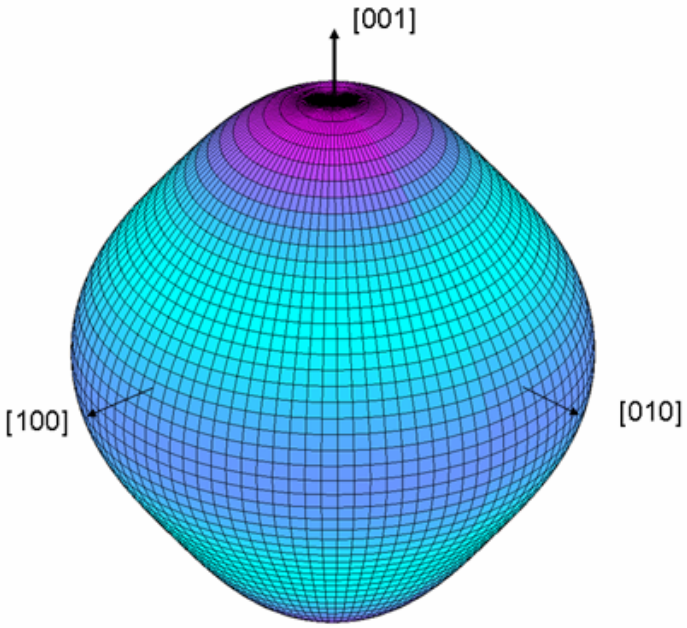

Figure 3.4: 3D representation of spatial variation of elastic constants.

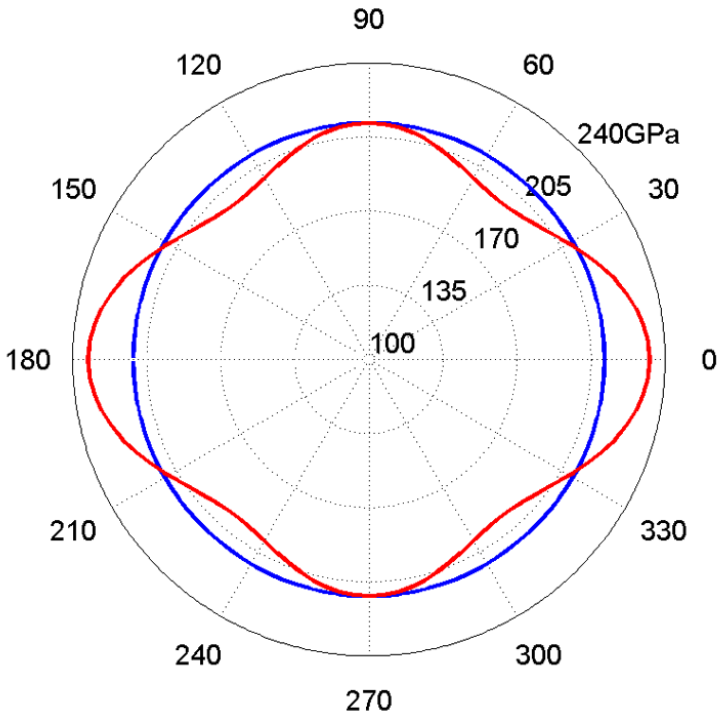

Figure 3.5: 2D representation of directional variation of elastic constants. Blue [100][010] isotropic plane. Red [100][001] plane .

3.3 Quasi-static and Dynamic Compression Tests

True stress versus true strain curves were obtained at three different deformation rates, one a quasi-static compression test (deformation rate $\simeq 0.01 sec^{-1}$) and two using the dynamic split Hopkinson bar tests. Three tests were averaged at each deformation rate. Samples were prepared using an EDM having in the case of quasi-static tests a nominal diameter of $12mm$ and length of $24mm$. For the split Hopkinson tests, samples of $4mm$ diameter by $4mm$ in length were utilized enclosing several thousand grains and assuring an average behavior.

The split Hopkinson bar apparatus consists of a striker bar, an incident bar, the test specimen, strain gages, and the output bar as shown in Figure 3.6. A rectangular compression wave of well defined amplitude and length is generated in the incident bar when the striker rod is fired from a gas gun and impacts the incident bar. When the wave reaches the specimen some of its energy is transmitted through it and some is reflected back through the incident bar. Strain gages are attached on the incident and output bars as shown in Figure 3.7, and the incident, transmitted, and reflected pulses are monitored and recorded by an oscilloscope. Figure 3.8 represents these pulses recorded in the experiment.

One dimensional wave propagation analysis determines high strain rate stress-strain curves from measurements of strain in the incident and output bars. Equation 3.6 converts the strain gages transmitted and reflected voltage signals $V_T^g/f_s V_e$ and $V_R^g/f_s V_e$ respectively into strain, being $f_s = 2.02$ the strain gage constant and $V_e = 30V$ the applied strain gage voltage. The reflected pulse measured by an oscilloscope is used to calculate the strain rate in a specimen as shown in Eq. 3.7, where L_s is the instantaneous specimen length, and C_0 the longitudinal wave speed in the rod. Equation 3.8 was used to compute C_0, in which $E_b = 200GPa$ and $\rho_b = 8100\ kg/m^3$ are the bar Young's modulus and density respectively. This strain rate is integrated with respect to time in order to obtain the strain (ε) in the specimen, as represented by Eq. 3.9. The transmitted pulse is used to calculate the true stress in the specimen with Eq. 3.10, being $A_b = 285.0mm^2$ the area of the bar, and A_s the instantaneous area of the specimen, which is computed assuming volume conservation (Eq. 3.11).

$$\varepsilon_T(t) = 2\frac{V_T^g}{f_s V_e}$$
$$\varepsilon_R(t) = 2\frac{V_R^g}{f_s V_e} \tag{3.6}$$

$$\dot{\varepsilon}(t) = 2\frac{C_0}{L_s}\varepsilon_R(t) \tag{3.7}$$

$$C_0 = \sqrt{\frac{E_b}{\rho_b}} \tag{3.8}$$

$$\varepsilon(t) = \int_0^t \dot{\varepsilon}(t) \tag{3.9}$$

$$\sigma(t) = E_b\frac{A_b}{A_s}\varepsilon_T(t) \tag{3.10}$$

$$V_s = A_s L_s = \text{constant} \tag{3.11}$$

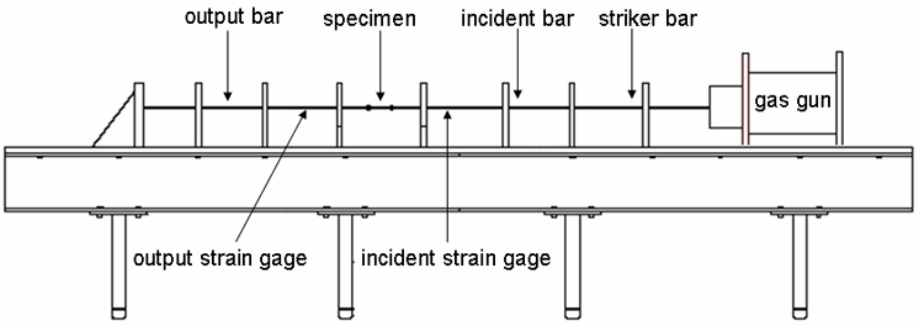

Figure 3.6: Split Hopkinson bar test rig.

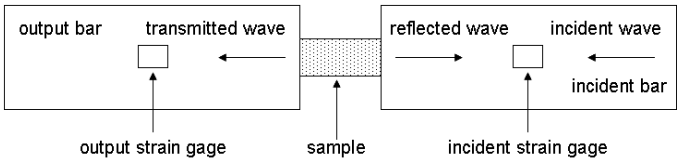

Figure 3.7: Split Hopkinson bar test rig. Close-up of sample and strain gages.

Figure 3.10 shows the results of the average of 3 compression tests at each strain rate. The static tests were stopped when the machine limit load was achieved ($\simeq 180kN$). The signal on the

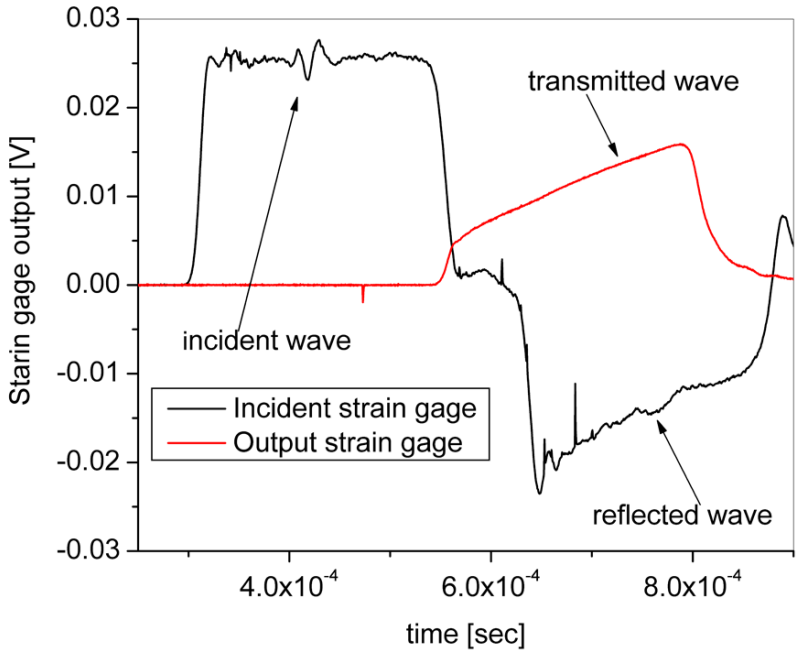

Figure 3.8: Strain gages signal obtained from split Hopkinson bar test.

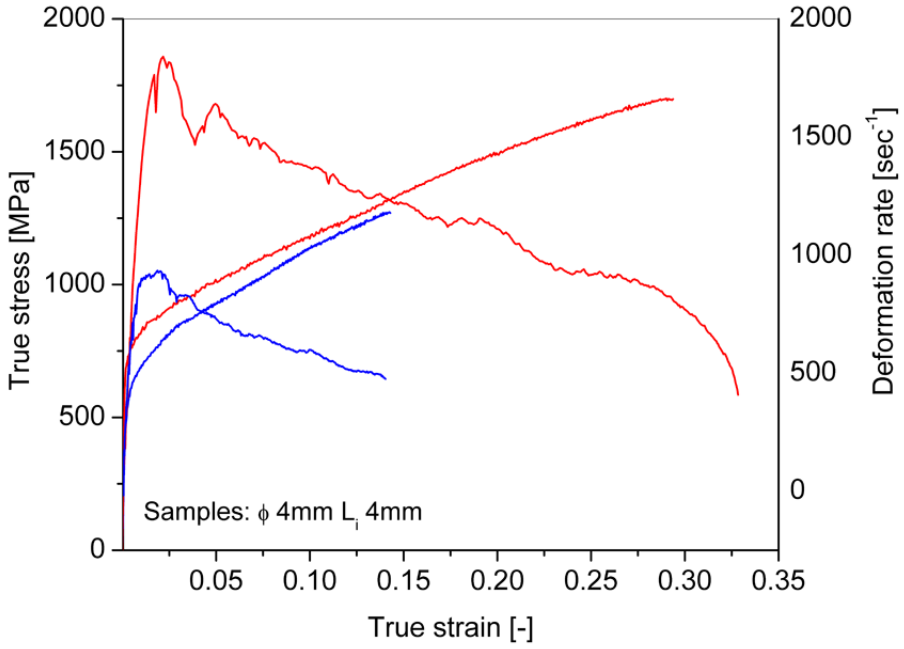

Figure 3.9: True stress and strain rate vs. true strain from split Hopkinson bar test. Three tests averaged.

dynamic tests was valid until the reflected wave from the end of the bars reached the strain gages ($\simeq 0.3msec$).

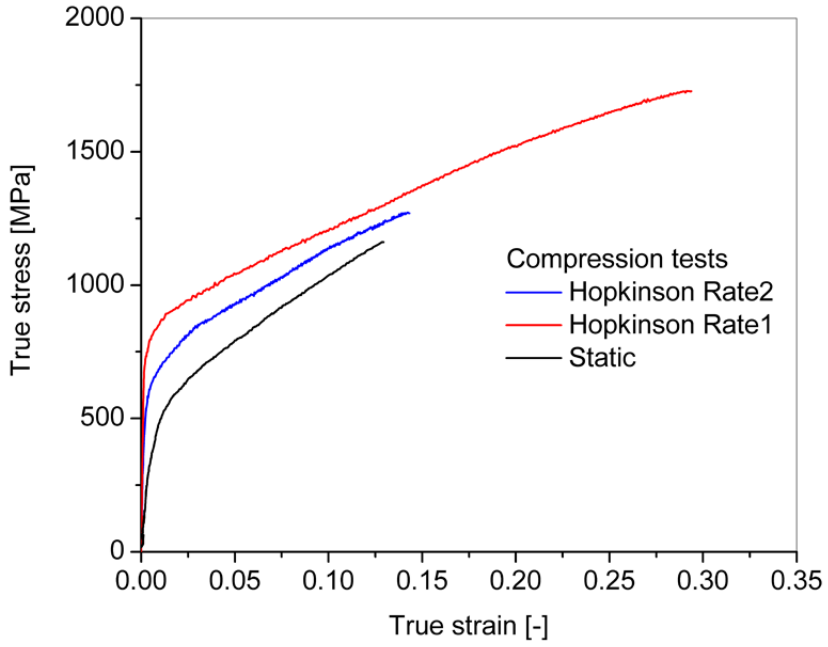

Figure 3.10: True stress vs. true strain curves. Average of 3 compression tests at each strain rate.

3.4 Indentation Tests

The elastic-plastic material response was also evaluated by indentation tests. Two different types of indentations were carried out, a Vickers microhardness test to obtain the material hardness value, and instrumented tests using a conical diamond indenter of $200\mu m$ tip radius to obtain hysteresis curves. The indentation of the Vickers test was smaller than the lamellae colony size and due to the material anisotropy indents were not symmetric. Six measurements were averaged giving a mean of $266HV_2$ with a standard deviation of $6HV_2$. The relatively small deviation of the average value was achieved by using the largest load admissible for the instrument ($\simeq 20N$), which averaged properties over a relatively large area. For the instrumented tests an Instron 5867 universal testing machine was utilized, acquiring load and machine head displacement under three maximum loads of $500N$, $1000N$, and $1500N$. The displacement rate was $0.05mm/min$. Figure 3.11 shows the force versus

displacement load and unload curves, with each curve being the average of three measurements. Machine compliance was accounted for with calibration curves. Figure 3.12 shows the macrography and 3D surface profilometry of an indentation edge, where the inhomogeneous deformation due to the different lamellae orientations can be seen in the out of roundness of the indentation edge and uneven surface topography.

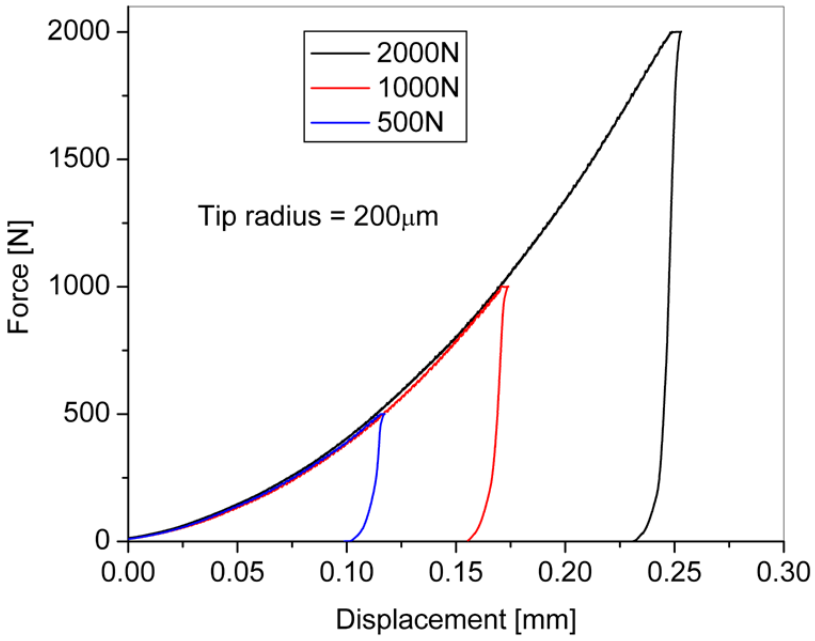

Figure 3.11: Indentation force versus displacement load unload curves.

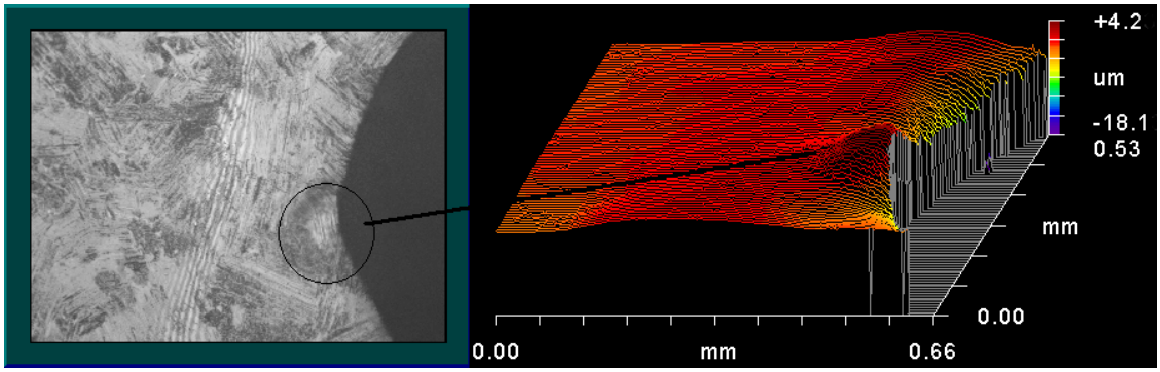

Figure 3.12: Macrography and 3D surface profilometry of indentation edge. Inhomogeneous deformation can be appreciated.

CHAPTER IV

PLASTIC DEFORMATION DEPTH MEASUREMENT METHOD

4.1 Introduction

Among the techniques utilized for measuring PDD, profiling of subsurface hardness is one of the most widespread, as that shown in the work of Field et al. (1972); Bentley et al. (1999); Jones and Eylon (1999). Since the size of the hardened zone is of the order of tens to hundred of microns, low load microindentation should be utilized and relatively large scatter accompanies the results, decreasing the sensitivity of the method. Optical microscopy utilizing Nomarski illumination (Robinson and Bradbury, 1992) is another technique to evaluate PDD. It is based on the observation of surface irregularities and a quantitative analysis can be made by using a reticle in the optics objective. As with any observational technique, the disadvantage is that the measurement is subjective.

The experimental technique which is developed in this chapter to quantify the PDD is based on the fact that in the machining of materials that exhibits a certain degree of ductility, a burr is formed at the lateral edges of the workpiece. This burr is caused by material side flow due to the unconstrained conditions at the workpiece boundaries along with the deformation imposed by a tool path close to the workpiece edge. This burr formation is schematically represented in Fig. 4.1, where the top surface is machined, V_w being normal to the page. This is sometimes called "Poisson" burr (Gillespie, 1977). Here a difference should be made between different types of burrs. What is usually seen in machine shops and removed by deburring is what is called a "hanging" burr (Gillespie, 1977). Once this hanging burr is removed, there is still a "side flow" type of burr, which is the one relevant for this study.

The implications of this burr formation are two fold. Firstly, the magnitude of this lateral flow should be taken into account for high precision parts. Tight fitting matching parts, such as seals,

might not be functional if this effect is not considered. Secondly, this lateral flow can be a sensitivity parameter to account for the interaction of material properties and machining conditions. If it is true, and an appropriate technique for its measurement can be developed, this can be a practical tool for machining evaluation.

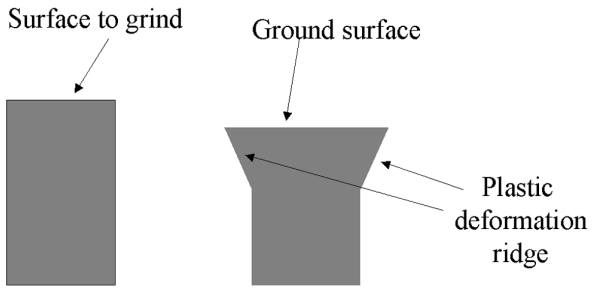

Figure 4.1: Exaggerated view of burr formed at the material lateral edges due to surface grinding.

4.2 Background of Method

The proposed technique is based on the works of Xu and Jahanmir (1994), and Nelson (1997). Xu and Jahanmir (1994) developed the bonded interface, or split specimen technique, to observe damage on machined ceramics using Nomarski microscopy. In their technique two polished surfaces of the sample are glued together with cyanoacrylate, the specimen machined and the two surfaces separated and placed under the microscope. Nelson (1997) utilized the bonded interface technique on ground $TiAl$ samples and further implemented the use of a profilometer to evaluate the damaged zone by changes in the surface roughness. Razavi (2000), and later Stone (2003) had used the same technique for measuring subsurface damage in their work. The technique requires that bonded surfaces spacing be of the order of $1\mu m$ or less to effectively neglect the effects of the interface. Razavi et al. (2003) reported surface flatness values of $400\mathring{A}$ over an area of $0.25mm^2$. Nevertheless, on samples with mating areas of $20mm$ by $10mm$, as the ones used for grinding experiments, the final surface separation might be of orders of magnitude larger than the one reported, in particular with relatively soft materials such as metals. The disadvantage of this technique lies in the difficulty of surface sample preparation, and the resulting variable spacing of the glued interfaces in the sample and, between samples, that leads to large variability of results due to variable mechanical constraint conditions.

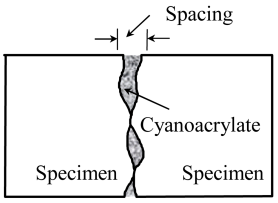

Figure 4.2: Bonded interface technique sample schematics.

4.3 Proposed Method

The proposed method is based on the measurement of the side flow, or the out of planarity of the surface. Since measurements are performed on a free surface, the variable constraint condition of the previous technique is eliminated. Surface preparation is also less stringent.

The experimental procedure to acquire the raw data for evaluation of PDD is detailed in Fig. 4.3 for surface grinding. Samples of $15mm$ high, $25mm$ long, and $5mm$ and $10mm$ wide were used. The lateral free surfaces of the sample were polished up to a roughness and planarity $< 1\mu m$ over a length of at least twice the expected value of PDD. Grinding was performed using a grinding wheel wider than the specimen width, allowing the analysis of PDD at both lateral surfaces of each sample in a single experiment. During grinding, side flow occurs beneath the new created surface. The displacement magnitude is a function of the material properties as well as of the machining conditions. A non-contact, three-dimensional, white-light optical scanning interferometry was utilized to acquire the data to be analyzed (Forman, 1979). An infinite conjugate interferometric objective of 2.5x magnification was chosen giving a field of view of $2.82mm$ by $2.11mm$. The fringe images were digitized with a camera resolution of 640x480pixels giving a spatial sampling of $4.4\mu m$. The vertical scan was of $40\mu m$ with a vertical resolution of the order of a few nanometers.

4.3.1 Consistency of Results

In order to obtain consistency of results, precautions were taken on PDD measurements. Figure 4.4 shows the sample lateral free surface with the different zones.

A coarse deburring of hanging burrs took place before measurements to avoid interfering shadows over the region of interest.

The measured surface was placed at normal incidence with respect to the microscope objective,

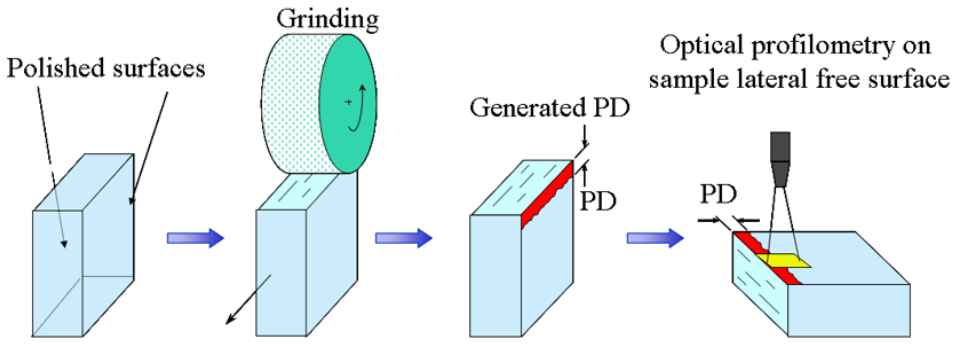

Figure 4.3: Experimental steps to obtain the raw data to analyze PDD.

and the sample edge parallel to the image border to minimize errors.

Sample edge identification is relevant for precision measurements. It has been observed that usually the edge of the specimen is less reflective than the polished zone. This is mainly due to the different roughness between both surfaces and also due to a burned zone that might be formed beneath the new created surface. Due to this difference in contrast it might be difficult to identify the sample edge, producing an error in the measurement. To avoid this error a sample clamp was made with a reflectivity of the same order as the one at the zone of interest on the sample.

For statistical purposes three images were taken at each lateral side giving a total of 384 PDD data points.

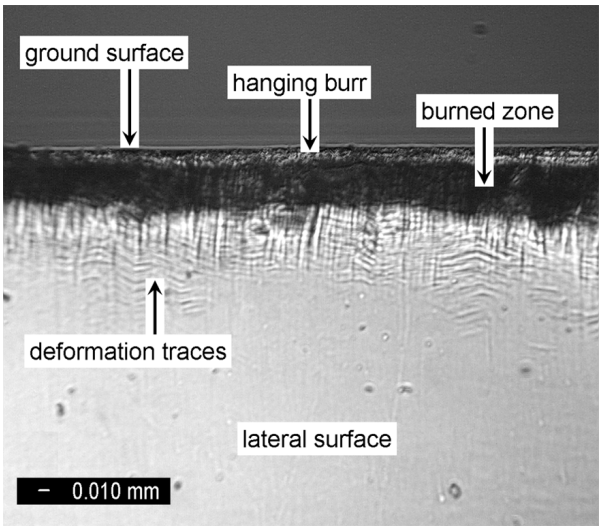

Figure 4.4: Lateral free surface on a sample showing different zones.

4.4 Data Analysis

Raw data were extracted from the profilometer and processed in order to obtain the value of PDD. Data analysis was implemented using Matlab v6.5.1, and it was composed of two main parts: data conditioning, and PDD measurement. For the data conditioning the processing steps taken were unwrapping, filtering, offset removal, and trimming. For the PDD measurements the process steps were fitting with the best plane on the undeformed zone of the scanned surface; defining a threshold value for PD; and finding the threshold value from the surface.

The raw data from the profilometer came in binary format giving information of intensity and phase. Data type conversion and unwrapping was done obtaining as a result the x, y, z coordinates of the discrete surface. This followed by assigning noisy pixels (the ones with amplitude outside a given threshold) the weighted average by distance of the nearest valid neighbor points. These noisy pixels were mainly caused by missing data, and a large default value was placed instead on the DAQ process. The image was trimmed at the lateral edges other than the edge where the new surface was created, removing the remaining noisy pixels. The last stage in conditioning involved data filtering by the implementation of a median filtering algorithm in which each output pixel was set to the median of the pixel values of its nearest neighbors. The median was chosen instead of the mean because it is less sensitive to extreme values. Figure 4.5 shows an example of conditioned data.

A contour plot and an averaging analysis were performed to determine the PDD, as shown in Figs. 4.6 and 4.7, respectively. In both methods a datum plane was fitted in the undeformed zone of the scanned area as a reference, and a threshold value was assigned to the magnitude of lateral displacement in order to separate the deformed from the undeformed zone. In the averaging method the vertical coordinate of each set of points parallel to the ground edge was averaged, and the distance to the datum plane computed. This distance is the mean value of the lateral displacement as shown in Fig. 4.7. A single value of PDD is obtained from each image by defining a lateral displacement threshold value as a criterion. The second method used contour plots at different threshold levels. For consideration of automatic analysis of the image, this method gives at least as many values as the sample wide/resolution gives, which might not give a function but a poly-valued relation of PDD in the sample wide, as shown in Fig. 4.6.

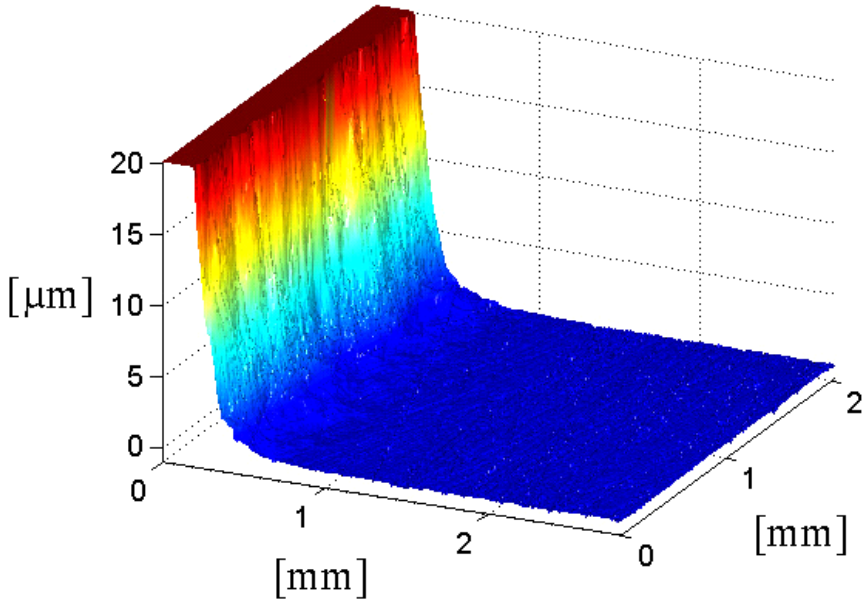

Figure 4.5: Conditioned data from 3D profilometer.

4.5 Capabilities and Limitations of the Method

The averaging method for determining PDD gives an average out-of-planarity measurement, with one data point/scanned image based on the fitting of best plane on the undeformed area and the measure of the surface average vertical deviation from a fitted plane as a function of distance from the ground surface. This method is robust with respect to missing points and surface finishing. Figure 4.8 shows the comparison of PDD for threshold values of $1\mu m$ and $3\mu m$. It can be seen that a good correlation exists between them. Figure 4.9 shows the comparison of PDD for threshold values of $1\mu m$ and $0.25\mu m$. It can be seen that the data spreads, being this threshold the limit of applicability of this technique.

The contour plot method gives a number of data points (image width/lateral spatial sampling resolution), allowing the computation of PDD variability with respect to grain morphology and material anisotropy. Since no data averaging takes place, this method is very sensitive to surface finishing giving false positives values of PDD for small deformation thresholds as shown in Figure 4.10. Therefore lower thresholds values of PDD can be adopted in the averaging method than in the contour one. Figure 4.11 compares the determination of PDD for these two different approaches for a threshold value of $1\mu m$. It can be seen that a good agreement exits between them.

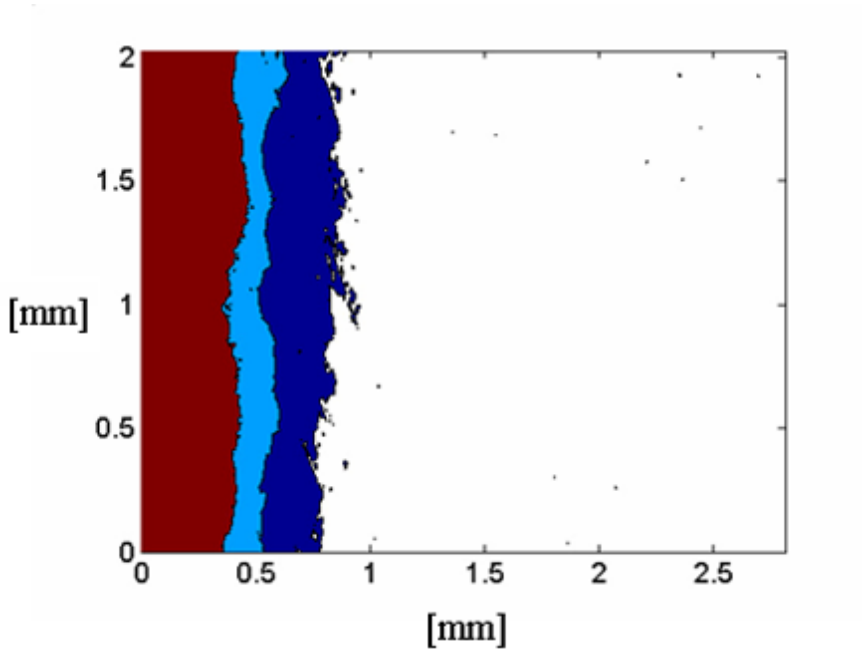

Figure 4.6: PDD contour plot for 3, 1 and 0.25μm of threshold.

4.6 Conclusions

The PDD evaluation method proposed, combines the quantitative capabilities of the microhardness measurement with the sensitivity of Nomarski microscopy. Quantitative analysis of the surface can be performed and an algorithm with the criterion to define the PDD zone can be used. This approach is less biased from the user's experience.

The method can be used to obtain a unique parameter for PDD or a complete mapping of the surface, according to the data analysis performed.

The averaging method of determining PDD is based on averaging the out-of-planarity of lines parallel to the surface. This method gives a unique value for PDD and it is robust with respect to missing points and surface finishing.

The contour plot method allows the computation of PDD variability with respect to grain morphology and material anisotropy. Since no data averaging takes place, this method is very sensitive to surface finishing.

The practical limitation of these methods is given by the quality of surface preparation, e.g. the surface roughness more important than its waviness. With a surface roughness of $Ra < 1\mu m$ it has been possible to work with an out-of-planarity threshold of $1\mu m$, thereby obtaining consistent

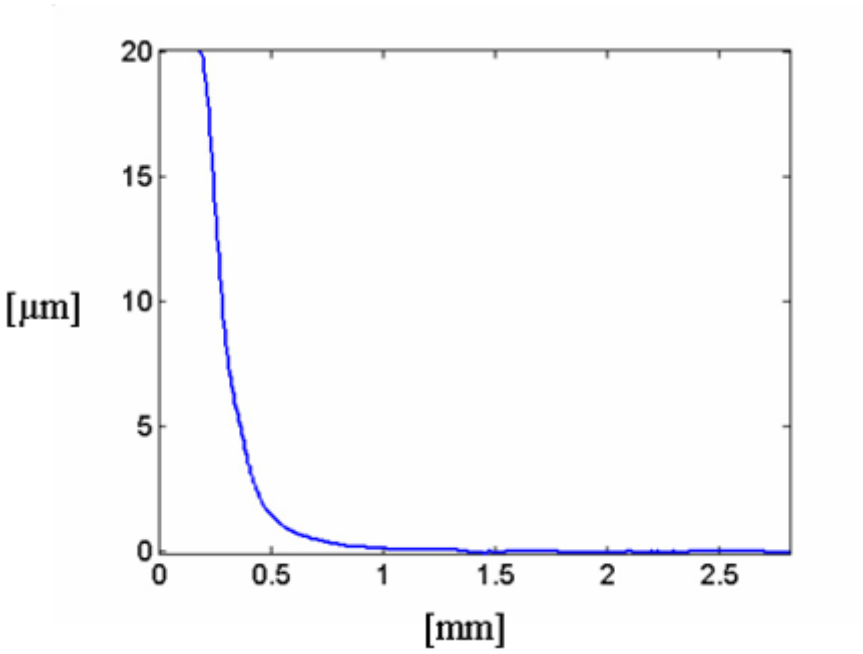

Figure 4.7: Plot of the mean value of the lateral material flow-datum distance.

results between replications and analysis techniques. An out-of-planarity threshold of $0.25\mu m$ has been of limited applicability for the present work.

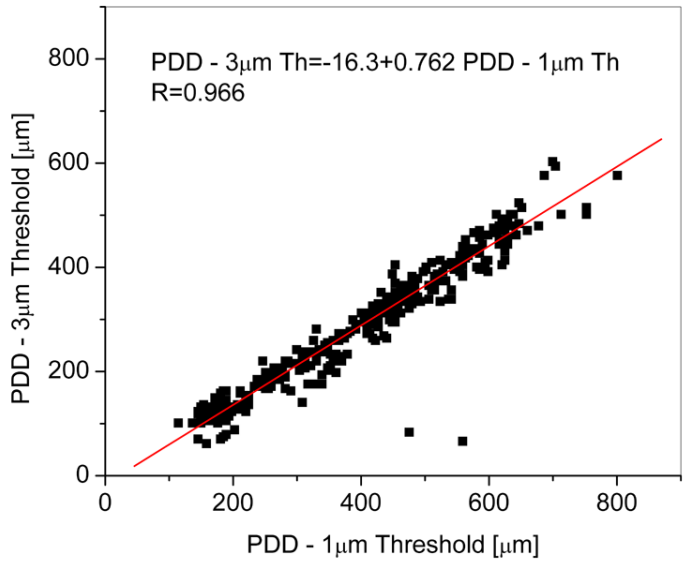

Figure 4.8: Comparison of PDD for threshold values of $3\mu m$ and $1\mu m$ for the averaging method.

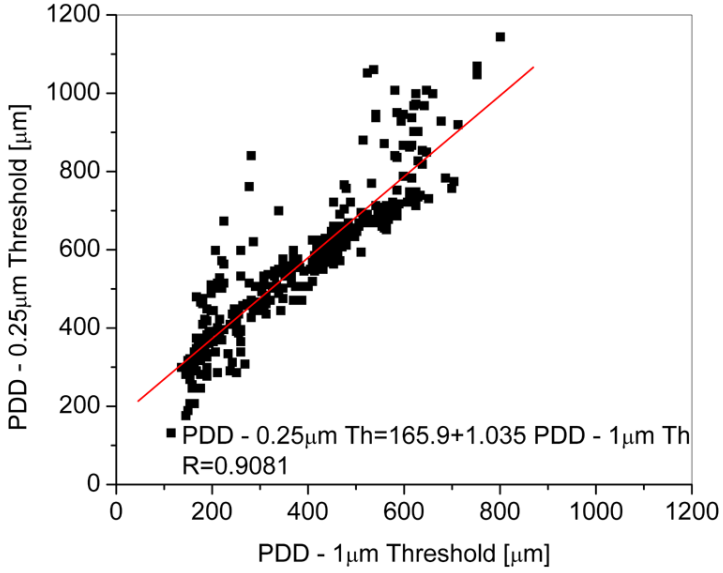

Figure 4.9: Comparison of PDD for threshold values of $0.25\mu m$ and $1\mu m$ for the averaging method.

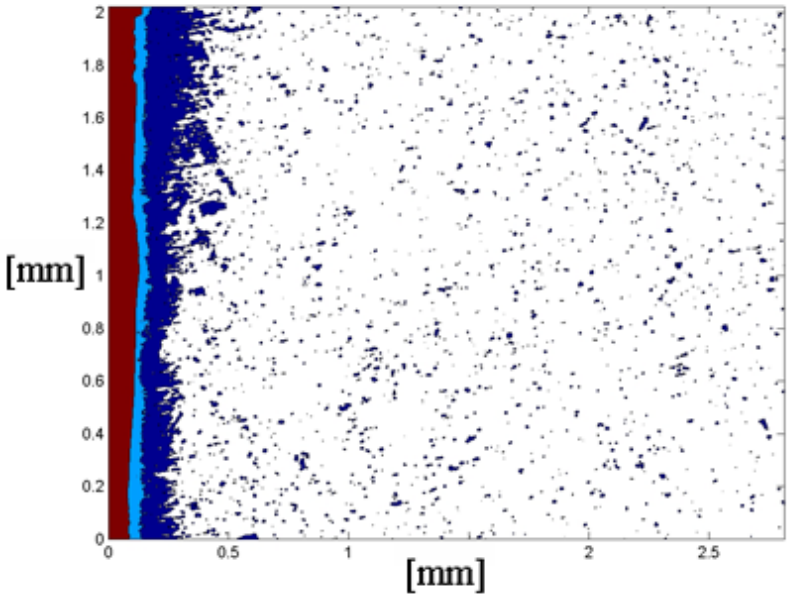

Figure 4.10: PDD contour plot for $3\mu m$, $1\mu m$ and $0.25\mu m$ of threshold. Technique limitation by data scatter.

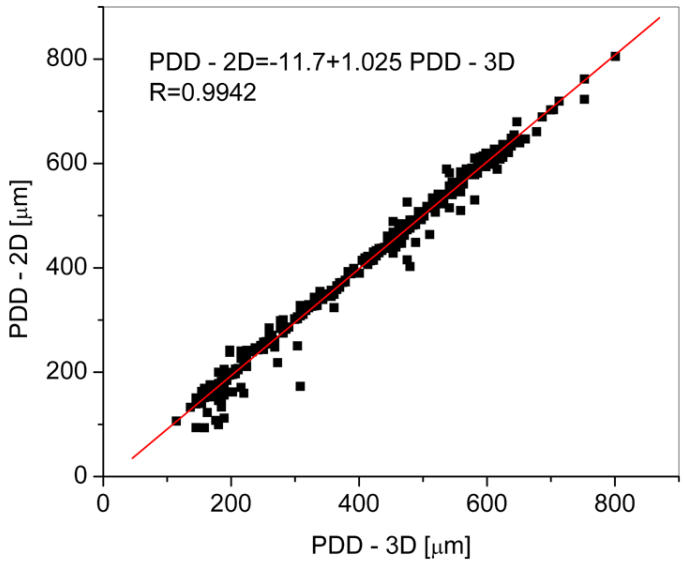

Figure 4.11: Comparison of PDD for $1\mu m$ threshold values for the averaging and contour plot methods.

CHAPTER V

GRINDING EXPERIMENTS

5.1 Introduction

This chapter describes the experimental technique employed in the surface grinding tests, including the design of experiments, precautions taken for consistency of results, data acquisition, and results in terms of obtained specific normal (F'_N) and tangential (F'_T) force, specific energy (E'_g), surface average roughness (R_a), bearing area (BA), grinding friction coefficient (C_f), and PDD. The main operation variables were the wheel's abrasive grit size (G_z) and shape (G_h), wheel depth of cut (DoC), workpiece or table speed (V_w), and wheel wear (W_r).

5.2 Design of Experiments

The objective of the grinding tests was to evaluate the effect of the wheel G_z, G_h, DoC, and V_w on the final grinding variables, in particular on the PDD. A two-level, five-variable, full factorial design of experiments was planned, with 32 different treatments and 2 replications, giving a total of 64 experiments. To increase the statistics of the results on the determination of the PDD, 3 measurements of PDD were made at the lateral sides of each specimen giving a total of 384 data points. Table 5.1 shows the levels used for each variable. Wheel peripheral speed was kept constant at $30 m/sec$.

Table 5.1: DOE for grinding tests.

	G_z μm	G_h	DoC μm	V_w mm/sec	W_r mm^3/mm^2
Low	54	angular (Ag)	20	20	0.05 (dressed)
High	232	blocky (Bk)	50	80	2.5 (worn)

5.3 Wheel Characteristics

Grinding wheels consist of abrasive grits bonded together by a matrix of resins, epoxy, rubber, metal, or vitrified glass materials. Because of the availability in different shapes and sizes and its adequacy for grinding intermetallic compounds (Kumar, 1990, 1993), diamond superabrasives were used in this research. Polycrystalline synthetic diamond manufactured by General Electric was embedded in a Ni based alloy by Noritake Abrasives in a wheel type 1A1 (peripheral, straight face with no recess). Wheel size was $178mm$ diameter, $12.2mm$ wide, and $32mm$ bore diameter, grade N, with an abrasive rim of $3.17mm$ on a steel core, and concentration 100 (25% of the volume is occupied by diamond). Since the bonding was Ni based, no metal clad grain was necessary to enhance abrasive retention. Abrasive grits are defined by their shape and mechanical properties, in particular friability, or the ability of the grit to fracture when the force is increased due to generation of wear flats. Friability is tested by means of statistical analysis of dynamic compressive fracture strength tests where grinding conditions are simulated. Shape classification is based on parameters such as "tau" (GE, 2000) which is a continuous parameter to measure more cubic or octahedral shapes, and the eccentricity factor or aspect ratio. Figure 5.1 shows the 4 different abrasive grits of the MBG300 and MBG660 types utilized. While the MBG660 is a low eccentricity crystal exhibiting well defined cubo-octahedral morphology, high bulk fracture and shear strength; the MBG300 type is of sharp, angular shape, of high eccentricity, and friable. Also two different grit sizes were chosen with average diameter of $54\mu m$ (small) and $232\mu m$ (large). Size also affects strength where the small grit is tougher than the large grit. Heat is conducted away from the grinding interface by the diamond (thermal conductivity $1000W/m\ K$ and $2600W/m\ K$), and the metal bonding (thermal conductivity estimated in $100W/m\ K$).

5.4 Consistency of Results

Grinding output parameters are very sensitive to the abrasive grit and cooling conditions. Grinding forces can vary by more than an order of magnitude if these conditions are not carefully controlled. Consistency of results or the possibility of conducting a literature comparison depends on the correct specification of such conditions. Even though these parameters are relevant, they are often neglected in literature. Precautions taken for consistency of results are presented.

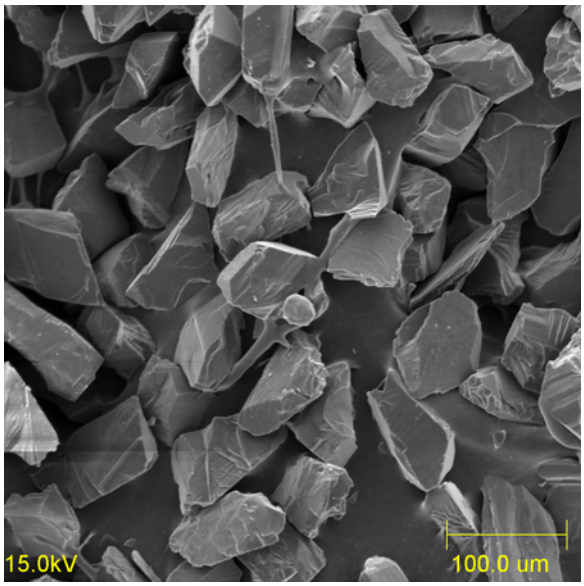

(a) Wheel 63: SA MBG300 Grit 270-325 (54μm avg.)

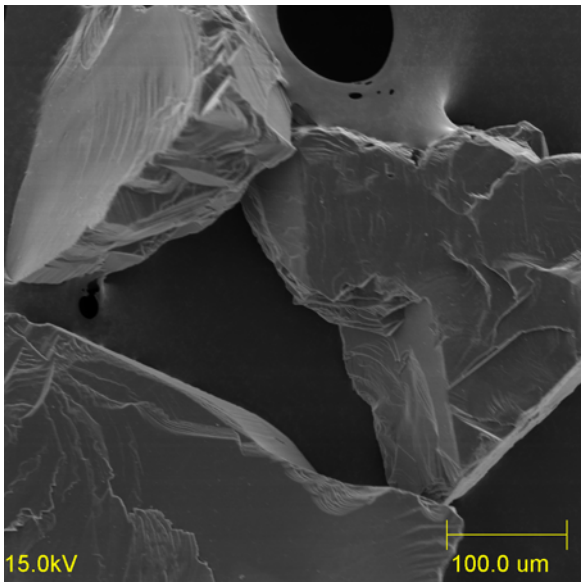

(b) Wheel 65: LA MBG300 Grit 60-80 (232μm avg.)

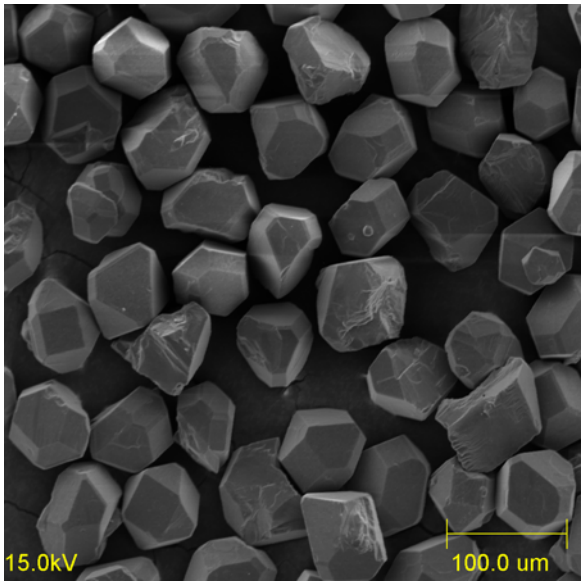

(c) Wheel 64: SB MBG660 Grit 270-325 (54μm avg.)

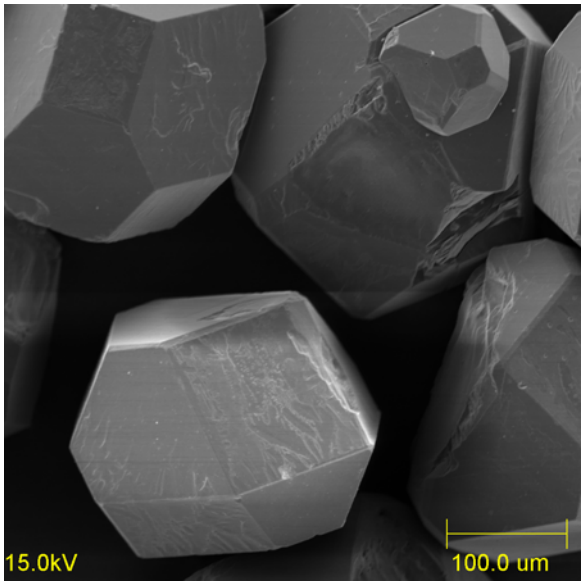

(d) Wheel 61: LB MBG660 Grit 60-80 (232μm avg.)

Figure 5.1: Grinding wheel diamond abrasives.

5.4.1 Wheel Wear

After the wheel is conditioned by truing and dressing, abrasives have sharp cutting edges that gradually become dull with use, mainly by generation of wear flats. The more friable the abrasive, the easier it can fracture allowing new edges to be generated. The process of wear flat generation and grit fracture might not reach an equilibrium, therefore grinding is generally done under variable conditions. Figure 5.2 shows the effects of the abrasive wear on the normal force. Each point on the plot represents a grinding reciprocating cycle. The first 5 to 10 points usually showed a step increase in the normal force due to the machine compliance and the displacement control given by the DoC. Machine compliance becomes irrelevant if DoC control is used and kept constant during the tests, while enough cycles are set and the steady state reached. The upper abscissa shows the specific material removal per unit width. The lower one shows the wheel specific material removal which adds the normalization by the wheel perimeter. This latter measure is not commonly used in the literature because a unique wheel diameter is assumed. The normal force is represented by its plateau value at each cycle, as shown in Figure 5.3. One way to control the wear effects is by implementing continuous dressing (Ohmori et al., 1996). To obtain consistent results, the same amount of material was removed in each test.

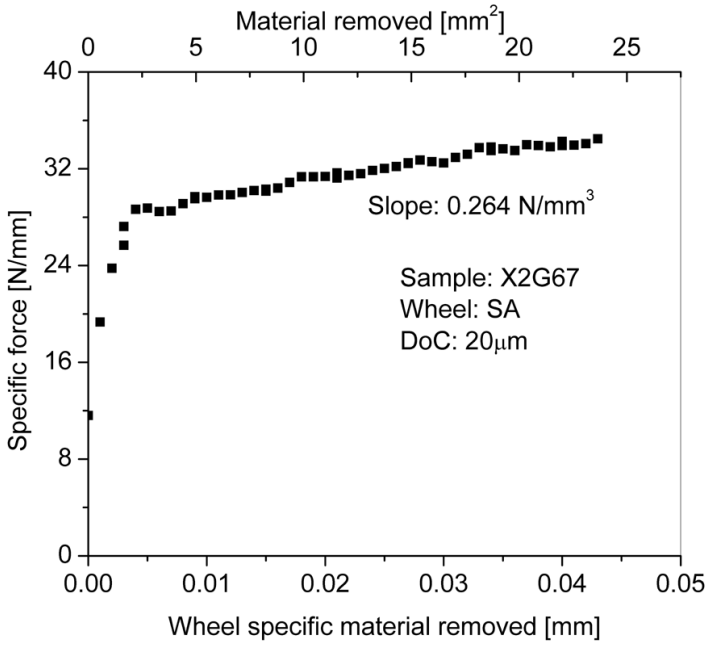

Figure 5.2: Effects of abrasive wear on the normal force.

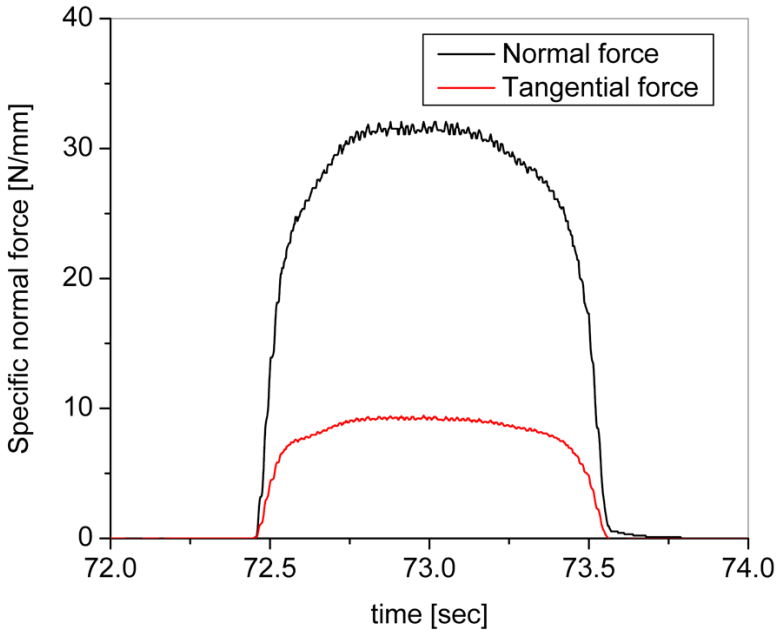

Figure 5.3: Normal and tangential force in a grinding cycle.

5.4.2 Dressing Conditions

"Dressing" is a conditioning operation that exposes and sharpens abrasive grits and has a great impact on performance. A sensitivity test for dressing was done. The wheel was trued, and one half was completely dressed while 15% of the other half was left without dressing. Each half of the wheel was utilized alternatively to grind the same sample under the same conditions. The tests where the complete wheel was trued and dressed was also performed for reference. Figure 5.4 shows the results. The black curves correspond to the two halves of the totally dressed conditions, and it can be seen that the response is homogeneous. The red curves represent the wheel with incomplete dressing.

5.4.3 Coolant

Coolant was utilized to remove heat and debris from the grinding zone, and reduce friction, wear and corrosion, and has a major impact on grinding (Guo and Malkin, 1992; Engineer et al., 1992; Ebbrell et al., 2000). Figure 5.5 shows an example of the effects of cooling conditions on the specific normal force (F'_N). Poorer cooling conditions increase the wear rate of the wheel. To minimize wear, several modifications were implemented on the grinder. To obtain an homogeneous flux over

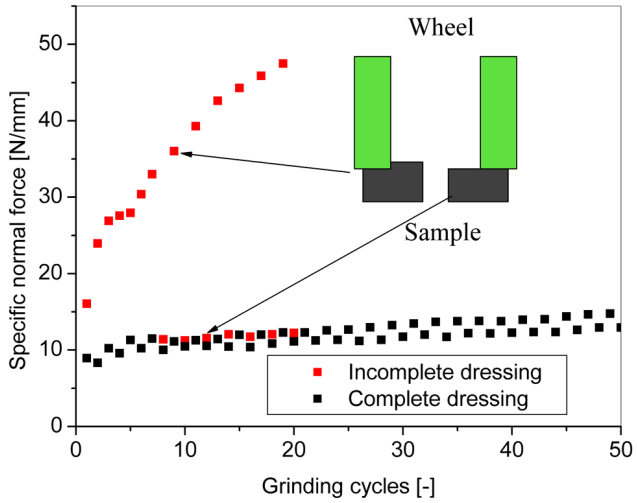

Figure 5.4: Plot of two different tests showing the effects of dressing on the normal force.

the wheel width, the coolant nozzles were changed from round to flat as shown in Fig. 5.6. Fluid

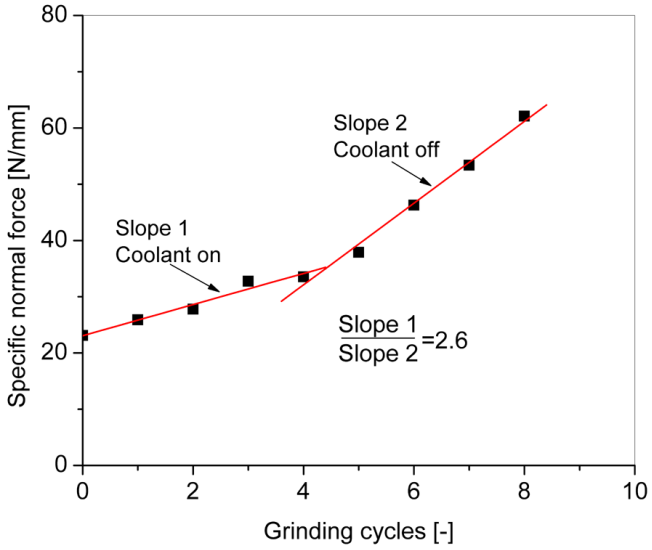

Figure 5.5: Effect of cooling conditions on the normal force.

flow and pressure were increased by adding a pump to enhance heat and debris removal. Measured coolant flow was $7.2 liter/min$ at $75 kPa$ for the front nozzle, and $3.3 liter/min$ at $40 kPa$ for the back nozzle. The coolant was composed of a Cimperial HD90 oil based water soluble 6% concentration. The concentration was periodically checked by means of an optical refractometer (Fig. 5.7).

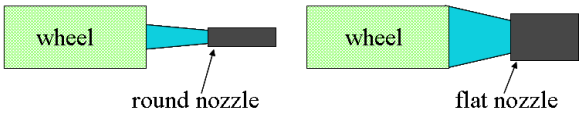

Figure 5.6: Nozzles modification allowing homogeneous flux on the wheel.

Figure 5.7: Refractometer and optical scale used to measure oil concentration.

5.4.4 Hydrodynamic Effects

Under some grinding conditions hydrodynamic effects may influence the measured forces as shown by Figure 5.8. When the coolant was on, an additional force was present. This extra force is generated by the converging gap between the wheel and the sample and their relative motion. This effect is not observed on freshly dressed wheels and it starts to manifest itself in a measurable way after some wear. It has to be noted that the bonding of these wheels, unlike resin or vitrified wheels, has no pores to allow fluid pressure to be released. This effect was reported and used as a measure of wheel wear by Furutani et al. (2002, 2003)

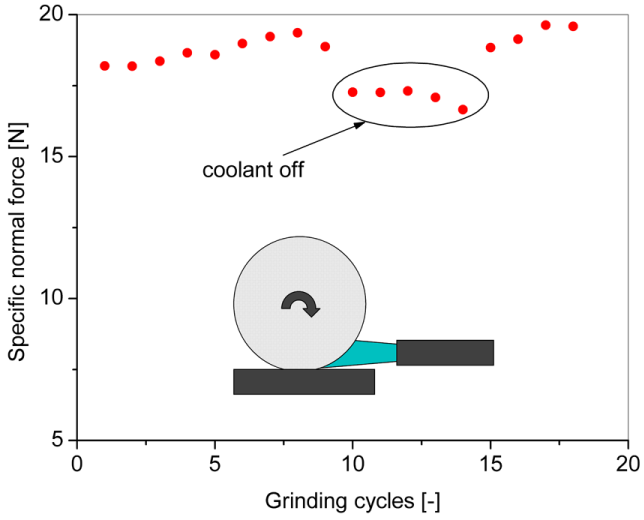

Figure 5.8: Effect of hydrodynamic pressure of the normal force.

5.5 Wheel Conditioning

Truing and dressing are wheel conditioning operations of great importance for consistency of results. Figure 5.9 shows the schematic of the processes. Truing was performed by wearing the diamond wheel with a SiC wheel until wheel roundness was of the order of a few microns. The SiC was driven by the diamond wheel and slipping was produced by misalignment of the rotation axes. The wear rate of the SiC wheel was more than an order of magnitude higher than that of the diamond wheel. Variables for truing include: traverse feed rate, DoC, wheel type, truing device, material removed, and coolant. Dressing was done by driving the wheel at a constant speed into an Al_3O_2 dressing stick. This process exposes the abrasives by removing the bonding in front of them. Variables for dressing include: plunge feed rate, stick type, material removed and coolant. Tables 5.2, and 5.3 show the truing and dressing conditions respectively.

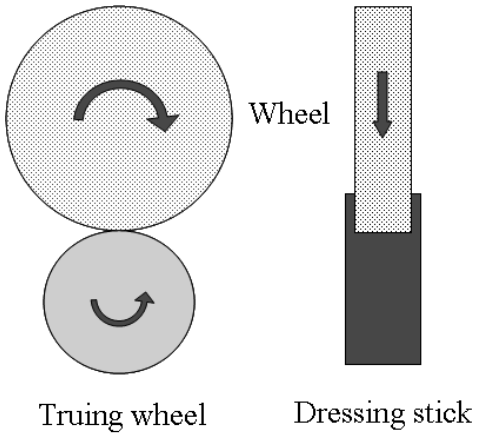

Figure 5.9: Schematics of wheel conditioning.

5.6 Grinder and Data Acquisition

Figure 5.10 shows the schematic of grinding. A Bridgeport Harig 618 EZSURF surface grinding machine with a nominal power of $1.125kW$ and table speed range from $10mm/sec$ to $130mm/sec$ was used. The table was driven by an hydraulic circuit working at open loop control. The controlling factor in the V_w lower limit was the stick-slip of the table sliders. The V_w upper limit was given by the limitations of the hydraulics, or the spindle power. The spindle downfeed was nominally controlled in increments of $2.5\mu m$. The coolant system was modified as mentioned in Section 5.4.3.

Table 5.2: Truing conditions

<table>
<tr><td rowspan="3">Diamond wheel</td><td colspan="4">Free wheel / non-collinear axis (7°) truing with coolant</td></tr>
<tr><td rowspan="2">Conditioning wheel</td><td colspan="2">Rough truing</td><td colspan="2">Finish truing</td></tr>
<tr><td>Downfeed</td><td>Crossfeed</td><td>Downfeed</td><td>Crossfeed</td></tr>
<tr><td>LB</td><td rowspan="2">$75mm\ OD$
$25mm\ b$
$37C60 - MVK$
SiC</td><td rowspan="3">$20\mu m$/pass</td><td rowspan="2">$110cm/min$
$0.9mm/rev$</td><td rowspan="3">$5\mu m$/pass</td><td rowspan="2">$75cm/min$
$0.6mm/rev$</td></tr>
<tr><td>LA</td></tr>
<tr><td>SB</td><td rowspan="2">$75mm\ OD$
$25mm\ b$
$37C60 - MVK$
Al_3O_2</td><td rowspan="2">$0.3mm$ total</td><td rowspan="2">$0.03mm$ total</td></tr>
<tr><td>SA</td><td>$55cm/min$
$0.45mm/rev$</td><td>$37cm/min$
$0.3mm/rev$</td></tr>
</table>

Table 5.3: Dressing conditions

<table>
<tr><td rowspan="2">Diamond wheel</td><td colspan="2">Dry plunge dressing</td></tr>
<tr><td>Conditioning stick</td><td>Conditions</td></tr>
<tr><td>LB</td><td rowspan="2">38A120-IVBE
$25mm\ x\ 25mm$</td><td rowspan="3">plunge rate:
$40mm/min$</td></tr>
<tr><td>LA</td></tr>
<tr><td>SB</td><td rowspan="2">38A120-IVBE
$25mm\ x\ 25mm$</td></tr>
<tr><td>SA</td><td>total removed:
$6.5cm^3$</td></tr>
</table>

The DAQ system was composed by a PCI-MIO-16E4 National Instruments card with 16 differential analog channels, 12bits of resolution on a $10V$ input signal, and maximum sampling rate of $500kS/s$ which ensured good resolution. Acquired variables were power, force components, and table speed. Power was acquired by a PH-3A Load Controls transducer, and force was given by a 3-components Kistler 9257B dynamometer placed below the specimen with the output conditioned by a Kistler 5010A charge amplifier. Since the machine lacked position output for monitoring or control, table speed was established by the sample time under the wheel and sample length. The speed computed in this way is the average V_w per cycle.

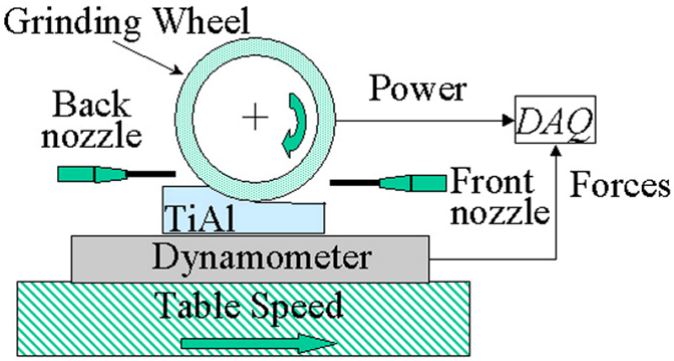

Figure 5.10: Grinding experimental setup.

A DAQ program was written using Labview 6.1. The front interface allowed a set of the sampling rate, power threshold for acquisition triggering and the number of points for walking average smoothing applied to the signal, so that live plots of ${F'}_N$, ${F'}_T$ and P'_w, as well as cycle values of V_w and C_f could be obtained. Since a large number of experiments were carried out, traceability of tests was essential. Three different files were generated with the date and time for tracking purposes. One of them had information on the sample, wheel, process variables, and comments. A second one with the complete acquired data of ${F'}_N$, ${F'}_T$, and ${P'}_w$. A third one with the summary of the test giving a point per grinding cycle of ${F'}_N$, ${F'}_T$, material removed, ${P'}_w$, V_w, and C_f. Charge amplifier drift was automatically corrected by the program for each grinding cycle, avoiding the manual reset of the amplifiers, possible loss of data and errors introduced by this artifact. After grinding, PDD and surface roughness parameters were measured and recorded.

5.7 Results

For easier data observation and due to the difference in their behavior, tests done with dressed and worn wheels will be first analyzed separately. The complete set of results can be found in Appendix A.

5.7.1 Dressed Wheels

Table 5.4 presents the data of the 16 different treatments and 2 replications. Data of PDD is the average of 12 measurements. Table 5.5 presents the ordered PDD values where homogeneous groups were evaluated using the Bonferroni test with a significance level $\alpha = 0.05$. Columns numbered 1 to 5 indicate the different treatments with statistically similar results. As shown in Table 5.5, the PDD measured for small G_z lies in the same range, as well as several groups of treatments for large G_z. Figures 5.11, and 5.12 show the ANOVA main and interaction effects respectively of the 4 predictor variables for PDD. As the plots show, the main factor is G_z, there being some influence of the G_h, and the interactions between G_z and G_h; and G_z and DoC. Table 5.6 presents the results of the ANOVA for the PDD. It can be seen that most of the result variance is explained by the G_z factor alone, V_w not being a relevant factor. Table 5.7 presents the linear model obtained by a stepwise regression for all the main factors and their interactions, using an F-statistics (F) of 4.00. Columns numbered 1 to 4 indicate the number of variables in the model which is composed of a constant term and the factor given in the row of the corresponding variable. The R-Sq value for the model $PDD[\mu m] = 78.1 + 2.007G_S$ is 87.9%. The PDD mean and standard deviation for small and large G_z is $186 \pm 40\mu m$, and $543 \pm 85\mu m$ respectively. The total PDD mean and standard deviation was of $365 \pm 191\mu m$.

Figures 5.13, and 5.14 show the ANOVA main and interaction effects respectively of the 4 predictor variables for C_f. As the plots show, all individual factors are relevant, and except for the interaction between DoC and V_w; and G_h and V_w, all others influence C_f. Grit size and shape have negative correlation with C_f, while the correlation with DoC and V_w is positive.

Table 5.8 shows the linear models for C_f obtained by best subset regression. The right set of columns indicates the individual and interaction variables. Column Vars indicates the number of variables in the model, and Adj. R-Sq is the R-Sq value penalized by the number of variables

Table 5.4: Summary for tests using dressed wheels.

ID	Sample ID		G_z [μm]	G_h	DoC [μm]	V_w $[\frac{mm}{sec}]$	F'_N $[\frac{N}{mm}]$	P'_w $[\frac{W}{mm}]$	C_f	PDD [μm]	Std [μm]
Ag1	X1G19	X1G08	232	Ag	50	20	15.00	139.12	0.250	511.5	65.2
Ag2	X1G54	X2G02	232	Ag	50	80	34.52	314.50	0.231	558.1	72.0
Ag3	X1G50	X2G10	54	Ag	20	80	8.18	84.68	0.286	172.3	26.6
Ag4	X1G51	X2G12	54	Ag	20	20	6.07	55.73	0.229	168.3	18.0
Ag5	X1G44	X1G07	232	Ag	20	20	12.45	103.89	0.213	459.4	49.5
Ag6	X1G56	X1G09	232	Ag	20	80	19.77	178.46	0.224	468.6	28.2
Ag7	X1G58	X2G13	54	Ag	50	20	10.42	104.36	0.262	166.5	17.9
Ag8	X1G55	X2G14	54	Ag	50	80	21.81	277.66	0.315	208.6	69.2
Bk1	X1G10	X1G06	232	Bk	50	20	33.34	218.72	0.167	662.9	73.3
Bk2	X2G51	X2G06	232	Bk	50	80	53.35	351.97	0.174	608.3	37.2
Bk3	X1G14	X2G07	54	Bk	20	80	10.13	107.14	0.270	211.2	40.2
Bk4	X1G16	X1G01	54	Bk	20	20	7.46	69.41	0.235	187.7	28.3
Bk5	X2G50	X2G05	232	Bk	20	80	30.35	214.56	0.179	550.0	36.4
Bk6	X1G11	X2G04	232	Bk	20	20	14.74	122.06	0.209	530.9	82.3
Bk7	X1G15	X2G08	54	Bk	50	20	11.03	111.08	0.262	173.4	10.7
Bk8	X1G13	X2G09	54	Bk	50	80	17.91	216.52	0.300	203.9	46.7

Table 5.5: Bonferroni test for homogeneous groups for dressed conditions$\alpha = 0.05$.

G_z [μm]	G_h	DoC [μm]	V_w $[\frac{mm}{sec}]$	PDD [μm]	1	2	3	4	5
54	Ag	50	20	166.5	**				
54	Ag	20	20	168.3	**				
54	Ag	20	80	172.3	**				
54	Bk	50	20	173.4	**				
54	Bk	20	20	187.7	**				
54	Bk	50	80	203.9	**				
54	Ag	50	80	208.6	**				
54	Bk	20	80	211.2	**				
232	Ag	20	20	459.4		**			
232	Ag	20	80	468.6		**			
232	Ag	50	20	511.5		**	**		
232	Bk	20	20	530.9		**	**		
232	Bk	20	80	550.0			**	**	
232	Ag	50	80	558.1			**	**	
232	Bk	50	80	608.3				**	**
232	Bk	50	20	662.9					**

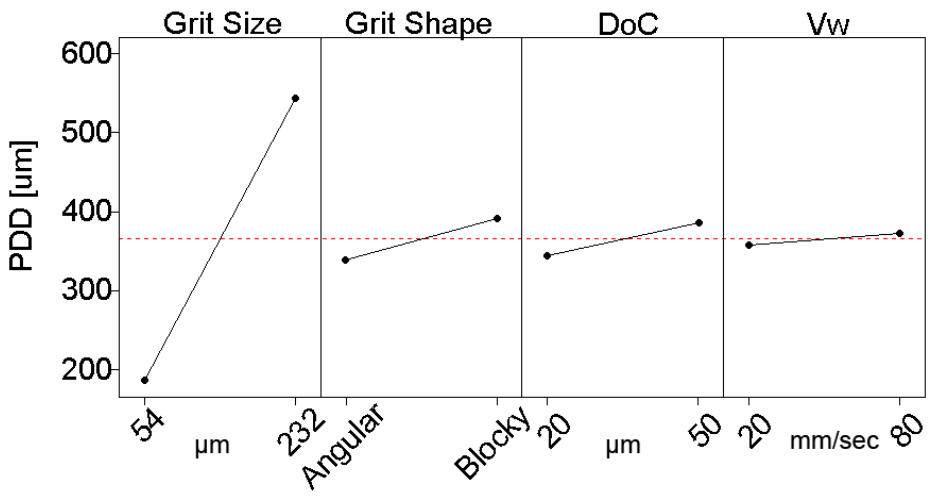

Figure 5.11: ANOVA plot for main effects on PDD.

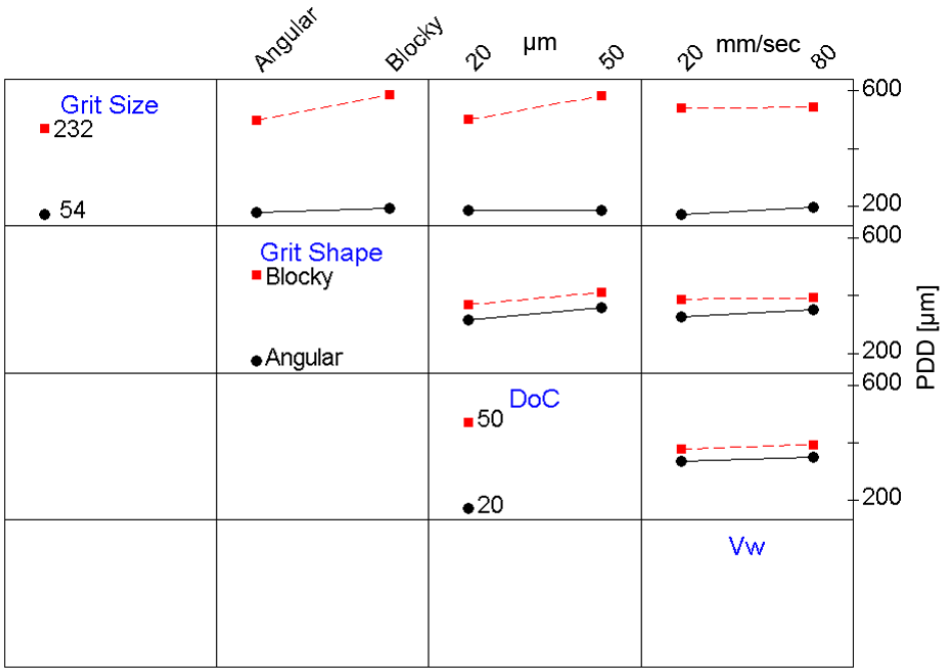

Figure 5.12: ANOVA plot for interaction effects on PDD.

Table 5.6: ANOVA for the PDD.

Source	DF	Seq SS	Adj SS	Adj MS	F	P
G_z	1	6125266	6125266	6125266	1865.5	0.000
G_h	1	129210	129210	129210	39.3	0.000
DoC	1	89096	89096	89096	27.1	0.000
V_w	1	10848	10848	10848	3.3	0.071
Error	187	613978	613978	3283		
Total	191	6968398				

Table 5.7: Stepwise regression model for PDD.

Step	1	2	3	4
Constant	78.12	78.12	78.12	65.6
G_z	2.007	2.007	1.608	1.608
T-Value	37.15	42.21	24.46	24.66
G_z-G_h		0.188	0.188	0.188
T-Value		7.5	8.61	8.69
G_z-DoC			0.114	0.114
T-Value			7.82	7.89
V_w				0.25
T-Value				2.06
S	66.6	58.6	51.1	50.6
R-Sq	87.9	90.68	92.96	93.12

contained by the model. As can be seen, G_z is the most relevant single factor, but it is also strongly interacting with G_h as shown in the multivariable models.

No cracking was observed on the ground surface under a magnification of $60X$.

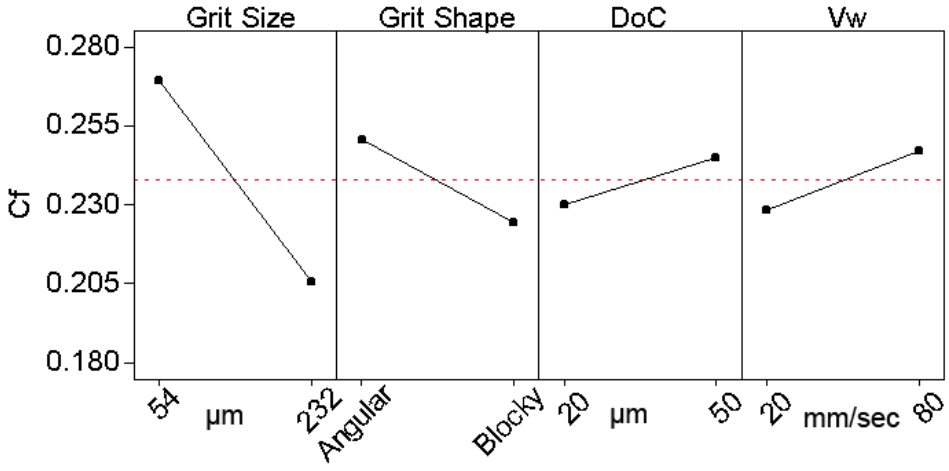

Figure 5.13: ANOVA plot for main effects on C_f.

Figures 5.15, and 5.16 show the ANOVA main and interaction effects respectively of the 4 predictor variables for F'_N. As shown in the plots, all individual factors, and the G_z and G_h interaction are relevant.

Figures 5.17, and 5.18 present the main effects for P'_w and E' respectively. Grit shape shows no effect on these variables.

Surface parameters are considered in Fig. 5.19, and 5.20 that present the main effects for R_a and 90% of BA respectively. It can be seen that the mean R_a value is in the range of $0.4\mu m$ to $0.7\mu m$, and the mean 90% BA of $3.9\mu m$. As in the previous plots G_z is the most relevant variable.

5.7.2 Worn Wheels

Table 5.9 presents the data of the 16 different treatments and 2 replications of the worn wheels. Data of PDD is the average of 12 measurements. Table 5.10 presents the ordered PDD values where homogeneous groups were evaluated using the Bonferroni test with a significance level $\alpha = 0.05$. Columns numbered 1 to 11 indicate the different treatments with statistically similar results. Unlike the case of dressed wheels, there is no unique main factor that dominates PDD. Figures 5.21, and 5.22 show the ANOVA main and interaction effects respectively of the 4 predictor variables

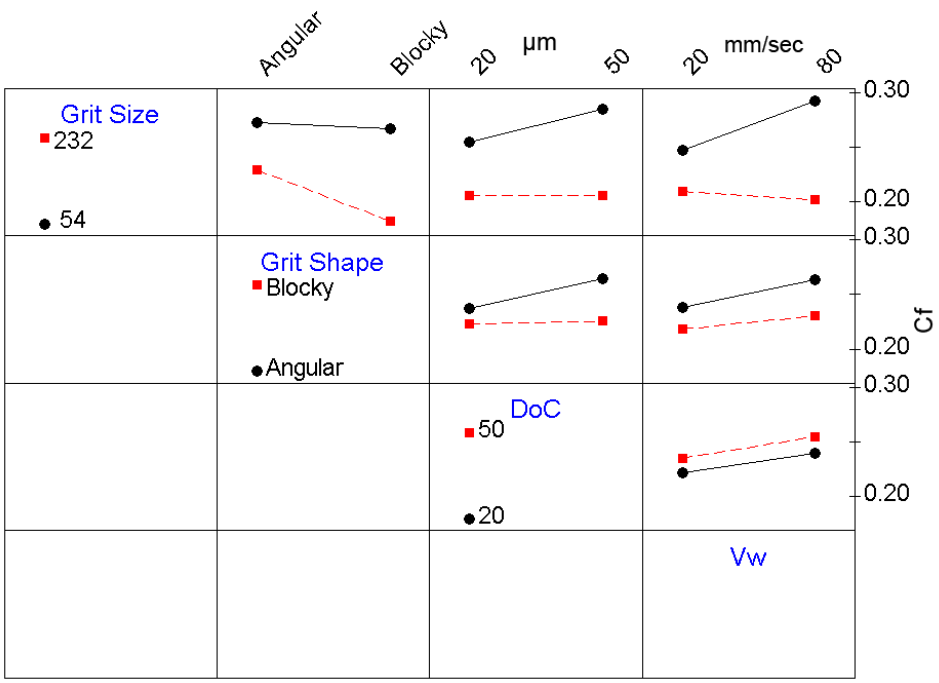

Figure 5.14: ANOVA plot for interaction effects on C_f.

Table 5.8: Best subset regression model for C_f.

Vars	R-Sq	Adj. R-Sq	C_p	s	G_z	DoC	V_w	G_h	MRR	G_z G_h	G_z DoC	G_z V_w	G_h DoC
1	53.6	53.3	667	0.029905	X								
1	28.8	28.4	1123.8	0.037043							X		
2	68.3	68	398	0.024782	X					X			
2	66.3	65.9	435.2	0.025558			X					X	
3	81	80.7	166.3	0.019242			X			X		X	
3	77.5	77.1	231	0.020946			X					X	X
4	83.8	83.4	117	0.017826		X	X			X		X	
4	83.2	82.8	127.8	0.018147			X		X	X		X	
5	87.7	87.3	47	0.015573		X	X			X	X	X	
5	85.1	84.7	94.5	0.017125			X		X	X	X	X	
6	88	87.6	42.5	0.015392	X	X	X			X	X	X	
6	88	87.6	43.1	0.015412		X	X			X	X	X	X
7	89.8	89.4	12.6	0.014273		X	X	X		X	X	X	X
7	88.3	87.9	38.7	0.015227	X	X	X			X	X	X	X
8	90.1	89.7	8.2	0.014066	X	X	X	X		X	X	X	X
8	89.8	89.3	14.4	0.014306		X	X	X	X	X	X	X	X
9	90.1	89.6	10	0.014098	X	X	X	X	X	X	X	X	X

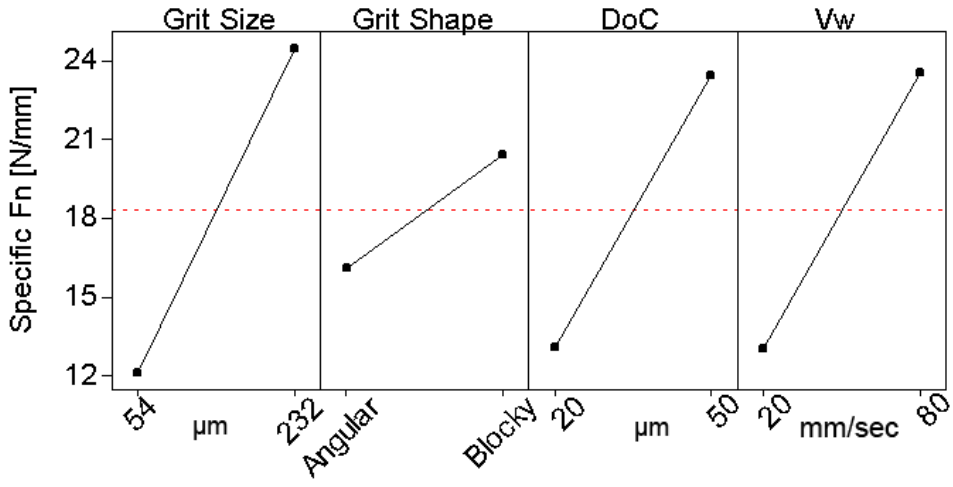

Figure 5.15: ANOVA plot for main effects on F'_N.

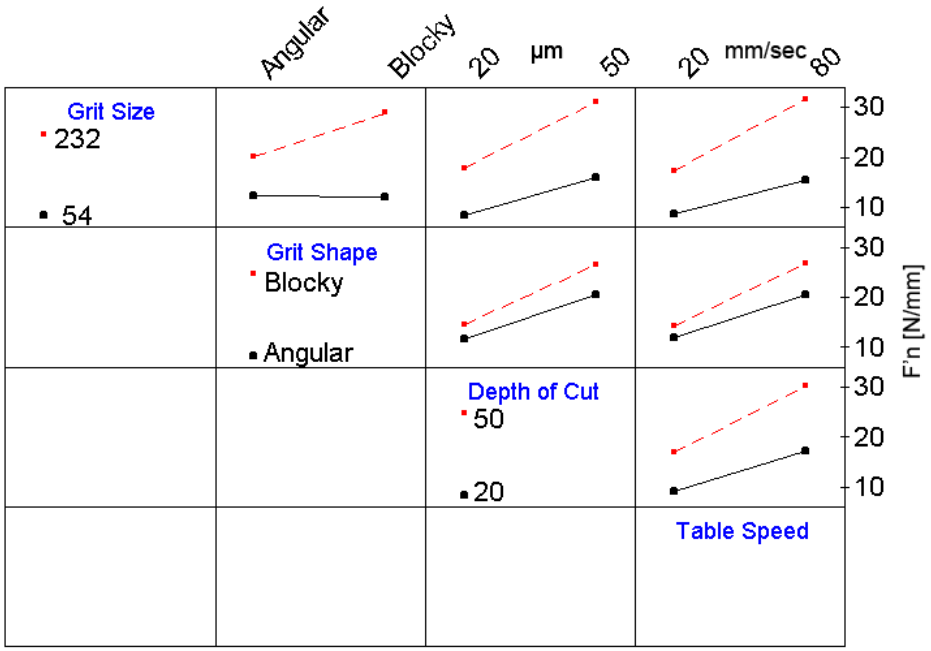

Figure 5.16: ANOVA plot for interaction effects on F'_N.

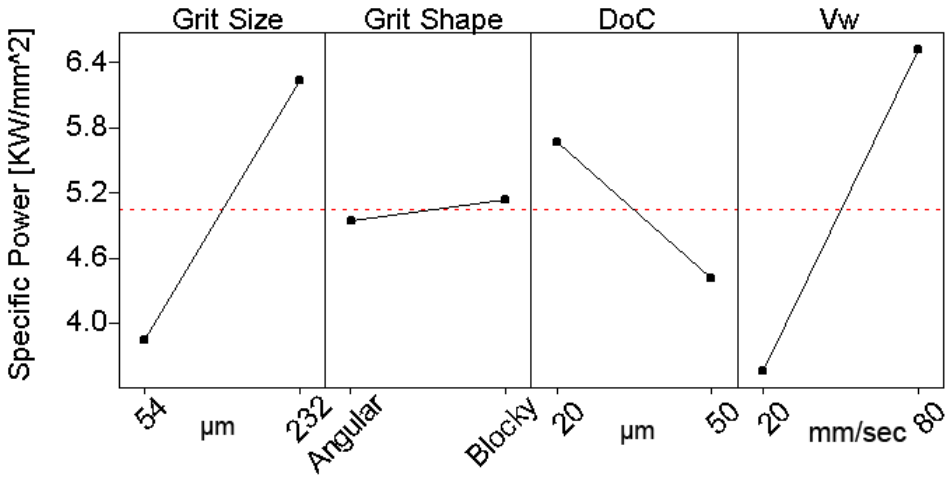

Figure 5.17: ANOVA plot for main effects on P'_w.

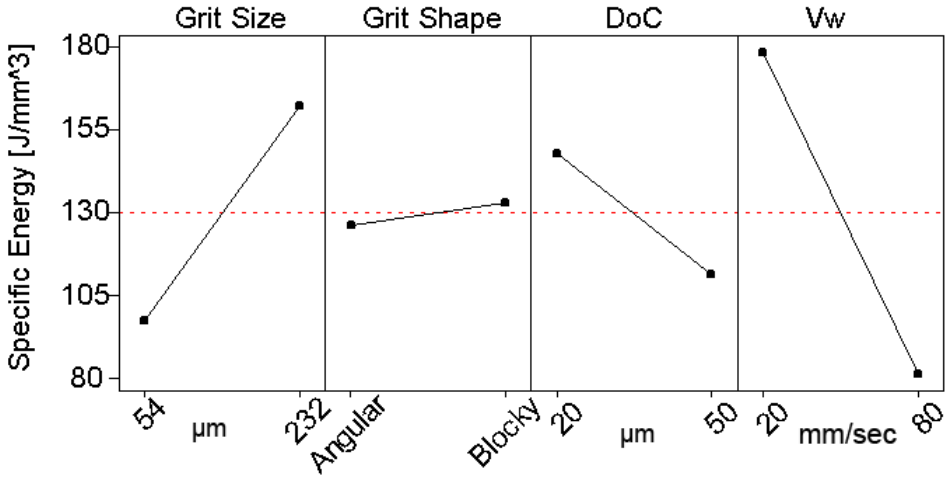

Figure 5.18: ANOVA plot for main effects on E'_g.

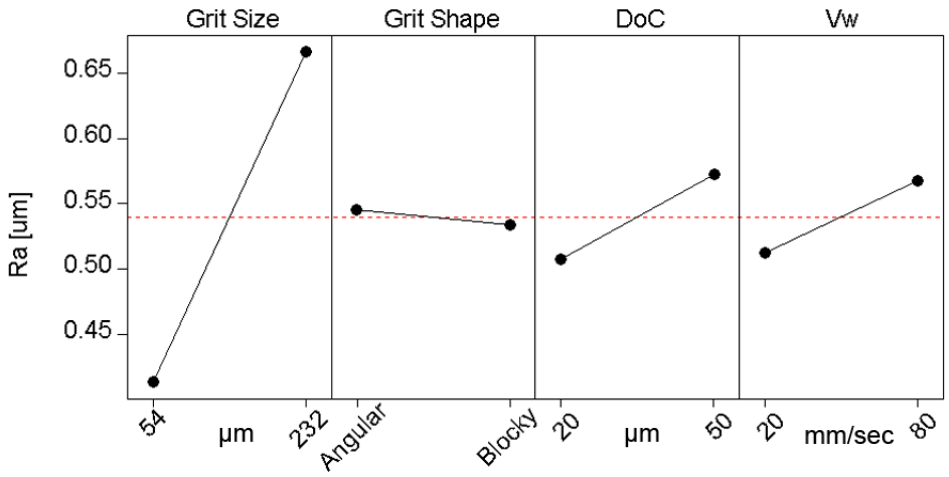

Figure 5.19: ANOVA plot for main effects on R_a.

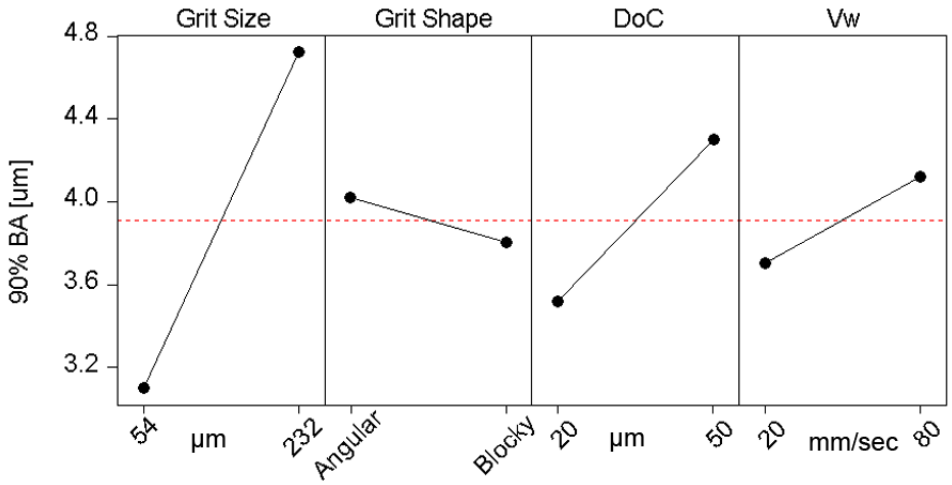

Figure 5.20: ANOVA plot for main effects on 90% BA.

for PDD. As shown in the plots, the main factors are DoC and V_w, which have positive correlation with PDD, therefore MRR also has a positive correlation with PDD. Grit size and shape are not so relevant in this case. Table 5.11 presents the results of the ANOVA for the PDD. The DoC explains half of the data variance followed in importance by V_w. Table 5.12 presents the linear model obtained by stepwise regression over all the main factors and their interactions, F being 4.00. Columns numbered 1 to 7 indicate the number of variables in the model which is composed of a constant term and the factor given in the row of the corresponding variable. Even considering most of the controlled variables and their interaction in a linear model, the R-Sq value is less than 82%. The PDD mean and standard deviation was of $407 \pm 120 \mu m$.

Table 5.9: Summary for tests using worn wheels.

ID	Sample ID		G_z [μm]	G_h	DoC [μm]	V_w $[\frac{mm}{sec}]$	F'_N $[\frac{N}{mm}]$	P'_w $[\frac{W}{mm}]$	C_f	PDD [μm]	Std [μm]
Ag1	X2G84	X2G77	232	Ag	50	20	33.93	288.15	0.213	445.1	18.0
Ag2	X2G80	X2G81	232	Ag	50	80	73.48	636.64	0.223	466.8	16.4
Ag3	X2G62	X2G68	54	Ag	20	80	38.32	434.80	0.279	238.0	39.2
Ag4	X2G71	X2G67	54	Ag	20	20	30.25	360.75	0.293	217.8	33.0
Ag5	X2G16	X2G66	54	Bk	20	80	62.29	559.14	0.229	377.7	75.3
Ag6	X2G85	X2G76	232	Ag	20	80	40.33	381.75	0.233	378.0	25.7
Ag7	X2G70	X2G69	54	Ag	50	20	45.23	524.54	0.280	352.4	17.6
Ag8	X2G63	X2G64	54	Ag	50	80	189.72	1082.88	0.160	613.8	59.9
Bk1	X2G59	X2G55	232	Bk	50	20	42.51	290.49	0.181	497.9	21.2
Bk2	X2G58	X2G54	232	Bk	50	80	92.56	624.23	0.174	553.3	19.8
Bk3	X2G86	X2G78	232	Ag	20	20	18.02	175.77	0.251	337.7	23.6
Bk4	X2G15	X2G17	54	Bk	20	20	35.06	407.07	0.279	287.1	32.2
Bk5	X2G60	X2G56	232	Bk	20	80	52.18	394.26	0.186	428.3	24.6
Bk6	X2G61	X2G57	232	Bk	20	20	16.88	165.14	0.249	305.1	68.4
Bk7	X2G73	X2G72	54	Bk	50	20	68.04	751.17	0.261	452.5	31.0
Bk8	X2G74	X2G65	54	Bk	50	80	162.07	1110.44	0.183	576.4	27.1

Figures 5.23, and 5.24 show the ANOVA main and interaction effects respectively of the 4 predictor variables for C_f. As shown in the plots, all individual factors are relevant, and their correlation is inverse to the one shown for PDD (Fig. 5.13). The interactions between G_z and the rest of the variables are relevant as shown in Table 5.13 of the linear models for C_f obtained by best subset regression. As can be seen, MRR is the most relevant factor (V_w and DoC), followed by G_z.

Table 5.10: Bonferroni test for homogeneous groups for worn conditions$\alpha = 0.05$.

G_z [μm]	G_h	DoC [μm]	V_w [$\frac{mm}{sec}$]	PDD [μm]	1	2	3	4	5	6	7	8	9	10	11
54	Ag	20	20	217.8	**										
54	Ag	20	80	238.0	**	**									
54	Bk	20	20	287.1		**	**								
232	Bk	20	20	305.1			**	**							
232	Ag	20	20	337.7			**	**	**						
54	Ag	50	20	352.4				**	**						
54	Bk	20	80	377.7					**	**					
232	Ag	20	80	378.0					**	**					
232	Bk	20	80	428.3						**	**				
232	Ag	50	20	445.1							**	**			
54	Bk	50	20	452.5							**	**			
232	Ag	50	80	466.8							**	**			
232	Bk	50	20	497.9								**	**		
232	Bk	50	80	553.3									**	**	
54	Bk	50	80	576.4										**	**
54	Ag	50	80	613.8											**

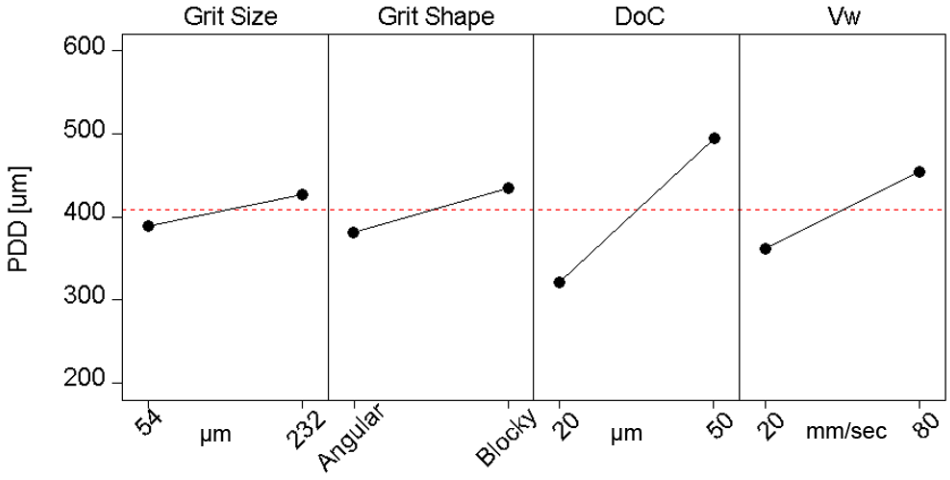

Figure 5.21: ANOVA plot for main effects on PDD.

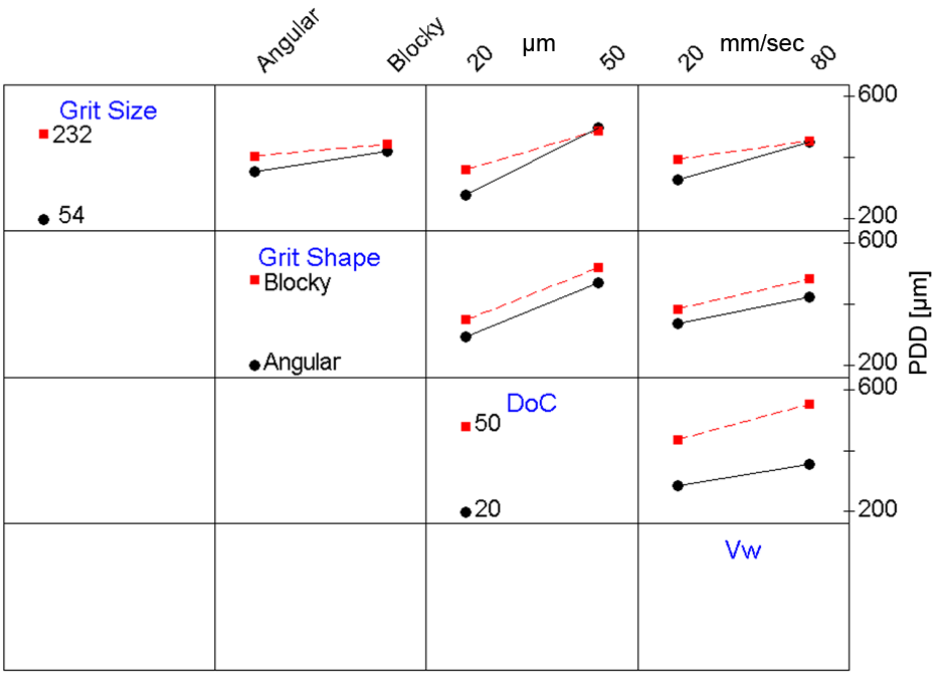

Figure 5.22: ANOVA plot for interaction effects on PDD.

Table 5.11: ANOVA for the PDD.

Source	DF	Seq SS	Adj SS	Adj MS	F	P
G_z	1	65994	65994	65994	18.1	0.000
G_h	1	137795	137795	137795	37.8	0.000
DoC	1	1446088	1446088	1446088	396.5	0.000
Vw	1	406972	406972	406972	111.6	0.000
Error	187	682057	682057	3647		
Total	191	2738905				

Table 5.12: Stepwise regression model for PDD.

Step	1	2	3	4	5	6	7
Constant	296.73	205.49	205.49	175.7	91.24	91.24	17.45
MRR	0.0636	0.0411	0.0411	0.0411	0.0411	0.0516	0.0261
T-Value	14.61	9.59	10.43	10.9	11.77	9.35	3.1
DoC		3.73	3.73	3.73	6.14	5.62	6.89
T-Value		9.56	10.39	10.86	11.53	9.89	10.8
G_h			26.8	26.8	26.8	26.8	26.8
T-Value			5.95	6.22	6.71	6.8	7.06
G_z				0.208	0.799	0.95	1.098
T-Value				4.31	7.02	7.4	8.48
G_z-DoC					-0.0169	-0.0169	-0.0169
T-Value					-5.65	-5.72	-5.93
G_z-V_w						-0.003	-0.006
T-Value						-2.43	-4.21
V_w							1.48
T-Value							3.88
S	82.4	67.8	62.4	59.7	55.3	54.6	52.6
R-Sq	52.91	68.25	73.28	75.69	79.25	79.89	81.41

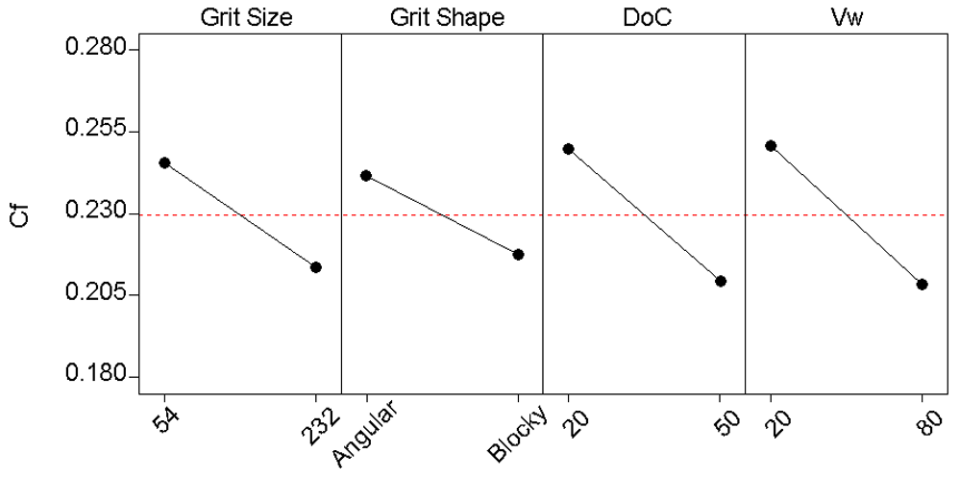

Figure 5.23: ANOVA plot for main effects on C_f.

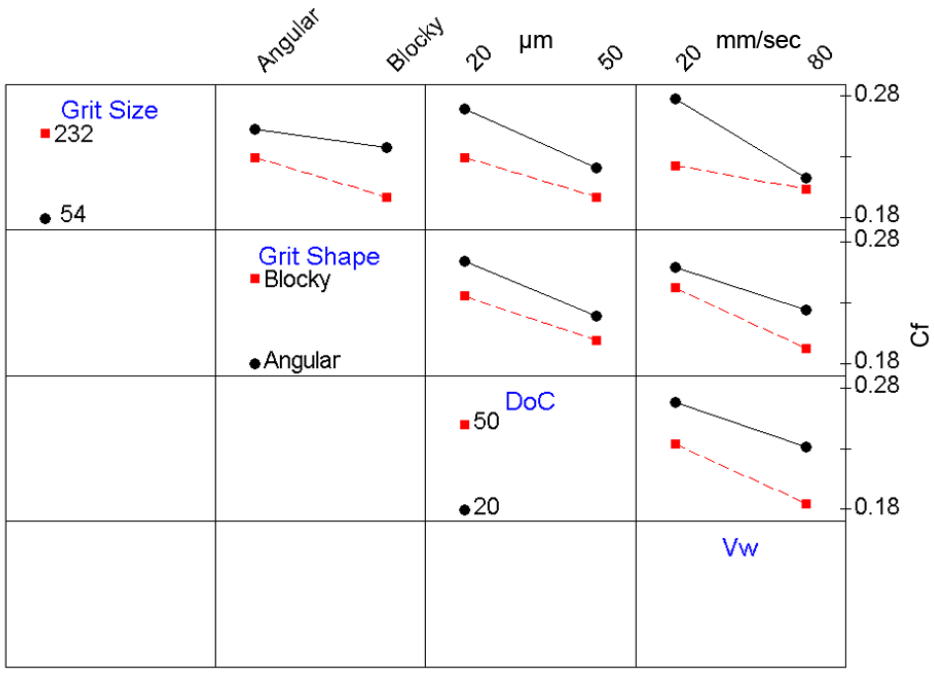

Figure 5.24: ANOVA plot for interaction effects on C_f.

Table 5.13: Best subset regression model for C_f.

Vars	R-Sq	Adj. R-Sq	C_p	G_z	DoC	V_w	G_h	MRR	G_z G_h	G_z DoC	G_z V_w	G_h DoC	G_h V_w
1	44.9	44.6	321.4					X					
1	26.3	25.9	492.6							X			
2	58.9	58.4	194.2	X				X					
2	55.8	55.4	222.1					X		X			
3	67.5	66.9	116.6	X				X	X				
3	67	66.5	121	X				X					X
4	71.7	71.1	79.8	X				X	X		X		
4	71.2	70.6	84.1	X				X			X		X
5	77.5	76.9	27.5	X	X	X			X		X		
5	77.1	76.5	31.8	X	X	X					X		X
6	78.6	77.9	19.4	X	X	X			X		X		X
6	78.5	77.8	20.7	X	X	X			X	X	X		
7	79.6	78.8	12.6	X	X	X			X	X	X		X
7	79.2	78.4	16.3	X	X	X		X	X		X		X
8	80.1	79.3	9.5	X	X	X		X	X	X	X		X
8	79.8	78.9	12.9	X	X	X			X	X	X	X	X
9	80.3	79.3	9.8	X	X	X		X	X	X	X	X	X
9	80.1	79.2	11.5	X	X	X	X	X	X	X	X		X
10	80.4	79.3	11	X	X	X	X	X	X	X	X	X	X

Figures 5.25, and 5.26 show the ANOVA main and interaction effects respectively of the 4 predictor variables for F'_N. As shown in the plots, all individual factors and the G_z and DoC; and DoC and V_w interactions are the most relevant. Unlike the case of dressed wheels, G_z has a negative correlation with F'_N.

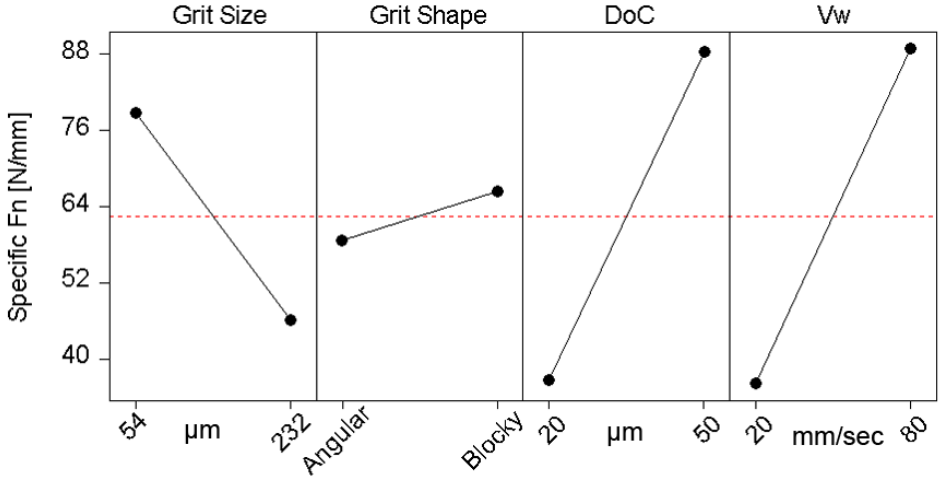

Figure 5.25: ANOVA plot for main effects on F'_N.

Figures 5.27, and 5.28 present the main effects for P'_w and E'_g respectively. Grit shape shows a strong effect on these variables.

Surface parameters are considered in Fig. 5.29, and 5.30 that present the main effects for R_a and 90% of BA respectively. It can be seen that the mean R_a value is in the range of $0.65\mu m$ to $0.95\mu m$, with a mean value for 90% BA of $5.7\mu m$, G_z being the most relevant variable.

Surface cracking was observed on tests using worn wheels, for small G_z, with $DoC = 50\mu m$, and $V_w = 80mm/sec$ for the Ag8 and Bk8 treatments. It was also observed for large G_z, with $DoC = 50\mu m$, and $V_w = 80mm/sec$ for the Bk2 treatment, and only one crack in a sample with Ag2 treatment. This cracking appears to be due to thermal effects. No single parameter correlates with cracking, which seems to be generated when the F'_N ¿ $70N/mm$, or $P'_w > 600W/mm$ and $C_f < 0.2$. The threshold in P'_w gives a level of energy to the workpiece, and the low C_f is indicating that most of that energy is dissipated in friction and plowing, with a small fraction going to chip generation. In this case the different behavior due to G_h can be appreciated. While extensive cracking was observed in the Bk2 treatment, only a single crack was observed in the Ag2 case. The

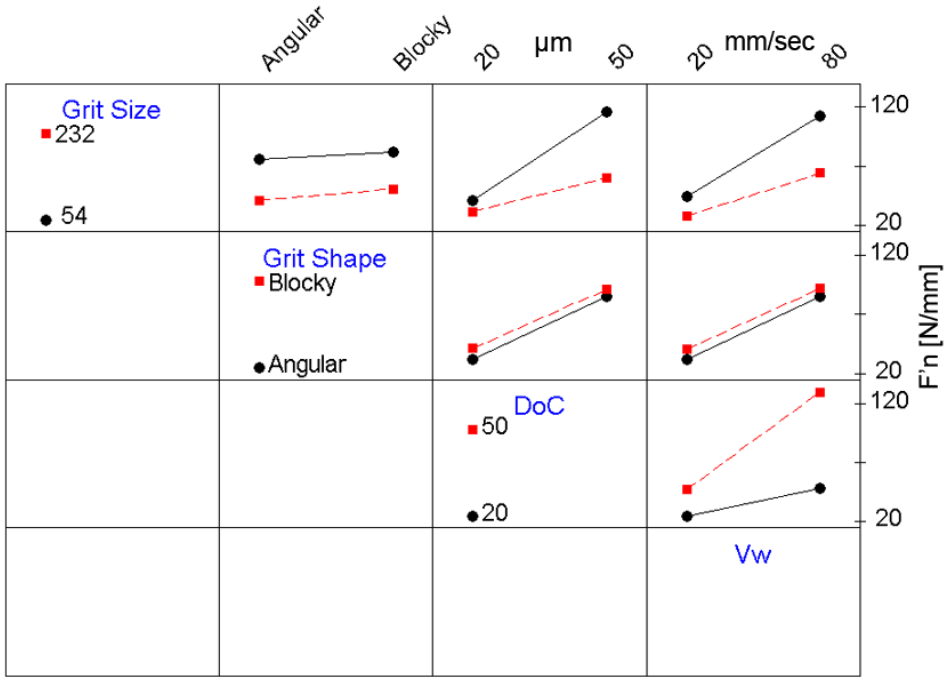

Figure 5.26: ANOVA plot for interaction effects on F'_N.

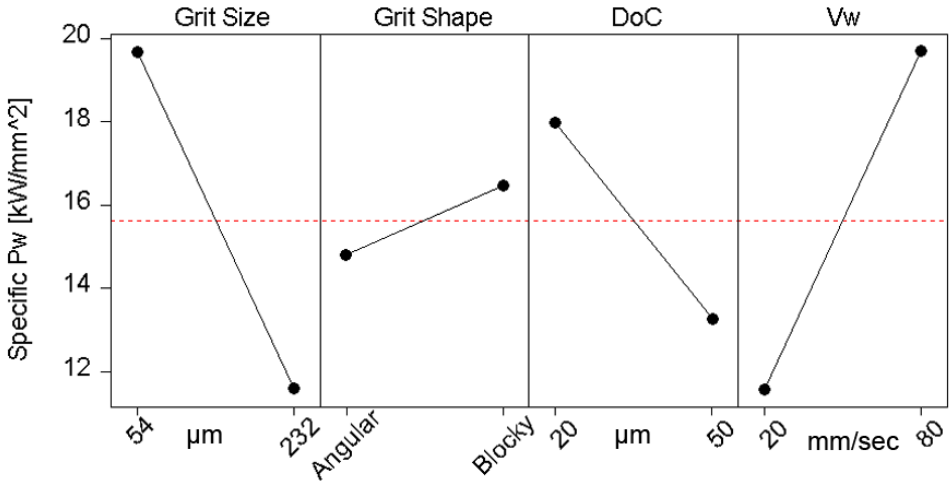

Figure 5.27: ANOVA plot for main effects on P'_w.

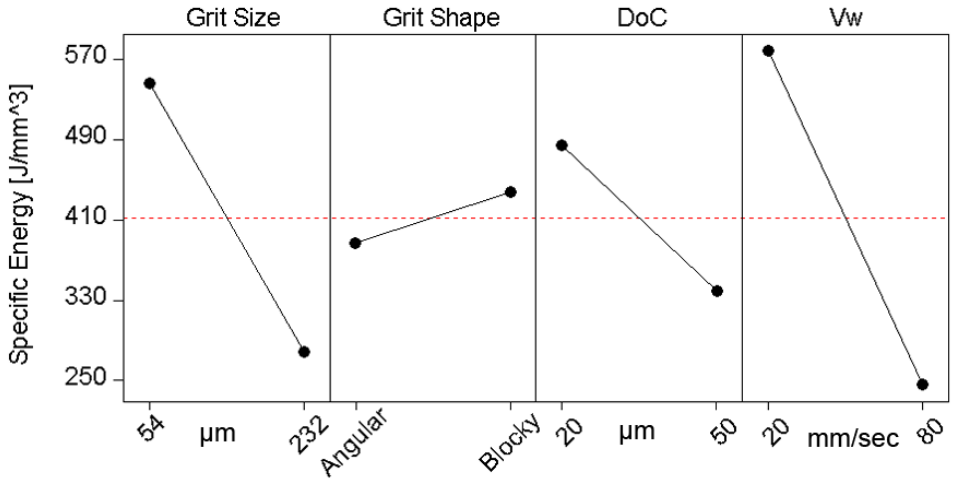

Figure 5.28: ANOVA plot for main effects on E'_g.

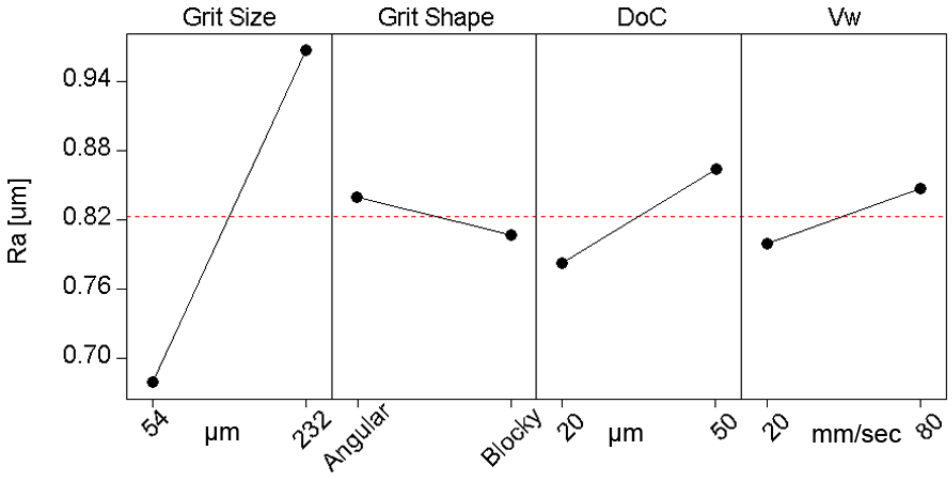

Figure 5.29: ANOVA plot for main effects on R_a.

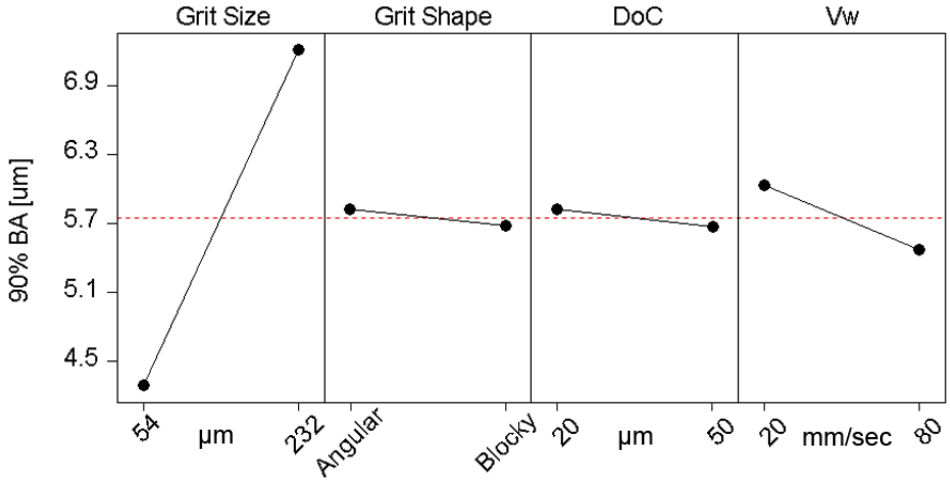

Figure 5.30: ANOVA plot for main effects on 90% BA.

Ag G_h presents a higher C_f than the Bk, due to its angular shape and higher friability with respect to the Bk. Wear flats on Bk shape abrasive grits increase redundant work and heat generation, decreasing C_f. Figure 5.7.2 shows the observed cracking on the ground surface. It can be observed that the cracks are perpendicular to the grinding direction.

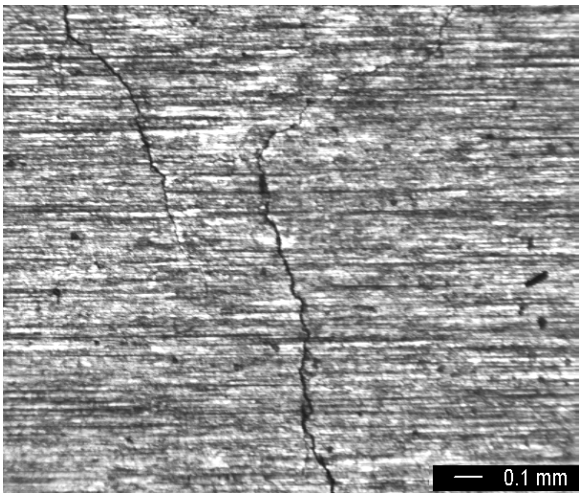

Figure 5.31: Observed cracking on ground surface. Cracking is perpendicular to the grinding direction.

5.7.3 All Wheels

Figures 5.32, and 5.33 show the ANOVA main and interaction effects respectively of the 4 predictor variables for PDD. As shown in the plots, the main individual factors are G_z and DoC which have a positive correlation with PDD. Wear strongly interacts with G_z and to a lesser degree with DoC, and V_w. Table 5.14 presents the linear model obtained by the best subset regression over all the main factors and their interactions, which corroborates that W_r and G_z interaction is relevant as well as the G_z, and DoC. A linear regression model is given in Eq. 5.1. Five variables were selected for the linear regression model giving a R-sq of 80.8% and adjusted R-sq of 80.6%. The addition of more variables does not improve significantly the variance explanation as seen in Table 5.14. Table 5.15 shows the ANOVA of the model. The most significant term in explaining the variance is G_z followed by the interaction of W_r and DoC; and then DoC.

$$PDD[\mu m] = 102 + 1.11G_z + 3.61DoC - 0.835W_rG_z + 2.73W_rDoC + 0.839W_rV_w \qquad (5.1)$$

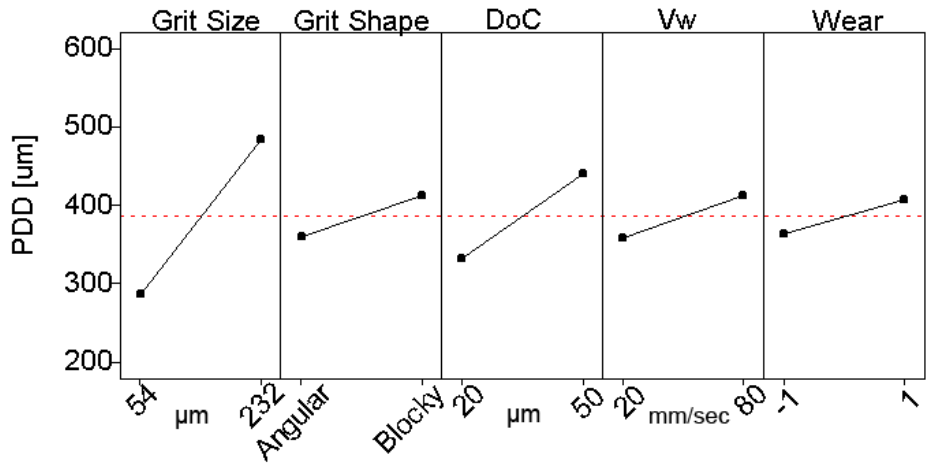

Figure 5.32: ANOVA plot for main effects on PDD.

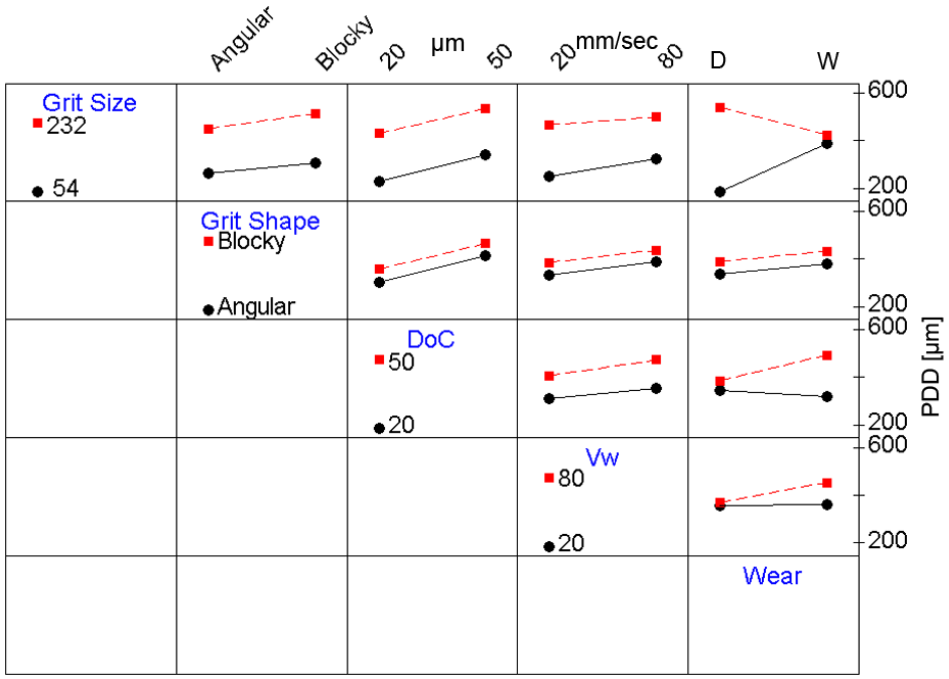

Figure 5.33: ANOVA plot for interaction effects on PDD.

Table 5.14: Best subset regression model for PDD.

Vars	R-Sq	Adj. R-Sq	C_p	s	W_r	G_z	DoC	V_w	G_h	MRR	G_h	G_z-DoC	G_z-V_w	G_h-DoC	G_h-V_w	W_r-G_z	W_r-G_h	W_r-DoC	W_r-V_w
1	42.9	42.8	1314	121								X							
1	37.8	37.6	1467	126		X													
2	49.2	48.9	1130	114		X	X												
2	48.4	48.1	1153	115		X				X									
3	71.4	71.1	473.6	86.2								X				X		X	
3	69.6	69.3	526.5	88.9	X							X				X			
4	77.6	77.4	290.5	76.4		X	X									X		X	
4	76.8	76.6	313	77.7		X				X						X		X	
5	80.8	80.6	197	70.8		X	X									X		X	X
5	80.4	80.2	208.2	71.5		X	X			X						X		X	
6	83.7	83.4	114.7	65.4		X	X			X						X		X	X
6	83.6	83.3	116.3	65.5		X	X	X								X		X	X
7	86.4	86.1	36.6	59.8		X	X		X	X						X		X	X
7	86.3	86.1	38.2	59.9		X	X	X	X							X		X	X
8	86.9	86.7	21.5	58.6	X	X	X		X	X						X		X	X
8	86.9	86.6	23.1	58.7	X	X	X	X	X							X		X	X
9	87.3	87	12.4	57.9	X	X	X	X	X				X			X		X	X
9	87.1	86.8	18.5	58.3	X	X	X	X			X		X			X		X	X
10	87.5	87.1	10.1	57.6	X	X	X	X	X	X			X			X		X	X
10	87.4	87.1	10.8	57.7	X	X	X	X	X		X		X			X		X	X
11	87.6	87.2	8.5	57.4	X	X	X	X	X	X	X		X			X		X	X
11	87.5	87.1	11.9	57.7	X	X	X	X	X	X		X	X			X		X	X
12	87.6	87.2	10.3	57.5	X	X	X	X	X	X	X	X	X			X		X	X
12	87.6	87.2	10.3	57.5	X	X	X	X	X	X	X		X		X	X		X	X
13	87.6	87.2	12.1	57.5	X	X	X	X	X	X	X	X	X		X	X		X	X
13	87.6	87.2	12.2	57.5	X	X	X	X	X	X	X	X	X	X		X		X	X
14	87.6	87.1	14	57.6	X	X	X	X	X	X	X	X	X	X	X	X		X	X
14	87.6	87.1	14.1	57.6	X	X	X	X	X	X	X	X	X		X	X	X	X	X
15	87.6	87.1	16	57.7	X	X	X	X	X	X	X	X	X	X	X	X	X	X	X

Table 5.15: ANOVA for the PDD regression model.

Source	DF	SS	MS	F	P
Regression	5	7988514	1597703	318.65	0.000
Residual Error	378	1895279	5014		
Total	383	9883794			

Source	DF	Seq SS
G_z	1	3731419
DoC	1	1126537
$W_r G_s$	1	222842
$W_r DoC$	1	2589681
$W_r V_w$	1	318037

Figures 5.34, and 5.35 show the ANOVA main and interaction effects respectively of the 4 predictor variables for C_f. As shown in the plots, G_z and G_h and their interaction are the most relevant factors, as well as the interactions between W_r and the rest of the factors except G_h.

Figures 5.36, and 5.37 show the ANOVA main and interaction effects respectively for F'_N. As shown in the plots, DoC, V_w and W_r are relevant, as well as most of the interactions of W_r except for the one with G_h, and the MRR.

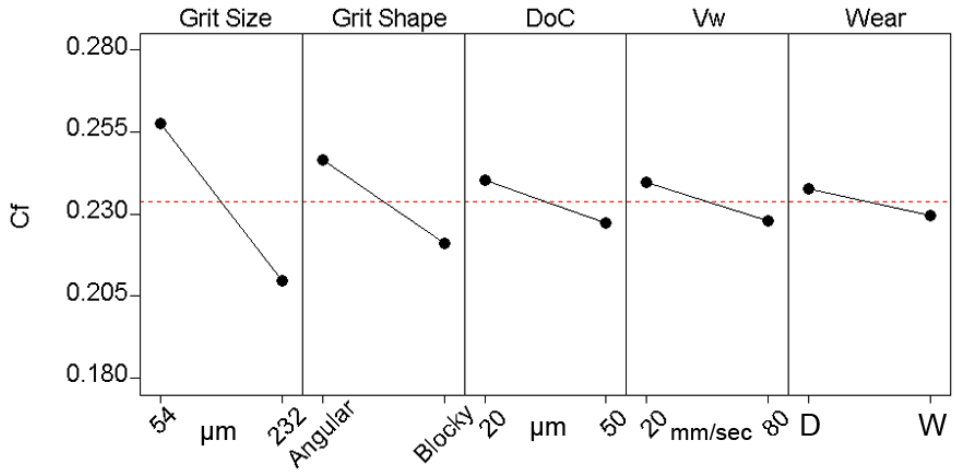

Figure 5.34: ANOVA plot for main effects on C_f.

Figures 5.38, and 5.37 show the ANOVA main and interaction effects respectively for R_a, while Figures 5.38, and 5.37 do so for 90% BA. It can be seen in the plots that G_z and W_r are the most important variables, being the interactions not so relevant.

Figures 5.42 to 5.45 show plots of the mean PDD and its standard deviation vs. F'_N, P'_w,

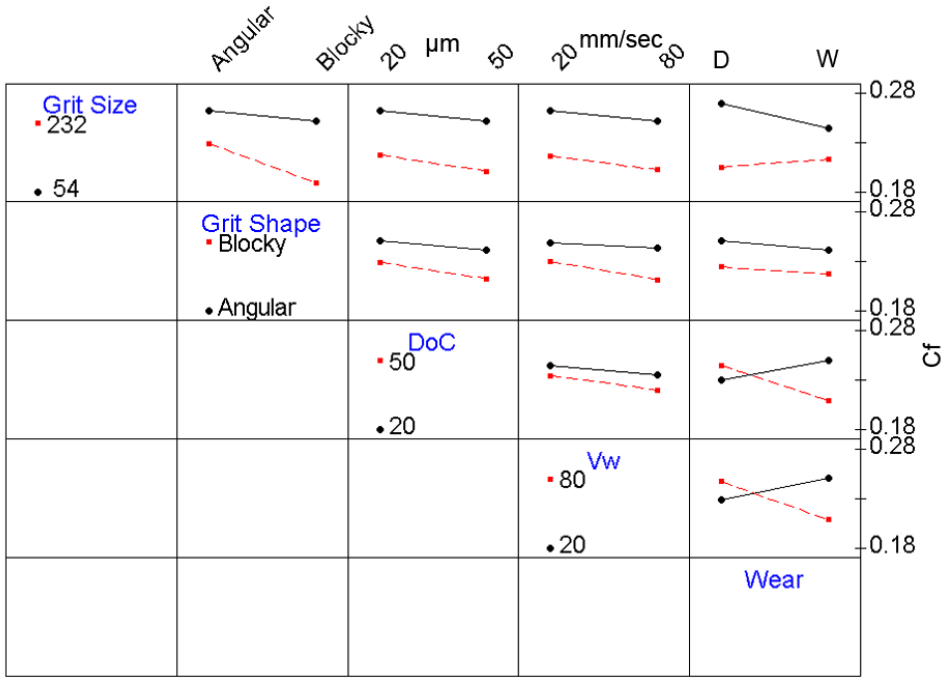

Figure 5.35: ANOVA plot for interaction effects on C_f.

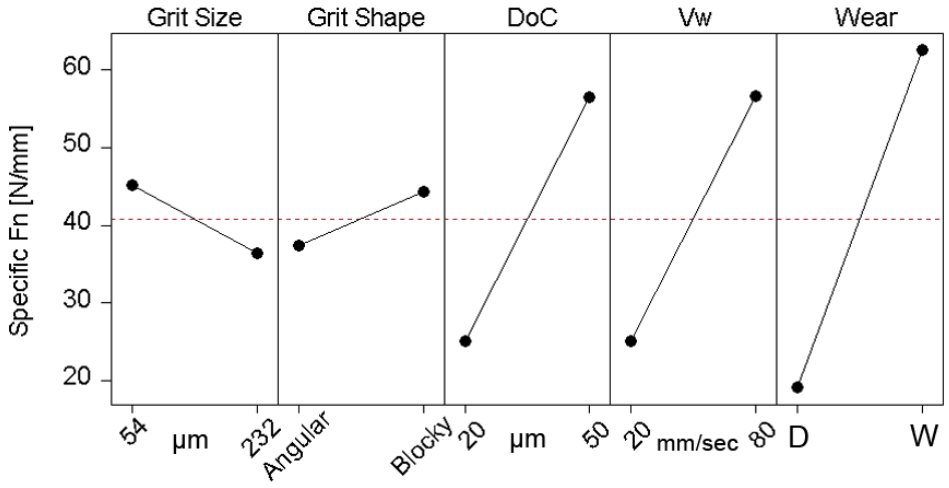

Figure 5.36: ANOVA plot for main effects on F'_N.

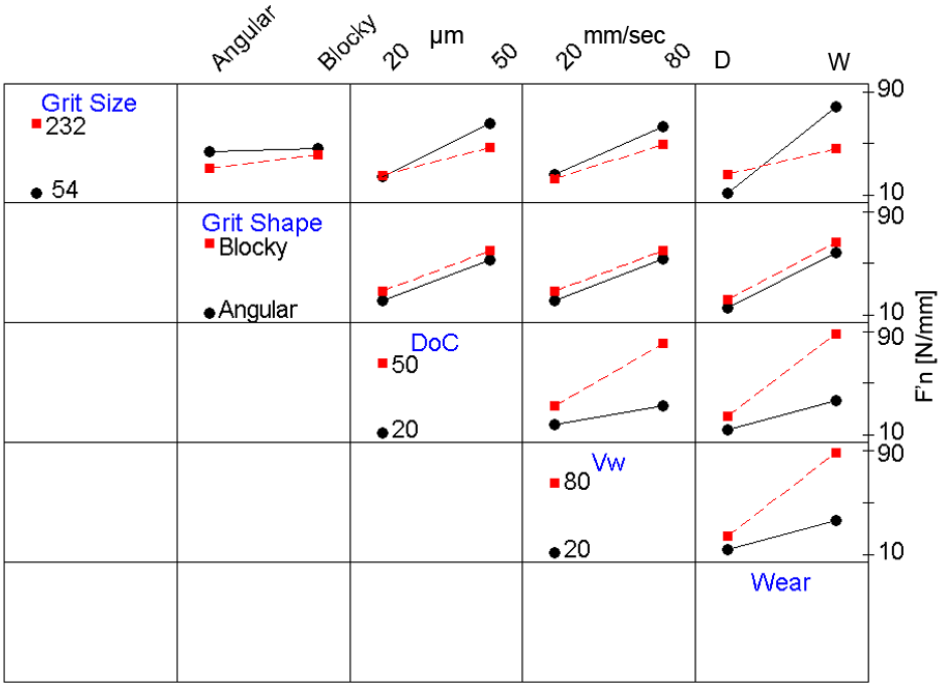

Figure 5.37: ANOVA plot for interaction effects on F'_N.

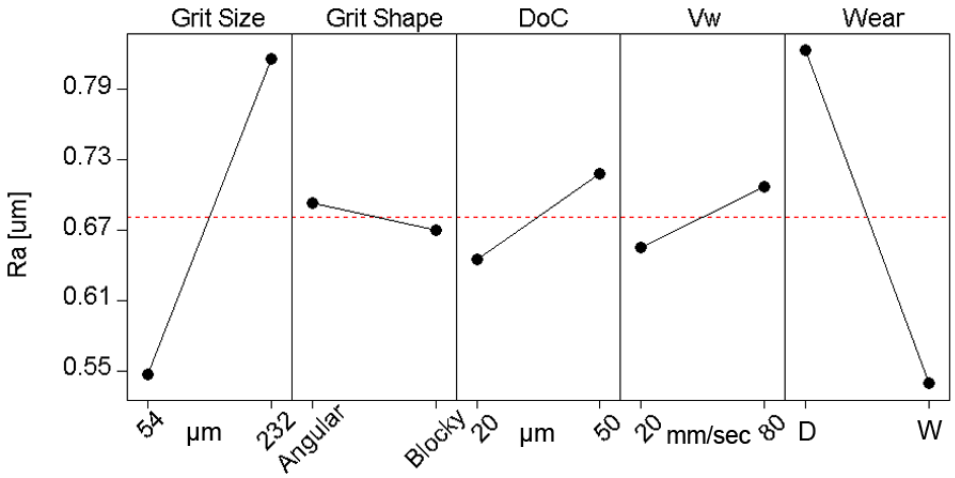

Figure 5.38: ANOVA plot for main effects on R_a.

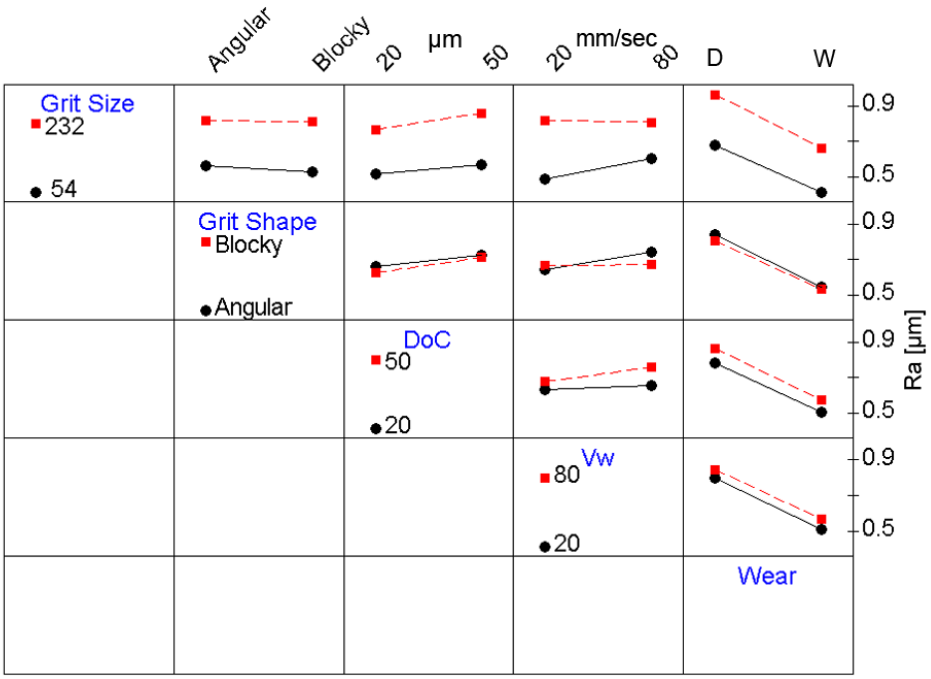

Figure 5.39: ANOVA plot for interactions on R_a.

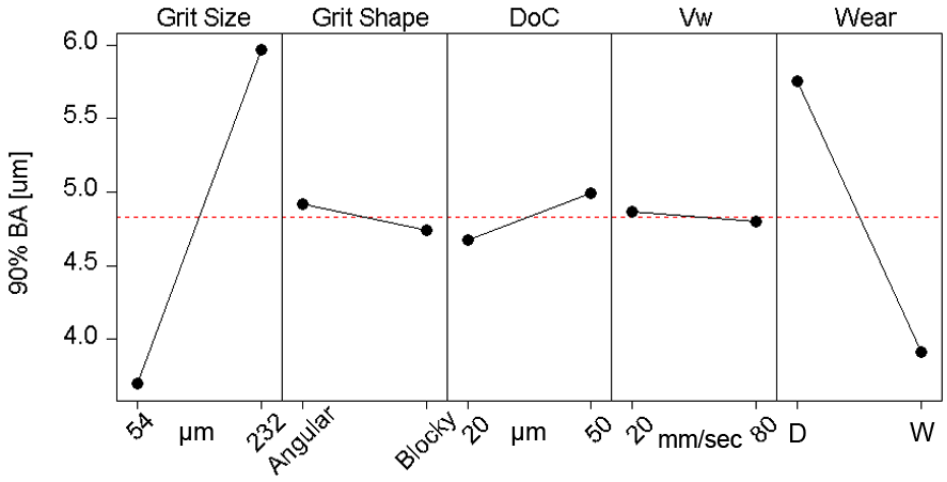

Figure 5.40: ANOVA Plot for main effects on 90% BA.

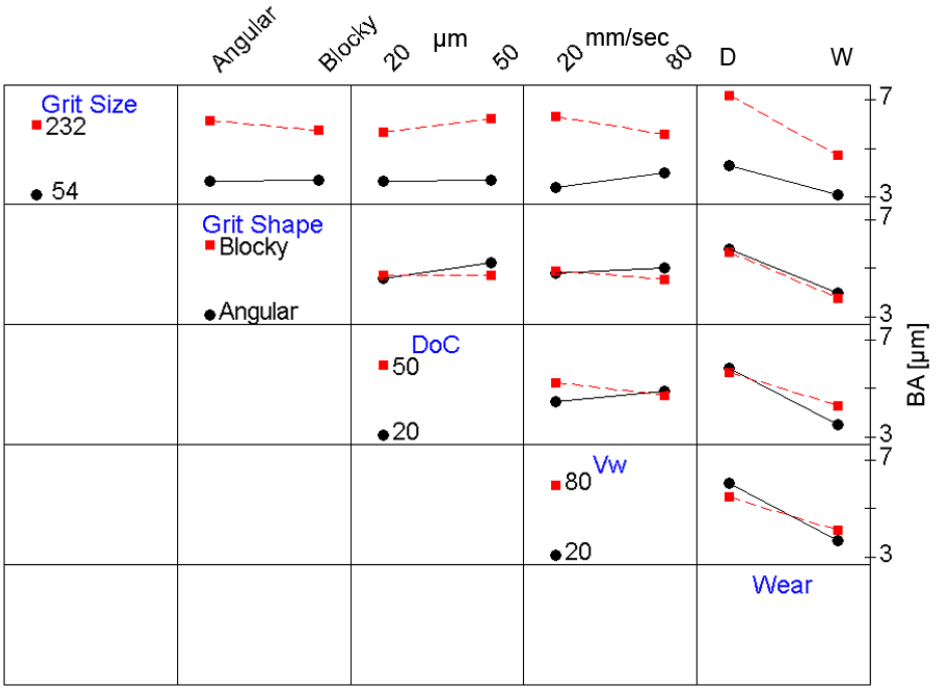

Figure 5.41: ANOVA plot for interactions on 90% BA.

E', and C_f respectively. As shown in the plots, of Figures 5.42 to 5.44, data for dressed wheels is clustered by G_z and data dispersion increases in the order of the plots. Figure 5.45 shows that except for some points in the combination of small G_z and dressed wheels, there is an inverse correlation between C_f and PDD.

5.8 Conclusions

It has been observed that grinding is very sensitive to wheel conditioning and wear. Complete truing and dressing conditions should be specified to obtain consistent results. Cooling conditions are also important.

The PDD mean value extended on an average of about two grains.

It has been observed that in the case of dressed conditions the PDD strongly depends on the G_z, while in the case of worn conditions it strongly depends on the MRR. It is believed that this change in behavior is produced by the increase of thermal effects with wheel wear, and the increase in the force per abrasive grit due to wear flats.

For large G_z it has been observed that the PDD decreases with W_r while the inverse behavior

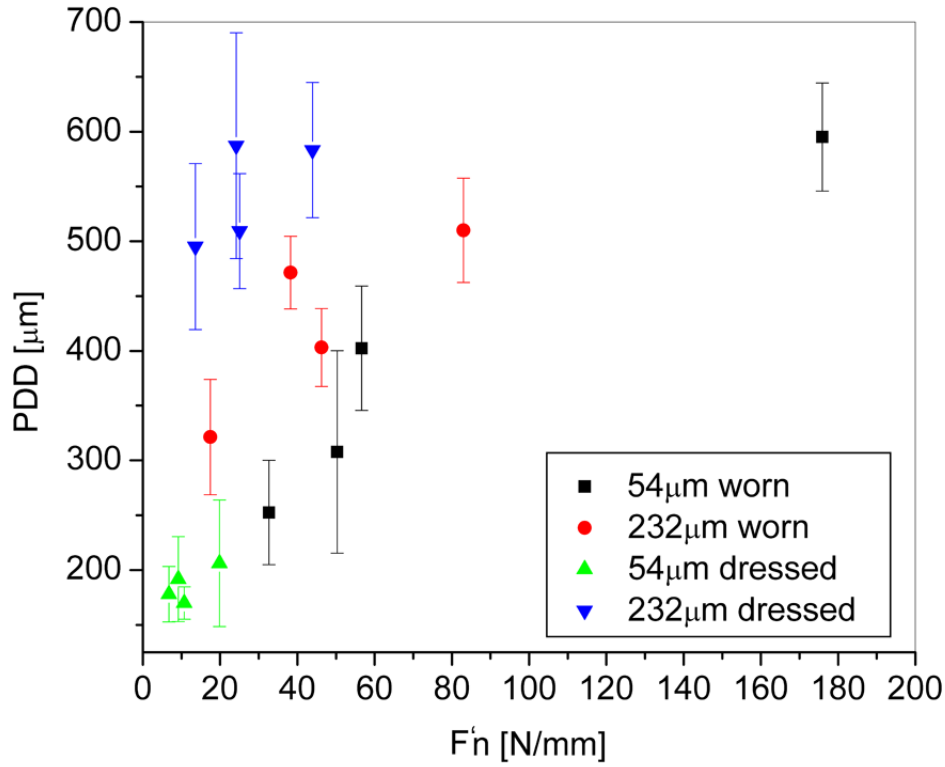

Figure 5.42: Plot of mean PDD and its standard deviation vs. F'_N.

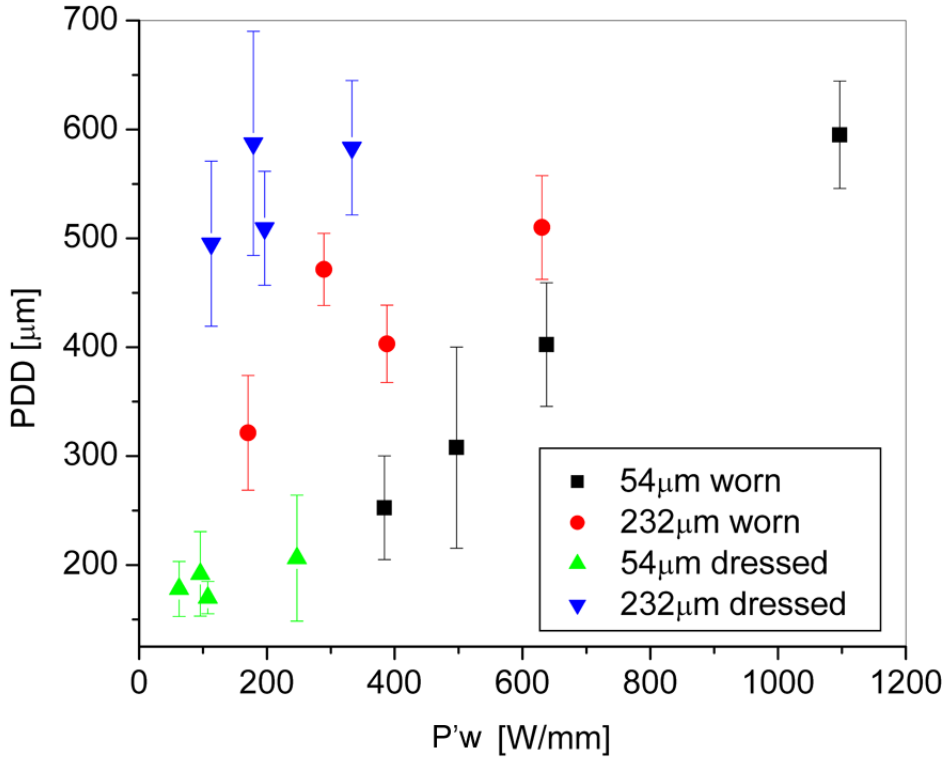

Figure 5.43: Plot of mean PDD and its standard deviation vs. P'_w.

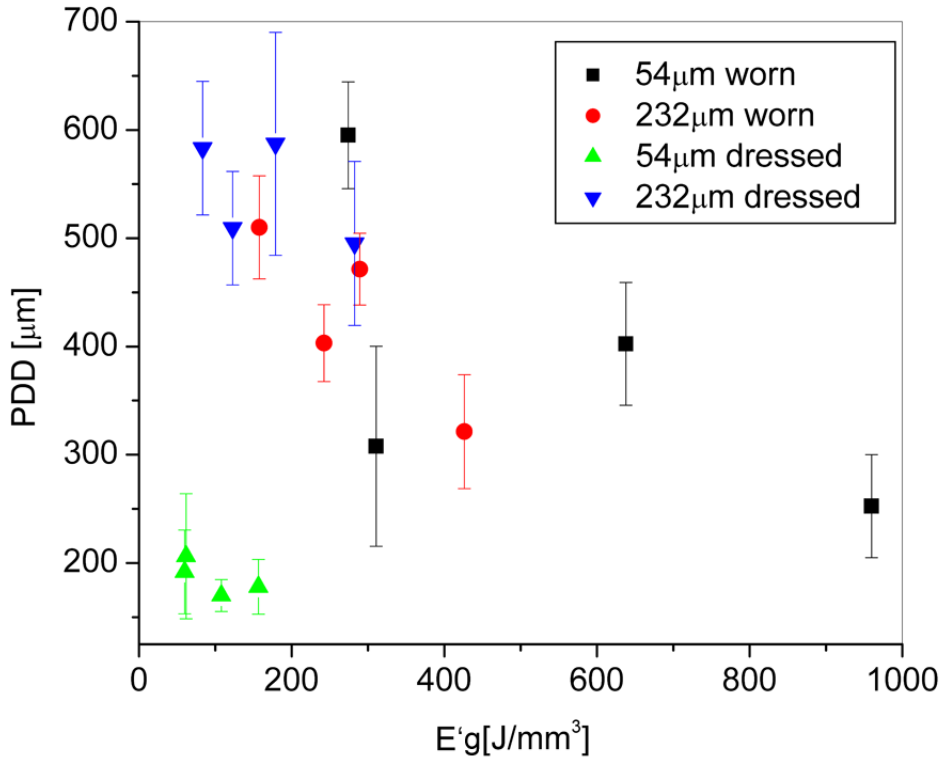

Figure 5.44: Plot of mean PDD and its standard deviation vs. E'_g.

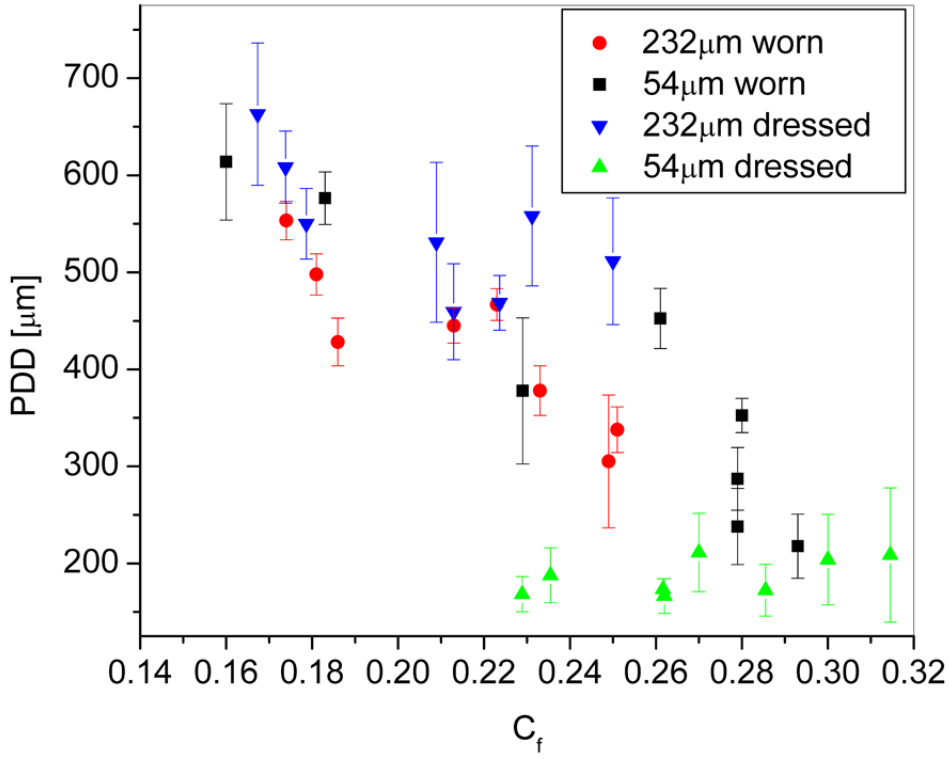

Figure 5.45: Plot of mean PDD and its standard deviation vs. C_f.

was observed for small G_z. While the P'_w was of the same order of magnitude for large G_z in the cases of worn and dressed conditions, it increased an average of 6 times for small G_z. This would indicate that in the case of large G_z the thermal effects were not very different for the two W_r conditions and the PDD was determined by the G_z. The decrease of the PDD could be explained by assuming that the worn wheel presented a narrower distribution of cutting edges than the dressed one. This could be due to some fracture of the abrasive grits during the first stages of grinding after dressing, resulting as if having a smaller grit size. In the case of small G_z can be assumed that the generation of wear flats increased the force per abrasive grit and temperature with the consequent increase of the PDD.

It has been observed that the PDD is inversely correlated to the C_f.

No cracking was observed on the ground surface under a magnification of $60X$ for dressed wheels.

Surface cracking was observed on tests using worn wheels for small G_z in the 4 treatments with the largest MRR. This cracking appears to be due to thermal effects and it was not related to the PDD. It has been observed that cracking was produced on treatments with high F'_N, or high P'_w and low C_f.

It was observed that the Ra and BA mean values increased with wear. This was probably due to the effect of plowing in the formation of side ridges.

5.8.1 PDD

The PDD mean value was of the order of $\simeq 400\mu m$ with an observed minimum and maximum of $\simeq 100\mu m$ and $\simeq 800\mu m$ respectively. Considering that the lamellae size was of the order of $\simeq 250\mu m$, the measured PDD extends on an average of about two grains.

In the case of dressed wheels the PDD measured for small G_z statistically lies in the same range, as well as several groups of treatments for large G_z. The PDD mean and standard deviation for small and large G_z are $186 \pm 40\mu m$, and $543 \pm 85\mu m$ respectively.

Most of the PDD variance can be explained by the G_z factor alone, V_w being not a relevant factor. There is some influence of the G_h, and the interactions between G_z and G_h; and G_z and DoC. The R-Sq value for the model $PDD[\mu m] = 78.1 + 2.007 G_S$ is 87.9%.

In the case of worn wheels, unlike the case of dressed wheels, there is no unique factor that dominates PDD. The main factors are DoC and V_w which have positive correlation with PDD, therefore MRR also has a positive correlation with PDD. Grit size and shape are not so relevant in this case. The DoC explains half of the data variance followed in importance by V_w. Even considering most of the controlled variables and their interaction in a linear model, the R-Sq value is less than 0.82. The PDD mean and standard deviation was of $407 \pm 120 \mu m$ for worn wheels and $365 \pm 191 \mu m$ for dressed ones

An R-sq value of 0.84 is obtained by a linear fit of PDD with C_f.

5.8.2 Grinding Friction Coefficient

Grit size and shape have a negative correlation with C_f, while the correlation with DoC and V_w is positive. In the case of worn wheels all individual factors, and the interactions between G_z and the rest of the variables are relevant for C_f, and their correlation is inverse to the one shown for PDD. While the C_f trend with G_z and G_h is the same as with dressed wheels, the dependence on DoC, and V_w is inverse. The negative correlation of the the C_f with DoC and V_w can be explained by considering the shape change in the abrasives.

5.8.3 Specific Normal Force

In the case of dressed wheels, ${F'}_N$ has a positive correlation with all the individual factors, and the G_z and G_h interaction.

In the case of dressed wheels, all individual factors and the G_z and DoC; and DoC and V_w interactions are relevant for ${F'}_N$. Unlike the case of dressed wheels, G_z has a negative correlation with ${F'}_N$, which can be explained by assuming that the relative wear flat in the small grit is larger than in the large grit. This can be due to the fact that poorer lubrication conditions might occur with smaller grits, with higher temperatures, and increased wear rate of the diamond.

5.8.4 Surface Parameters

For the dressed conditions, the mean R_a value is in the range of $0.4 \mu m$ to $0.7 \mu m$, and the mean 90% BA of $3.9 \mu m$, G_z being is the most relevant factor.

For the worn conditions, the mean R_a value is in the range of $0.65\mu m$ to $0.95\mu m$, with a mean value for 90% BA of $5.7\mu m$, G_z being the most relevant variable.

The Ra mean value increased $\simeq 0.25\mu m$ from the dressed wheel condition to the worn one, and a similar trend was observed for BA. Worn wheels have a narrower spatial cutting edges distribution than in dressed conditions, also the chip thickness is smaller. Therefore, a possible explanation for the increase in roughness is the plowing increase with the formation of scratching side ridges.

5.8.5 Cracking

Surface cracking was observed on tests using worn wheels, for small G_z, with $DoC = 50\mu m$, and $V_w = 80mm/sec$ for the Ag8 and Bk8 treatments. It was also observed in the case of large G_z, with $DoC = 50\mu m$, and $V_w = 80mm/sec$ for the Bk2 treatment, and only one crack in a sample with Ag2 treatment. This cracking appears to be due to thermal effects. Cracking seems to be generated when the F'_N ¿ $70N/mm$, or $P'_w > 600W/mm$ and $C_f < 0.2$. The threshold in P'_w gives a level of energy to the workpiece, and the low C_f is indicating that most of that energy is dissipated in friction and plowing, with a small fraction going to chip generation. In this case the different behavior due to G_h can be appreciated. While extensive cracking was observed in the Bk2 treatment, only a single crack was observed in the Ag2 case. The Ag G_h presents a higher C_f than the Bk, due to its angular shape and higher friability with respect to the Bk. Wear flats on Bk shape abrasive grits increase redundant work and heat generation, decreasing C_f.

CHAPTER VI

RESIDUAL STRESS MEASUREMENTS

6.1 Introduction

Residual stresses are self-equilibrating internal stresses in a body without any external forces or constraints. They can be introduced into the material by any mechanical, thermal or chemical processes. For crystalline solids x-ray diffraction is a widely used technique to measure residual stresses, and it is based on the measurement of the change of the interplanar spacing $d_{\{hkl\}}$ for a given family of planes $\{hkl\}$ with respect to its relaxed state spacing $d^0_{\{hkl\}}$. A basic schematic of the interplanar spacing measurement is given in Fig. 6.1.

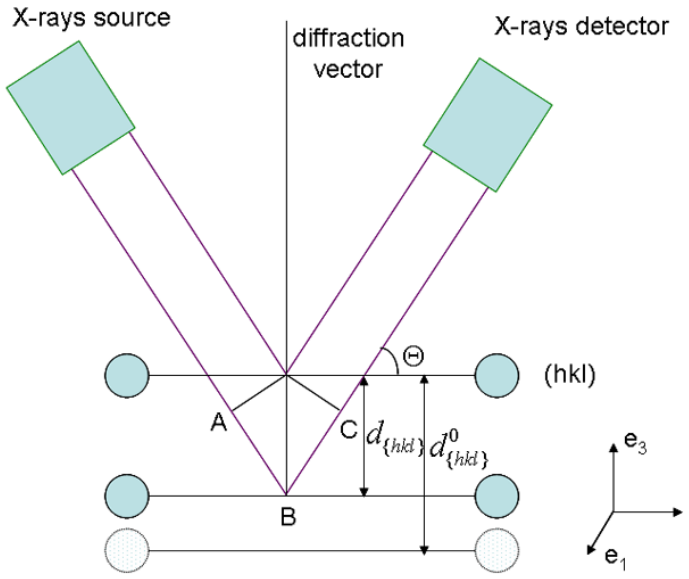

Figure 6.1: Measurement of interplanar spacing $d_{\{hkl\}}$.

By the application of Bragg's law the pathlength difference between beams diffracted by parallel planes is equal to the order of the reflection n of the monochromatic wavelength $\overline{AB} + \overline{BC} = 2d_{\{hkl\}} \sin\Theta = n\lambda$ where $d_{\{hkl\}}$ can be computed. This interplanar spacing is compared with the stress free interplanar spacing $d^0_{\{hkl\}}$. The component ε_{33} of the strain tensor in the sample reference system of unit vectors e'_i is given by Eq. 6.1. From this strain the stress can be obtained by applying

the appropriate coordinate transformation and linear elasticity theory.

$$\varepsilon'_{33} = \frac{d_{\{hkl\}} - d^0_{\{hkl\}}}{d^0_{\{hkl\}}} \tag{6.1}$$

This chapter describes the technique used to prepare the samples, collect, and analyze the diffraction data. The design of experiments and the strain and stress results are reported as well as the analysis of the obtained data. The purpose of these measurements is to evaluate the subsurface profile of the residual stress and its correlation with PDD.

6.2 Design of Experiments

The measurement and analysis of residual stresses is a time consuming process, therefore the study was limited to analyze the effects of the magnitude of PDD on the residual stress for dressed conditions. A total of 4 samples were analyzed with measurement at the machined surface and at several depths, up to around $300\mu m$. Two of the samples were taken from the batch having a PDD mean value of $186\mu m$, and two more with a PDD mean value of $543\mu m$. Since there was no appreciable effect of the G_h on the PDD, this variable was considered irrelevant for selecting the samples. Otherwise, the same conditions were chosen. Table 6.1 presents the specimens used and corresponding mean PDD.

Table 6.1: DOE for residual stress measurements.

Sample ID	PDD μm
X1G06	720.1
X1G10	605.7
X1G15	177.5
X2G08	168.4

6.3 Experimental Technique

The x-ray diffraction data acquisition was carried out at the ORNL (Oak Ridge National Laboratory) High Temperature Materials Laboratory. A rotating anode Scintag XDS 2000 diffractometer machine with a Cu target was used with a setting of 40kV and 200mA (8kW), providing a near

monochromatic radiation of wavelength $\lambda\,(Cu_{K\alpha}) = 1.54059\,\mathring{\text{A}}$ with a line focus of 0.5mm x 10 mm (Figure 6.3).

Prior to measurement the samples were ultrasonically cleaned in an acetone solution, mounted on a quartz zero background plate and positioned for proper alignment with the collimated x-ray beam (Figure 6.4). In the case of subsurface measurements the sample was electropolished in a NaCl saturated water solution. A removal rate of 10μm/min was used with a potential of 25V and a current density of 6.7E3 A/m^2. The samples were masked at the sides to minimize the formation of rounded edges. To control the amount of material removed, measurements of the sample height were made pre and post electropolishing at 3 different points, the mean height of the removed layer was reported, and its typical relative deviation was around 3%.

Since the triaxial stress state was desired, a minimum of six θ (polar or Bragg angle) detector scans were made at independent pairs of Φ (azimuthal) and Ψ (tilt) angles that form a non-singular Jacobian matrix. The type of angle measurement utilized is the so-called Ω-goniometer. The tilt axis lies in the specimen surface, perpendicular to the diffraction and the diffraction vector, which is parallel to the normal to the diffracted plane (Fig. 6.2). Scans were made either by maintaining Ψ constant and varying Φ or vice versa (Noyan and Cohen, 1987). The intensity as a function of the 2Θ angular position was acquired at regular $\Delta\theta$ steps of typically 0.04° with a counting time of typically $10 sec/step$.

The normalized detected intensity was plotted against the 2Θ angle or the equivalent interplanar spacing "d-spacing," calculated from Bragg's law for each of the phases. A calculated plot of 2Θ vs. relative intensity for $\gamma - TiAl$ with 10% of Ti_3Al is shown in Fig. 6.5. Because the sensitivity of the method increases with Θ, the selected peaks to be measured were in the range of $135^\circ \leq 2\Theta \leq 144^\circ$ as shown in the calculated plot in Fig. 6.6. Since the $TiAl$ is the predominant phase, interplanar spacing was measured in that phase. Another consideration in peak selection was that they should be separate enough from each other to minimize overlapping. The compromise solution was to select the {224} and {422} $TiAl$ peaks. An advantage of selecting these peaks is that within a reasonable $\Delta 2\Theta$ scan interval, two peaks can be tracked independently increasing the data statistics. This is possible because the tetragonality of the $TiAl$ cell (sides relation of 1.02), which is also given by the relation of $d^0_{\{224\}}/d^0_{\{422\}}$. It has to be noted that due to symmetry considerations the multiplicity of

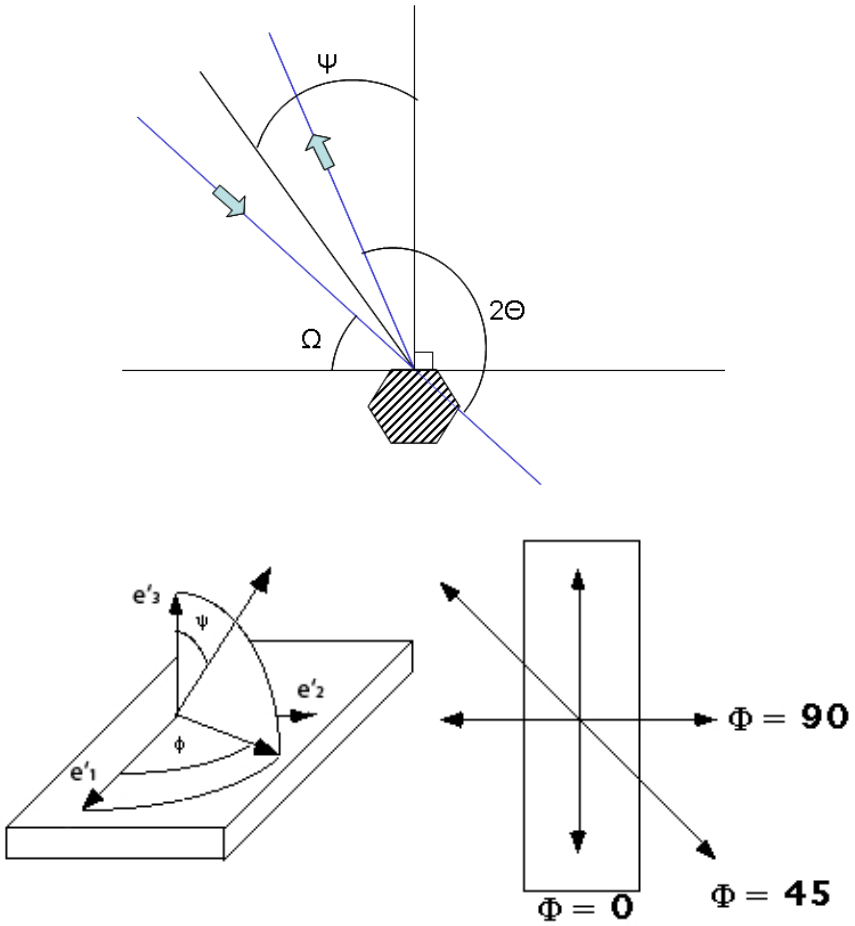

Figure 6.2: Angles convention.

the $d_{\{224\}}$ family of planes is of 8 while the $d_{\{422\}}$ is of 16, having their peaks a theoretical intensity relation of $r_i = 3.0/6.4$.

Figure 6.7 presents an experimental plot of the normalized intensity in CPS (counts per second) vs. 2Θ. The $\{224\}$ and $\{422\}$ peaks can be clearly seen and are composed by the doublet $K_{\alpha 1}$ and $K_{\alpha 2}$ radiation from the Cu target. The standard approach (Ely et al., 1999) is to separate the total intensity as composed by the intensity of the peak, in this case a doublet, and the background contribution (Eq. 6.2).

$$\begin{aligned} I_{2\Theta} &= I_{peak}[\textit{shape function}] + [\textit{background}] \\ \textit{(shape function)}_{doublet} &= \textit{(shape function)}_{\mathrm{K}_{\alpha 1}} + \textit{(shape function)}_{\mathrm{K}_{\alpha 2}} \end{aligned} \tag{6.2}$$

Where $I_{2\Theta}$ is the intensity at the specified angle 2Θ and the shape function can be one of several standard functions (Gaussian, pseudo Voigt, Pearson-VII, etc.). Typically, the shape function is defined so that it varies in magnitude between 0 and 1 hence, the need for the scale parameter I_{peak} in Eq. 6.2 to adjust the fitting function to the same vertical scale as that of the data. Prior to the data fit, the background energy was subtracted assuming a linear dependence with 2Θ. All four peaks were fitted together to the Pearson-VII function considering least-squares error minimization. Figure 6.7 shows the partial fits and the total fit which is a good approximation to the acquired data. The value of the $d_{\{hkl\}}$ spacing was obtained from the 2Θ at maximum intensity of the respective $K_{\alpha 1}$ peak using Bragg's law. In theory each peak should be a Dirac delta function at the theoretical $d_{\{hkl\}}$ value. In practice this is not possible. Factors such as the fact that radiation is not monochromatic, and $d_{\{hkl\}}$ spacing is not constant in the irradiated volume widen the peak. Therefore, there is an associated indetermination on the position of the peak maximum which will be propagated to the final residual stress.

Accurate lattice strain can only be determined if the irradiated area of the specimen has a sufficient number of randomly oriented grains of the phase of interest. This condition is not fulfilled in coarse grained material as in this case. To improve this situation, the specimen was mounted on a reciprocating stage which was moving in the range of $\pm 5mm$ during the acquisition, enlarging the irradiated area.

Another important issue is to determine $d^0_{\{hkl\}}$ since the analysis is very sensitive to this value.

In theory this value should be obtained from diffraction data from an annealed powder sample of the same material, and no theoretical calculation is a good approximation since minimal variations in the chemical composition or thermomechanical history have a strong effect on $d^0_{\{hkl\}}$. In this work, such value was obtained from the average of several measurements of $d^0_{\{hkl\}}$ in sample zones where it was assumed no stresses were present. Table B.1 and B.2 on Appendix B presents the measurements for the determination of the $d^0_{\{224\}}$ and $d^0_{\{422\}}$ values with their respective mean and deviation.

Figure 6.3: X-ray diffraction machine utilized for measurements.

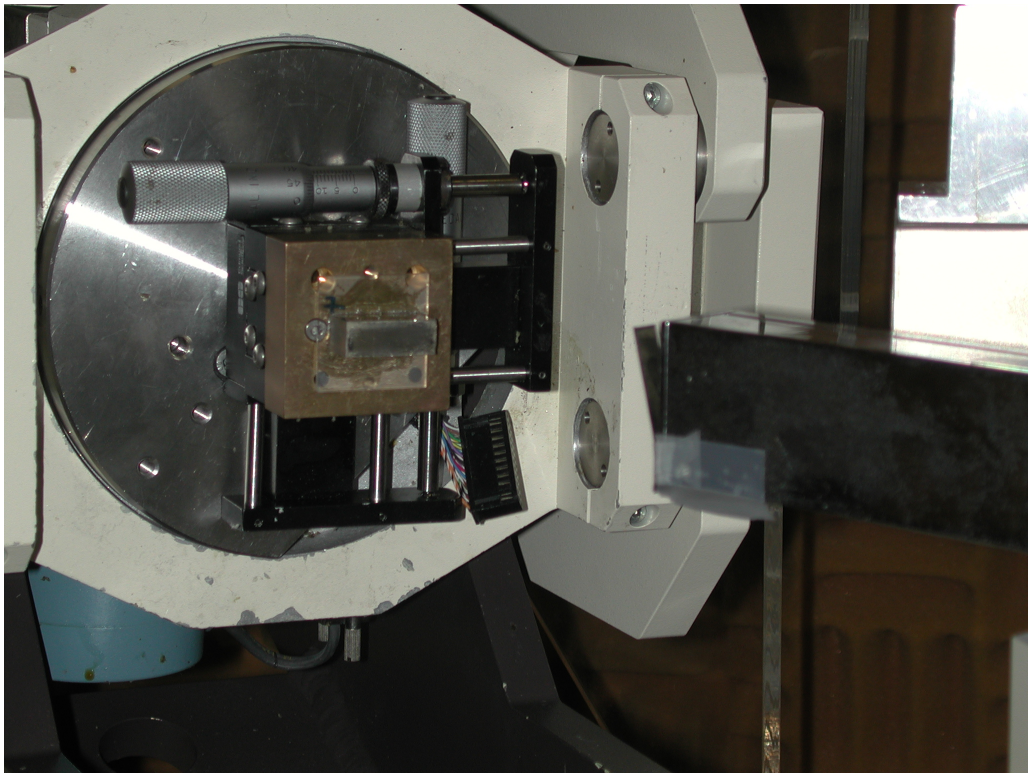

Figure 6.4: X-ray diffraction machine. Close-up of mounted specimen.

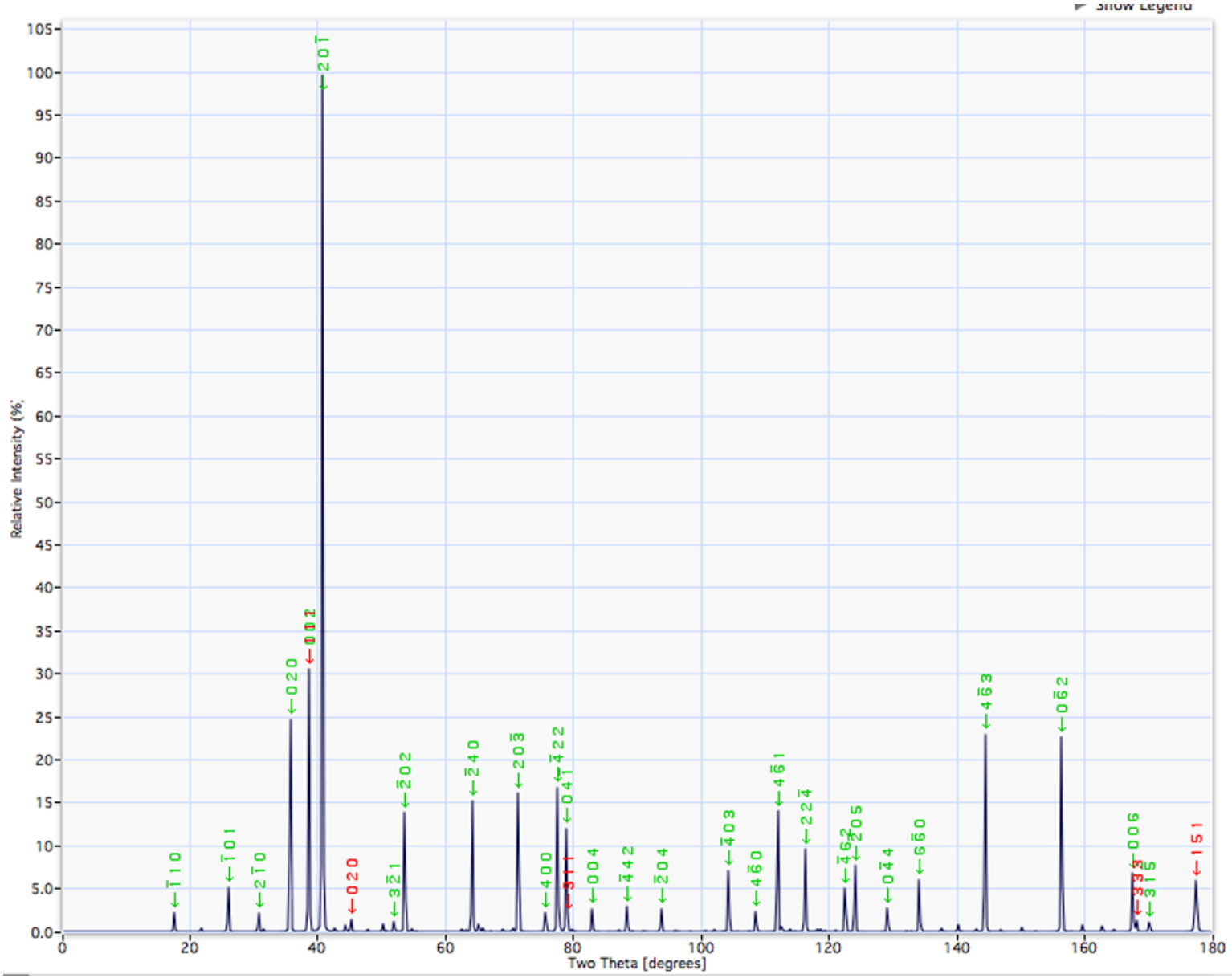

Figure 6.5: Calculated 2Θ vs. relative intensity. Green TiAl. Red Ti_3Al. Full range.

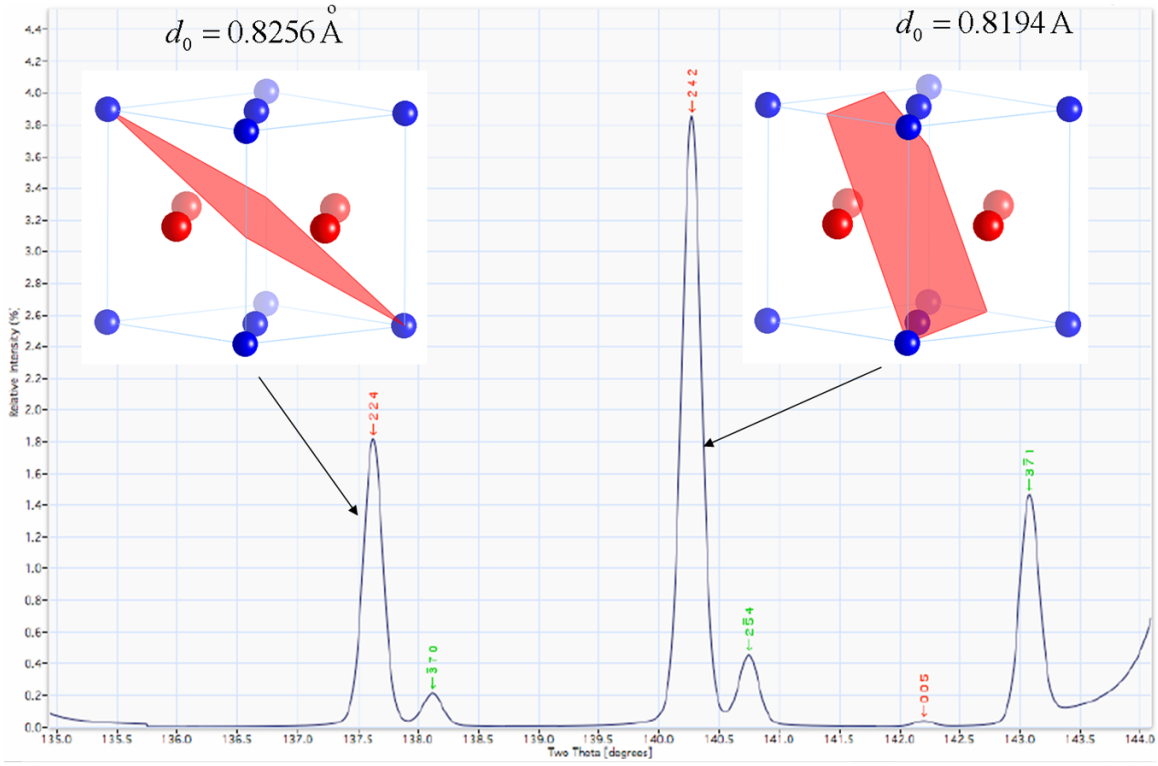

Figure 6.6: Measured peaks in the calculated 2Θ vs. relative intensity. Range of interest.

6.4 Data Analysis

A theoretical framework is required to obtain strain and stress measures from the intensity plots. The standard technique proposed by Dölle and Hauk (1976, 1977) is widely used, which assumes a linear relation of the $d_{\{hkl\}}$ vs. $sin^2\Psi$ plot in which the slope is related to the stress. This physically means the absence of shear stress components and stress gradients in the irradiated volume. Another widely used simplifying assumption is a planar stress state with the stress component normal to the surface $\sigma_{33} = 0$. How well the data falls on a straight line is an indicator of how well the results fit theory. This method is referred to as the differential $sin^2\Psi$ method. A modification of the analysis can manage the existence of shear stresses and a "Ψ splitting" would be observed on the $d_{\{hkl\}}$ vs. $sin^2\Psi$ plots in this case.

In this case, the data shows strong nonlinearity in the $d_{\{hkl\}}$ vs. $sin^2\Psi$ plots invalidating this type of analysis. Instead, a generalized statistical analysis is proposed based on Winholtz and Cohen (1988). This method considerably reduces the stress variance due to counting statistics and

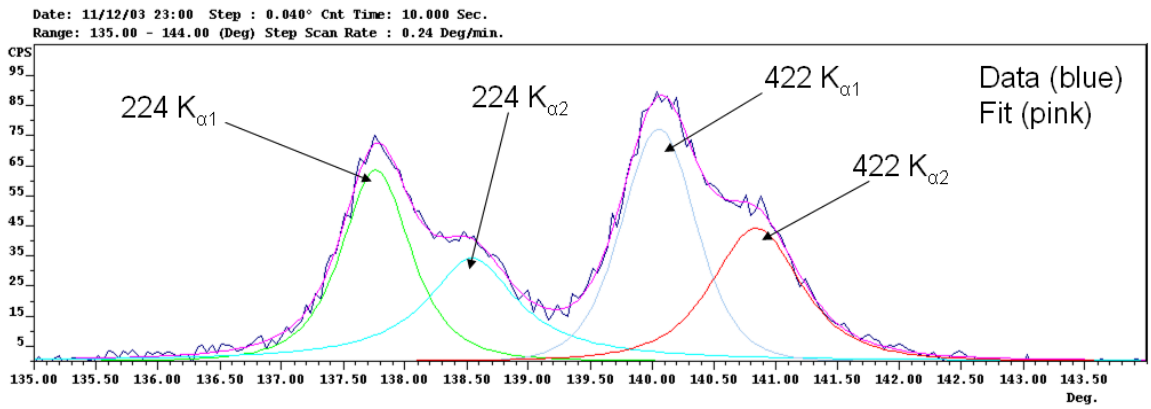

Figure 6.7: Acquired data, partial and total fits in the 2Θ vs. relative intensity plot.

gradients. In this method each strain measurement contributes to the determination of each strain tensor, which is more efficient and accurate than the Dölle and Hauk (1976, 1977) method. Winholtz and Cohen (1988) proposed an error propagation analysis to obtain the final measurement error and did not include the variability on $d^0_{\{hkl\}}$. In this work the error of the strain measurements are computed by a Monte Carlo method, assuming independent variability in each of the measured values included $d^0_{\{hkl\}}$. Similar to what Winholtz and Cohen (1988) have proposed, the measurements are weighted according to their variance for the obtention of the strain tensor.

For the analysis the specific coefficients of $\gamma - TiAl$ were computed. The relative absorption as a function of the depth z is given by Eq. 6.3

$$G(z) = 1 - e^{-\left(\frac{\mu(\lambda)z}{\frac{1}{\sin\Omega} - \frac{1}{\sin(2\Theta-\Omega)}}\right)} \tag{6.3}$$

with

$$\Omega = \Theta + \Psi$$

Since two phases are present in the material, the linear absorption coefficient is given by the weighted average of the linear absorption coefficients of the constituents which are $TiAl$ and Ti_3Al, considering the constituent elements, i.e.,

$$\mu(\lambda) = \left(\left(\frac{atm_{Ti}}{atm_{Ti} + atm_{Al}} \left(\frac{\mu(\lambda)}{\rho} \right)_{Ti} + \frac{atm_{Al}}{atm_{Ti} + atm_{Al}} \left(\frac{\mu(\lambda)}{\rho} \right)_{Al} \right) \left(\frac{TiAl}{TiAl + Ti_3Al} \right) + \left(\frac{3atm_{Ti}}{3atm_{Ti} + atm_{Al}} \left(\frac{\mu(\lambda)}{\rho} \right)_{Ti} + \frac{atm_{Al}}{3atm_{Ti} + atm_{Al}} \left(\frac{\mu(\lambda)}{\rho} \right)_{Al} \right) \left(\frac{Ti_3Al}{TiAl + Ti_3Al} \right) \right) \rho_{mix} \quad (6.4)$$

with

$$atm_{Ti} = 47.87 \qquad atm_{Al} = 26.98$$

$$\left(\frac{\mu}{\rho} \right)_{Ti} = 202.4 \frac{cm^2}{gm} \qquad \left(\frac{\mu}{\rho} \right)_{Al} = 50.23 \frac{cm^2}{gm}$$

$$\rho_{TiAl} = 3.81603 \frac{gm}{cm^3} \qquad \rho_{Ti_3Al} = 4.19537 \frac{gm}{cm^3}$$

$$\rho_{mix} = 3.8540 \frac{gm}{cm^3} \qquad \lambda(Cu_{K\alpha}) = 1.542 \, \mathring{\text{A}}$$

$$\mu(Cu_{K\alpha}) = 580.52 cm^{-1}$$

The resulting absorption as a function of depth is plotted in Fig. 6.8. Also, the maximum penetration depth for constant energy absorption and an angle $2\Theta = 137^\circ$ is obtained approximately at $\Omega = 68^\circ$ as shown in Fig. 6.9.

Equation 6.1 gives the component ε'_{33} of the strain tensor in the laboratory (e'_i) reference system as shown in Figure 6.10. To obtain the strain in the sample reference system (e_i) the appropriate transformation has to applied, i.e.,

$$\underset{\sim}{\varepsilon}' = \underset{\sim}{R} \underset{\sim}{\varepsilon} \underset{\sim}{R}^T \quad (6.5)$$

$$\underset{\sim}{\varepsilon}' = \underset{\sim}{R}_{\Psi} \underset{\sim}{R}_{\Phi} \underset{\sim}{R}_{X} \underset{\sim}{\varepsilon} \underset{\sim}{R}_{X}^T \underset{\sim}{R}_{\Phi}^T \underset{\sim}{R}_{\Psi}^T \quad (6.6)$$

$$\begin{pmatrix} \varepsilon'_{11} & \varepsilon'_{12} & \varepsilon'_{13} \\ & \varepsilon'_{22} & \varepsilon'_{23} \\ sym & & \varepsilon'_{33} \end{pmatrix} = \begin{pmatrix} R_{11} & R_{12} & R_{13} \\ R_{21} & R_{22} & R_{23} \\ R_{31} & R_{32} & R_{33} \end{pmatrix} \begin{pmatrix} \varepsilon_{11} & \varepsilon_{12} & \varepsilon_{13} \\ & \varepsilon_{22} & \varepsilon_{23} \\ sym & & \varepsilon_{33} \end{pmatrix} \begin{pmatrix} R_{11} & R_{21} & R_{31} \\ R_{12} & R_{22} & R_{32} \\ R_{13} & R_{23} & R_{33} \end{pmatrix} \quad (6.7)$$

To solve for the strain in the sample reference system the number of measurements n needed is 6. To improve the accuracy of the method n is usually more than 6 and each measurement

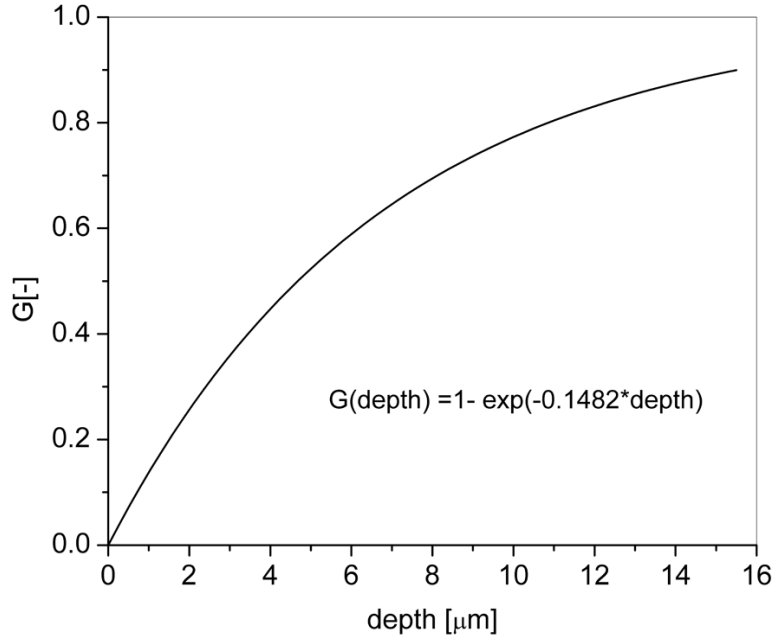

Figure 6.8: Intensity absorption vs. depth.

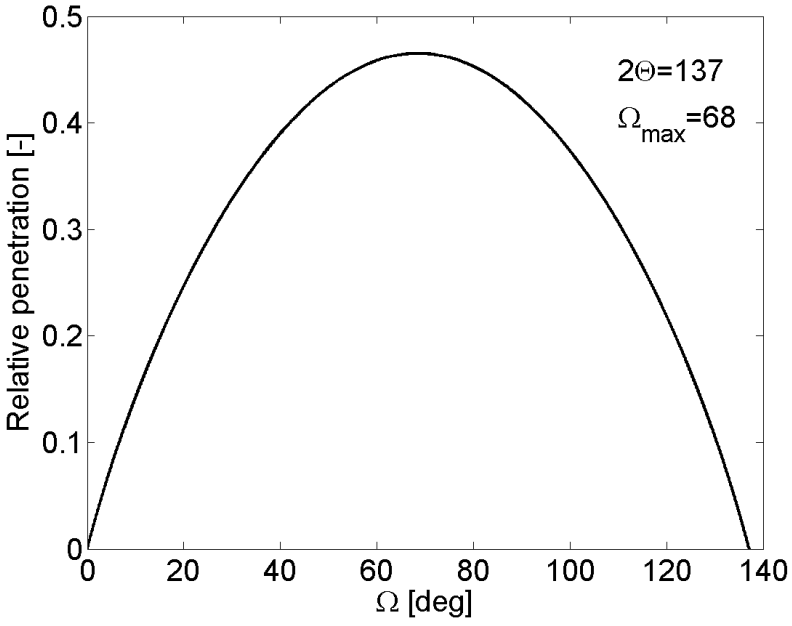

Figure 6.9: Penetration depth as a function of the tilt angle for a constant Bragg angle and absorption.

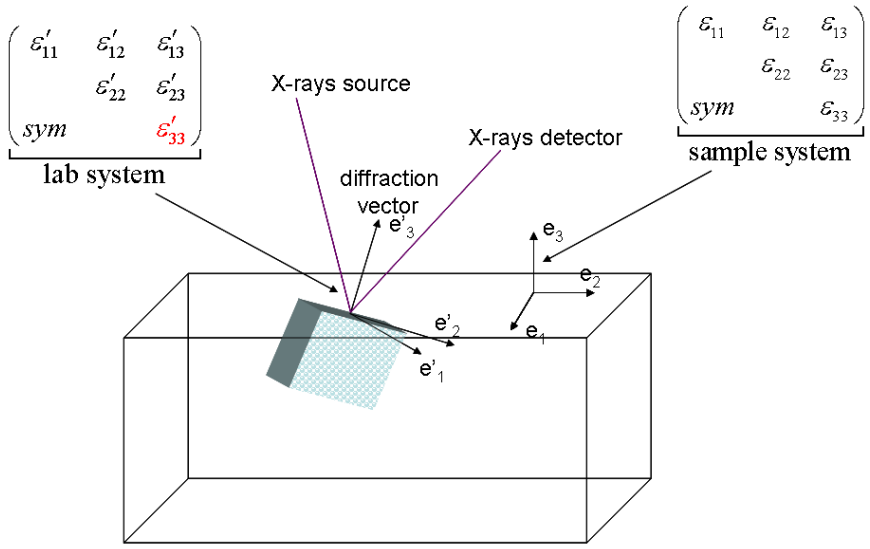

Figure 6.10: Laboratory and sample reference systems for data acquisition. ε'_{33} is the measured strain component.

corresponds to a set of angles Ψ_i, Φ_i, χ_i that gives form to a transformation matrix $\underset{\sim}{R}_i$, and the solution is found by minimization. Each measurement has its associated variance:

$$\begin{aligned}
&\Psi_1, \Phi_1, \mathrm{X}_1 \rightarrow \left(d_{\{hkl\}}\right)_1 \pm sd\left(d_{\{hkl\}}\right)_1, \underset{\sim}{R}_1 \\
&\Psi_2, \Phi_2, \mathrm{X}_2 \rightarrow \left(d_{\{hkl\}}\right)_2 \pm sd\left(d_{\{hkl\}}\right)_2, \underset{\sim}{R}_2 \\
&\ldots \\
&\Psi_n, \Phi_n, \mathrm{X}_n \rightarrow \left(d_{\{hkl\}}\right)_n \pm sd\left(d_{\{hkl\}}\right)_n, \underset{\sim}{R}_n \\
&n > 6
\end{aligned} \tag{6.8}$$

A Monte Carlo method was utilized to obtain the mean strain value and its deviation. For each measurement $(d_{\{hkl\}})_i$ and the obtained $d^0_{\{hkl\}}$ for that family of planes, m values of these variables were randomly generated (Eq. 6.9), that gave a matrix of $[m, n]$ components of the ε'_{33} strain component on the laboratory system, i.e.,

$$\begin{aligned}
&\left(d_{\{hkl\}}\right)_{i,j} = \left(d_{\{hkl\}}\right)_i \pm rnd\,(0,1)_j\, sd\left(d_{\{hkl\}}\right)_i \\
&\left(d^0_{\{hkl\}}\right)_j = \left(d^0_{\{hkl\}}\right) \pm rnd\,(0,1)_j\, sd\left(d^0_{\{hkl\}}\right) \\
&1 \leqslant i \leqslant n \text{ and } 1 \leqslant j \leqslant m = 20
\end{aligned} \tag{6.9}$$

$$\left(\varepsilon'_{33}\right)_{i,j} = \frac{\left(d_{\{hkl\}}\right)_{i,j} - \left(d_0^{hkl}\right)_j}{\left(d^0_{\{hkl\}}\right)_j} \tag{6.10}$$

A weighted minimization was performed on the square of the difference of the ε'_{33} strain component with the same component of the theoretical strain tensor considered in the laboratory coordinate system as shown in Eq. 6.11. Since all measurements for a given family of planes {hkl} have the same variance of $d^0_{\{hkl\}}$ this variance does not have any effect in the weighting and only the variance of $d_{\{hkl\}}$ was considered. In Eq. 6.11 the strain at the sample reference system $\underset{\sim}{\varepsilon}_j$ of the j Monte Carlo simulation is expressed in the laboratory reference system by rotating it by the tensor $\underset{\sim}{R}_i$ of the i^{th} measurement, and the $\underset{\sim}{\varepsilon}_{j\,33}$ strain component is subtracted from the measured strain component $\left(\varepsilon'_{33}\right)_{i,j}$ of the i^{th} measurement, and j^{th} Monte Carlo simulation. The result is squared and weighted with the standard deviation of the i^{th} measured strain. The sum is performed over the m Monte Carlo simulations. For each of the m simulations, there is a strain tensor $\underset{\sim}{\varepsilon}_j$ that minimizes the sum of squares. The mean strain tensor and its variance were obtained by considering the mean of the strain tensors of the m Monte Carlo simulations and their variance (Eq. 6.12).

$$\min\left(\sum_{j=1}^{m} \frac{1}{sd\left(d_{\{hkl\}}\right)_i}\left(\left(\varepsilon'_{33}\right)_{i,j} - \left[\underset{\sim}{R}_i \underset{\sim}{\varepsilon}_j \underset{\sim}{R}_i^T\right]_{33}\right)^2\right) \tag{6.11}$$

$$\bar{\underset{\sim}{\varepsilon}} = mean\begin{pmatrix} \varepsilon_{11} & \varepsilon_{12} & \varepsilon_{13} \\ & \varepsilon_{22} & \varepsilon_{23} \\ sym & & \varepsilon_{33} \end{pmatrix}_j \pm sd\begin{pmatrix} \varepsilon_{11} & \varepsilon_{12} & \varepsilon_{13} \\ & \varepsilon_{22} & \varepsilon_{23} \\ sym & & \varepsilon_{33} \end{pmatrix}_j \tag{6.12}$$

To obtain the stress tensor Hooke's law was used considering isotropic elastic constants with Young's modulus E=178MPa and Poisson's ratio $\nu = 0.23$, i.e.,

$$\bar{\underset{\sim}{\sigma}} = \underset{\sim}{\underset{\sim}{C}}^{\{hkl\}} : \bar{\underset{\sim}{\varepsilon}} \tag{6.13}$$

Crystal orientation should be taken into account for orthotropic elastic constants. It has to be noted that in diffraction the normals to the diffracting planes {224} and {422} are parallel to their respective diffraction vector, but different diffracting grains can be in different planar orientations, having as their normal the same diffraction vector (Fig. 6.11). A Monte Carlo simulation similar to the described above should be run to obtain the stress tensor considering this uncertainty, i.e.,

$$\bar{\underset{\sim}{\sigma}} = mean\left(\underset{\sim}{R}_k \underset{\sim}{R}_k \underset{\sim}{\underset{\sim}{C}}^{\{hkl\}} \underset{\sim}{R}_k^T \underset{\sim}{R}_k^T\right) : \bar{\underset{\sim}{\varepsilon}} \tag{6.14}$$

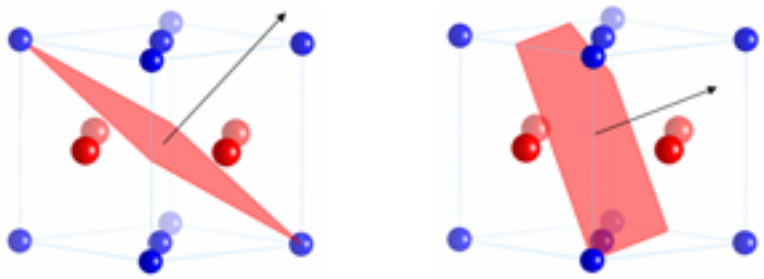

Figure 6.11: Indetermination on the orientation of the crystal normal to the diffracted plane.

The stress tensor would be given by Eq.6.15.

$$\bar{\underset{\sim}{\sigma}} = mean \begin{pmatrix} \sigma_{11} & \sigma_{12} & \sigma_{13} \\ & \sigma_{22} & \sigma_{23} \\ sym & & \sigma_{33} \end{pmatrix}_k \pm sd \begin{pmatrix} \sigma_{11} & \sigma_{12} & \sigma_{13} \\ & \sigma_{22} & \sigma_{23} \\ sym & & \sigma_{33} \end{pmatrix}_k \tag{6.15}$$

6.5 Results

The calculated diffraction profile is shown in Figure 6.6. A good approximation to it is shown in Figure 6.7. Several deviations from the theoretical diffraction profile were observed in the measurements. Figure 6.14 shows the data obtained from the surface layer of the samples with high PDD. It can be seen that peak widening prevents a clear definition of peak position. The material subjected to plastic deformation formed substructures such as "crystallites" or subgrains with diverse strain states in the irradiated volume. In order to circumvent peak broadening smaller irradiated volumes should be scanned, with the theoretical limit of a point where the strain is uniquely defined. While this solution is possible with the x-ray diffraction technique at a synchrotron, it is beyond the scope of this work. As a work around the peaks corresponding to the $K_{\{\alpha 1\}}$ of the {224} and {422} planes were force fit, and the result was a large indetermination on the stress state at the surface. Figure 6.15 shows the same condition for the samples with low PDD. In this case the peaks start to be resolved.

Figure 6.16 shows an unusual difference between the intensities of the {224} and {422} peaks, which could have been caused by some texture. In these cases the low intensity peak was discarded.

Figure 6.17 shows $K_{\{\alpha 2\}}$ peaks of almost same intensity as the $K_{\{\alpha 1\}}$. This could be caused by the contribution of the $\{254\}$ peak in the Ti_3Al phase.

In the case of subsurface measurements, electropolishing was used to remove material, which also affected the stress state on the measured layer. Also prolonged electropolishing caused the increase of the material surface roughness. Figure 6.18 shows a contour plot of a 3D profilometry of an electropolished sample. The peak to valley distance was approximately 60μm. The measurement of a sample which such roughness would not indicate the stress state at the material bulk but rather one at the asperities since the "shadow" produced by the asperities will prevent the radiation from penetrating the surface below the asperities. Therefore, after electropolishing the sample was hand polished using sand paper of grit 1200, 2400 and 4000 successively so that the surface roughness was of a few microns. There is a modification of the residual stress due to this hand polishing especially in the very superficial layers of the material considering that the energy of the x-rays decays exponentially with the depth (i.e., the signal from the surface has more weight), however this effect was not quantified in this work.

Plots for comparison of the fit of the theoretical strain to that measured are shown in Figures 6.12, and 6.13. The ordinates are the strain ε'_{33} while the abscissa shows the test number. The segments joining adjacent points are only for representation purposes.

The summary of stress results is shown in Table 6.2. Figure 6.19 shows the longitudinal stress for both high and low PDD. Figures 6.20, and 6.21 show the longitudinal and transversal stresses in the case of high and low PDD respectively. Tables with an extended summary of results separated by sample and family of planes can be found in Appendix B as well as the complete results of the measurements and plots of goodness of fit comparisons.

6.6 Conclusions

Residual stresses were measured in 4 ground samples analyzing the effect of high and low PDD value.

A generalized statistical data analysis was proposed based on the work of Winholtz and Cohen (1988). This method considerably reduces the stress variance due to counting statistics and gradients. In this method each strain measurement contributes to the determination of each strain

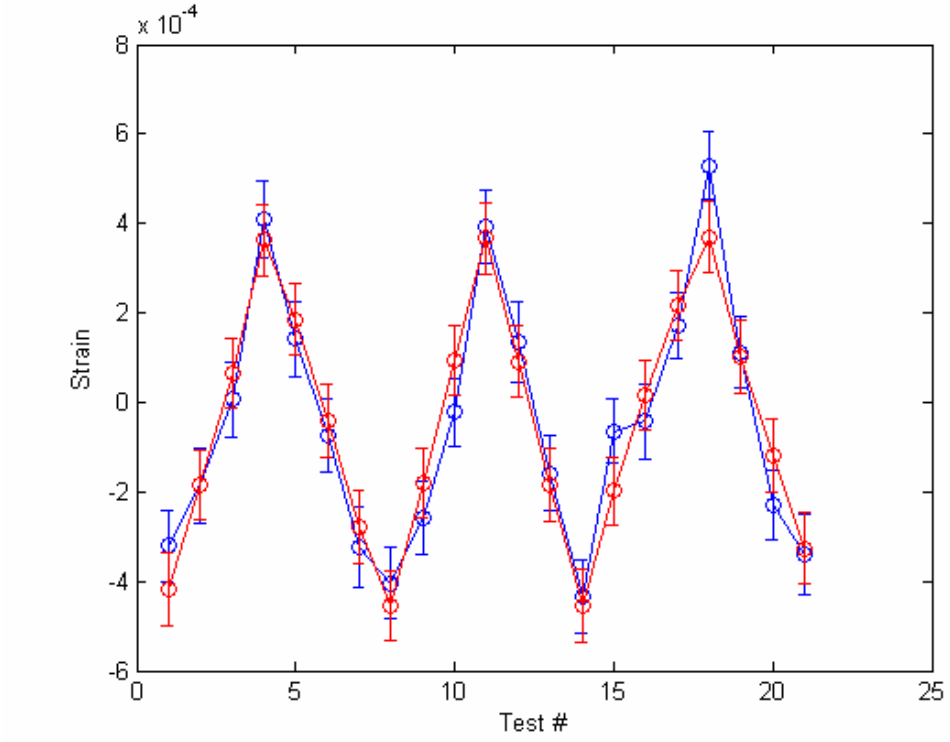

Figure 6.12: Comparison of the theoretical strain (red) with the measured one.

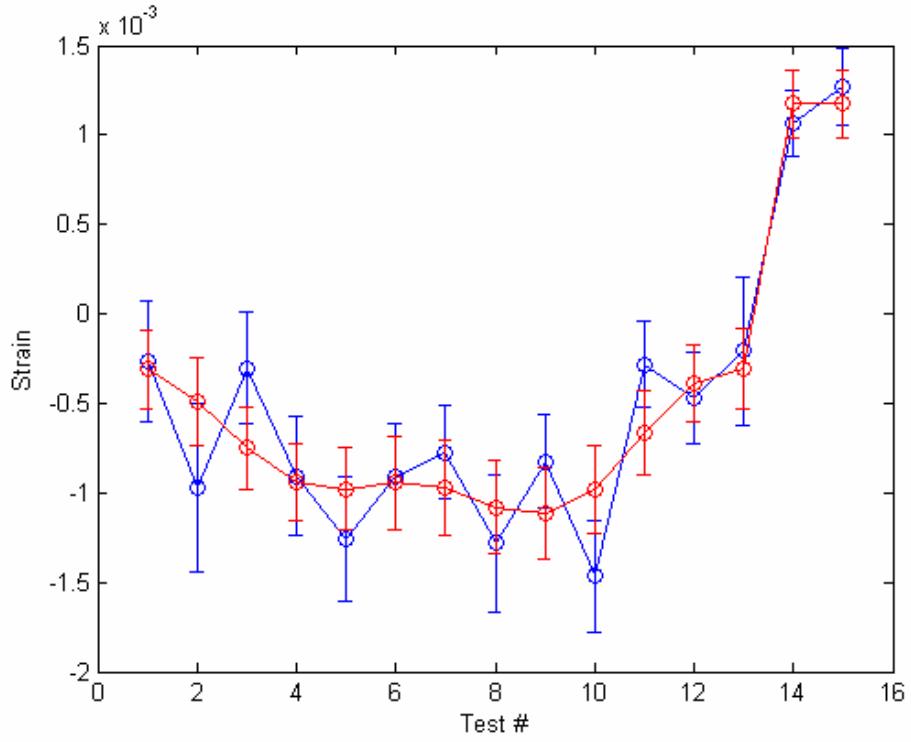

Figure 6.13: Comparison of the theoretical strain (red) with the measured one.

Table 6.2: Residual stress summary of results

					Mean			Std		
Sample ID	Test ID	Depth μm	Hydro MPa	Mises MPa	σ_I MPa	σ_{II} MPa	σ_{III} MPa	σ_I MPa	σ_{II} MPa	σ_{III} MPa
X1G06	13732	0	-365.0	726.9	-1048.5	-273.6	218.8	469.8	287.7	224.1
X1G06	13802	76	-59.2	68.2	-107.2	-68.2	-5.3	30.6	30.4	28.9
X1G10	13883	124	-65.4	41.1	-101.0	-60.9	-29.9	44.6	44.6	44.6
X1G10	13919	154	-57.2	67.7	-121.2	-63.6	-8.0	39.9	39.6	35.4
X1G06	10273	254	-0.6	35.9	-35.5	4.0	35.5	54.0	51.3	45.4
X1G06	10318	318	11.0	17.3	-5.8	9.6	29.4	61.4	59.2	58.1
X1G08/15	711-836	0	-523.0	506.9	-832.9	-634.6	-105.6	70.1	73.6	47.5
X1G15	13853	17	-75.6	25.4	-94.6	-77.7	-54.6	30.3	32.3	30.9
X1G15	13886	47	-119.5	59.4	-158.8	-118.6	-68.2	30.6	30.5	29.8
X2G08	13781	72	-85.1	100.8	-143.5	-86.7	-11.8	49.7	42.3	44.6
X1G15	13934	117	-6.1	33.5	-33.6	-2.6	17.7	56.4	57.0	56.5
X2G08	10289	122	6.04	28.59	-15.22	10.97	38.20	34.46	35.14	33.91

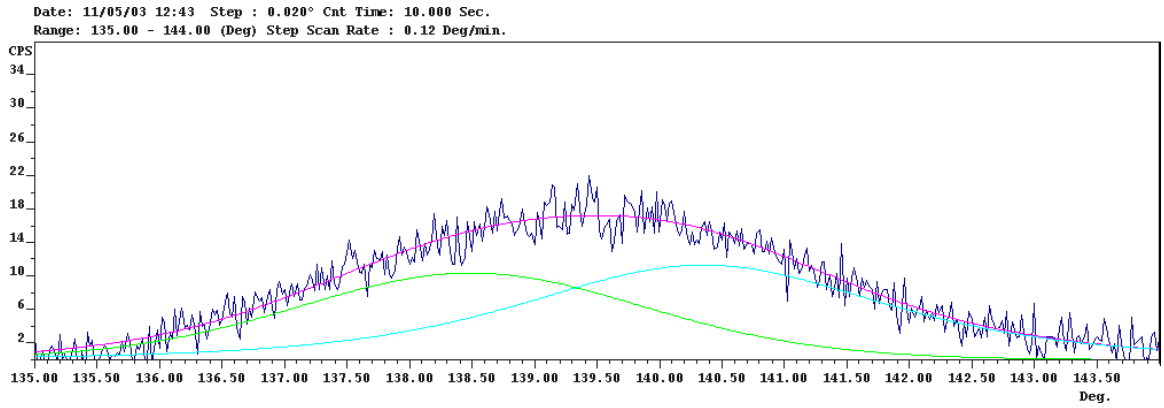

Figure 6.14: Surface layer data where peak broadening can be observed. Peaks are resolved by force fitting.

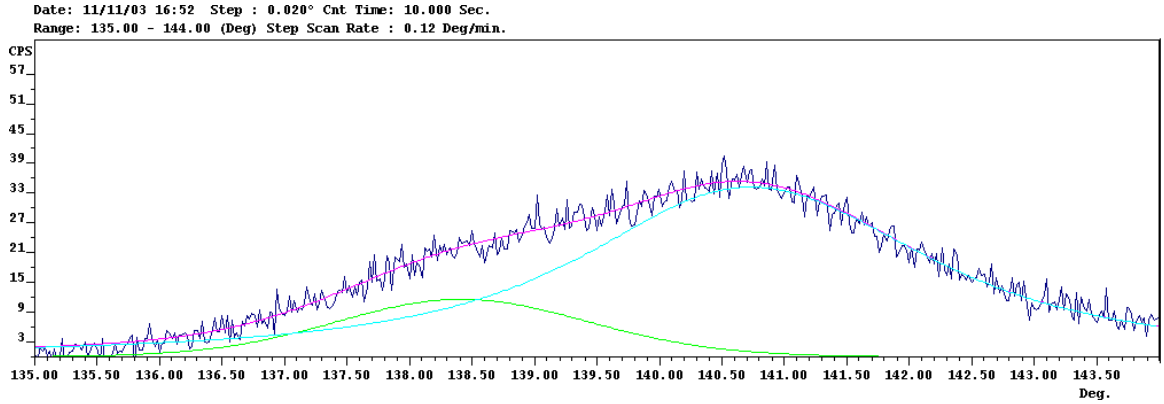

Figure 6.15: Surface layer data. Peaks start resolving in cases of milder grinding conditions.

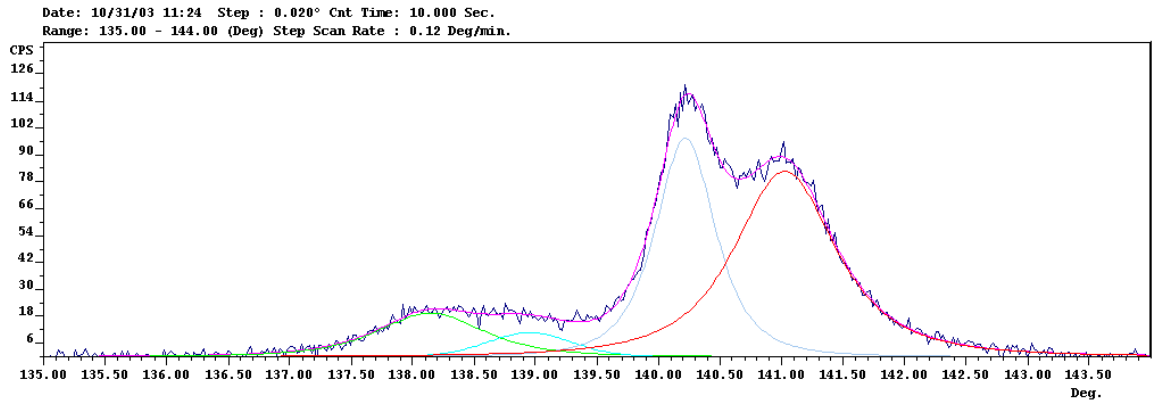

Figure 6.16: Low intensity and resolution in {224} peak, probably due to some texture formation.

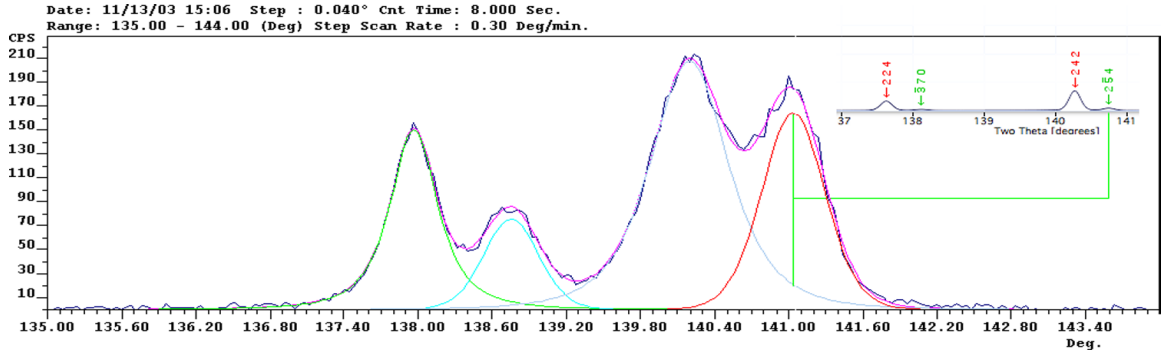

Figure 6.17: High intensity in the $K_{\alpha 2}$ secondary peaks probably due to contribution of the {254} peak on the Ti_3Al phase (green peaks in subfigure).

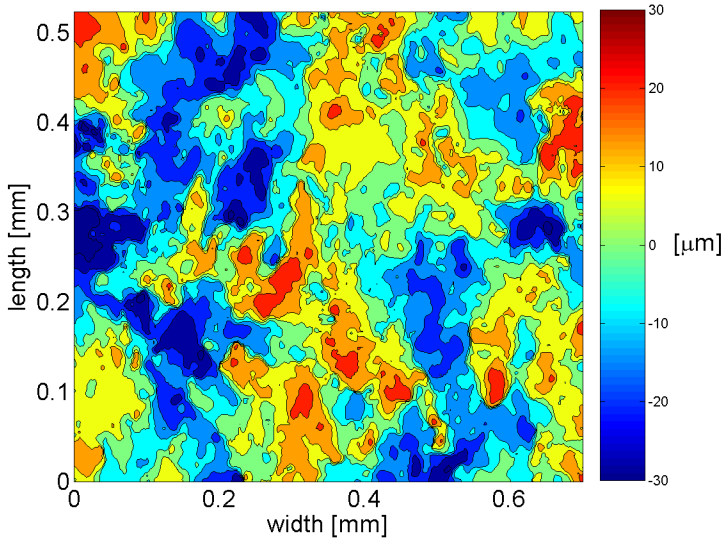

Figure 6.18: Contour plot of a 3D profilometry on an electro-polished specimen. Peak to valley distance is of the order of 50μm.

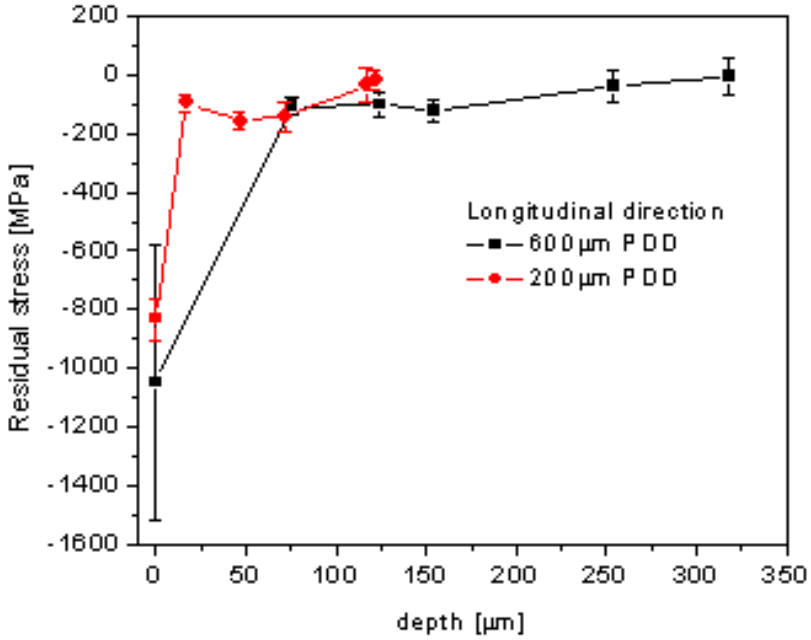

Figure 6.19: Longitudinal residual stresses results.

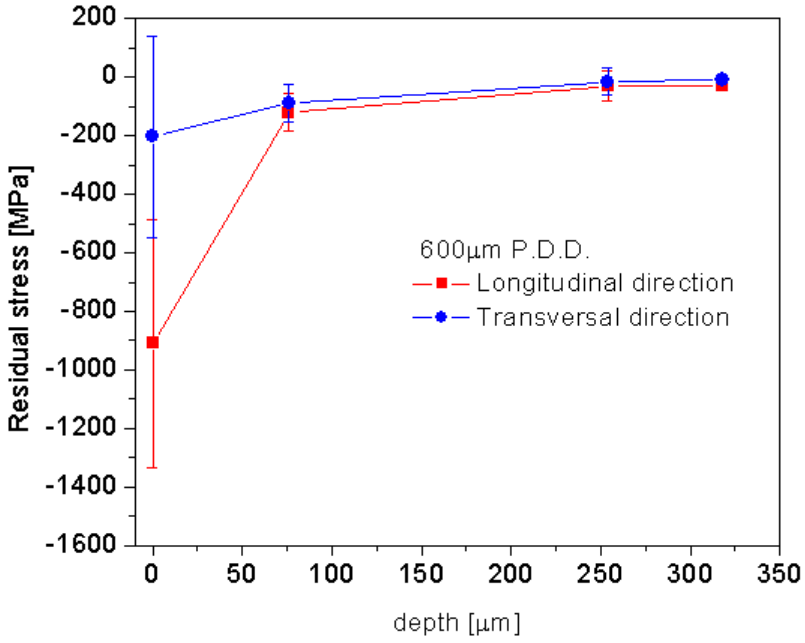

Figure 6.20: Residual stresses results for samples with 600μm PDD.

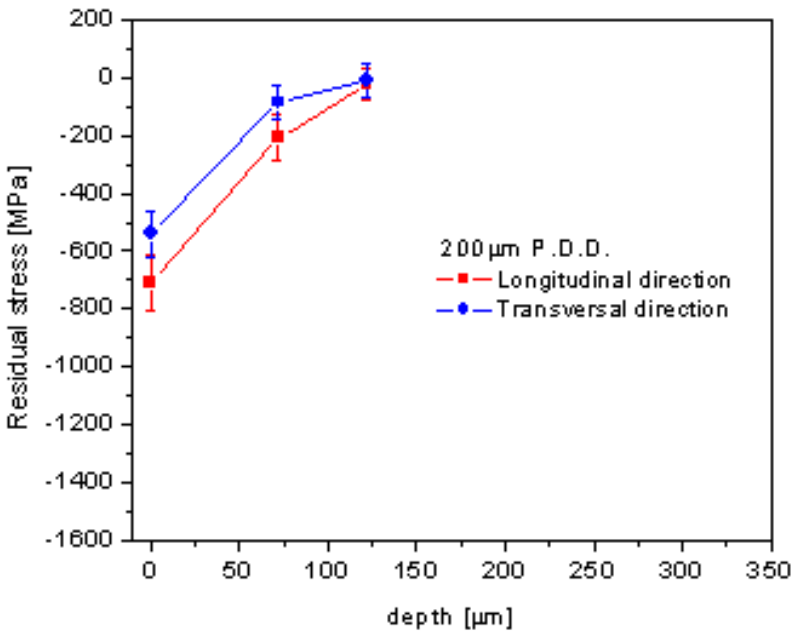

Figure 6.21: Residual stresses results for samples with 200μm PDD.

tensor, which is more efficient and accurate than the Dölle and Hauk (1976, 1977) method. In this work the error of the strain measurements are computed by a Monte Carlo method, assuming independent variability in each of the measured values included $d^0_{\{hkl\}}$. Similar to what Winholtz and Cohen (1988) have proposed, the measurements are weighted according to their variance to obtain the strain tensor.

It was observed that compressive stresses are close to the GPa on the surface.

Numerous experimental difficulties produced a high variance of the results and the impossibility to obtain data in zones which are presumed to have high stress gradients.

The RS analysis technique can be improved by considering the radiation attenuation in the subsurface, and stress gradients (Suominen and Carr, 1999; Behnken and Hauk, 2001; Ely et al., 1999; Wern, 1999; Zhu et al., 1995)

The use of x-ray diffraction technique at a synchrotron can improve the stress resolution at the surface of highly deformed materials, and avoid the artifacts introduced by the layer removal technique, since the penetration depth of the radiation is of the order of millimeters. This solution was beyond the scope of this work.

CHAPTER VII

ANALYTICAL MODELING

In this Chapter the indentation model proposed by Lawn and Wilshaw (1975); Aurora et al. (1979) and used by Nelson (1997); Razavi (2000); and Stone (2003) to predict the depth of damage is analyzed. The model proposed by Hecker (2002) to find the force per abrasive grit is used to modify the indentation model and correlate it to PDD.

7.1 Indentation Model

Lawn and Wilshaw (1975) and Aurora et al. (1979) considered a brittle solid subjected to a normal force F''_N by a sharp pyramid indenter. A plastic zone was developed, and its extension (h_0) given by Eq. 7.1, where β is a dimensionless constant determined by plastic deformation zone geometry and given by the ratio of h_0 to half diagonal of the indentation, δ is a dimensionless constant determined by the indenter geometry, and H_v is the Vickers hardness. The concept of this phenomenological model is that the contact pressure generates a plastic zone which depends on the indenter geometry, and the PDD, called here h_0, independent of the indented size for a constant force. It assumes that the contact pressure for inelastic deformation is independent of the indenter size and equal to the material hardness, as assumed by the friction model proposed by Bowden and Tabor (1950).

$$h_0 = \left(\frac{\beta^2}{\delta \pi H_v}\right)^{0.5} F''^{0.5}_N \tag{7.1}$$

This model developed for a single indenter was modified by Nelson (1997) to include the normal force in grinding using geometric and kinematic variables as proposed by Hahn and Lindsay (1982a,b) and shown in Eq. 7.2, where H_g is the grinding hardness, b is the grinding width, E_w the workpiece Young's modulus, V_w the workpiece speed, and V_s the wheel's tangential speed.

$$h_0 = \left(\frac{b\beta^2 E_w}{\delta \pi H_g}\right)^{0.5} \left(\frac{aV_w}{V_s}\right)^{0.5} \tag{7.2}$$

Razavi (2000) used this model under force controlled conditions. Stone (2003) introduced the hardness dependence on temperature into the model. The model proposed by Lawn and Wilshaw

(1975); and Aurora et al. (1979) considers an individual indenter under normal loads while in the mentioned modifications the total grinding force was considered as the variable that controls PDD. If the wheel total force F_N and wheel/material area of contact ($l_c b$) are considered for a typical case, the mean contact pressure will be of the order of few MPa's which could not explain the existence of plastic deformation. Even though the original model as well as the modified model are phenomenological in nature some physics is lost in the use of the total wheel normal force F_N instead of the individual grit normal force F_N''. In this change in the scale of the model there is no explicit account for the grit size of the abrasive, neither its concentration. It has been observed in the results in Chapter 5 that wheels with different grit size produce different PDD under the same F_N. A direct address of the number of abrasives engaged in the process seems to be a more sensible treatment to predict PDD. From the kinematic point of view these models only addressed the dependence of PDD with $F_n^{0.5}$. Differences in the number of active abrasives, bonding type, and other grinding operation variables are considered by fitting the factor in front of F_N for the different conditions, limiting the results only to the case of study. Furthermore, some deviations of the model with the data were observed by Nelson (1997) and correction factors were applied by considering a force controlled setup (Razavi, 2000) and temperature effects (Stone, 2003) without too much success.

This work proposes to explicitly address the influence of the number of abrasives in contact, find the average force per abrasive, and used it as a predictor for PDD. The model developed by Hecker (2002) was used.

7.2 Force per Abrasive Model

Several factors should be considered to model the force per grit. Grinding is a stochastic process, with the wheel having a spatial distribution of abrasive grits. After dressing the wheel, some grits will be exposed and a number will be active in the material removal process. In static measurements, i.e. without any force or constraint acting on the wheel surface, it is possible to determine the distribution of cutting edges versus distance to the wheel surface (z). With this information and the grinding conditions it is possible to know how many abrasives will be engaged in the material removal process in a few steps, but there are two effects that further modify this value. One is the

local displacement the engaged abrasives are subjected to when a force is applied. This displacement is a function of the force applied to the grit, its geometry, and the bond elastic properties where it is attached. This effect will modify the cutting edges probability distribution function (pdf) causing more abrasive grits to be actively engaged in material removal. A second effect is the shadow that abrasive grits produce. If material is removed by one abrasive grit, another grit will probably pass by the groove produced by the first one, without or partially removing material. This effect is opposite to the first one and will decrease the number of actively engaged grits. Which effect will predominate depends on the wheel and workpiece properties as well as on the grinding kinematic conditions. The amount of engaged grits computed in this way is called the dynamic cutting edge density.

The inputs to the model are: i) kinematic conditions given by the DoC, V_w, V_s; ii) geometric characteristics as wheel diameter (d_s), abrasive cone angle θ_a, static cutting edge density (C_s), abrasive grit diameter (D_g); iii) material properties as workpiece Brinell hardness (HB_w), grinding coefficient of friction (C_f), and critical abrasive penetration (h_{cr}). The model assumes a Rayleigh pdf of undeformed chip thickness to find the average force per grit and integrate it to find the total grinding force components (F_N and F_T), and power (P_w). Figure 7.1 shows the block diagram used by the model. A coupled system of equations is solved to obtain the model output parameters.

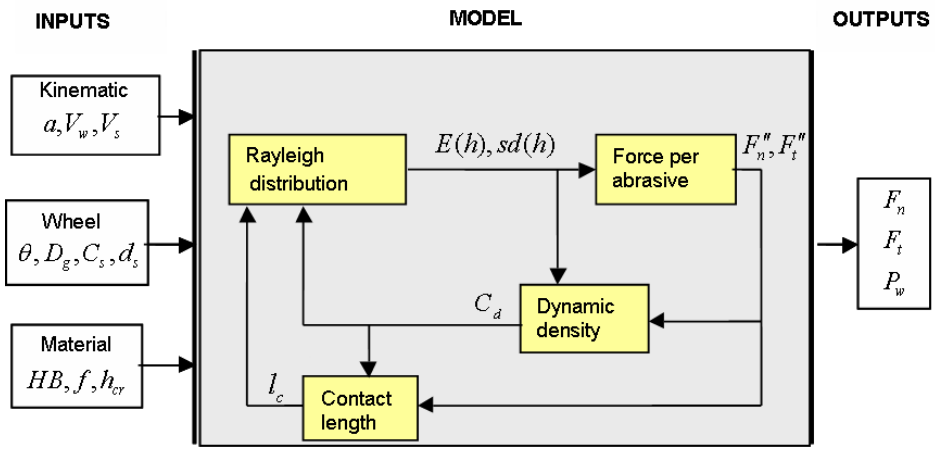

Figure 7.1: Block diagram of the grinding model (Hecker, 2002).

Figure 7.2 shows a single grit that enters the contact. The abrasive is bonded to the wheel and the bonding compliance is represented by the spring. At the initial stage of contact only friction of

elastic bodies is generated. The second stage of plowing is produced by the abrasive pushing into the workpiece without material removal, and at the third stage, after the critical penetration (h_{cr}) has been reached, material is removed. This value depends on most of the grinding variables. For the sake of simplicity, the chip thickness is assumed with triangular uniform cross section with an internal angle $2\theta_a$. The cross section area of the chip is given by $A_{ch} = h^2 \tan\theta_a$, with $b_c/2h = tan\theta_a$, and b_c being the undeformed chip thickness. There is a distribution of chip thickness due to the random nature of the process. As proposed by Younis and Alawi (1984) a Rayleigh pdf is used to describe the chip thickness distribution. The shape of this probability function is similar to the logarithmic standard distribution used to describe the chip thickness (König and Lortz, 1975) but it is defined by only one variable (σ_R) as shown in Eq. 7.3

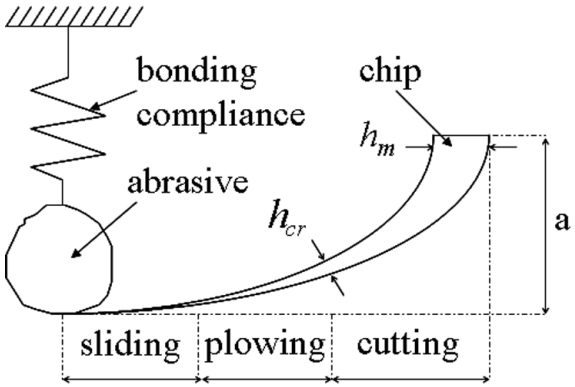

Figure 7.2: Schematics of single abrasive grit material interaction.

$$f(h) = \frac{h}{\sigma_R^2} \exp\left(\frac{-h^2}{2\sigma_R^2}\right) \tag{7.3}$$

By kinematic considerations and conservation of mass the previous expressions can be expressed as a function of grinding variables as shown in Eq. 7.4

$$\begin{aligned} E(h) &= \sqrt{\frac{\pi}{2}\left(\frac{aV_w}{2V_s}\frac{1}{l_c C_d}\frac{1}{\tan(\theta_a)} - \frac{h_{cr}^2}{2}\right)} \\ std(h) &= \sqrt{\frac{4-\pi}{2}\left(\frac{aV_w}{2V_s}\frac{1}{l_c C_d}\frac{1}{\tan(\theta_a)} - \frac{h_{cr}^2}{2}\right)} \end{aligned} \tag{7.4}$$

where the factor aV_w/V_s represents the kinematic effects and $1/\tan\theta_a$ accounts for the cutting edge geometry. The variables l_c and C_d (dynamic cutting edge density) depend on the dynamic effects. The expression used for l_c is the one proposed by Rowe et al. (1993) and shown in Eq. 7.5. It

takes into account the static contact length $(a\ d_s)^{0.5}$, and the length increase by elastic contact of a cylinder on a plane accounting for the roughness of the surfaces in contact by an empirical constant R_r. F'_N is the normal force per contact length, and E^* the contact modulus given by Eq. 7.6, where E_i and ν_i are the Young's modulus and Poisson's ratio of the wheel and workpiece.

$$l_c = \left(a d_s + \frac{8 R_r^2 F'_N d_s}{\pi E^*} \right)^{0.5} \tag{7.5}$$

$$\frac{1}{E^*} = \frac{1 - \nu_s^2}{E_s} + \frac{1 - \nu_w^2}{E_w} \tag{7.6}$$

The static cumulative pdf of cutting edges density can be described as shown in Eq. 7.7, where z is the depth into the wheel and A and k constants. The dynamic effect of the inward displacement of the grits due to the normal force applied is considered as a local effect by Nakayama et al. (1971), and it is accounted for by the modification of the static grain distribution function as given by Eq. 7.8, where $E\left(F''_N\right)$ is the expected value of the normal force per grit and K_g is the equivalent grain spring constant

$$C_{s(z)} = A\left(z\right)^k \tag{7.7}$$

$$C_{s(z')} = A\left(z + E\left(F''_N\right) K_g\right)^k = A\left(z'\right)^k \tag{7.8}$$

The dynamic cumulative pdf of cutting edges density $C_{d(z^*)}$ can be obtained by Eq. 7.9, where both effects, grit displacement and shadowing, are accounted for. The term $\tan\left(\varepsilon_s\right)$ is obtained by Eq. 7.10 as proposed by Verkerk and Peters (1977), ϖ_s being the angle of shadow, and z^* the wheel engagement for given grinding conditions (Eq. 7.11).

$$C_{d(z^*)} = \frac{C_{s(z')}}{1 + \frac{C_{s(z')}}{4} \frac{\tan(\theta)}{\tan(\varpi_s)} \frac{\sigma_R^3}{z^*}} \tag{7.9}$$

$$\tan\left(\varepsilon_s\right) = \frac{2 V_w a}{V_s d_s} \tag{7.10}$$

$$z^* = E\left(h\right) + 3 std\left(h\right) \tag{7.11}$$

The specific normal force F'_N (Eq. 7.12) is obtained by accounting for the normal load per grit F''_N and the specific active number of cutting edges N'_d (Eq. 7.13).

$$F'_N = F''_N N'_d \tag{7.12}$$

$$N'_d = l_c C_d \tag{7.13}$$

The normal force per grit F''_N acting in the direction of the attack angle α_g can be obtained from the definition of Brinell hardness (Eq. 7.14) and basic trigonometry as shown in Eqs. 7.15, and 7.16, and in Fig. 7.3. In Eq. 7.14, D_f accounts for dynamic indentation effects.

$$HB_w = \frac{2F''}{D_f \pi D_g \left(D_g - \left(\sqrt{D_g^2 - b_{in}^2}\right)\right)} \tag{7.14}$$

$$F''_n = F'' \left(\cos\alpha_g - f_g \sin\alpha_g\right) \tag{7.15}$$

$$\alpha_g = \cos^{-1}\left(1 - \frac{2h}{D_g}\right) \tag{7.16}$$

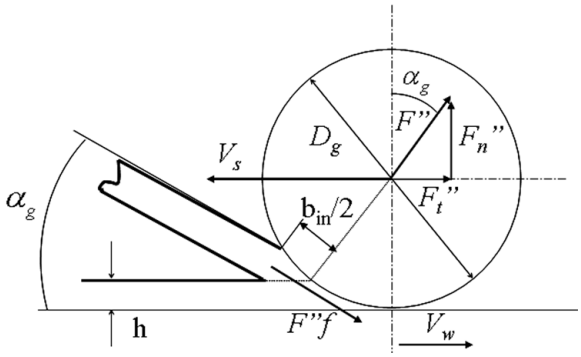

Figure 7.3: Schematics of the force per abrasive grit (Shaw, 1972).

7.3 Implementation

The model has been implemented for tests with dressed and worn wheel conditions, separated also by G_h. One relevant input needed by the model is the static pdf of grits. This pdf was obtained experimentally by Hecker (2002) using a replica technique in which the wheel was pressed against a lead block leaving the indentations of the abrasives on the lead. This block was scanned under a 3D profilometer and further analyzed to extract the peaks distribution. Other replica techniques were used by Blunt and Ebdon (1996); and Butler et al. (2002). In the latter case a wheel surface replica was obtained by use of Polysiloxane (used for dental replicas) and a second replica (positive image) on the Polysiloxane was obtained by using a fast-curing methyl methacrylate-based resin. Some other researchers have used microscopy to determine this profile (Matsuno et al., 1975).

In this work an analytical function for the static distribution of grits is proposed. Some assumptions were made: i) abrasive grits were assumed to have spherical shape, ii) during dressing the abrasive grits which have been exposed more than $D_g/2$, were assumed to fall off the wheel, iii) abrasive grits were not fractured or worn during dressing, iv) abrasive grits were homogeneously distributed in the wheel. The wheels have an abrasive concentration of 100, meaning that 25% of their volume is occupied by abrasive, the rest being Ni-based metal bonding. Making use of the theorem that states that volume concentration equals area, line and point concentration (Underwood, 1970), and hypothesis (i), (ii), and (iv), the maximum area concentration of exposed abrasive grits would be 12.5%; and by (iii) the furthest cutting edge would be at a distance $D_g/2$ from the maximum concentration plane as shown in Fig. 7.4. Also by (iv) the cumulative density function of cutting edges will be linear with z. It remains to be determined how many abrasive grits represent

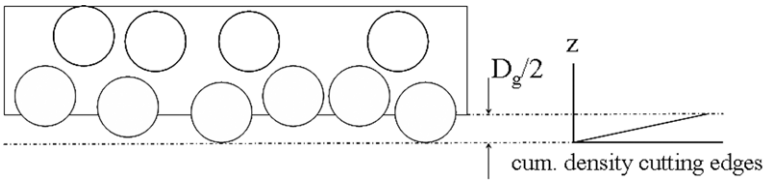

Figure 7.4: Exposed abrasive grits after dressing showing cumulative distribution of density of cutting edges.

a 12.5% concentration for the large and small G_z, which were computed considering that at $D_g/2$ the bonding plane randomly sections abrasive grits. The mean area of the circle formed by the intersection of a sphere with an arbitrary cutting plane is given by Eq. 7.17, therefore the mean area of an abrasive grit at $D_g/2$ will be $31.70E-3\ mm^2$ for the mesh 60 and $1.72E-3\ mm^2$ for the mesh 270, giving a maximum grit density of approximately $4\#/mm^2$ and $73\#/mm^2$ for mesh 60 and 270 respectively. The volume density of abrasive grits in the bulk of the wheel will be approximately $38\#/mm^3$ and $3000\#/mm^3$ for mesh 60 and 270 respectively. Therefore, the constants for Eq. 7.7 are $A = 0.034\#/mm^2/\mu m$, and $A = 2.70\#/mm^2/\mu m$ for large and small abrasive grit respectively, and the exponent is considered constant for all the cases ($k = 1$).

The grain factor (G_f) parameter has been used to modify the D_g in the model, and it considers that the abrasive grit tip radius can be smaller or larger than the actual one. A wear factor (W_f) that modifies the slope (A) has been considered in Eq. 7.7. The friction coefficient has been taken

constant for all the tests with a value $f_g = 1$. Error minimization was considered by comparing the model and experimental force components, and allowing the G_f, D_f, to vary for the dressed wheel tests, and adding W_f for worn wheel tests.

$$A_m = \frac{3}{16}\pi D_g^2 \tag{7.17}$$

7.4 Results

Plots of test results are presented. Test numbers are labelled as shown in Tables 5.4, and 5.9 for dressed and worn conditions respectively. The first 4 tests were used to adjust the model constants and the remaining as validation. The fitted value of the model parameters are given in 7.1.

Table 7.1: Fitted parameters

Parameter		G_f	W_f	D_f
Dressed	A_g	1.7	1.0	2.0
	B_k	2.5	1.0	2.0
Worn	A_g	2.5	0.5	4.5
	B_k	2	0.6	4.0

7.4.1 Dressed Wheel Tests

In the case of tests using dressed wheels with Ag abrasive grits, Fig. 7.5 presents the static and dynamic number of cutting edges as computed by the model, Fig. 7.6 presents the expected chip thickness and its standard deviation as given by the model, Figs. 7.7, and 7.8 presents the experimental vs. theoretical comparison of the P'_w, and of the force components respectively. Figs. 7.9 to 7.12 present the same data for tests using dressed wheels with Bk abrasive grits.

As the plots show, the dynamic number of cutting edges is smaller than the static one indicating that the shadowing effect is larger than the local compliance of the abrasive grit/bonding. The cutting edge density is of the order of $3\#/mm^2$ to $6\#/mm^2$ for small G_z, and less than $0.5\#/mm^2$ for large G_z. Model and test P'_w and forces are in reasonable agreement, but in some cases all these values differ by a factor of 2 (test Ag5, Bk1, Bk6).

Chip thickness is of the order of $2.1\mu m$ to $4.5\mu m$ for large G_z, and in the order of $0.5\mu m$ to $1.1\mu m$ for small G_z. These values are in agreement with the ones found in the literature (Malkin, 1989).

Fig. 7.13, and 7.14 show a plot of the model average chip thickness and $F_N''^{0.5}$ versus the experimental mean PDD respectively. As shown in the plots, $F_N''^{0.5}$ seems to be a good predictor for PDD.

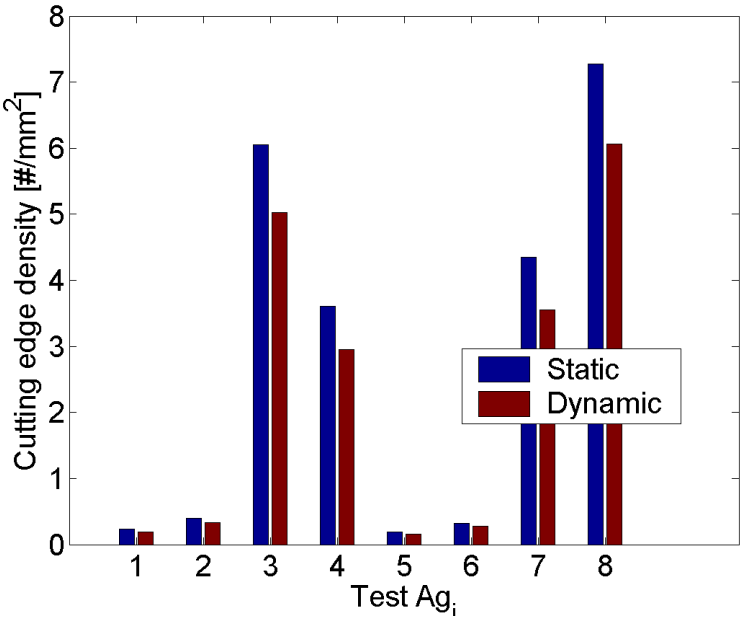

Figure 7.5: Model dynamic and static cutting edges. Ag-dressed wheels.

7.4.2 Worn Wheel Tests

In the case of tests using worn wheels with Ag abrasive grits all the model constants were left at the value used for dressed wheels and the best fitting of the constant of the cumulative static cutting edge distribution on Eq. 7.7 was found. Fig. 7.15 presents the static and dynamic number of cutting edges as computed by the model, Fig. 7.16 presents the expected chip thickness and its standard deviation as given by the model, Figs. 7.17, and 7.18 presents the experimental vs. theoretical comparison of the P'_w, and of the force components respectively. Figs. 7.19 to 7.22 present the same data for tests using worn wheels with Bk abrasive grits.

As shown in the plots for worn wheels, the dynamic number of cutting edges is also smaller

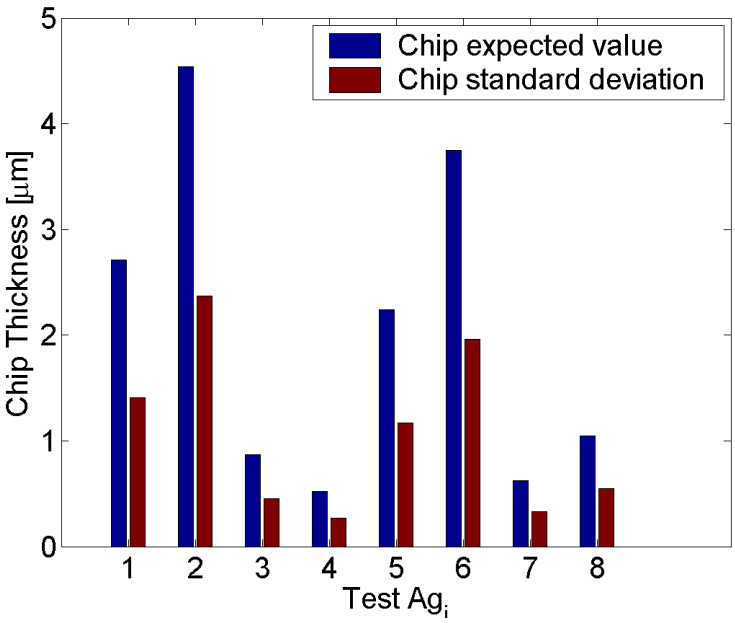

Figure 7.6: Expected chip thickness and standard deviation. Ag-worn wheels.

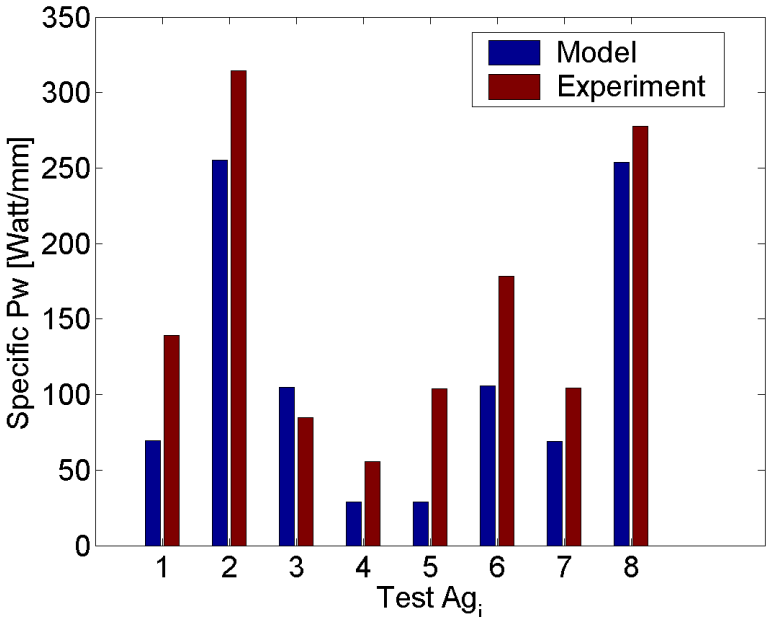

Figure 7.7: Model and measured P'_w. Ag-dressed wheels.

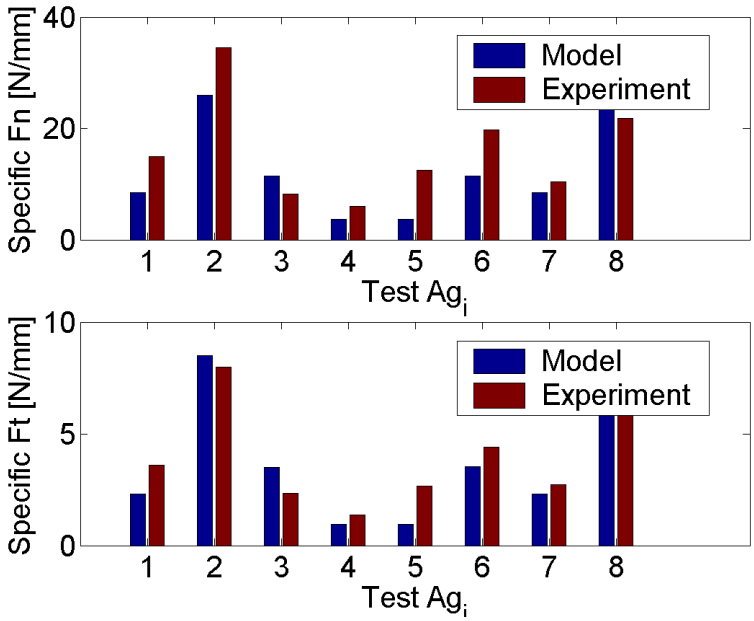

Figure 7.8: Model and measured F'_N and F'_T. Ag-dressed wheels.

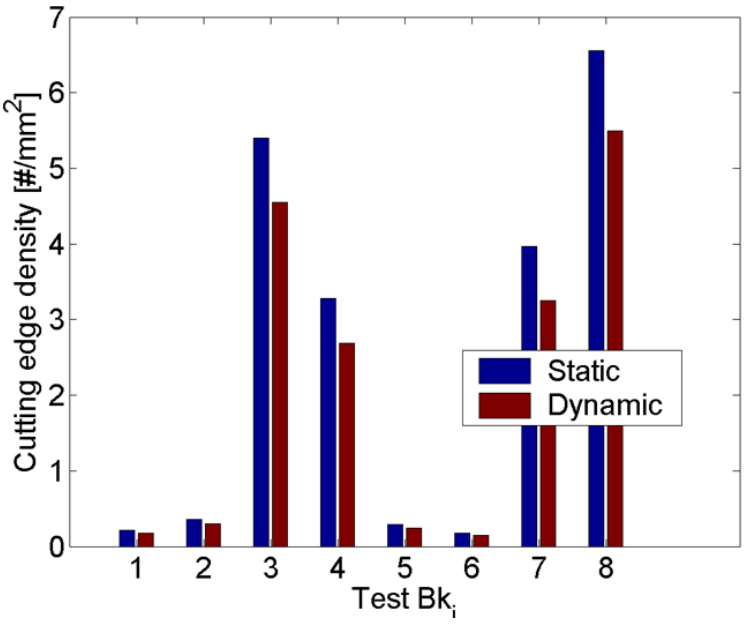

Figure 7.9: Model dynamic and static cutting edges. Bk-dressed wheels.

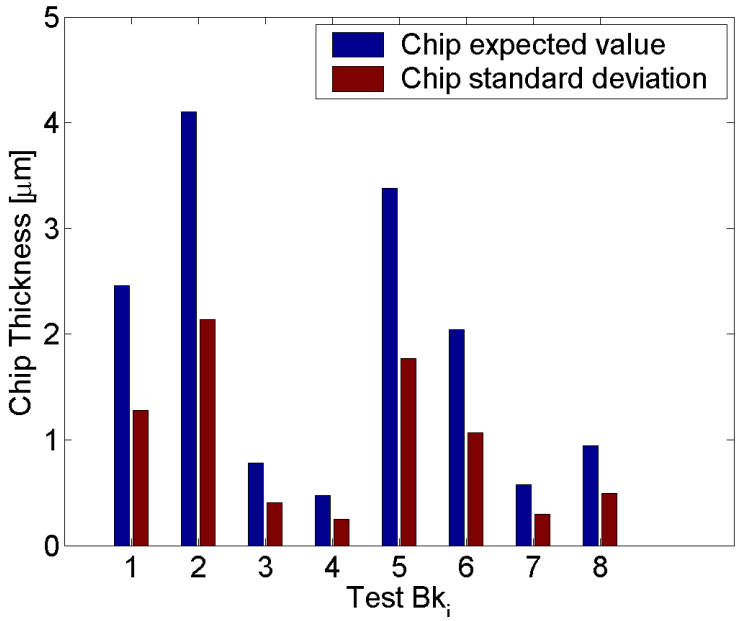

Figure 7.10: Expected chip thickness and standard deviation. Bk-worn wheels.

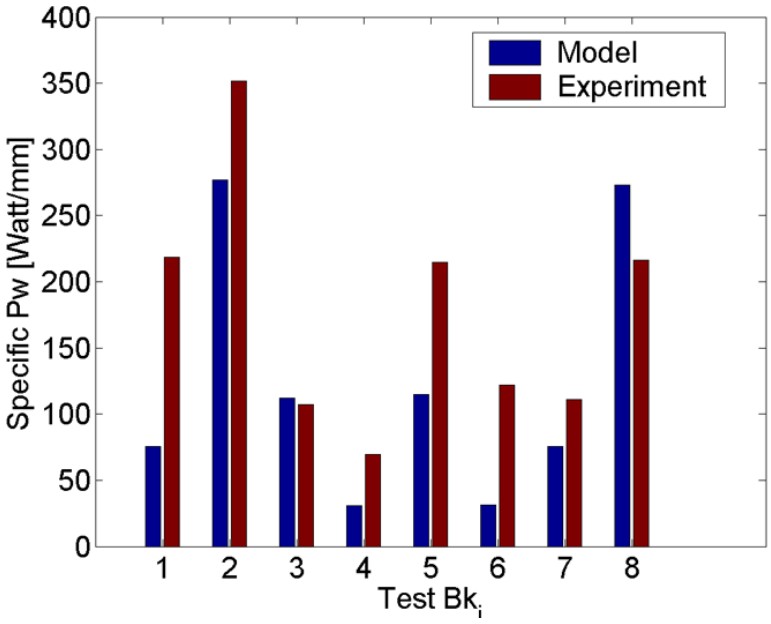

Figure 7.11: Model and measured P'_w. Bk-dressed wheels.

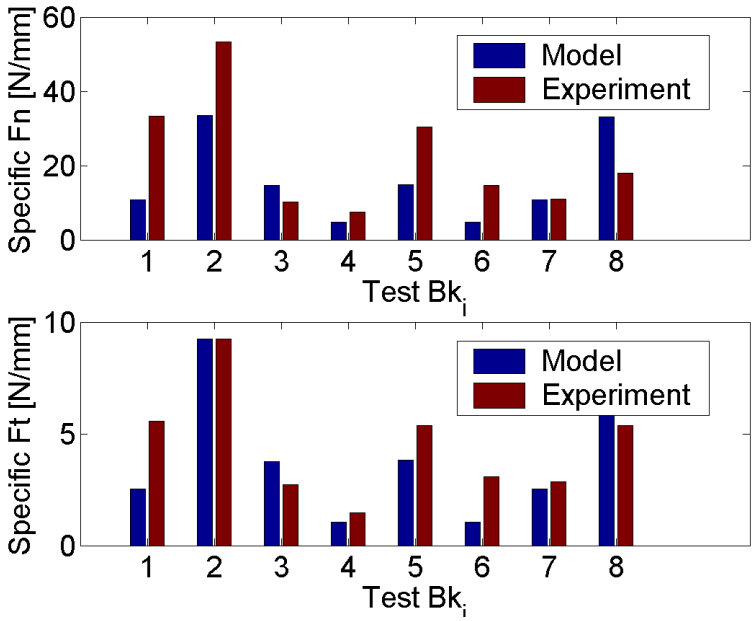

Figure 7.12: Model and measured F'_N and F'_T. Bk-dressed wheels.

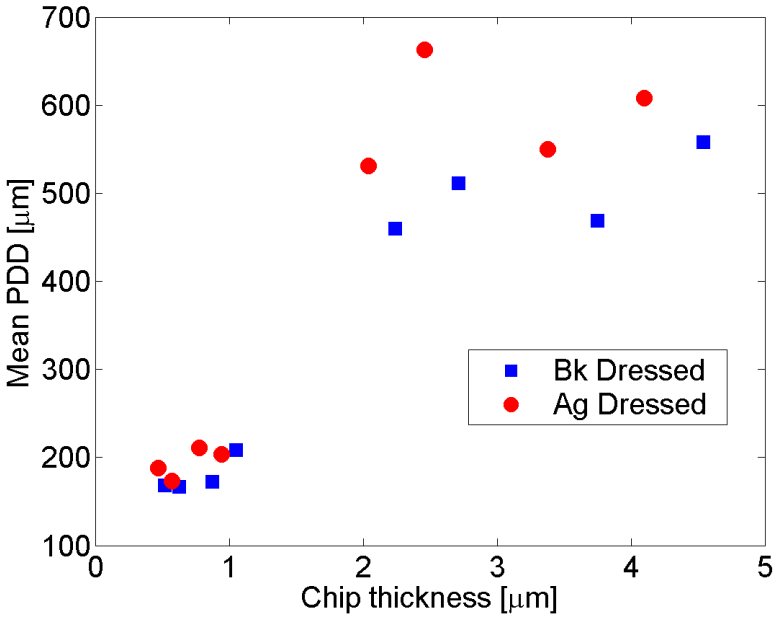

Figure 7.13: Model average chip thickness versus mean PDD. Test with dressed wheels.

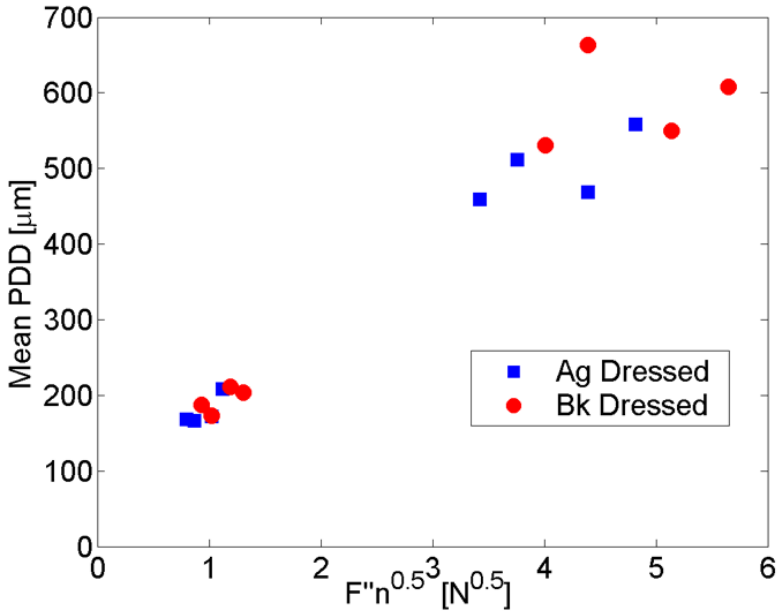

Figure 7.14: Model average square root of normal force per grit versus mean PDD. Test with dressed wheels.

than the static ones, and the number of cutting edges is larger than in the case of dressed wheels, indicating that the distribution of abrasive grit cutting edges narrowed due to wear and fracture effects. The cutting edge density is of the order of $4\#/mm^2$ to $8\#/mm^2$ for small G_z, and less than $0.6\#/mm^2$ for large G_z. Model and test P'_w and forces are in reasonable agreement, but the fit is not as good as in the case of dressed wheels.

Chip thickness is of the order of $1.5\mu m$ to $3.2\mu m$ for large G_z, and in the order of $0.2\mu m$ to $0.7\mu m$ for small G_z. As expected these values are smaller than the ones found for dressed wheels.

Fig. 7.23, and 7.24 show a plot of the model average chip thickness and $F''^{0.5}_N$ versus the experimental mean PDD respectively. Neither of the variables can predict PDD. In the case of Fig. 7.24, the two clusters of points correspond to the small (left) and large G_z.

7.5 Conclusions

An analytical model was used to obtain the force per grit and tests the fitness of the indentation model as a predictor of the PDD. By use of the analytical model, the number of active cutting edges, chip thickness, and force per grit were obtained, and the PDD has shown a good correlation with $F''^{0.5}_N$, as proposed by the indentation model of Lawn and Wilshaw (1975); Aurora et al.

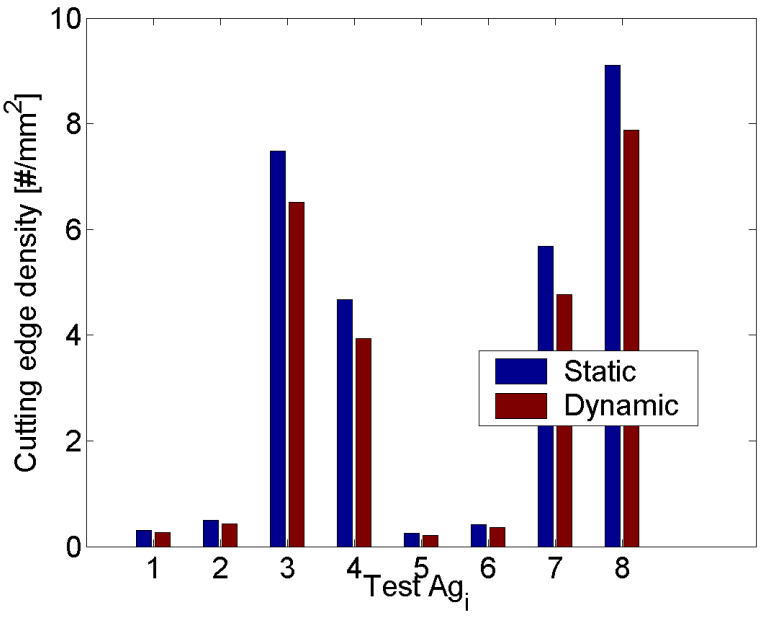

Figure 7.15: Model dynamic and static cutting edges. Ag-worn wheels.

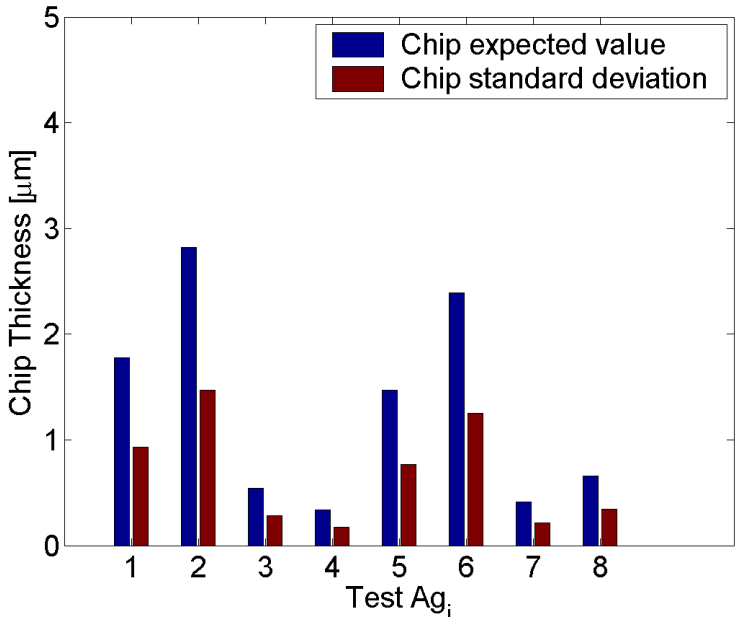

Figure 7.16: Expected chip thickness and standard deviation. Ag-worn wheels.

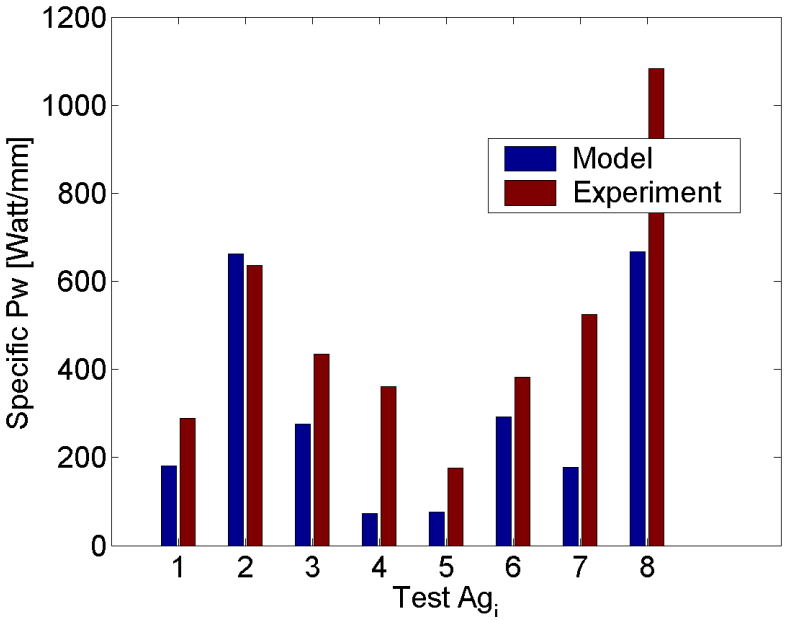

Figure 7.17: Model and measured P'_w. Ag-worn wheels.

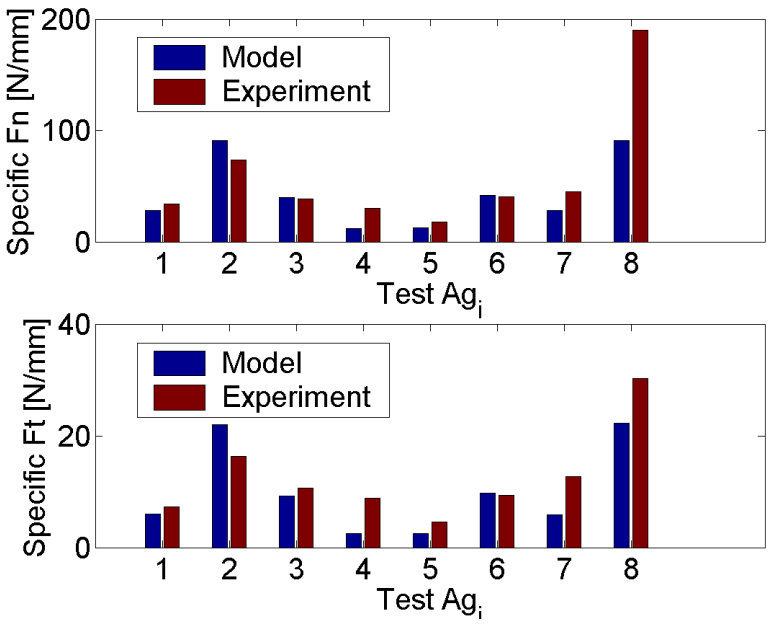

Figure 7.18: Model and measured F'_N and F'_T. Ag-worn wheels.

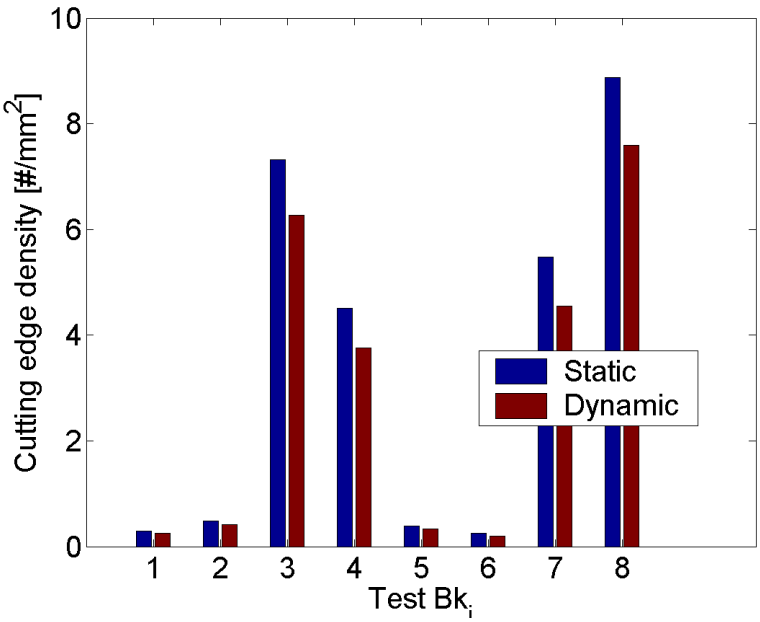

Figure 7.19: Model dynamic and static cutting edges. Bk-worn wheels.

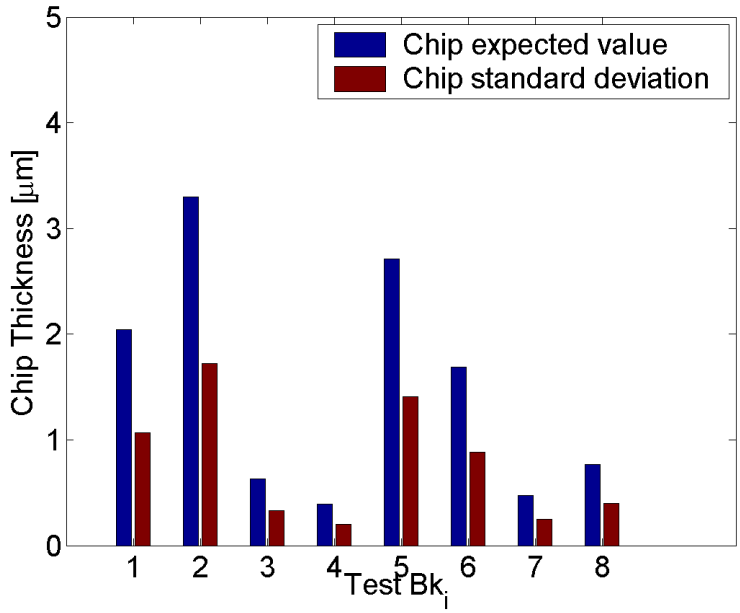

Figure 7.20: Expected chip thickness and standard deviation. Bk-worn wheels.

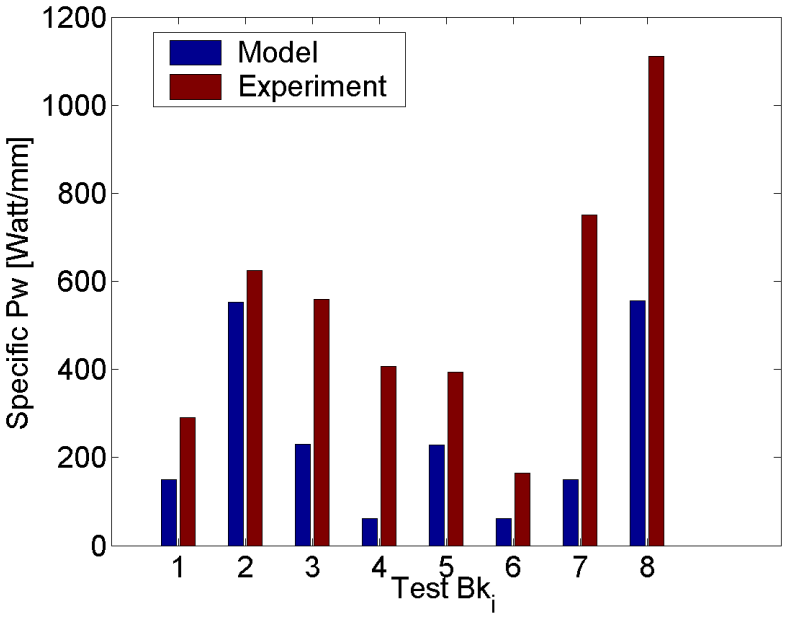

Figure 7.21: Model and measured P'_w. Bk-worn wheels.

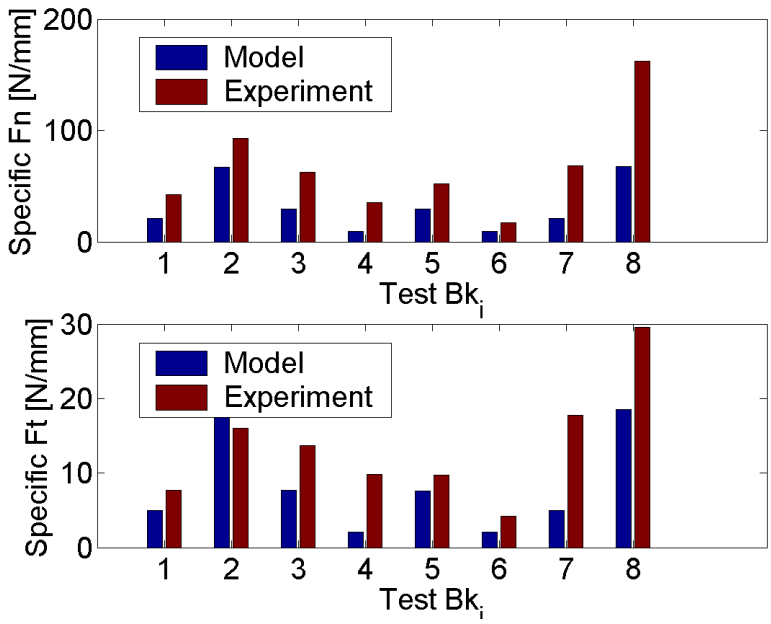

Figure 7.22: Model and measured F'_N and F'_T. Bk-worn wheels.

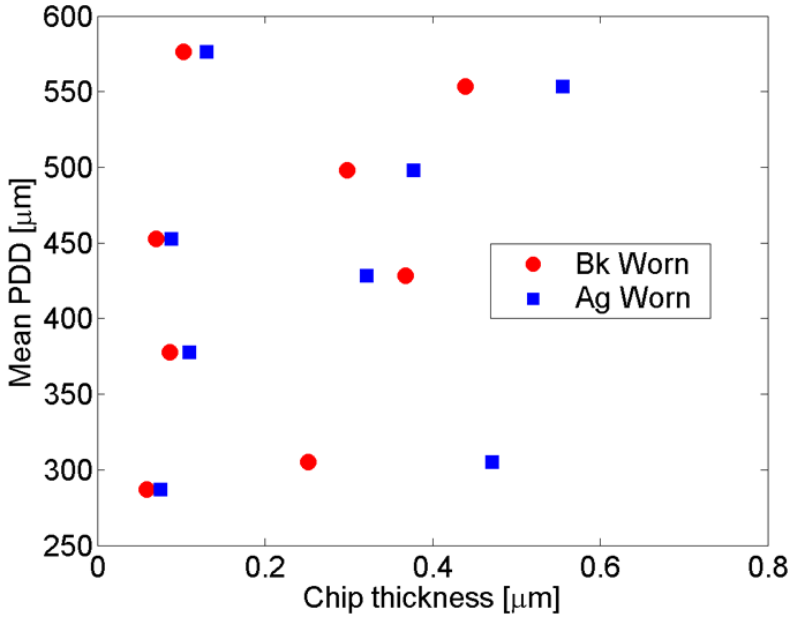

Figure 7.23: Model average chip thickness versus mean PDD. Test with worn wheels.

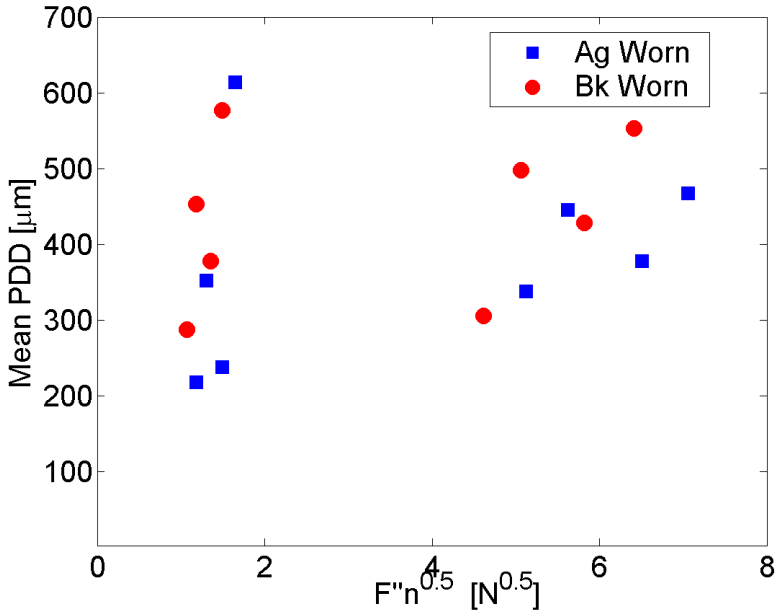

Figure 7.24: Model average square root of normal force per grit versus mean PDD. Test with worn wheels.

(1979). This suggests that the indentation model is still valid for grinding if the force per grit is used instead of the total grinding force.

The model captures the difference in the number of cutting edges and chip thickness for the different G_z.

The results show that the model captures the effect of wear by fitting the values of grinding total force in an acceptable manner. Nevertheless, the model attributes the increase of the normal force in the case of worn wheels to dynamic effects. The fitted dynamic factor D_f for the worn wheel was twice from the one obtained for dressed wheels. The number of cutting edges and the force per grit remains approximately in the same range for the two wear conditions, which is a dubious result.

For the dressed conditions, the analytical model predicts a cutting edge density of the order of $3\#/mm^2$ to $6\#/mm^2$ for small G_z, and less than $0.5\#/mm^2$ for large G_z. Model and test P'_w and forces are in reasonable agreement, but in some cases all these values differ by a factor of 2.

Chip thickness is of the order of $2.1\mu m$ to $4.5\mu m$ for large G_z, and in the order of $0.5\mu m$ to $1.1\mu m$ for small G_z. These values are in agreement with the ones found in the literature.

The analytical model predicts for the worn conditions that‘ the cutting edge density is of the order of $4\#/mm^2$ to $8\#/mm^2$ for small G_z, and less than $0.6\#/mm^2$ for large G_z. The chip thickness is of the order of $1.5\mu m$ to $3.2\mu m$ for large G_z, and in the order of $0.2\mu m$ to $0.7\mu m$ for small G_z. As expected these values are smaller than the ones found for dressed wheels.

The resulting fitted factors of the analytical model might indicate that the model works well for dressed conditions by capturing expected trends, but it does not give good predictions for worn conditions. This difference might be due to variables not accounted for such as temperature, possible contact of bond material with the workpiece for small G_z, or a probability density function of cutting edges density different from the one assumed in this work.

CHAPTER VIII

NUMERICAL MODELING

An isotropic rate dependent elastic-plastic model, and an anisotropic elastic-viscoplastic crystal plasticity model were used in 2D and 3D geometric models under different BC's to analyze: i) behavior of the PDD vs. F_n'' plots for different indenter sizes; ii) validity of Eq. 7.1 to predict PDD under scratching conditions; iii) PDD relation for PE vs. PS and its implications to the PDD measuring technique described in Chapter 4; iv) effect of lamellae orientation and lamellae boundary on PDD; v) verification of the force per grit obtained by the model presented in Chapter 7. The models were implemented in ABAQUS v6.3. Due to the nonlinearity of the material response and large sliding conditions, the explicit integration scheme was used. Adaptive meshing was used to improve the element aspect ratio under large deformations. To increase stability, bulk viscosity was activated with a linear parameter of 0.12 and a quadratic one of 2.4 (Abaqus, 2001). The indenter was modeled as an analytical surface (rigid body). The friction coefficient was set at 0.1 for all tests.

8.1 Isotropic Elastic-plastic Model Simulations

The material isotropic elastic properties used were $E = 178E3$, and $\nu = 0.23$. The isotropic plastic properties were modeled by entering the piecewise curves of Fig. 3.10. Von Mises plasticity criterion was used with isotropic hardening.

8.1.1 Model Validation

The model was validated by the simulation of indentation tests and their comparison with experimental results. A 2D model of a $3.5mm$ radius by $3mm$ high cylinder was meshed using CAX4R 4-node bilinear, reduced integration with hourglass control, axisymmetric solid elements. The model had 10002 elements with a total of 20404 DOF (degrees of freedom). The element resolution at the contact zone was of $3.5\mu m$. The indenter geometry was sphero-conic with $200\mu m$ tip radius and 60° cone semiangle. Figures 8.1, and 8.2 show the complete, and contact zone close-up of the

mesh respectively. Figure 8.3 shows the resulting PEEQ at the indenter zone for a case of $500N$ maximum applied load after removing it. Figure 8.4 shows the test and model comparison for three load unload curves at different maximum loads, where a reasonable agreement can be seen.

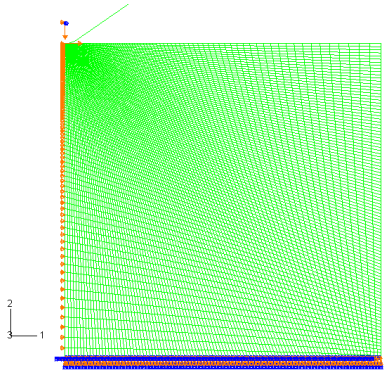

Figure 8.1: Axisymmetric indentation model mesh and BC'c.

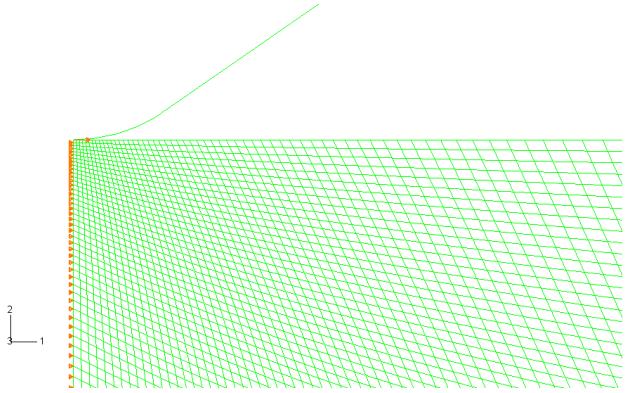

Figure 8.2: Axisymmetric indentation model mesh. Contact zone close-up.

8.1.2 3D Scratching

Three dimensional simulations were carried out to find the PDD vs. normal load relation for different indenter sizes. A parallelepiped of $0.5mm$ long, $0.15mm$ wide, by $0.25mm$ high was meshed using C3D4 4-node linear, tetrahedron solid elements, which represents half of the model. The model had 32512 elements with a total of 22422 DOF. The element resolution at the contact zone was of $2.5\mu m$. The indenter geometry was spherical with diameters of $54\mu m$, and $232\mu m$ resembling the abrasive small and large size. The sliding speed was $5mm/sec$. Figures 8.5, and 8.6 show the total and contact zone close-up of the mesh respectively. Figures 8.7, and 8.8 show

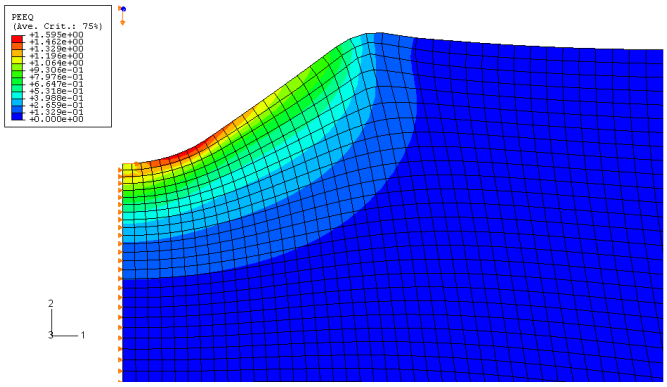

Figure 8.3: PEEQ under the indenter for $500N$ normal load.

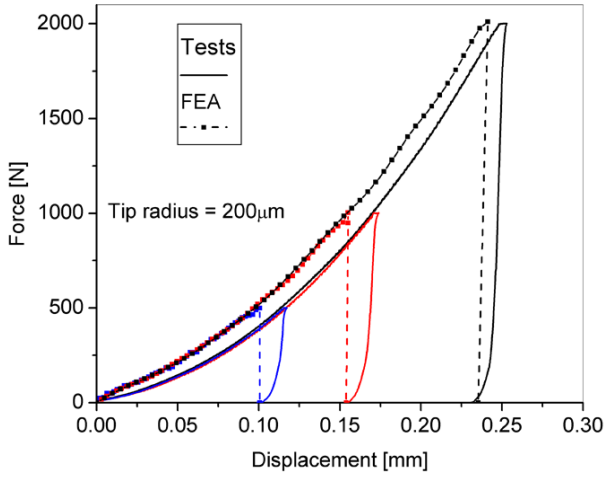

Figure 8.4: Experimental and numerical comparison of indentation curves for $200\mu m$ indenter radius.

the resulting PEEQ at the indenter zone for a case of $0.5\mu m$ penetration depth. Figure 8.9, and 8.10 show the PDD vs. $F_N''^{0.5}$ for different levels of PEEQ for the large and small indenter size respectively. The plots show an approximately linear behavior, and the PDD for the smaller indenter is larger for a given load.

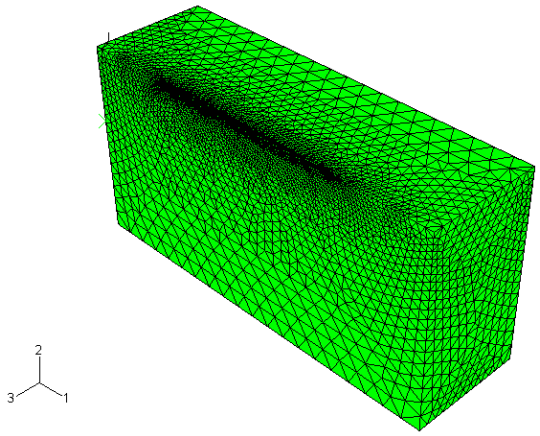

Figure 8.5: Half of the 3D scratching model mesh.

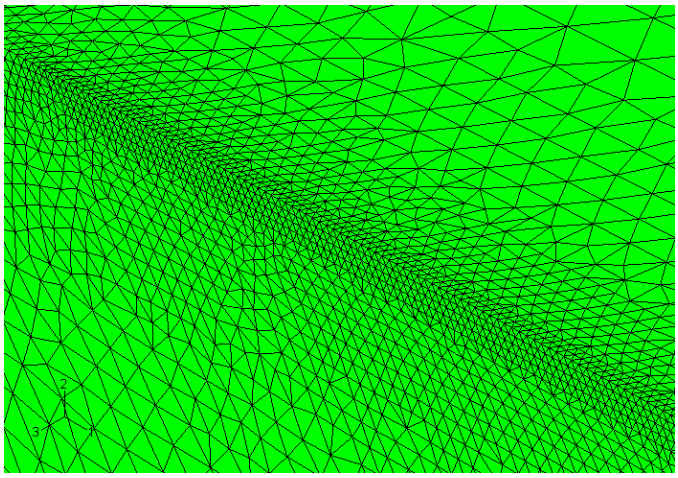

Figure 8.6: Half of the 3D scratching model mesh. Close-up of sliding zone.

8.1.3 Plane Strain vs. Plane Stress Comparison

Two dimensional indentation simulations were carried out to find the PDD vs. boundary conditions for different indenter sizes. A rectangle of $5mm$ long, by $2mm$ high was meshed using either CPE3 3-node linear, PE (plane strain); or CPS3 3-node linear, PS (plane stress), solid elements. The model had 29246 elements with a total of 29918 DOF. The element resolution at the contact zone

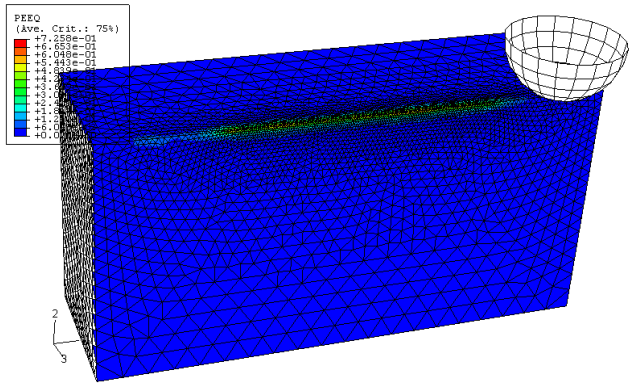

Figure 8.7: PEEQ under the scratching zone for $0.5\mu m$ penetration depth.

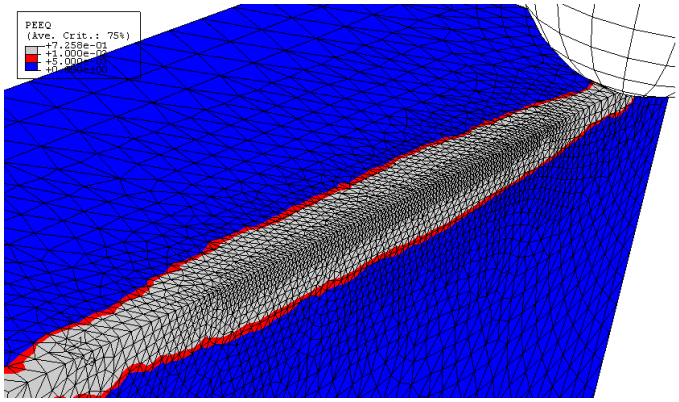

Figure 8.8: PEEQ under the scratching zone for $0.5\mu m$ penetration depth. Close-up of sliding zone.

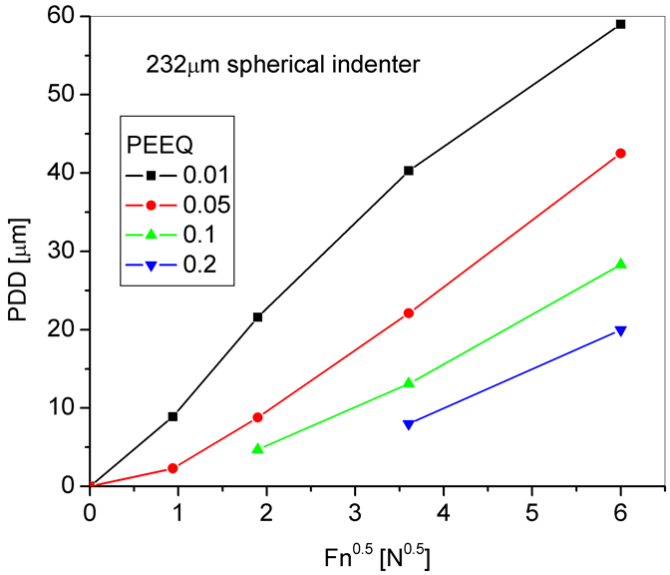

Figure 8.9: PDD vs. $F''n^{0.5}$ for different levels of PEEQ; $232\mu m$ diameter indenter.

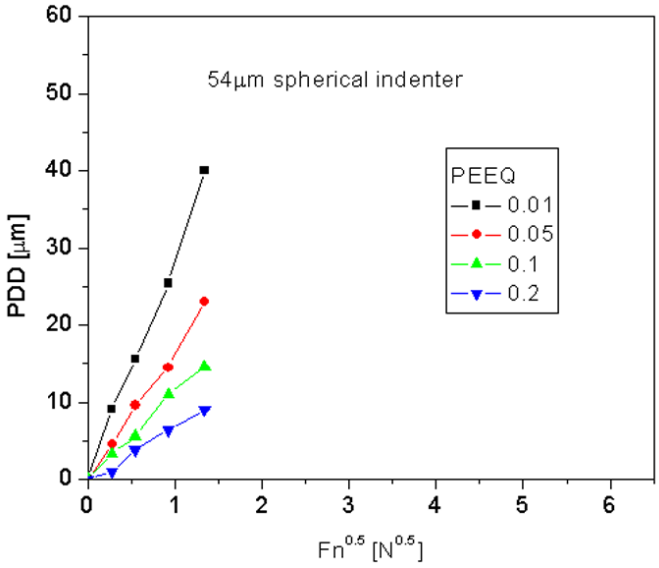

Figure 8.10: PDD vs. $F''n^{0.5}$ for different levels of PEEQ; $54\mu m$ diameter indenter.

was of $1\mu m$. The indenter geometry was cylindrical with diameters of $54\mu m$, and $232\mu m$ resembling the small and large size grit.

One question that arises after the measurements of PDD is how this value obtained at a free surface is related to the PDD at the bulk. It can be argued that on grinding, where usually DoC is the controlled variable, the abrasive grits will have a uniform distribution of penetration depths on the workpiece width, and the forces will be given accordingly to the different constraint, i.e. lower at active grits closer to the edge. Figures 8.11, and 8.12 show the total and contact zone close-up of the mesh respectively. Figure 8.13 shows the resulting PEEQ at the indentation zone for a case of $1.0\mu m$ penetration depth for PE and PS using the small indenter size. Figure 8.14, shows the PEEQ vs. indentation depth for PE, PS and small and large indenters. It can be observed that the PDD is larger for PE, and as expected, is larger for the larger indenter size.

Figure 8.15 presents the PEEQ for $1.0\mu m$ penetration depth for the large indenter, to the left is shown the PE case, to the right the PS. The top part presents the PD zone for a $PEEQ \geq 0.003$ threshold, and the bottom for $PEEQ \geq 0.055$. As shown in the lower part of the figure, for a larger threshold of PEEQ, the plastic zone for PS is larger than for PE.

The indentation model predicts that the PDD for a given force is independent of the G_z. Figure 8.16 shows the PEEQ vs. F''_N for PE, PS and small and large indenters. It can be observed

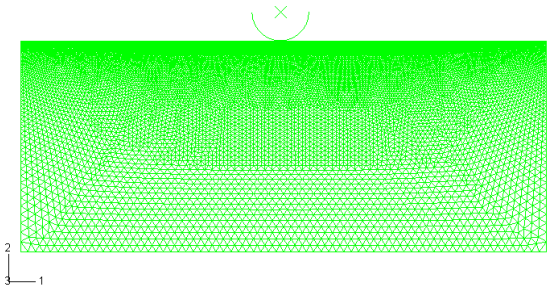

Figure 8.11: Two dimensional PE-PS indentation model mesh.

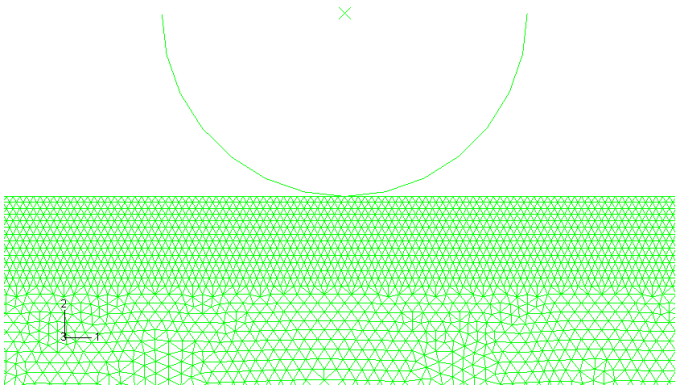

Figure 8.12: Two dimensional PE-PS indentation model mesh. Contact zone close-up.

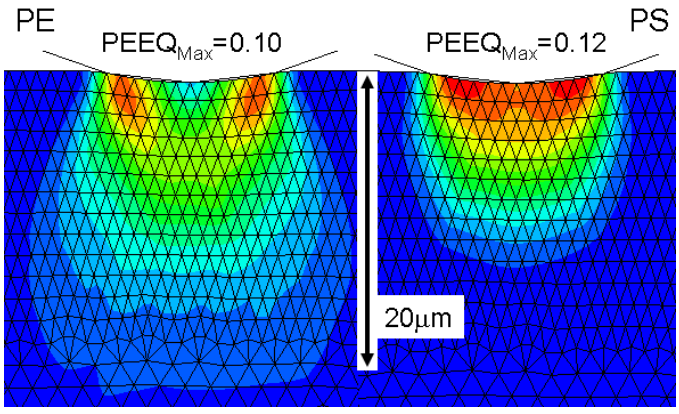

Figure 8.13: PEEQ under the indentation zone for $1.0\mu m$ penetration depth. Left PE. Right PS.

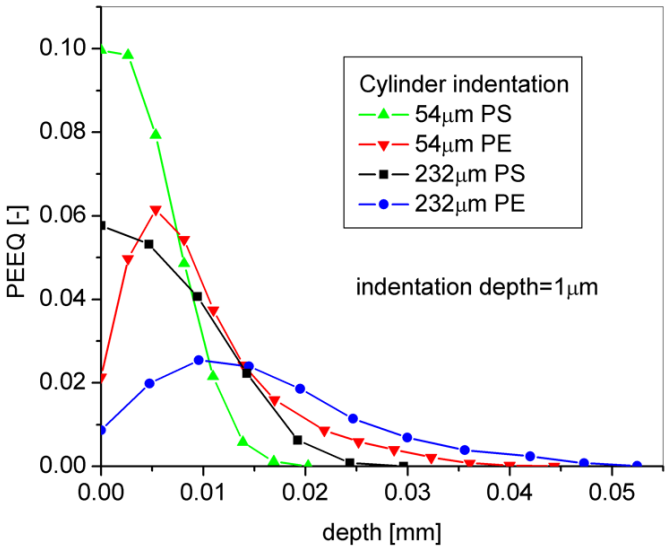

Figure 8.14: PEEQ under the constant indentation depth of $1.0\mu m$. PE, PS, large and small indenter cases.

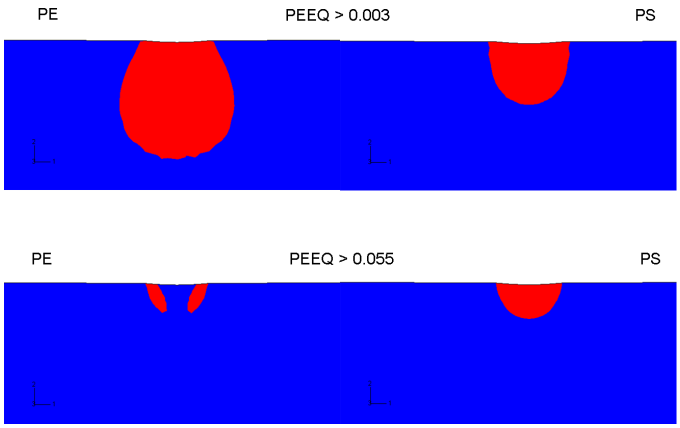

Figure 8.15: PEEQ for $1.0\mu m$ penetration depth. Left PE. Right PS. Top $PEEQ \geq 0.003$. Bottom $PEEQ \geq 0.055$.

that the smallest the PEEQ threshold is, the less sensitive the PDD becomes on the G_z. In general, for an arbitrary PEEQ threshold the PDD depends on the indenter size.

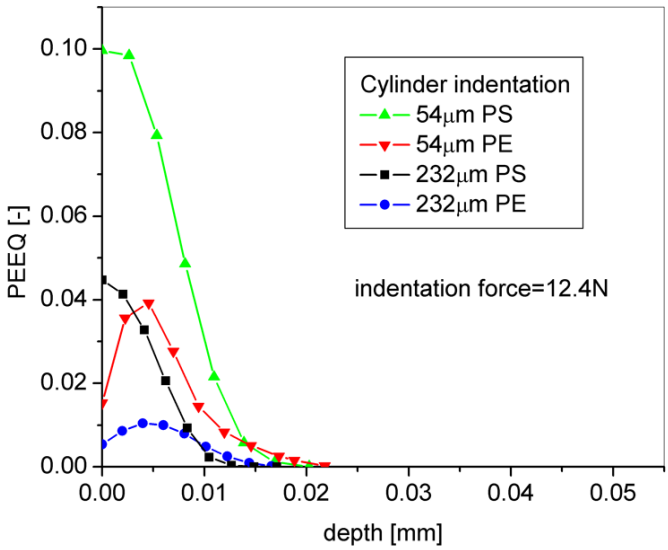

Figure 8.16: PEEQ under the constant indentation force of $12.4N$. PE, PS, large and small indenter cases.

8.2 Hyperelastic Model

A hyperelastic rate-dependent model of (poly)crystal plasticity using an explicit integration scheme is described based on the works of Lee (1969); Asaro (1983a,b); Cuitio and Ortiz (1992); Kad et al. (1995); McGinty and McDowell (1999), and McGinty (2001). This model is based on the multiplicative decomposition of the deformation gradient $\underset{\sim}{F}$ proposed by Lee (1969), i.e.,

$$\underset{\sim}{F} = \underset{\sim}{F}^e \underset{\sim}{F}^p \tag{8.1}$$

Figure 8.17 shows the multiplicative decomposition of the deformation gradient, where X represents the Lagrangian, reference, undeformed, or initial configuration; x represents the Eulerian, spatial, deformed, or current configuration; tilde ($\tilde{}$) represents the intermediate unstressed configuration where the plasticity constitutive modeling is better described. The push-forward and backward between the bar ($\bar{}$) and breve ($\breve{}$) configurations is done by accounting for the continuum rotation tensor $\underset{\sim}{R}$. The hat ($\hat{}$) configuration is corotational with the continuum rotation $\underset{\sim}{R}$. The figure also describes the native or natural configuration where the several rate tensors are represented. The only physically meaningful configuration is the current one which is coincident with the reference

one at $t = 0$. The model was implemented in Abaqus explicit using the VUMAT material subroutine

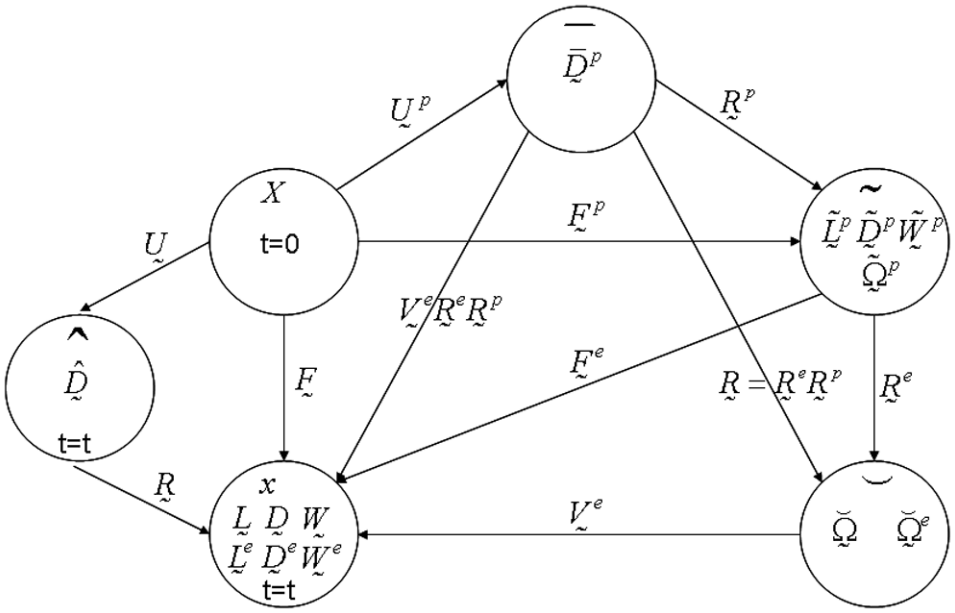

Figure 8.17: Multiplicative decomposition of the deformation gradient.

in Fortran90. The VUMAT subroutine provides the deformation gradient tensor at each material point from the previous time step $\underset{\sim}{F}_{i-1}$ and at the current one $\underset{\sim}{F}_{i}$, as well as for the right stretch tensors $\underset{\sim}{U}_{i-1}$ and $\underset{\sim}{U}_{i}$ obtained from the multiplicative polar decomposition, i.e.,

$$\underset{\sim}{F} = \underset{\sim}{R}\underset{\sim}{U} = \underset{\sim}{V}\underset{\sim}{R} \tag{8.2}$$

The subroutine asks for the Cauchy stress expressed in the corotational current configuration, along with user defined internal state variables (ISV). The resolved shear stress in each slip system τ^α was obtained by the scalar product of the initial Schmid tensor defined in the intermediate configuration $\left(\underset{\sim}{s}_0^\alpha \otimes \underset{\sim}{n}_0^\alpha\right)$ times the second Piola-Kirchhoff stress $\tilde{\underset{\sim}{\sigma}}^{pk(2)}$ (Eq. 8.3). Given that $\tilde{\underset{\sim}{\sigma}}^{pk(2)}$ is defined in the tilde configuration there is no need to update the Schmid tensor since in classical crystal plasticity it is assumed that the plastic part of the deformation gradient ($\underset{\sim}{F}^p$) does not produce rotation of the underlying crystal lattice.

$$\tau_i^\alpha = (s_0^\alpha \otimes n_0^\alpha) : \tilde{\underset{\sim}{\sigma}}_{i-1}^{pk(2)} \tag{8.3}$$

This resolved shear stress is the driving force for slip system activity. The shear rate in each slip system $\dot{\gamma}^\alpha$ is given by the viscoplastic power law of Eq. 8.4 where $\dot{\gamma}_0$ is the reference shear rate, g^α

the drag stress in each slip system, and m the flow exponent or inverse of the strain rate sensitivity exponent. For simplicity this flow rule does not present a threshold for stress, and the back-stress which is related to the kinematic hardening is considered zero. The direction of the flow at each slip system is given by the sign of its resolved shear stress.

$$\dot{\gamma}_i^\alpha = \dot{\gamma}_0 \left| \frac{\tau_i^\alpha}{g_i^\alpha} \right|^m \operatorname{sgn}(\tau_i^\alpha) \tag{8.4}$$

The plastic part of the velocity deformation gradient $\tilde{\underset{\sim}{L}}^p$ is given by Eq. 8.5

$$\tilde{\underset{\sim}{L}}_i^p = \sum_{\alpha=1}^{nss} \left(s_0^\alpha \otimes n_0^\alpha \right) \dot{\gamma}_i^\alpha \tag{8.5}$$

The updated plastic part of the deformation gradient $\underset{\sim}{F}^p$ given in Eq. 8.6 is obtained by the time integral of $\tilde{\underset{\sim}{L}}^p$ computed as a truncated series expansion containing the first 4 terms of the series(Eq. 8.7)

$$\underset{\sim}{F}_i^p = \exp\left(\tilde{\underset{\sim}{L}}_i^p dt \right) \underset{\sim}{F}_{i-1}^p \tag{8.6}$$

$$\exp\left(\tilde{\underset{\sim}{L}}_i^p dt \right) = \sum_{n=0}^{3} \frac{\left(\tilde{\underset{\sim}{L}}_i^p dt \right)^n}{n!} \tag{8.7}$$

The plastic right Cauchy-Green tensor $\underset{\sim}{C}^p$ defined in the reference configuration is given by Eq. 8.8, from where the plastic right stretch tensor $\underset{\sim}{U}^p$ and plastic rotation $\underset{\sim}{R}^p$ are obtained in Eqs. 8.9 and 8.10, respectively.

$$\underset{\sim}{C}_i^p = \underset{\sim}{F}_i^{pT} \underset{\sim}{F}_i^p \tag{8.8}$$

$$\underset{\sim}{U}_i^p = \sqrt{\underset{\sim}{C}_i^p} \tag{8.9}$$

$$\underset{\sim}{R}_i^p = \underset{\sim}{F}_i^p \underset{\sim}{U}_i^{p-1} \tag{8.10}$$

From Eq. 8.1 the updated elastic part of the deformation gradient can be obtained (Eq. 8.11). The elastic right Cauchy-Green tensor $\tilde{\underset{\sim}{C}}^e$ defined in the intermediate configuration is given by Eq. 8.12, from where the elastic right stretch tensor in the intermediate configuration $\tilde{\underset{\sim}{U}}^e$ and elastic rotation $\tilde{\underset{\sim}{R}}^e$ are obtained in Eqs. 8.13 and 8.14 respectively.

$$\underset{\sim}{F}_i^e = \underset{\sim}{F}_i \underset{\sim}{F}_i^{p-1} \tag{8.11}$$

$$\tilde{\underset{\sim}{C}}_i^e = \underset{\sim}{F}_i^{eT} \underset{\sim}{F}_i^e \tag{8.12}$$

$$\tilde{\underset{\sim}{U}}^e_i = \sqrt{\tilde{\underset{\sim}{C}}^e_i} \tag{8.13}$$

$$\underset{\sim}{R}^e_i = \underset{\sim}{F}^e_i \underset{\sim}{U}^{e-1}_i \tag{8.14}$$

The Green-Saint Venant strain defined in the intermediate configuration is given by Eq. 8.15, from where the updated $\tilde{\underset{\sim}{\sigma}}^{pk(2)}$ can be obtained. This stress tensor is corotational with the underlying crystal lattice but not with the continuum rotation as needed by the material subroutine. The Cauchy stress can be obtained by pushing forward $\tilde{\underset{\sim}{\sigma}}^{pk(2)}$ to the current configuration as shown in Eq. 8.17, where $J^e = \det \underset{\sim}{F}^e$ is the determinant of the non-singular Jacobian matrix of the transformation and represents the relative change in volume of the continuum in the current configuration with respect to the initial one.

$$\tilde{\underset{\sim}{E}}^e = \tfrac{1}{2}(\tilde{\underset{\sim}{C}}^e_i - \underset{\sim}{I}) \tag{8.15}$$

$$\tilde{\underset{\sim}{\sigma}}^{pk(2)}_i = \underset{\sim}{\underset{\sim}{C}} : \tilde{\underset{\sim}{E}}^e \tag{8.16}$$

$$\underset{\sim}{\sigma} = J^{e-1} \underset{\sim}{F}^e_i \tilde{\underset{\sim}{\sigma}}^{pk(2)}_i \underset{\sim}{F}^{eT}_i \tag{8.17}$$

The Cauchy stress is expressed in the corotational frame ($\hat{}$) by rotating it backwards with $\underset{\sim}{R}$ as shown in Eq. 8.18. Abaqus will produce internally the inverse transformation of Eq. 8.18 and use it for force and momentum balance computation and display.

$$\hat{\underset{\sim}{\sigma}}_i = \underset{\sim}{R}^T_i \underset{\sim}{\sigma}_i \underset{\sim}{R}_i \tag{8.18}$$

This approach can be simplified if it is assumed that elastic deformations are small, which is true in the case of metals at large deformations as this case. The elastic stretch from the left polar decomposition $\underset{\sim}{V}^e \simeq \underset{\sim}{I}$. Therefore, the Cauchy stress in Eq. 8.17 can be simplified as Eq. 8.19 since $\underset{\sim}{R}$ is proper orthogonal,

$$\underset{\sim}{\sigma} = \underset{\sim}{R}^{\ e}_i \tilde{\underset{\sim}{\sigma}}^{pk(2)}_i \underset{\sim}{R}^{eT}_i \tag{8.19}$$

that pushed-backwards to the corotational system will be expressed as Eq. 8.20

$$\begin{aligned}
\hat{\underset{\sim}{\sigma}} &= \underset{\sim}{R}^T_i \underset{\sim}{R}^e_i \tilde{\underset{\sim}{\sigma}}^{pk(2)}_i \underset{\sim}{R}^{eT}_i \underset{\sim}{R}_i \\
\hat{\underset{\sim}{\sigma}} &= \left(\underset{\sim}{R}^e_i \underset{\sim}{R}^p_i\right)^T \underset{\sim}{R}^e_i \tilde{\underset{\sim}{\sigma}}^{pk(2)}_i \underset{\sim}{R}^{eT}_i \underset{\sim}{R}^e_i \underset{\sim}{R}^p_i \\
\hat{\underset{\sim}{\sigma}} &= \underset{\sim}{R}^{pT}_i \tilde{\underset{\sim}{\sigma}}^{pk(2)}_i \underset{\sim}{R}^p_i
\end{aligned} \tag{8.20}$$

The updated drag stress is obtained considering the hardening the slip activity produced in the slip systems as shown in Eq. 8.21 where $h_{\alpha\beta}$ are the coefficients of the hardening matrix given by Eq. 8.22. It has to be noted that the hardening in a slip system α does not only depend on the dislocation activity in that system (self-hardening) but also on the activity of all other systems (cross-hardening), being the second effect larger.

$$g_i^\alpha = g_0^\alpha + \sum_\beta^{nss} h_{\alpha\beta} \left| \dot{\gamma}^\beta \right| dt \tag{8.21}$$

$$h_{\alpha\beta} = qh + (1-q)\, h\delta_{\alpha\beta} \tag{8.22}$$

The measure used to compute plastic deformation is given by (Eq. 8.23); its integral, the cumulative plastic deformation Eq. 8.24 was used for plotting results. A measure of cumulative plastic deformation per slip system is given by Eq. 8.25.

$$E_{eff}^p = \sqrt{\tfrac{2}{3}\left(\underset{\sim}{E}_l^p : \underset{\sim}{E}_l^p\right)} \tag{8.23}$$

$$E_{cum}^p = \sum \Delta \underset{\sim}{E}_{eff}^p \tag{8.24}$$

$$E_i^p = E_{i-1}^p + \sum_{\alpha=1}^{nss} \dot{\gamma}_i^\alpha dt \tag{8.25}$$

where

$$\underset{\sim}{E}_l^p = \ln \underset{\sim}{U}_i^p \tag{8.26}$$

8.3 Material Properties

8.3.1 Elastic Constants

Using Voigt notation, the fourth order stiffness tensor will be written as shown in Eq. 8.27 LHS for general orthotropic material. In the case of $\gamma - TiAl$, the material presents transverse isotropy, having the stiffness matrix with only 5 independent constants as shown in RHS of Eq. 8.27, where

the matrix is represented in its principal direction.

$$\underset{\sim}{C} = \begin{bmatrix} C_{11} & C_{12} & C_{13} & 0 & 0 & 0 \\ C_{21} & C_{22} & C_{23} & 0 & 0 & 0 \\ C_{31} & C_{32} & C_{33} & 0 & 0 & 0 \\ 0 & 0 & 0 & C_{44} & 0 & 0 \\ 0 & 0 & 0 & 0 & C_{55} & 0 \\ 0 & 0 & 0 & 0 & 0 & C_{66} \end{bmatrix} = \begin{bmatrix} 211.6 & 66.0 & 40.6 & 0 & 0 & 0 \\ & 211.6 & 40.6 & 0 & 0 & 0 \\ & & 232.8 & 0 & 0 & 0 \\ & & & 72.6 & 0 & 0 \\ & Sym & & & 66.9 & 0 \\ & & & & & 66.9 \end{bmatrix} \tag{8.27}$$

8.3.2 Planar Triple Slip

A planar triple slip system was used to model the visco-plastic material behavior as proposed by Kad et al. (1995) for modeling lamellar $TiAl$, and Goh (2003) for fretting of $Ti-6Al-4V$. The basal slip system was parallel to the lamellae interface and modeled as an easy slip system, the other two slip systems were considered at an angle of $\pi 5/12 rad$ from the basal and considered hard slip systems. The graphic representation of the slip systems can be seen in Fig. 8.18. The unnormalized slip systems are defined as

$$\underset{\sim}{s}_1 = \{1,0,0\}; \qquad \underset{\sim}{n}_1 = \{0,-1,0\}$$
$$\underset{\sim}{s}_2 = \{-\tan\left(\frac{5\pi}{12}\right),1,0\}; \qquad \underset{\sim}{n}_2 = \{1,\tan\left(\frac{5\pi}{12}\right),0\}$$
$$\underset{\sim}{s}_3 = \{\tan\left(\frac{5\pi}{12}\right),1,0\}; \qquad \underset{\sim}{n}_3 = \{-1,\tan\left(\frac{5\pi}{12}\right),0\}$$

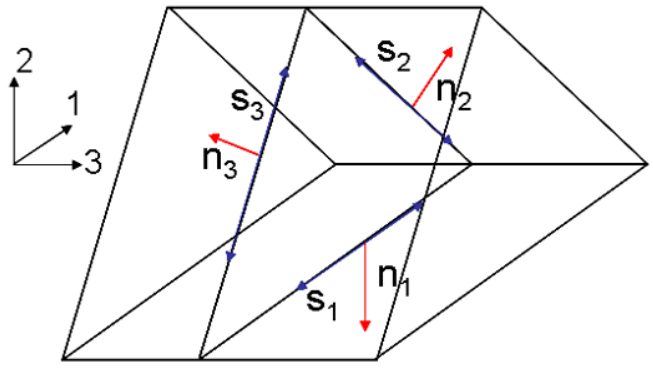

Figure 8.18: Slip systems directions and slip plane normals.

8.3.3 Visco-plastic Parameters Calibration

The viscoplastic parameters of Eq. 8.4 were calibrated by best fitting to the true strain vs. true stress plots shown in Fig. 3.10. The numerical model used 64 randomly oriented grains, each of which was represented by a unique element. The elements used were CPE3, PE, 3-node linear; and the BC's allow stretching of the model sides. Compression was simulated, and its rate was given by scaling the rate curves of Fig. 3.9 by entering it as piecewise table. In the case of quasi static tests, mass scaling was utilized to accelerate the computation time without appreciably affecting the outcome. A typical representation of the deformed state is shown in Fig. 8.19, where plastic deformation is represented. The best fitting parameters are given in Table 8.1. Figure 8.20 shows the comparison of experimental and FEA true stress-true strain plots.

Table 8.1: Slip systems contants.

	m	39
easy slip	g_0	$58MPa$
hard slip	g_0	$232MPa$
$i \neq j$	h_{ij}	$504MPa$
$i = j$	h_{ij}	$360MPa$
	$\dot{\gamma}_0$	0.001

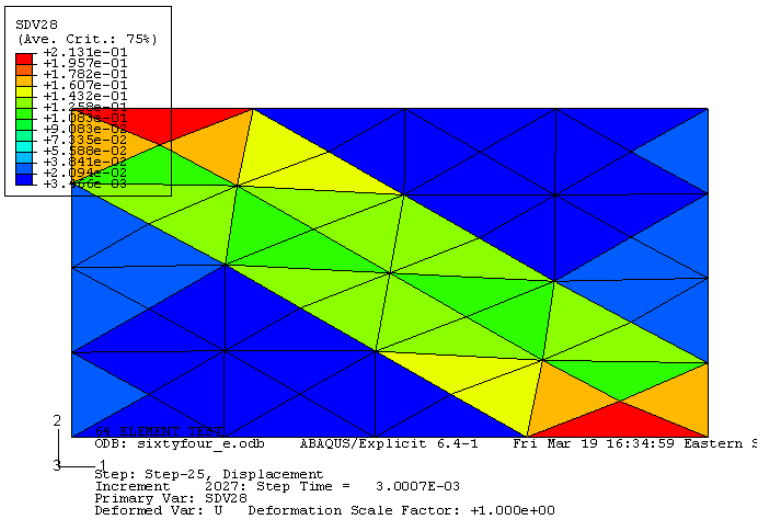

Figure 8.19: Typical representation of the deformed state for model used in parameters calibration.

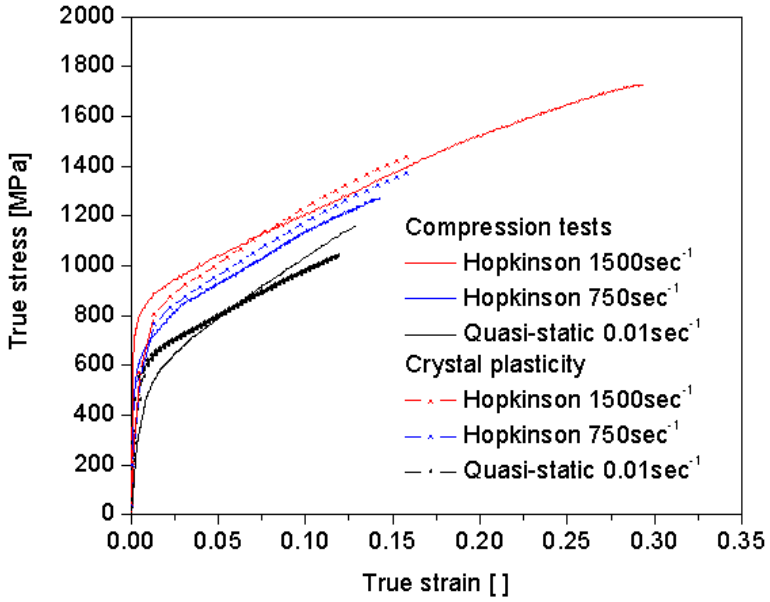

Figure 8.20: Experimental and numerical comparison of true stress vs. true strain curves.

8.4 Implementation and Results

A 2D model containing 117 idealized hexagonal grains representing lamellae colonies was meshed as shown in Fig. 8.21. The model implemented a hybrid 2D-3D rotation scheme to assign the initial orientation of the grains. The elastic constants were rotated to any random spatial orientation, but the slip systems were restricted to (random) in plane rotations. Figure 8.22 represents the initial angles in which the slip systems were oriented. Eight different runs were performed at scratching

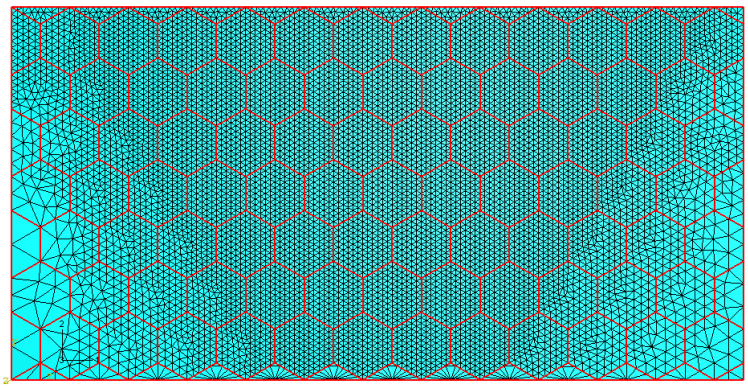

Figure 8.21: Hexagonal lamellae colonies and mesh used for scratching tests.

depths of $0.125\mu m$, $0.250\mu m$, $0.5\mu m$, and $1.0\mu m$ with indenters of $54\mu m$ and $232\mu m$ diameter.

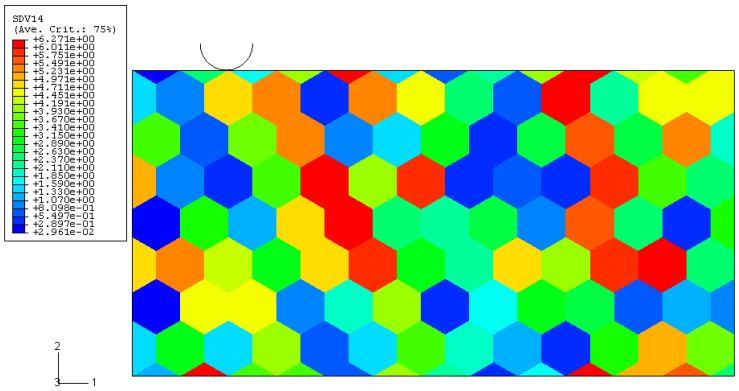

Figure 8.22: Slip systems initial orientation angles.

The plastic deformation results are represented in Figs. 8.23, and 8.24 respectively. It has been observed that in average, the larger G_z produced a larger PDD. Also, the smaller G_z produced a larger deformation gradient. As shown in Fig. 8.25, grain boundaries act as effective barriers for deformation propagation, and orientation affects the local PDD.

8.5 Conclusions

From the results of the 2D models that analyzed the PE vs PS, it seems that for practical purposes the measured PDD at the free surface can be used as a upper boundary value.

It was also shown that in the case of indentation the PDD can be considered independent of the G_z for a specific PDD threshold, being generally size dependent.

The use of an idealized crystal plasticity of the lamellar $\gamma - TiAl$ considering triple planar slip captures the effects of grain boundaries and material anisotropy on the PD. It has been observed that in average, the larger G_z produced a larger PDD. Also, the smaller G_z produced a larger deformation gradient. Grain boundaries act as effective barriers for deformation propagation, and orientation affects the local PDD.

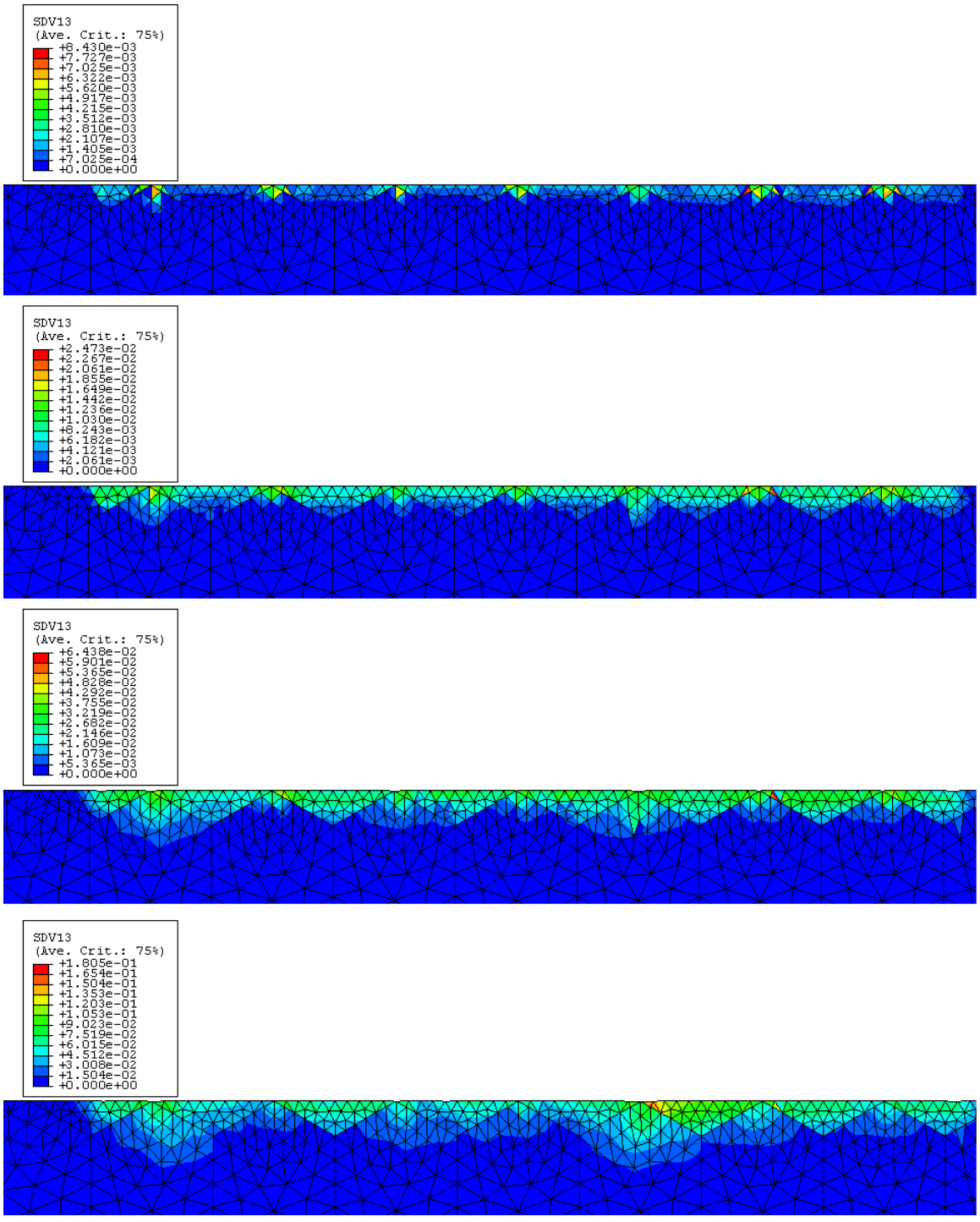

Figure 8.23: Plastic deformation for small indenter. From top to bottom $0.125\mu m$, $0.250\mu m$, $0.5\mu m$, and $1\mu m$ penetration depth.

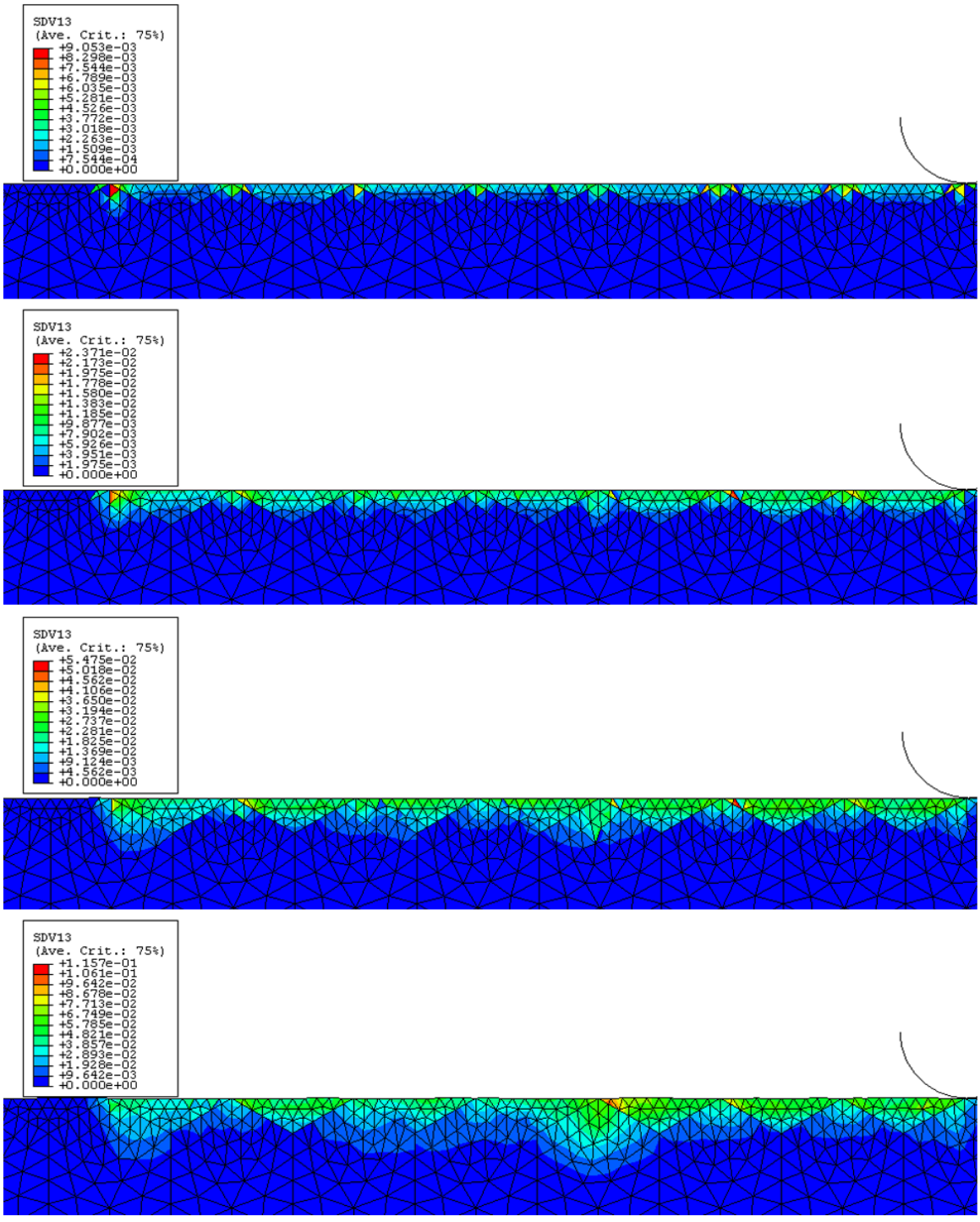

Figure 8.24: Plastic deformation for large indenter. From top to bottom $0.125\mu m$, $0.250\mu m$, $0.5\mu m$, and $1\mu m$ penetration depth.

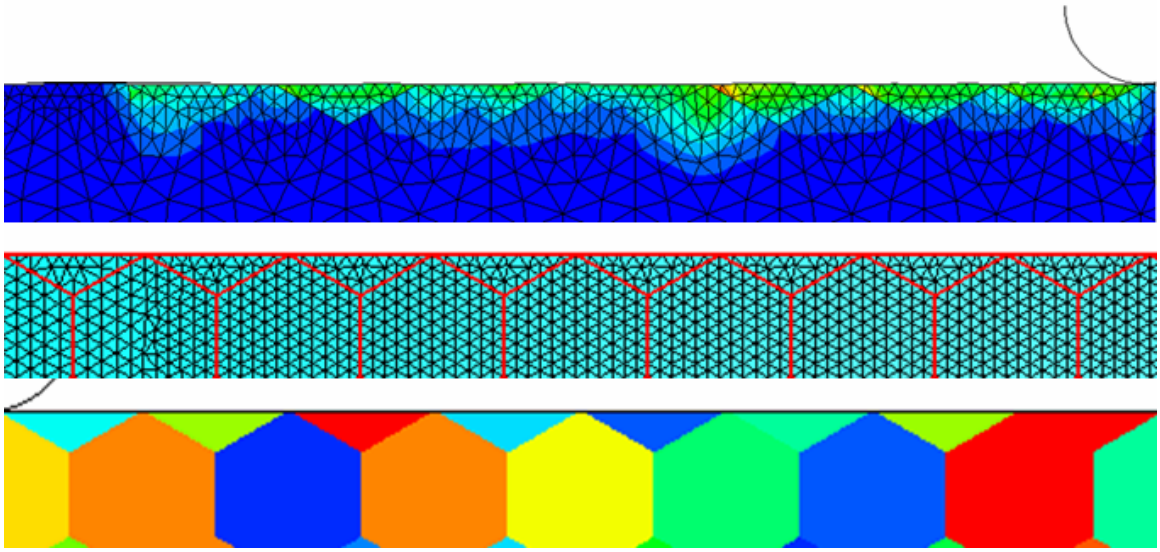

Figure 8.25: Grain boundary and orientation effect on plastic deformation.

CHAPTER IX

DISCUSSION

9.1 Grinding

This work has shown that PDD has a negative correlation with C_f. Also, G_z and G_h have a negative correlation with C_f, while the correlation with DoC and V_w is positive. The C_f involves every variable of the process, as shown by Meng and Ludema (1995). The effect of G_z and G_h on C_f for dressed wheels can be explained by considering factors related with chip thickness, and coolant. Figures. 7.6, and 7.10 obtained with the analytical model of Chapter 7, show that chip thickness for large and small G_z, as well as the D_g, is about 4/1. This means that active abrasive grits are geometrically equivalent, in particular they exhibit the same rake angle. If size effects on deformation mechanisms are not accounted for, this equivalency will produce the same C_f. Therefore, lubrication could be the factor that produces the C_f difference, and the larger the G_z, the larger the gap for the coolant between the wheel and workpiece. Also, it is possible that an hydrodynamic lubrication film can be more effectively formed by individual large grits due to the larger length so that a pressure build-up is produced, or the grits act as fluid impellers. The positive correlation of the C_f with DoC and V_w can be explained by assuming that the depth of engagement of abrasive grits correlates positively with these variables, since F_T'' increases proportionally faster than the F_N'' with the engagement depth. In the case of worn grits it can be argued that the general trend in C_f is dominated by the wear flats of the abrasive grits, chip thickness, and the interfacial space between wheel and workpiece. Wear flats increase the F_N'' necessary for indentation but do not proportionally increase the F_T'', since the same area of material has to be removed. Chip thickness acts in a similar way. Given an indenter, and assuming scratching of a non-hardening material for simplicity purposes, the normal force will be almost independent of the penetration depth, while the tangential force will increase with the penetration depth due to the increase of the chip thickness.

9.2 PDD Controlling Factors

From the results shown in Fig. 5.42, it can be seen that the PDD does not show a good correlation with ${F'_N}^{0.5}$, as proposed by Nelson (1997); Razavi (2000); Stone (2003). For dressed conditions the PDD data in Fig. 5.42 is clustered by G_z.

By using the analytical model of Chapter 7, the number of active cutting edges, chip thickness, and force per grit were obtained. Fig. 7.14 shows that PDD has a good correlation with ${F''_N}^{0.5}$, as proposed by the indentation model of Lawn and Wilshaw (1975); Aurora et al. (1979). This suggests that the indentation model is still valid for grinding if the force per grit is used instead of the total grinding force.

A peculiar correlation has been observed (Fig. 5.45) between PDD and C_f, with a R-sq value of 0.84 obtained from a linear fit considering the complete set of data.

The PDD has been shown to be strongly dependent on G_z for the dressed conditions, and on MRR for the worn conditions, and almost independent on the G_z. Furthermore, Fig. 5.42 shows that in the case of large G_z, the average PDD is smaller for worn conditions, while for small G_z it is noticeably larger. This seems to indicate that other variables are controlling the PDD. For dressed wheels, it appears that a purely mechanical approach is able describe the PDD; however this model does not work for worn conditions. This is probably due to thermal effects. Therefore, for large G_z in the dressed and worn conditions, and the small G_z in the dressed conditions the purely mechanical approach seems to be appropriate, while in the case of small G_z in the worn conditions, thermal effects seems to be dominant.

9.3 Force per Grit Analytical Model

Table 7.1 gives the fitted factors for the dressed and worn conditions separated by G_h which were obtained by best fitting in the model presented in Chapter 7. The $G_f > 1$ for all cases, indicates that the grit acts as if it had a larger size. In the case of dressed wheels this factor is larger in the case of Bk G_h. This is reasonable not only for the grit shape itself, but also for the Bk G_h being less friable than the Ag G_h. In the case of worn wheels the model gives the inverse relation, which does not seem to be correct. The W_f modifies the slope of the static cumulative pdf of cutting edges density in Eq. 7.7. It was set to a value of 1 for tests using dressed wheels. The obtained $W_f > 1$

for worn wheels indicates that the probability distribution function is narrower, as expected.

The D_f modifies the static hardness accounting for dynamic effects. In the case of dressed wheels the fitted values were 2.0 for the Ag and Bk G_h, while for worn wheels a value of $D_f = 4.5$ for Ag and $D_f = 4.0$ for Bk. While all the values are larger than unity there is no explanation for assuming that this value is different as a result of wheel condition.

The resulting fitted factors might indicate that the model works well for dressed conditions, but that it breaks for worn conditions. This disagreement might be due to variables not accounted for, such as temperature, possible contact of bond material with the workpiece for small G_z, or a different probability distribution function of cutting edges density than the one assumed in this work.

The model is not capturing the increase on the F_N'' with wear. Figure 9.1 shows an individual grit in the dressed and worn conditions. It is assumed that the same volume of chip will be removed in both conditions, therefore the shaded area, or chip area, should be the same for both cases, and can be computed by

$$A_{ch} = \frac{G_z^2}{4} \tan^{-1} \left[\sqrt{\left(\frac{G_z}{d_g^w} \right)^2 - 1} \right] - \frac{d_g^w}{4} \sqrt{G_z^2 - {d_g^w}^2}$$

It can be observed that with increase wear the abrasive grit diameter at the grit depth of cut d_g^w increases. The F_N'' will be given by the indentation depth, and if we assume an elastic perfectly plastic material that deforms at a contact pressure equal to the material hardness, the F_N'' will be given by

$$F_N'' = \frac{\pi}{8} {d_g^w}^2 Hv$$

The F_T'' has two components, one due to chip removal and the second due to the friction. The chip removal component of F_T'' is independent of the wear condition, while the frictional component will depend on F_N'' and therefore on wear, i.e.,

$$F_T'' = A_{ch} Hv + F_N'' f$$

The C_f can be computed by

$$C_f \simeq \frac{F_T''}{F_N''}$$

and the P''_w, proportional to F''_T, as

$$P''_w = (A_{ch} H v + F_N f)\, V_s$$

Figures 9.2 and 9.3 present the qualitative variation of C_f and P'_w or F'_T with W_r. It is observed that while grinding C_f decreases with W_r the inverse behavior is shown by the forces and power. This effect, which is not captured by the analytical model presented, explains the inverse correlation of the PDD with W_r. It also confirms that the abrasive condition is of great importance in grinding as observed on the tests.

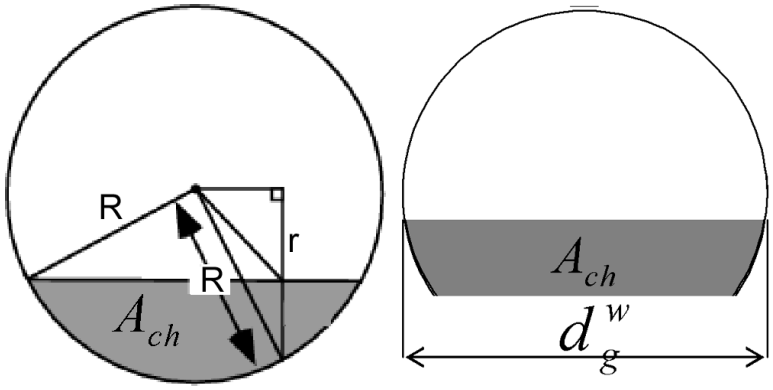

Figure 9.1: Dressed (left) and worn abrasive grit. Chip area is assumed constant (shaded).

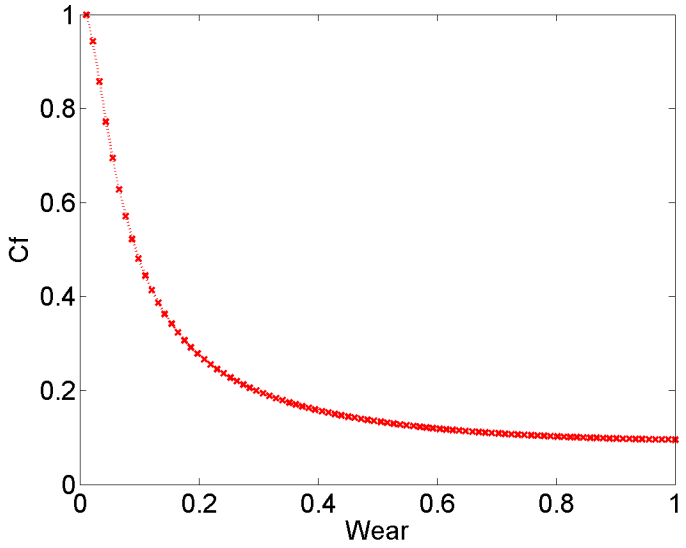

Figure 9.2: Qualitative variation of C_f with W_r.

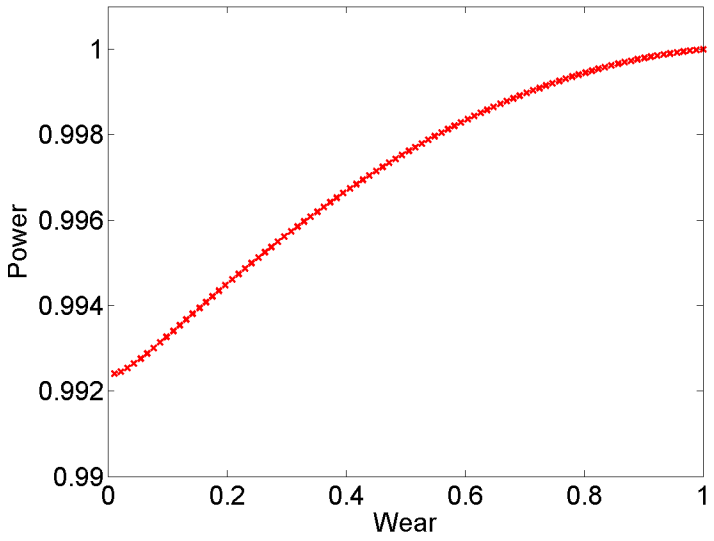

Figure 9.3: Qualitative variation of P'_w with W_r.

9.4 Significance of PDD Measurement Technique

9.4.1 Significance as PDD Evaluation Method

As shown by Jones (1997), the indentation technique is less sensitive than the Nomarski microscopy for PDD evaluation. Since optical profilometry uses the same principle of light interference as Nomarski microscopy, they have a similar resolution. The advantage in the proposed technique is that quantitative analysis of the 3D profile can be performed and an algorithm with the criterion to define the PDD zone can be used. This approach is less biased from a user's criteria and allows one to obtain more information from the surface, i.e. the effect of grain size on PDD.

9.4.2 Significance in Terms of Mechanical Performance

As shown by Jones (1997); Jones and Eylon (1999), $TiAl$ machined parts designed to be utilized in high temperature applications, might recrystallize on a subsurface layer during operation. The recrystallization depth depends on the machining conditions, alloy chemistry, and temperature and time. This recrystallized zone has usually a smaller grain size than the original one, improving HCF performance by more than an order of magnitude. Figure 9.4 shows an example of a recrystallized layer of a $TiAl$ machined alloy after 1hr at $750°C$. The proposed PDD measurement technique might be instrumental in predicting the depth of the recrystallized zone.

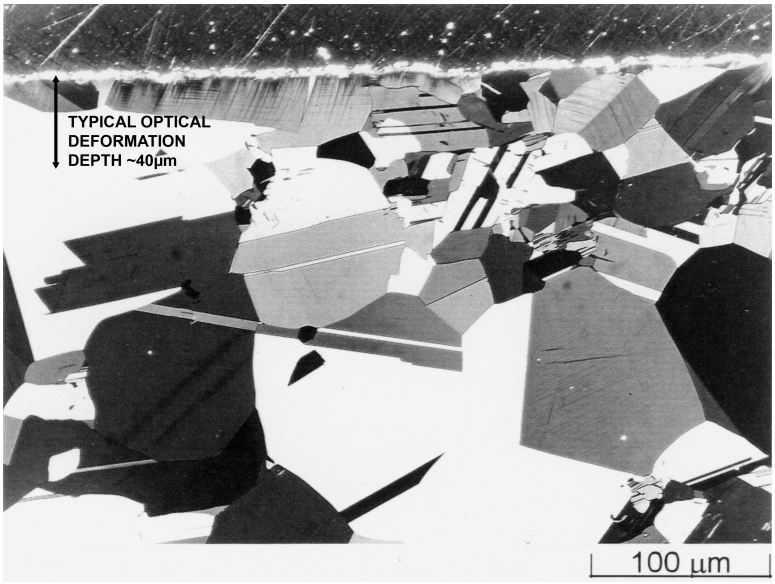

Figure 9.4: Recrystallized zone at the machined subsurface (Jones, 1997).

9.4.3 Relation with PDD at Bulk

One question that arises after the measurements of PDD is how this value obtained at a free surface is related to the PDD at the bulk. Figure 8.15 presented the PEEQ for two different PEEQ thresholds. With decreasing PEEQ threshold the PDD shows to be larger at the bulk with respect to the surface. It is not clear which is the actual deformation threshold that the proposed technique can measure. It is also not clear which would be the necessary level of PD to produce an effect on the material performance. Further research is necessary in this area.

9.4.4 PDD, Microstructure, and Cracking

The PDD mean value was of the order of $\simeq 400\mu m$ with an observed minimum and maximum of $\simeq 100\mu m$ and $\simeq 800\mu m$ respectively. Considering that the lamellae size was of the order of $\simeq 250\mu m$, the measured PDD extends to an average of about two grains. Figure 9.5 shows the PDD observed by Nomarski microscopy for $\gamma - TiAl$ after machining. It can be seen that the surface grains have undergone plastic deformation. Also, the orientation of the deformation lines varies with the crystallographic orientation of the lamellae colony. This was also observed by Nelson (1997). This behavior is captured by the proposed PDD measurement technique as shown in Fig. 4.6, and the crystal plasticity model presented in Chapter 8, where Figs. 8.23, and 8.24 show the deformation

pattern for different G_z and penetration depth for single grit scratching. It can be observed that the grain boundaries act as effective barriers for plastic deformation propagation, and the lamellae orientation also affects the local PDD.

The PDD did not present a correlation with the samples where cracking was observed. This suggests that the PDD is restricted to the surface grains, but the amount of PD being different in each case. This is also captured by the crystal plasticity model presented on Chapter 8. Figures 8.23, and 8.24 show that the deformation depth is larger in the case of large G_z, and the plastic deformation deformation gradient is larger for the small G_z for constant indentation depth. This trend is not followed in the case of the smallest indentation depth, probably due to a coarse meshing.

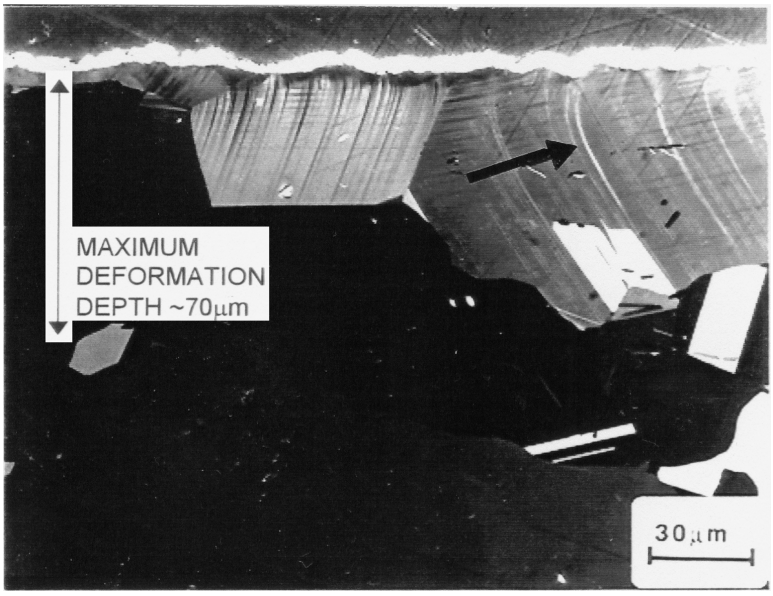

Figure 9.5: Plastic deformation observed on the surface grains (Jones, 1997) .

9.4.5 Scratching Model and Indentation Model

The 3D numerical scratching model presented in Chapter 8 shows a linear relation of PDD with ${F''_N}^{0.5}$ for a $PEEQ = 0.01$, this trend seems to disappear at larger $PEEQ$ values (Figs.8.9 and 8.10). Also the slope of PDD vs. ${F''_N}^{0.5}$ depends on the G_z. In the indentation model of Lawn and Wilshaw (1975); Aurora et al. (1979), the PDD vs. ${F''_N}^{0.5}$ relation is linear and independent of G_z. The parameter β in the indentation model relates the indentation diagonal with the PDD

depth. Nevertheless, this parameter is loosely defined since the definition of the PDD depends on the experimental technique. The parameter β may take a range of values and the linearity of PDD with ${F''_N}^{0.5}$ might not be observed for the range. The dependence of PDD with G_z for a constant load is observed for 2D modeling of indentation as shown in Fig. 8.16. The PDD can be considered independent of the G_z only at a particular deformation threshold. Size dependence is also seen for simulations of 3D scratching.

From the 3D numerical scratching model it can also be seen that a single scratching pass produces a PDD of approximately an order of magnitude smaller than the ones measured. A probable cause for this is that the deformation history due to successive scratching in grinding is not accounted for in the model.

9.5 Residual Stress

Two different types of x-ray scans were used to acquire data: the so-called detector scan, and Ψ scans. In the detector scan the azimuth angle of the x-ray changes for the different conditions, thereby changing the beam penetration depth. In the case of presence of step stress gradients on the specimen the hypothesis of uniform stress in the measured region would be violated. In the case of Φ scans the azimuth angle is kept constant, obtaining different measurements at different Φ angles. The disadvantage of this method is that the measured interplanar distances are close to each other, and errors are amplified.

CHAPTER X

CONCLUSIONS AND RECOMMENDATIONS

10.1 Conclusions

10.1.1 PDD Evaluation Technique

The PDD evaluation method proposed, combines the quantitative capabilities of the microhardness measurement with the sensitivity of Nomarski microscopy. Quantitative analysis of the surface can be performed and an algorithm with the criterion to define the PDD zone can be used. This approach is less biased from the user's experience.

The method can be used to obtain a unique parameter for PDD or a complete mapping of the surface, according to the data analysis performed.

The averaging method of determining PDD is based on averaging the out-of-planarity of lines parallel to the surface. This method gives a unique value for PDD and is robust with respect to missing points and surface finishing.

The contour plot method allows the computation of PDD variability with respect to grain morphology and material anisotropy. Since no data averaging takes place, this method is very sensitive to surface finishing.

The practical limitation of these methods is given by the quality of surface preparation, e.g. the surface roughness is more important than its waviness. With a surface roughness of $Ra < 1\mu m$ it has been possible to work with an out-of-planarity threshold of $1\mu m$, thereby obtaining consistent results between replications and analysis techniques. An out-of-planarity threshold of $0.25\mu m$ has been of limited applicability for the present work.

10.1.2 Grinding

It has been observed that grinding is very sensitive to wheel conditioning and wear. Complete truing and dressing conditions should be specified to obtain consistent results. Cooling conditions are also important.

10.1.2.1 Plastic Deformation

The PDD mean value was of the order of $\simeq 400\mu m$ with an observed minimum and maximum of $\simeq 100\mu m$ and $\simeq 800\mu m$ respectively. Considering that the lamellae size was of the order of $\simeq 250\mu m$, the measured PDD extends on an average of about two grains.

It has been observed that for dressed conditions the PDD strongly depends on G_z. The PDD mean and standard deviation for small and large G_z is $186 \pm 40\mu m$, and $543 \pm 85\mu m$ respectively. Most of the PDD variance can be explained by the G_z factor alone, V_w being not a relevant factor. There is some influence of the G_h, and the interactions between G_z and G_h; and G_z and DoC. The R-Sq value for the model $PDD[\mu m] = 78.1 + 2.007 G_S$ is 87.9%.

In the case of worn conditions the PDD strongly depends on DoC and V_w, therefore MRR also correlates with PDD. The DoC explains half of the data variance followed in importance by V_w. Even considering most of the controlled variables and their interaction in a linear model, the R-Sq value was less than 0.82. The PDD mean and standard deviation was of $407 \pm 120\mu m$ for worn wheels and $365 \pm 191\mu m$ for dressed ones.

The change in behavior from dressed to worn conditions is believed to be produced by the increase of thermal effects and force per abrasive grit due to wear flats.

In the case of large G_z it has been observed that the PDD decreases with W_r while the inverse behavior was observed for small G_z. While the P'_w was of the same order of magnitude for large G_z for worn and dressed conditions, it increased an average of 6 times for small G_z. This would indicate that for large G_z the thermal effects were not very different for the two W_r conditions and the PDD was determined by the G_z. The decrease of the PDD could be explained by assuming that the worn wheel presented a narrower distribution of cutting edges than the dressed one. This could be due to some fracture of the abrasive grits during the first stages of grinding after dressing, which results as if having a smaller grit size. In the case of small G_z, it can be assumed that the generation of wear flats increased the force per abrasive grit and temperature with the consequent increase of the PDD.

It has been observed that the PDD is inversely correlated to the C_f. A R-sq value of 0.84 is obtained by a linear fit of PDD with C_f.

10.1.2.2 Grinding Friction Coefficient

Grit size and shape have a negative correlation with C_f, while the correlation with DoC and V_w is positive. In the case of worn wheels all individual factors, and the interactions between G_z and the rest of the variables are relevant for C_f, and their correlation is inverse to the one shown for PDD. While the C_f trend with G_z and G_h is the same as with dressed wheels, the dependence on DoC, and V_w is inverse. The negative correlation of the C_f with DoC and V_w can be explained by considering the shape change in the abrasives with W_r.

10.1.2.3 Specific Normal Force

In the case of dressed wheels, F'_N has a positive correlation with all the individual factors, and the G_z and G_h interaction.

In the case of dressed wheels, all individual factors and G_z and DoC; and DoC and V_w interactions are relevant for F'_N. Unlike the case of dressed wheels, G_z has a negative correlation with F'_N, which can be explained by assuming that the relative wear flat in the small grit is larger than in the large grit. This can be due to the fact that poorer lubrication conditions might occur with smaller grits, and therefore higher temperatures increase the wear rate of the diamond.

10.1.2.4 Surface Parameters

It was observed that the Ra and BA mean values increased with wear. This was probably due to the effect of plowing in the formation of side ridges.

For the dressed conditions, the mean R_a value is in the range of $0.4\mu m$ to $0.7\mu m$, and the mean 90% BA of $3.9\mu m$, G_z being is the most relevant factor.

For the worn conditions, the mean R_a value is in the range of $0.65\mu m$ to $0.95\mu m$, with a mean value for 90% BA of $5.7\mu m$, G_z being the most relevant variable.

10.1.2.5 Cracking

The PDD was not correlated with cracking, as might be expected before the present work.

No cracking was observed on the ground surface under a magnification of $60X$ for dressed wheels.

Surface cracking was observed on tests using worn wheels for small G_z in the 4 treatments with the largest MRR. This cracking appears to be due to thermal effects and it was not related to PDD. It has been observed that cracking was produced on treatments with high F'_N, or high P'_w and low C_f.

Surface cracking was observed on tests using worn wheels, for the Ag8 and Bk8 treatments. It was also observed for the large G_z for the Bk2 treatment, and only one crack in a sample with Ag2 treatment. While extensive cracking was observed in the Bk2 treatment, only a single crack was observed in the Ag2 case. The Ag G_h presents a higher C_f than the Bk, due to its angular shape and higher friability with respect to the Bk. Wear flats on Bk shape abrasive grits increase redundant work and heat generation, decreasing C_f.

10.1.3 Residual Stresses

Residual stresses were measured in 4 ground samples analyzing the effect of a high and low PDD value. It can be seen that compressive stresses are close to the GPa on the surface.

Numerous experimental difficulties produced a high variance of the results and the impossibility to obtain results in zones of apparently high stress gradients.

10.1.4 Analytical Modeling

By use of the analytical model of the number of active cutting edges, chip thickness, and force per grit were obtained, and the PDD has shown a good correlation with ${F''_N}^{0.5}$, as proposed by the indentation model of Lawn and Wilshaw (1975); Aurora et al. (1979). This suggests that the indentation model is still valid for grinding if the force per grit is used instead of the total grinding force.

The model captures the difference in the number of cutting edges and chip thickness for the different G_z.

The resulting fitted factors of the analytical model might indicate that the model works well for dressed conditions by capturing expected trends, but it breaks for worn conditions. This disagreement might be due to variables not accounted for such as temperature, possible contact of bond material with the workpiece for small G_z, or a different probability density function of the cutting edges density than the one assumed in this work.

The analytical model predicts for the dressed conditions a cutting edge density of the order of $3\#/mm^2$ to $6\#/mm^2$ for small G_z, and less than $0.5\#/mm^2$ for large G_z. Model and test P'_w and forces are in reasonable agreement, but in some cases all these values differ by a factor of 2.

Chip thickness is of the order of $2.1\mu m$ to $4.5\mu m$ for large G_z, and in the order of $0.5\mu m$ to $1.1\mu m$ for small G_z. These values are in agreement with the ones found in the literature.

The analytical model predicts for the worn conditions that the cutting edge density is of the order of $4\#/mm^2$ to $8\#/mm^2$ for small G_z, and less than $0.6\#/mm^2$ for large G_z. Chip thickness is of the order of $1.5\mu m$ to $3.2\mu m$ for large G_z, and in the order of $0.2\mu m$ to $0.7\mu m$ for small G_z. As expected these values are smaller than the ones found for dressed wheels.

The resulting fitted factors of the analytical model might indicate that the model works well for dressed conditions by capturing expected trends, but it does not give good predictions for worn conditions. This disagreement might be due to variables not accounted for such as temperature, possible contact of bond material with the workpiece for small G_z, or a different probability density function of the cutting edges density than the one assumed in this work.

10.1.5 Numerical Modeling

From the results of the 2D models that analyzed the PE vs PS, it seems that for practical purposes the measured PDD at the free surface can be used as a upper boundary value.

It was also shown that in the case of indentation the PDD can be considered independent of the G_z for a specific PDD threshold, being generally size dependent.

The use of an idealized crystal plasticity of the lamellar $\gamma - TiAl$ considering triple planar slip captures the effects of grain boundaries and material anisotropy on the PD. It has been observed that in average, the larger G_z produced a larger PDD. Also the smaller G_z produced a larger deformation gradient. Grain boundaries act as effective barriers for deformation propagation, and orientation affects the local PDD.

10.2 Recommendations

Further characterization of the deformed zone may include not only the PDD, as in the present work, but also the first and second derivatives of the out-of-planarity profile shown in Fig. 4.6, and their relation to cracking.

Two relevant factors were left for modeling in future work: thermal effects, and deformation history. While thermal effects can be added with state-of-the-art FEA, the implementation of models that account for history effects under localized loads under large sliding and deformation conditions presents some difficulties. Finite element codes working in an Eulerian framework might be instrumental for these purposes.

The crystal plasticity model has shown that grain boundaries act as effective barriers for PD. An implementation of random grain sizes and geometry by use of Voronoi tesselation would be useful to further analyze the deformation dependence on these variables and approximate the model to the actual test.

Other modeling improvements might include the addition of more slip systems, explicit modeling of the two phases, improved hardening modeling, consideration of time dependent properties per slip system, fracture and fatigue modeling, actual abrasive shape, and 3D geometry.

One of the possible reasons for the departure of the force per grit model from the tests can be related to the use of an incorrect probability density function of the cutting edges to describe the wheel surface. The use of replicas and the work and errors associated with them can be avoided if modifications are introduced to present generation of 3D profilometers by designing the devices with similar stage capabilities as metallurgical microscopes, giving room for a grinding wheel to fit in the instrument. The inconvenience of dismounting the wheel from the grinder and later truing processes is a minor one compared with the benefits of direct measurement.

The RS analysis technique can be improved by considering the radiation attenuation in the subsurface, and stress gradients (Suominen and Carr, 1999; Behnken and Hauk, 2001; Ely et al., 1999; Wern, 1999; Zhu et al., 1995)

The measurement of residual stresses with neutron diffraction can be used to improve the resolution of the stress at the surface of highly deformed material, and to avoid the artifacts introduced by the layer removal technique, since the penetration depth of the radiation is of the order of millimeters.

Machined parts designed to be utilized in high temperature applications might recrystallize on a subsurface layer during operation. The recrystallization depth depends on the machining conditions, alloy chemistry, temperature and time. A further correlation of the proposed PDD

measurement technique with the recrystallized depth would be of interest.

One question that arises after the measurements of PDD is how this value obtained at a free surface is related to the PDD at the bulk. With decreasing PEEQ threshold the PDD shows to be larger at the bulk with respect to the surface. It is not clear which is the actual deformation threshold that the proposed technique can measure. It is also not clear which would be the necessary level of PD to produce an effect on the material performance. Further research is necessary in this area.

APPENDIX A

GRINDING EXPERIMENTAL RESULTS

Table A.1: Complete set of tests for dressed conditions. PDD 5 last columns.

Sample ID	G_z [μm]	G_h	DoC [μm]	V_w [$\frac{mm}{sec}$]	F'_N [$\frac{N}{mm}$]	F'_t [$\frac{N}{mm}$]	P'_w [$\frac{W}{mm}$]	E'_g [$\frac{J}{mm^3}$]	C_f	3D 1[μm] [μm]	2D 1[μm] [μm]	2D Std [μm]	3D 3[μm] [μm]	3D 0.25[μm] [μm]
X1G07	232	Ag	20	20	11.92	2.56	100.58	251.45	0.215	466.4	477.8	43.3	338.8	651.2
X1G07	232	Ag	20	20	11.92	2.56	100.58	251.45	0.215	523.6	541.2	53.0	334.4	1051.6
X1G07	232	Ag	20	20	11.92	2.56	100.58	251.45	0.215	475.2	526.0	78.1	321.2	765.6
X1G07	232	Ag	20	20	11.92	2.56	100.58	251.45	0.215	541.2	582.1	72.6	338.8	937.2
X1G07	232	Ag	20	20	11.92	2.56	100.58	251.45	0.215	536.8	589.3	87.6	338.8	1060.4
X1G07	232	Ag	20	20	11.92	2.56	100.58	251.45	0.215	453.2	488.9	86.5	325.6	721.6
X1G09	232	Ag	20	80	22.28	4.91	199.37	124.60	0.220	475.2	478.0	31.4	343.2	704.0
X1G09	232	Ag	20	80	22.28	4.91	199.37	124.60	0.220	541.2	556.9	48.0	356.4	946.0
X1G09	232	Ag	20	80	22.28	4.91	199.37	124.60	0.220	426.8	428.6	38.3	330.0	563.2
X1G09	232	Ag	20	80	22.28	4.91	199.37	124.60	0.220	488.4	448.7	120.4	343.2	721.6
X1G09	232	Ag	20	80	22.28	4.91	199.37	124.60	0.220	479.6	402.5	184.6	343.2	756.8
X1G09	232	Ag	20	80	22.28	4.91	199.37	124.60	0.220	453.2	459.8	35.6	352.0	660.0
X2G04	232	Bk	20	20	12.51	2.63	101.35	253.38	0.210	624.8	618.3	22.5	431.2	972.4
X2G04	232	Bk	20	20	12.51	2.63	101.35	253.38	0.210	624.8	618.5	28.3	413.6	998.8
X2G04	232	Bk	20	20	12.51	2.63	101.35	253.38	0.210	585.2	600.0	54.8	396.0	950.4

Table A.1: Continued.

Sample ID	G_z [μm]	G_h	DoC [μm]	V_w [$\frac{mm}{sec}$]	F'_N [$\frac{N}{mm}$]	F'_t [$\frac{N}{mm}$]	P'_w [$\frac{W}{mm}$]	E'_g [$\frac{J}{mm^3}$]	C_f	3D 1[μm] [μm]	2D 1[μm] [μm]	2D Std [μm]	3D 3[μm] [μm]	3D 0.25[μm] [μm]
X2G04	232	Bk	20	20	12.51	2.63	101.35	253.38	0.210	598.4	602.5	49.6	391.6	866.8
X2G04	232	Bk	20	20	12.51	2.63	101.35	253.38	0.210	598.4	619.9	52.6	413.6	946.0
X2G04	232	Bk	20	20	12.51	2.63	101.35	253.38	0.210	616.0	589.0	100.4	444.4	937.2
X1G06	232	Bk	50	20	28.79	4.99	196.54	196.54	0.173	800.8	805.2	49.5	576.4	1144.0
X1G06	232	Bk	50	20	28.79	4.99	196.54	196.54	0.173	712.8	719.4	49.3	501.6	919.6
X1G06	232	Bk	50	20	28.79	4.99	196.54	196.54	0.173	642.4	654.6	53.7	462.0	968.0
X1G06	232	Bk	50	20	28.79	4.99	196.54	196.54	0.173	752.4	723.0	49.8	501.6	1047.2
X1G06	232	Bk	50	20	28.79	4.99	196.54	196.54	0.173	752.4	761.9	40.9	514.8	1069.2
X1G06	232	Bk	50	20	28.79	4.99	196.54	196.54	0.173	660.0	647.0	62.5	470.8	998.8
X2G05	232	Bk	20	80	25.74	4.77	188.05	117.53	0.185	598.4	593.9	36.4	462.0	787.6
X2G05	232	Bk	20	80	25.74	4.77	188.05	117.53	0.185	479.6	485.9	45.7	382.8	611.6
X2G05	232	Bk	20	80	25.74	4.77	188.05	117.53	0.185	510.4	517.9	36.8	409.2	594.0
X2G05	232	Bk	20	80	25.74	4.77	188.05	117.53	0.185	580.8	530.2	119.1	435.6	840.4
X2G05	232	Bk	20	80	25.74	4.77	188.05	117.53	0.185	501.6	499.3	54.9	396.0	646.8
X2G05	232	Bk	20	80	25.74	4.77	188.05	117.53	0.185	585.2	587.5	33.7	426.8	836.0
X1G01	54	Bk	20	20	7.40	1.80	71.04	177.60	0.245	189.2	205.5	40.9	136.4	277.2

Table A.1: Continued.

Sample ID	G_z [μm]	G_h	DoC [μm]	V_w [$\frac{mm}{sec}$]	F'_N [$\frac{N}{mm}$]	F'_t [$\frac{N}{mm}$]	P'_w [$\frac{W}{mm}$]	E'_g [$\frac{J}{mm^3}$]	C_f	3D 1[μm] [μm]	2D 1[μm] [μm]	2D Std [μm]	3D 3[μm] [μm]	3D 0.25[μm] [μm]
X1G01	54	Bk	20	20	7.40	1.80	71.04	177.60	0.245	220.0	239.8	49.0	127.6	572.0
X1G01	54	Bk	20	20	7.40	1.80	71.04	177.60	0.245	224.4	242.0	53.5	136.4	673.2
X1G01	54	Bk	20	20	7.40	1.80	71.04	177.60	0.245	224.4	228.8	40.1	145.2	563.2
X1G01	54	Bk	20	20	7.40	1.80	71.04	177.60	0.245	206.8	206.0	16.2	136.4	598.4
X1G01	54	Bk	20	20	7.40	1.80	71.04	177.60	0.245	198.0	238.0	72.6	132.0	510.4
X2G07	54	Bk	20	80	9.64	2.72	106.03	66.27	0.282	277.2	298.7	56.4	198.0	761.2
X2G07	54	Bk	20	80	9.64	2.72	106.03	66.27	0.282	281.6	300.3	71.8	193.6	840.4
X2G07	54	Bk	20	80	9.64	2.72	106.03	66.27	0.282	211.2	207.1	19.1	136.4	514.8
X2G07	54	Bk	20	80	9.64	2.72	106.03	66.27	0.282	202.4	199.5	17.9	127.6	501.6
X2G07	54	Bk	20	80	9.64	2.72	106.03	66.27	0.282	259.6	273.6	46.4	180.4	598.4
X2G07	54	Bk	20	80	9.64	2.72	106.03	66.27	0.282	220.0	217.4	17.0	145.2	501.6
X2G08	54	Bk	50	20	10.21	2.84	108.65	108.65	0.278	176.0	160.5	19.7	101.2	466.4
X2G08	54	Bk	50	20	10.21	2.84	108.65	108.65	0.278	180.4	162.9	12.2	145.2	462.0
X2G08	54	Bk	50	20	10.21	2.84	108.65	108.65	0.278	167.2	160.1	14.3	123.2	479.6
X2G08	54	Bk	50	20	10.21	2.84	108.65	108.65	0.278	167.2	176.0	46.2	127.6	374.0
X2G08	54	Bk	50	20	10.21	2.84	108.65	108.65	0.278	180.4	199.9	55.4	158.4	475.2

Table A.1: Continued.

Sample ID	G_z [μm]	G_h	DoC [μm]	V_w [$\frac{mm}{sec}$]	F'_N [$\frac{N}{mm}$]	F'_t [$\frac{N}{mm}$]	P'_w [$\frac{W}{mm}$]	E'_g [$\frac{J}{mm^3}$]	C_f	3D 1[μm] [μm]	2D 1[μm] [μm]	2D Std [μm]	3D 3[μm] [μm]	3D 0.25[μm] [μm]
X2G08	54	Bk	50	20	10.21	2.84	108.65	108.65	0.278	145.2	150.8	32.6	101.2	281.6
X2G10	54	Ag	20	80	8.72	2.57	85.12	53.20	0.295	224.4	210.8	23.0	154.0	514.8
X2G10	54	Ag	20	80	8.72	2.57	85.12	53.20	0.295	211.2	206.4	16.2	158.4	286.0
X2G10	54	Ag	20	80	8.72	2.57	85.12	53.20	0.295	211.2	204.4	16.6	162.8	400.4
X2G10	54	Ag	20	80	8.72	2.57	85.12	53.20	0.295	158.4	93.6	60.9	61.6	255.2
X2G10	54	Ag	20	80	8.72	2.57	85.12	53.20	0.295	154.0	139.9	35.2	110.0	281.6
X2G10	54	Ag	20	80	8.72	2.57	85.12	53.20	0.295	158.4	157.0	16.8	105.6	308.0
X2G12	54	Ag	20	20	5.94	1.40	56.31	140.77	0.235	189.2	111.9	75.3	105.6	334.4
X2G12	54	Ag	20	20	5.94	1.40	56.31	140.77	0.235	180.4	146.6	51.7	70.4	409.2
X2G12	54	Ag	20	20	5.94	1.40	56.31	140.77	0.235	189.2	160.4	46.6	79.2	448.8
X2G12	54	Ag	20	20	5.94	1.40	56.31	140.77	0.235	180.4	145.6	53.7	123.2	374.0
X2G12	54	Ag	20	20	5.94	1.40	56.31	140.77	0.235	189.2	156.1	47.9	140.8	325.6
X2G12	54	Ag	20	20	5.94	1.40	56.31	140.77	0.235	176.0	107.7	65.0	123.2	470.8
X2G13	54	Ag	50	20	9.70	2.67	100.83	100.83	0.275	202.4	162.0	45.1	88.0	444.4
X2G13	54	Ag	50	20	9.70	2.67	100.83	100.83	0.275	184.8	155.5	47.0	162.8	422.4
X2G13	54	Ag	50	20	9.70	2.67	100.83	100.83	0.275	176.0	171.9	18.1	132.0	316.8

Table A.1: Continued.

Sample ID	G_z [μm]	G_h	DoC [μm]	V_w [$\frac{mm}{sec}$]	F'_N [$\frac{N}{mm}$]	F'_t [$\frac{N}{mm}$]	P'_w [$\frac{W}{mm}$]	E'_g [$\frac{J}{mm^3}$]	C_f	3D 1[μm] [μm]	2D 1[μm] [μm]	2D Std [μm]	3D 3[μm] [μm]	3D 0.25[μm] [μm]
X2G13	54	Ag	50	20	9.70	2.67	100.83	100.83	0.275	189.2	178.2	23.5	123.2	418.0
X2G13	54	Ag	50	20	9.70	2.67	100.83	100.83	0.275	162.8	156.5	16.6	118.8	206.8
X2G13	54	Ag	50	20	9.70	2.67	100.83	100.83	0.275	167.2	152.5	24.1	105.6	316.8
X1G08	232	Ag	50	20	10.21	2.84	108.65	108.65	0.278	532.4	541.3	48.7	374.0	770.0
X1G08	232	Ag	50	20	10.21	2.84	108.65	108.65	0.278	558.8	571.8	48.7	382.8	871.2
X1G08	232	Ag	50	20	10.21	2.84	108.65	108.65	0.278	580.8	610.1	56.6	400.4	1007.6
X1G08	232	Ag	50	20	10.21	2.84	108.65	108.65	0.278	514.8	534.0	49.3	356.4	880.0
X1G08	232	Ag	50	20	10.21	2.84	108.65	108.65	0.278	594.0	614.5	49.2	409.2	928.4
X1G08	232	Ag	50	20	10.21	2.84	108.65	108.65	0.278	620.4	627.6	38.5	404.8	968.0
X2G02	232	Ag	50	80	32.00	7.37	285.78	71.45	0.230	616.0	614.4	32.1	479.6	783.2
X2G02	232	Ag	50	80	32.00	7.37	285.78	71.45	0.230	629.2	624.5	32.9	457.6	827.2
X2G02	232	Ag	50	80	32.00	7.37	285.78	71.45	0.230	616.0	614.0	32.5	453.2	866.8
X2G02	232	Ag	50	80	32.00	7.37	285.78	71.45	0.230	620.4	608.2	40.6	444.4	902.0
X2G02	232	Ag	50	80	32.00	7.37	285.78	71.45	0.230	629.2	632.6	39.3	444.4	902.0
X2G02	232	Ag	50	80	32.00	7.37	285.78	71.45	0.230	646.8	646.4	23.3	484.0	1007.6
X2G06	232	Bk	50	80	50.05	9.02	344.98	86.25	0.181	611.6	611.2	46.8	466.4	862.4

Table A.1: Continued.

Sample ID	G_z [μm]	G_h	DoC [μm]	V_w [$\frac{mm}{sec}$]	F'_N [$\frac{N}{mm}$]	F'_t [$\frac{N}{mm}$]	P'_w [$\frac{W}{mm}$]	E'_g [$\frac{J}{mm^3}$]	C_f	3D 1[μm] [μm]	2D 1[μm] [μm]	2D Std [μm]	3D 3[μm] [μm]	3D 0.25[μm] [μm]
X2G06	232	Bk	50	80	50.05	9.02	344.98	86.25	0.181	677.6	660.8	59.9	479.6	928.4
X2G06	232	Bk	50	80	50.05	9.02	344.98	86.25	0.181	646.8	679.9	55.4	523.6	849.2
X2G06	232	Bk	50	80	50.05	9.02	344.98	86.25	0.181	629.2	635.0	37.7	488.4	734.8
X2G06	232	Bk	50	80	50.05	9.02	344.98	86.25	0.181	638.0	648.4	51.3	479.6	853.6
X2G06	232	Bk	50	80	50.05	9.02	344.98	86.25	0.181	638.0	633.5	55.3	501.6	818.4
X2G09	54	Bk	50	80	19.67	5.93	239.25	59.81	0.302	264.0	270.6	6.1	206.8	457.6
X2G09	54	Bk	50	80	19.67	5.93	239.25	59.81	0.302	277.2	283.8	12.4	206.8	514.8
X2G09	54	Bk	50	80	19.67	5.93	239.25	59.81	0.302	215.6	240.7	2.0	132.0	528.0
X2G09	54	Bk	50	80	19.67	5.93	239.25	59.81	0.302	198.0	242.1	0.7	123.2	488.4
X2G09	54	Bk	50	80	19.67	5.93	239.25	59.81	0.302	198.0	197.4	10.9	132.0	444.4
X2G09	54	Bk	50	80	19.67	5.93	239.25	59.81	0.302	286.0	282.4	18.4	215.6	620.4
X2G14	54	Ag	50	80	22.96	7.35	293.54	73.38	0.320	233.2	238.8	11.1	171.6	334.4
X2G14	54	Ag	50	80	22.96	7.35	293.54	73.38	0.320	255.2	256.8	18.7	189.2	391.6
X2G14	54	Ag	50	80	22.96	7.35	293.54	73.38	0.320	176.0	174.1	33.5	127.6	246.4
X2G14	54	Ag	50	80	22.96	7.35	293.54	73.38	0.320	308.0	172.8	175.0	140.8	523.6
X2G14	54	Ag	50	80	22.96	7.35	293.54	73.38	0.320	259.6	284.9	94.4	176.0	532.4

Table A.1: Continued.

Sample ID	G_z [μm]	G_h	DoC [μm]	V_w [$\frac{mm}{sec}$]	F'_N [$\frac{N}{mm}$]	F'_t [$\frac{N}{mm}$]	P'_w [$\frac{W}{mm}$]	E'_g [$\frac{J}{mm^3}$]	C_f	3D 1[μm] [μm]	2D 1[μm] [μm]	2D Std [μm]	3D 3[μm] [μm]	3D 0.25[μm] [μm]
X2G14	54	Ag	50	80	22.96	7.35	293.54	73.38	0.320	338.8	347.1	180.0	176.0	699.6
X1G44	232	Ag	20	20	12.98	2.74	107.20	268.00	0.211	418.0	413.5	24.2	303.6	602.8
X1G44	232	Ag	20	20	12.98	2.74	107.20	268.00	0.211	413.6	406.7	34.0	308.0	585.2
X1G44	232	Ag	20	20	12.98	2.74	107.20	268.00	0.211	418.0	417.3	33.6	325.6	594.0
X1G44	232	Ag	20	20	12.98	2.74	107.20	268.00	0.211	431.2	431.7	25.8	321.2	585.2
X1G44	232	Ag	20	20	12.98	2.74	107.20	268.00	0.211	422.4	416.8	30.6	312.4	576.4
X1G44	232	Ag	20	20	12.98	2.74	107.20	268.00	0.211	413.6	406.3	32.9	303.6	576.4
X1G56	232	Ag	20	80	17.25	3.92	157.56	98.48	0.227	466.4	470.9	27.3	347.6	611.6
X1G56	232	Ag	20	80	17.25	3.92	157.56	98.48	0.227	444.4	437.1	33.1	343.2	594.0
X1G56	232	Ag	20	80	17.25	3.92	157.56	98.48	0.227	462.0	463.7	34.5	334.4	598.4
X1G56	232	Ag	20	80	17.25	3.92	157.56	98.48	0.227	470.8	467.9	29.2	347.6	607.2
X1G56	232	Ag	20	80	17.25	3.92	157.56	98.48	0.227	453.2	428.1	75.3	325.6	611.6
X1G56	232	Ag	20	80	17.25	3.92	157.56	98.48	0.227	462.0	455.2	26.0	347.6	629.2
X1G11	232	Bk	20	20	16.98	3.53	142.77	356.92	0.208	479.6	476.3	39.6	360.8	624.8
X1G11	232	Bk	20	20	16.98	3.53	142.77	356.92	0.208	462.0	446.8	57.9	356.4	620.4
X1G11	232	Bk	20	20	16.98	3.53	142.77	356.92	0.208	422.4	430.1	42.6	308.0	602.8

Table A.1: Continued.

Sample ID	G_z [μm]	G_h	DoC [μm]	V_w [$\frac{mm}{sec}$]	F'_N [$\frac{N}{mm}$]	F'_t [$\frac{N}{mm}$]	P'_w [$\frac{W}{mm}$]	E'_g [$\frac{J}{mm^3}$]	C_f	3D 1[μm] [μm]	2D 1[μm] [μm]	2D Std [μm]	3D 3[μm] [μm]	3D 0.25[μm] [μm]
X1G11	232	Bk	20	20	16.98	3.53	142.77	356.92	0.208	448.8	452.1	32.7	316.8	629.2
X1G11	232	Bk	20	20	16.98	3.53	142.77	356.92	0.208	466.4	447.2	62.7	360.8	616.0
X1G11	232	Bk	20	20	16.98	3.53	142.77	356.92	0.208	444.4	452.6	53.7	321.2	611.6
X1G10	232	Bk	50	20	37.90	6.11	240.90	240.90	0.161	611.6	598.5	55.4	466.4	748.0
X1G10	232	Bk	50	20	37.90	6.11	240.90	240.90	0.161	620.4	616.3	54.4	492.8	734.8
X1G10	232	Bk	50	20	37.90	6.11	240.90	240.90	0.161	624.8	617.4	47.1	470.8	748.0
X1G10	232	Bk	50	20	37.90	6.11	240.90	240.90	0.161	585.2	592.3	35.0	470.8	717.2
X1G10	232	Bk	50	20	37.90	6.11	240.90	240.90	0.161	585.2	597.1	37.6	466.4	752.4
X1G10	232	Bk	50	20	37.90	6.11	240.90	240.90	0.161	607.2	606.6	41.2	475.2	721.6
X2G50	232	Bk	20	80	34.96	6.00	241.07	150.67	0.172	554.4	548.2	36.5	422.4	660.0
X2G50	232	Bk	20	80	34.96	6.00	241.07	150.67	0.172	554.4	547.5	52.1	422.4	695.2
X2G50	232	Bk	20	80	34.96	6.00	241.07	150.67	0.172	554.4	547.7	38.7	422.4	660.0
X2G50	232	Bk	20	80	34.96	6.00	241.07	150.67	0.172	558.8	545.6	36.8	440.0	655.6
X2G50	232	Bk	20	80	34.96	6.00	241.07	150.67	0.172	580.8	578.3	30.3	466.4	708.4
X2G50	232	Bk	20	80	34.96	6.00	241.07	150.67	0.172	541.2	515.1	44.8	409.2	712.8
X1G16	54	Bk	20	20	7.52	1.70	67.77	169.43	0.225	145.2	139.2	11.8	118.8	294.8

Table A.1: Continued.

Sample ID	G_z [μm]	G_h	DoC [μm]	V_w [$\frac{mm}{sec}$]	F'_N [$\frac{N}{mm}$]	F'_t [$\frac{N}{mm}$]	P'_w [$\frac{W}{mm}$]	E'_g [$\frac{J}{mm^3}$]	C_f	3D 1[μm] [μm]	2D 1[μm] [μm]	2D Std [μm]	3D 3[μm] [μm]	3D 0.25[μm] [μm]
X1G16	54	Bk	20	20	7.52	1.70	67.77	169.43	0.225	149.6	144.0	14.4	101.2	316.8
X1G16	54	Bk	20	20	7.52	1.70	67.77	169.43	0.225	184.8	137.8	51.0	74.8	334.4
X1G16	54	Bk	20	20	7.52	1.70	67.77	169.43	0.225	176.0	175.7	14.9	127.6	325.6
X1G16	54	Bk	20	20	7.52	1.70	67.77	169.43	0.225	154.0	152.3	14.7	136.4	281.6
X1G16	54	Bk	20	20	7.52	1.70	67.77	169.43	0.225	180.4	176.7	14.9	123.2	347.6
X1G14	54	Bk	20	80	10.63	2.74	108.24	67.65	0.258	184.8	182.2	14.6	123.2	347.6
X1G14	54	Bk	20	80	10.63	2.74	108.24	67.65	0.258	180.4	178.3	12.9	127.6	343.2
X1G14	54	Bk	20	80	10.63	2.74	108.24	67.65	0.258	189.2	181.7	13.6	145.2	382.8
X1G14	54	Bk	20	80	10.63	2.74	108.24	67.65	0.258	171.6	168.4	14.1	118.8	321.2
X1G14	54	Bk	20	80	10.63	2.74	108.24	67.65	0.258	184.8	179.4	18.0	140.8	343.2
X1G14	54	Bk	20	80	10.63	2.74	108.24	67.65	0.258	171.6	166.7	14.0	149.6	338.8
X1G15	54	Bk	50	20	11.86	2.91	113.51	113.51	0.245	176.0	174.6	13.9	127.6	347.6
X1G15	54	Bk	50	20	11.86	2.91	113.51	113.51	0.245	184.8	133.3	44.5	136.4	352.0
X1G15	54	Bk	50	20	11.86	2.91	113.51	113.51	0.245	180.4	99.5	61.1	123.2	347.6
X1G15	54	Bk	50	20	11.86	2.91	113.51	113.51	0.245	180.4	166.7	12.8	127.6	343.2
X1G15	54	Bk	50	20	11.86	2.91	113.51	113.51	0.245	167.2	155.9	15.0	123.2	325.6

Table A.1: Continued.

Sample ID	G_z [μm]	G_h	DoC [μm]	V_w [$\frac{mm}{sec}$]	F'_N [$\frac{N}{mm}$]	F'_t [$\frac{N}{mm}$]	P'_w [$\frac{W}{mm}$]	E'_g [$\frac{J}{mm^3}$]	C_f	3D 1[μm] [μm]	2D 1[μm] [μm]	2D Std [μm]	3D 3[μm] [μm]	3D 0.25[μm] [μm]
X1G15	54	Bk	50	20	11.86	2.91	113.51	113.51	0.245	176.0	162.6	13.6	123.2	325.6
X1G50	54	Ag	20	80	7.64	2.11	84.23	52.64	0.276	149.6	145.7	13.9	101.2	281.6
X1G50	54	Ag	20	80	7.64	2.11	84.23	52.64	0.276	154.0	150.4	11.3	132.0	268.4
X1G50	54	Ag	20	80	7.64	2.11	84.23	52.64	0.276	162.8	158.1	12.5	123.2	338.8
X1G50	54	Ag	20	80	7.64	2.11	84.23	52.64	0.276	162.8	158.0	10.2	105.6	338.8
X1G50	54	Ag	20	80	7.64	2.11	84.23	52.64	0.276	158.4	156.3	12.9	110.0	294.8
X1G50	54	Ag	20	80	7.64	2.11	84.23	52.64	0.276	162.8	157.0	11.9	105.6	338.8
X1G51	54	Ag	20	20	6.19	1.38	55.16	137.90	0.222	158.4	156.4	16.9	110.0	246.4
X1G51	54	Ag	20	20	6.19	1.38	55.16	137.90	0.222	149.6	148.2	16.8	132.0	189.2
X1G51	54	Ag	20	20	6.19	1.38	55.16	137.90	0.222	162.8	122.7	36.0	114.4	316.8
X1G51	54	Ag	20	20	6.19	1.38	55.16	137.90	0.222	154.0	142.3	35.3	105.6	299.2
X1G51	54	Ag	20	20	6.19	1.38	55.16	137.90	0.222	136.4	132.8	20.6	101.2	299.2
X1G51	54	Ag	20	20	6.19	1.38	55.16	137.90	0.222	154.0	163.0	31.0	114.4	206.8
X1G58	54	Ag	50	20	11.14	2.77	107.89	107.89	0.249	154.0	152.8	9.8	132.0	294.8
X1G58	54	Ag	50	20	11.14	2.77	107.89	107.89	0.249	154.0	145.7	14.1	105.6	299.2
X1G58	54	Ag	50	20	11.14	2.77	107.89	107.89	0.249	158.4	151.3	12.1	118.8	316.8

Table A.1: Continued.

Sample ID	G_z [μm]	G_h	DoC [μm]	V_w [$\frac{mm}{sec}$]	F'_N [$\frac{N}{mm}$]	F'_t [$\frac{N}{mm}$]	P'_w [$\frac{W}{mm}$]	E'_g [$\frac{J}{mm^3}$]	C_f	3D 1[μm] [μm]	2D 1[μm] [μm]	2D Std [μm]	3D 3[μm] [μm]	3D 0.25[μm] [μm]
X1G58	54	Ag	50	20	11.14	2.77	107.89	107.89	0.249	145.2	142.4	9.4	123.2	294.8
X1G58	54	Ag	50	20	11.14	2.77	107.89	107.89	0.249	154.0	147.6	13.2	114.4	321.2
X1G58	54	Ag	50	20	11.14	2.77	107.89	107.89	0.249	149.6	140.9	11.1	105.6	290.4
X1G19	232	Ag	50	20	19.79	4.38	169.58	169.58	0.222	462.0	468.9	25.5	334.4	646.8
X1G19	232	Ag	50	20	19.79	4.38	169.58	169.58	0.222	470.8	462.4	30.0	343.2	646.8
X1G19	232	Ag	50	20	19.79	4.38	169.58	169.58	0.222	431.2	428.9	39.2	325.6	616.0
X1G19	232	Ag	50	20	19.79	4.38	169.58	169.58	0.222	457.6	448.9	30.9	330.0	616.0
X1G19	232	Ag	50	20	19.79	4.38	169.58	169.58	0.222	431.2	431.9	35.7	321.2	624.8
X1G19	232	Ag	50	20	19.79	4.38	169.58	169.58	0.222	484.0	488.7	38.7	356.4	642.4
X1G54	232	Ag	50	80	37.05	8.60	343.22	85.80	0.232	479.6	479.9	30.3	365.2	629.2
X1G54	232	Ag	50	80	37.05	8.60	343.22	85.80	0.232	488.4	482.9	40.4	378.4	638.0
X1G54	232	Ag	50	80	37.05	8.60	343.22	85.80	0.232	475.2	472.8	34.7	83.6	633.6
X1G54	232	Ag	50	80	37.05	8.60	343.22	85.80	0.232	497.2	492.3	40.0	391.6	642.4
X1G54	232	Ag	50	80	37.05	8.60	343.22	85.80	0.232	501.6	501.5	34.8	400.4	651.2
X1G54	232	Ag	50	80	37.05	8.60	343.22	85.80	0.232	497.2	503.2	29.5	391.6	633.6
X2G51	232	Bk	50	80	56.64	9.46	358.95	89.74	0.167	585.2	586.5	38.4	470.8	712.8

Table A.1: Continued.

Sample ID	G_z [μm]	G_h	DoC [μm]	V_w [$\frac{mm}{sec}$]	F'_N [$\frac{N}{mm}$]	F'_t [$\frac{N}{mm}$]	P'_w [$\frac{W}{mm}$]	E'_g [$\frac{J}{mm^3}$]	C_f	3D 1[μm] [μm]	2D 1[μm] [μm]	2D Std [μm]	3D 3[μm] [μm]	3D 0.25[μm] [μm]
X2G51	232	Bk	50	80	56.64	9.46	358.95	89.74	0.167	585.2	581.5	36.5	462.0	699.6
X2G51	232	Bk	50	80	56.64	9.46	358.95	89.74	0.167	576.4	591.0	41.5	466.4	721.6
X2G51	232	Bk	50	80	56.64	9.46	358.95	89.74	0.167	585.2	584.6	40.7	462.0	708.4
X2G51	232	Bk	50	80	56.64	9.46	358.95	89.74	0.167	558.8	509.8	132.5	66.0	682.0
X2G51	232	Bk	50	80	56.64	9.46	358.95	89.74	0.167	567.6	582.8	40.5	435.6	708.4
X1G13	54	Bk	50	80	16.16	4.82	193.79	48.45	0.298	167.2	166.5	11.8	123.2	338.8
X1G13	54	Bk	50	80	16.16	4.82	193.79	48.45	0.298	162.8	162.7	12.4	114.4	294.8
X1G13	54	Bk	50	80	16.16	4.82	193.79	48.45	0.298	176.0	171.2	16.8	123.2	281.6
X1G13	54	Bk	50	80	16.16	4.82	193.79	48.45	0.298	158.4	169.1	28.5	105.6	308.0
X1G13	54	Bk	50	80	16.16	4.82	193.79	48.45	0.298	176.0	172.8	20.0	114.4	374.0
X1G13	54	Bk	50	80	16.16	4.82	193.79	48.45	0.298	167.2	166.4	19.7	110.0	290.4
X1G55	54	Ag	50	80	20.66	6.39	261.79	65.45	0.309	145.2	93.7	24.1	70.4	176.0
X1G55	54	Ag	50	80	20.66	6.39	261.79	65.45	0.309	114.4	106.4	6.5	101.2	132.0
X1G55	54	Ag	50	80	20.66	6.39	261.79	65.45	0.309	167.2	163.6	14.1	105.6	347.6
X1G55	54	Ag	50	80	20.66	6.39	261.79	65.45	0.309	167.2	157.0	16.2	132.0	343.2
X1G55	54	Ag	50	80	20.66	6.39	261.79	65.45	0.309	167.2	156.1	13.7	127.6	347.6

Table A.1: Continued.

Sample ID	G_z [μm]	G_h	DoC [μm]	V_w [$\frac{mm}{sec}$]	F'_N [$\frac{N}{mm}$]	F'_t [$\frac{N}{mm}$]	P'_w [$\frac{W}{mm}$]	E'_g [$\frac{J}{mm^3}$]	C_f	3D 1[μm] [μm]	2D 1[μm] [μm]	2D Std [μm]	3D 3[μm] [μm]	3D 0.25[μm] [μm]
X1G55	54	Ag	50	80	20.66	6.39	261.79	65.45	0.309	171.6	164.1	11.8	140.8	352.0

Table A.2: Complete set of tests for worn conditions. PDD 5 last columns.

Sample ID	G_z [μm]	G_h	DoC [μm]	V_w [$\frac{mm}{sec}$]	F'_N [$\frac{N}{mm}$]	F'_t [$\frac{N}{mm}$]	P'_w [$\frac{W}{mm}$]	E'_g [$\frac{J}{mm^3}$]	C_f	3D 1[μm] [μm]	2D 1[μm] [μm]	2D Std [μm]	3D 3[μm] [μm]	3D 0.25[μm] [μm]
X2G78	232	Ag	20	20	18.45	4.61	180.22	450.55	0.250	378.4	376.4	36.6	272.8	563.2
X2G78	232	Ag	20	20	18.45	4.61	180.22	450.55	0.250	365.2	358.6	21.0	264.0	523.6
X2G78	232	Ag	20	20	18.45	4.61	180.22	450.55	0.250	352.0	347.5	28.6	233.2	554.4
X2G78	232	Ag	20	20	18.45	4.61	180.22	450.55	0.250	338.8	340.2	24.7	237.6	541.2
X2G78	232	Ag	20	20	18.45	4.61	180.22	450.55	0.250	365.2	365.4	27.0	272.8	536.8
X2G78	232	Ag	20	20	18.45	4.61	180.22	450.55	0.250	338.8	341.7	23.4	242.0	541.2
X2G76	232	Ag	20	80	40.63	9.38	385.24	240.78	0.231	391.6	398.8	44.0	281.6	545.6
X2G76	232	Ag	20	80	40.63	9.38	385.24	240.78	0.231	413.6	412.6	44.4	290.4	550.0
X2G76	232	Ag	20	80	40.63	9.38	385.24	240.78	0.231	391.6	390.3	45.0	290.4	506.0
X2G76	232	Ag	20	80	40.63	9.38	385.24	240.78	0.231	347.6	346.4	37.7	250.8	501.6
X2G76	232	Ag	20	80	40.63	9.38	385.24	240.78	0.231	404.8	414.3	37.3	294.8	550.0
X2G76	232	Ag	20	80	40.63	9.38	385.24	240.78	0.231	413.6	408.2	33.2	272.8	545.6
X2G57	232	Bk	20	20	17.61	4.40	172.86	432.15	0.250	312.4	311.5	16.9	220.0	435.6
X2G57	232	Bk	20	20	17.61	4.40	172.86	432.15	0.250	303.6	306.0	21.8	215.6	448.8
X2G57	232	Bk	20	20	17.61	4.40	172.86	432.15	0.250	303.6	250.5	89.4	211.2	492.8

Table A.2: Continued.

Sample ID	G_z [μm]	G_h	DoC [μm]	V_w [$\frac{mm}{sec}$]	F'_N [$\frac{N}{mm}$]	F'_t [$\frac{N}{mm}$]	P'_w [$\frac{W}{mm}$]	E'_g [$\frac{J}{mm^3}$]	C_f	3D 1[μm] [μm]	2D 1[μm] [μm]	2D Std [μm]	3D 3[μm] [μm]	3D 0.25[μm] [μm]
X2G57	232	Bk	20	20	17.61	4.40	172.86	432.15	0.250	365.2	361.5	25.7	259.6	514.8
X2G57	232	Bk	20	20	17.61	4.40	172.86	432.15	0.250	422.4	414.6	29.4	299.2	558.8
X2G57	232	Bk	20	20	17.61	4.40	172.86	432.15	0.250	435.6	434.5	34.7	312.4	585.2
X2G55	232	Bk	50	20	43.64	7.76	293.37	293.37	0.178	514.8	515.8	44.6	365.2	682.0
X2G55	232	Bk	50	20	43.64	7.76	293.37	293.37	0.178	519.2	506.8	48.2	374.0	668.8
X2G55	232	Bk	50	20	43.64	7.76	293.37	293.37	0.178	506.0	515.8	35.1	338.8	664.4
X2G55	232	Bk	50	20	43.64	7.76	293.37	293.37	0.178	506.0	514.3	47.8	365.2	668.8
X2G55	232	Bk	50	20	43.64	7.76	293.37	293.37	0.178	519.2	519.8	45.9	387.2	677.6
X2G55	232	Bk	50	20	43.64	7.76	293.37	293.37	0.178	448.8	454.7	34.2	312.4	646.8
X2G56	232	Bk	20	80	54.07	9.75	398.60	249.13	0.180	466.4	463.0	31.3	365.2	572.0
X2G56	232	Bk	20	80	54.07	9.75	398.60	249.13	0.180	457.6	439.9	49.9	334.4	589.6
X2G56	232	Bk	20	80	54.07	9.75	398.60	249.13	0.180	413.6	422.1	55.0	312.4	558.8
X2G56	232	Bk	20	80	54.07	9.75	398.60	249.13	0.180	444.4	437.7	44.9	316.8	585.2
X2G56	232	Bk	20	80	54.07	9.75	398.60	249.13	0.180	431.2	431.0	44.4	352.0	567.6
X2G56	232	Bk	20	80	54.07	9.75	398.60	249.13	0.180	453.2	448.7	40.2	338.8	585.2
X2G17	54	Bk	20	20	44.35	12.50	528.12	1320.30	0.282	281.6	274.8	24.1	220.0	466.4

Table A.2: Continued.

Sample ID	G_z [μm]	G_h	DoC [μm]	V_w [$\frac{mm}{sec}$]	F'_N [$\frac{N}{mm}$]	F'_t [$\frac{N}{mm}$]	P'_w [$\frac{W}{mm}$]	E'_g [$\frac{J}{mm^3}$]	C_f	3D 1[μm] [μm]	2D 1[μm] [μm]	2D Std [μm]	3D 3[μm] [μm]	3D 0.25[μm] [μm]
X2G17	54	Bk	20	20	44.35	12.50	528.12	1320.30	0.282	299.2	302.4	25.1	242.0	466.4
X2G17	54	Bk	20	20	44.35	12.50	528.12	1320.30	0.282	308.0	308.0	26.0	237.6	532.4
X2G17	54	Bk	20	20	44.35	12.50	528.12	1320.30	0.282	330.0	332.9	24.3	281.6	501.6
X2G17	54	Bk	20	20	44.35	12.50	528.12	1320.30	0.282	325.6	326.3	19.3	259.6	506.0
X2G17	54	Bk	20	20	44.35	12.50	528.12	1320.30	0.282	334.4	327.9	27.0	242.0	501.6
X2G66	54	Bk	20	80	84.89	17.33	721.46	450.91	0.204	453.2	440.4	29.8	404.8	563.2
X2G66	54	Bk	20	80	84.89	17.33	721.46	450.91	0.204	448.8	439.7	32.5	387.2	580.8
X2G66	54	Bk	20	80	84.89	17.33	721.46	450.91	0.204	453.2	449.8	31.7	369.6	563.2
X2G66	54	Bk	20	80	84.89	17.33	721.46	450.91	0.204	431.2	429.5	42.1	330.0	550.0
X2G66	54	Bk	20	80	84.89	17.33	721.46	450.91	0.204	462.0	456.6	32.7	343.2	589.6
X2G66	54	Bk	20	80	84.89	17.33	721.46	450.91	0.204	440.0	438.6	29.0	334.4	607.2
X2G72	54	Bk	50	20	66.86	16.73	736.22	736.22	0.250	453.2	468.2	42.0	294.8	655.6
X2G72	54	Bk	50	20	66.86	16.73	736.22	736.22	0.250	492.8	504.1	33.9	334.4	646.8
X2G72	54	Bk	50	20	66.86	16.73	736.22	736.22	0.250	479.6	491.7	41.5	330.0	651.2
X2G72	54	Bk	50	20	66.86	16.73	736.22	736.22	0.250	484.0	487.7	31.8	343.2	668.8
X2G72	54	Bk	50	20	66.86	16.73	736.22	736.22	0.250	492.8	507.8	37.1	334.4	655.6

Table A.2: Continued.

Sample ID	G_z [μm]	G_h	DoC [μm]	V_w [$\frac{mm}{sec}$]	F'_N [$\frac{N}{mm}$]	F'_t [$\frac{N}{mm}$]	P'_w [$\frac{W}{mm}$]	E'_g [$\frac{J}{mm^3}$]	C_f	3D 1[μm] [μm]	2D 1[μm] [μm]	2D Std [μm]	3D 3[μm] [μm]	3D 0.25[μm] [μm]
X2G72	54	Bk	50	20	66.86	16.73	736.22	736.22	0.250	475.2	478.4	42.0	325.6	655.6
X2G68	54	Ag	20	80	47.38	12.93	542.76	339.23	0.273	303.6	304.1	43.8	202.4	444.4
X2G68	54	Ag	20	80	47.38	12.93	542.76	339.23	0.273	255.2	258.6	24.9	184.8	387.2
X2G68	54	Ag	20	80	47.38	12.93	542.76	339.23	0.273	250.8	248.9	23.1	167.2	391.6
X2G68	54	Ag	20	80	47.38	12.93	542.76	339.23	0.273	259.6	253.8	20.8	171.6	391.6
X2G68	54	Ag	20	80	47.38	12.93	542.76	339.23	0.273	299.2	301.3	34.9	215.6	453.2
X2G68	54	Ag	20	80	47.38	12.93	542.76	339.23	0.273	259.6	261.8	23.4	180.4	396.0
X2G67	54	Ag	20	20	34.06	10.07	413.36	1033.40	0.296	224.4	239.4	17.4	149.6	396.0
X2G67	54	Ag	20	20	34.06	10.07	413.36	1033.40	0.296	215.6	226.2	12.7	136.4	422.4
X2G67	54	Ag	20	20	34.06	10.07	413.36	1033.40	0.296	237.6	243.8	15.1	176.0	409.2
X2G67	54	Ag	20	20	34.06	10.07	413.36	1033.40	0.296	255.2	257.5	19.3	167.2	435.6
X2G67	54	Ag	20	20	34.06	10.07	413.36	1033.40	0.296	290.4	286.3	17.2	162.8	506.0
X2G67	54	Ag	20	20	34.06	10.07	413.36	1033.40	0.296	242.0	243.6	13.5	180.4	435.6
X2G69	54	Ag	50	20	48.46	13.64	569.74	569.74	0.281	352.0	350.0	21.2	211.2	532.4
X2G69	54	Ag	50	20	48.46	13.64	569.74	569.74	0.281	378.4	373.0	30.3	233.2	576.4
X2G69	54	Ag	50	20	48.46	13.64	569.74	569.74	0.281	347.6	345.1	29.2	206.8	558.8

Table A.2: Continued.

Sample ID	G_z [μm]	G_h	DoC [μm]	V_w [$\frac{mm}{sec}$]	F'_N [$\frac{N}{mm}$]	F'_t [$\frac{N}{mm}$]	P'_w [$\frac{W}{mm}$]	E'_g [$\frac{J}{mm^3}$]	C_f	3D 1[μm] [μm]	2D 1[μm] [μm]	2D Std [μm]	3D 3[μm] [μm]	3D 0.25[μm] [μm]
X2G69	54	Ag	50	20	48.46	13.64	569.74	569.74	0.281	347.6	346.6	26.4	202.4	576.4
X2G69	54	Ag	50	20	48.46	13.64	569.74	569.74	0.281	356.4	345.2	35.2	220.0	550.0
X2G69	54	Ag	50	20	48.46	13.64	569.74	569.74	0.281	369.6	362.6	28.1	228.8	598.4
X2G77	232	Ag	50	20	33.41	7.04	295.50	295.50	0.211	448.8	437.2	35.7	294.8	642.4
X2G77	232	Ag	50	20	33.41	7.04	295.50	295.50	0.211	426.8	431.8	27.5	308.0	611.6
X2G77	232	Ag	50	20	33.41	7.04	295.50	295.50	0.211	426.8	433.1	27.8	299.2	594.0
X2G77	232	Ag	50	20	33.41	7.04	295.50	295.50	0.211	475.2	475.0	45.5	321.2	655.6
X2G77	232	Ag	50	20	33.41	7.04	295.50	295.50	0.211	444.4	441.7	36.8	299.2	616.0
X2G77	232	Ag	50	20	33.41	7.04	295.50	295.50	0.211	426.8	428.9	34.5	286.0	602.8
X2G81	232	Ag	50	80	74.73	16.61	648.83	162.21	0.222	453.2	464.2	38.0	334.4	624.8
X2G81	232	Ag	50	80	74.73	16.61	648.83	162.21	0.222	466.4	481.5	48.6	334.4	638.0
X2G81	232	Ag	50	80	74.73	16.61	648.83	162.21	0.222	506.0	517.7	49.0	365.2	660.0
X2G81	232	Ag	50	80	74.73	16.61	648.83	162.21	0.222	475.2	415.2	140.7	352.0	660.0
X2G81	232	Ag	50	80	74.73	16.61	648.83	162.21	0.222	466.4	467.7	54.0	360.8	651.2
X2G81	232	Ag	50	80	74.73	16.61	648.83	162.21	0.222	462.0	455.5	36.7	312.4	602.8
X2G54	232	Bk	50	80	89.86	15.31	596.29	149.07	0.170	585.2	603.2	48.1	457.6	686.4

Table A.2: Continued.

Sample ID	G_z [μm]	G_h	DoC [μm]	V_w [$\frac{mm}{sec}$]	F'_N [$\frac{N}{mm}$]	F'_t [$\frac{N}{mm}$]	P'_w [$\frac{W}{mm}$]	E'_g [$\frac{J}{mm^3}$]	C_f	3D 1[μm] [μm]	2D 1[μm] [μm]	2D Std [μm]	3D 3[μm] [μm]	3D 0.25[μm] [μm]
X2G54	232	Bk	50	80	89.86	15.31	596.29	149.07	0.170	563.2	580.8	42.9	448.8	712.8
X2G54	232	Bk	50	80	89.86	15.31	596.29	149.07	0.170	532.4	530.5	39.9	404.8	677.6
X2G54	232	Bk	50	80	89.86	15.31	596.29	149.07	0.170	528.0	522.8	34.5	391.6	668.8
X2G54	232	Bk	50	80	89.86	15.31	596.29	149.07	0.170	554.4	563.8	44.5	404.8	690.8
X2G54	232	Bk	50	80	89.86	15.31	596.29	149.07	0.170	567.6	578.4	47.1	435.6	677.6
X2G65	54	Bk	50	80	154.98	29.02	1101.99	275.50	0.187	558.8	560.7	47.4	413.6	695.2
X2G65	54	Bk	50	80	154.98	29.02	1101.99	275.50	0.187	558.8	557.2	39.2	418.0	664.4
X2G65	54	Bk	50	80	154.98	29.02	1101.99	275.50	0.187	558.8	562.0	46.3	440.0	708.4
X2G65	54	Bk	50	80	154.98	29.02	1101.99	275.50	0.187	572.0	580.2	37.4	435.6	704.0
X2G65	54	Bk	50	80	154.98	29.02	1101.99	275.50	0.187	567.6	589.5	44.5	422.4	690.8
X2G65	54	Bk	50	80	154.98	29.02	1101.99	275.50	0.187	545.6	564.1	46.7	409.2	695.2
X2G64	54	Ag	50	80	166.85	27.77	1034.90	258.73	0.167	563.2	565.2	36.5	440.0	699.6
X2G64	54	Ag	50	80	166.85	27.77	1034.90	258.73	0.167	563.2	563.0	31.5	453.2	655.6
X2G64	54	Ag	50	80	166.85	27.77	1034.90	258.73	0.167	558.8	560.9	39.5	404.8	690.8
X2G64	54	Ag	50	80	166.85	27.77	1034.90	258.73	0.167	563.2	560.6	46.6	418.0	712.8
X2G64	54	Ag	50	80	166.85	27.77	1034.90	258.73	0.167	554.4	550.9	47.2	391.6	695.2

Table A.2: Continued.

Sample ID	G_z [μm]	G_h	DoC [μm]	V_w [$\frac{mm}{sec}$]	F'_N [$\frac{N}{mm}$]	F'_t [$\frac{N}{mm}$]	P'_w [$\frac{W}{mm}$]	E'_g [$\frac{J}{mm^3}$]	C_f	3D 1[μm] [μm]	2D 1[μm] [μm]	2D Std [μm]	3D 3[μm] [μm]	3D 0.25[μm] [μm]
X2G64	54	Ag	50	80	166.85	27.77	1034.90	258.73	0.167	563.2	563.7	66.6	440.0	651.2
X2G86	232	Ag	20	20	17.59	4.43	171.32	428.30	0.252	321.2	329.3	36.8	237.6	470.8
X2G86	232	Ag	20	20	17.59	4.43	171.32	428.30	0.252	334.4	338.9	33.2	237.6	510.4
X2G86	232	Ag	20	20	17.59	4.43	171.32	428.30	0.252	308.0	314.2	83.4	220.0	457.6
X2G86	232	Ag	20	20	17.59	4.43	171.32	428.30	0.252	312.4	311.0	50.6	206.8	484.0
X2G86	232	Ag	20	20	17.59	4.43	171.32	428.30	0.252	308.0	327.8	48.2	215.6	510.4
X2G86	232	Ag	20	20	17.59	4.43	171.32	428.30	0.252	330.0	343.4	46.4	220.0	532.4
X2G85	232	Ag	20	80	40.03	9.43	378.25	236.41	0.236	347.6	349.4	34.8	255.2	475.2
X2G85	232	Ag	20	80	40.03	9.43	378.25	236.41	0.236	343.2	339.4	36.9	250.8	444.4
X2G85	232	Ag	20	80	40.03	9.43	378.25	236.41	0.236	382.8	392.8	34.9	277.2	554.4
X2G85	232	Ag	20	80	40.03	9.43	378.25	236.41	0.236	374.0	371.9	40.0	264.0	506.0
X2G85	232	Ag	20	80	40.03	9.43	378.25	236.41	0.236	369.6	371.4	29.9	268.4	470.8
X2G85	232	Ag	20	80	40.03	9.43	378.25	236.41	0.236	356.4	356.9	23.5	259.6	536.8
X2G61	232	Bk	20	20	16.15	4.02	157.41	393.53	0.249	237.6	246.7	33.0	184.8	290.4
X2G61	232	Bk	20	20	16.15	4.02	157.41	393.53	0.249	250.8	243.6	30.1	198.0	286.0
X2G61	232	Bk	20	20	16.15	4.02	157.41	393.53	0.249	259.6	260.5	30.8	189.2	365.2

Table A.2: Continued.

Sample ID	G_z [μm]	G_h	DoC [μm]	V_w [$\frac{mm}{sec}$]	F'_N [$\frac{N}{mm}$]	F'_t [$\frac{N}{mm}$]	P'_w [$\frac{W}{mm}$]	E'_g [$\frac{J}{mm^3}$]	C_f	3D 1[μm] [μm]	2D 1[μm] [μm]	2D Std [μm]	3D 3[μm] [μm]	3D 0.25[μm] [μm]
X2G61	232	Bk	20	20	16.15	4.02	157.41	393.53	0.249	259.6	263.7	26.5	193.6	338.8
X2G61	232	Bk	20	20	16.15	4.02	157.41	393.53	0.249	268.4	248.2	46.6	189.2	308.0
X2G61	232	Bk	20	20	16.15	4.02	157.41	393.53	0.249	242.0	242.6	29.8	184.8	312.4
X2G59	232	Bk	50	20	41.38	7.63	287.61	287.61	0.184	510.4	463.9	116.2	356.4	695.2
X2G59	232	Bk	50	20	41.38	7.63	287.61	287.61	0.184	484.0	491.8	43.0	365.2	664.4
X2G59	232	Bk	50	20	41.38	7.63	287.61	287.61	0.184	484.0	486.1	32.3	343.2	668.8
X2G59	232	Bk	50	20	41.38	7.63	287.61	287.61	0.184	484.0	483.2	41.6	338.8	664.4
X2G59	232	Bk	50	20	41.38	7.63	287.61	287.61	0.184	484.0	481.9	37.0	347.6	633.6
X2G59	232	Bk	50	20	41.38	7.63	287.61	287.61	0.184	514.8	521.3	37.0	382.8	673.2
X2G60	232	Bk	20	80	50.30	9.64	389.91	243.69	0.191	387.2	388.5	33.7	299.2	470.8
X2G60	232	Bk	20	80	50.30	9.64	389.91	243.69	0.191	409.2	419.1	46.1	294.8	519.2
X2G60	232	Bk	20	80	50.30	9.64	389.91	243.69	0.191	431.2	437.1	52.0	325.6	567.6
X2G60	232	Bk	20	80	50.30	9.64	389.91	243.69	0.191	435.6	433.2	35.2	325.6	567.6
X2G60	232	Bk	20	80	50.30	9.64	389.91	243.69	0.191	409.2	410.8	37.0	286.0	567.6
X2G60	232	Bk	20	80	50.30	9.64	389.91	243.69	0.191	400.4	389.7	33.2	312.4	506.0
X2G15	54	Bk	20	20	25.77	7.09	286.02	715.05	0.275	272.8	218.4	63.8	184.8	462.0

Table A.2: Continued.

Sample ID	G_z [μm]	G_h	DoC [μm]	V_w [$\frac{mm}{sec}$]	F'_N [$\frac{N}{mm}$]	F'_t [$\frac{N}{mm}$]	P'_w [$\frac{W}{mm}$]	E'_g [$\frac{J}{mm^3}$]	C_f	3D 1[μm] [μm]	2D 1[μm] [μm]	2D Std [μm]	3D 3[μm] [μm]	3D 0.25[μm] [μm]
X2G15	54	Bk	20	20	25.77	7.09	286.02	715.05	0.275	268.4	261.5	23.2	198.0	457.6
X2G15	54	Bk	20	20	25.77	7.09	286.02	715.05	0.275	246.4	245.8	23.0	220.0	418.0
X2G15	54	Bk	20	20	25.77	7.09	286.02	715.05	0.275	246.4	251.3	34.0	171.6	448.8
X2G15	54	Bk	20	20	25.77	7.09	286.02	715.05	0.275	250.8	257.7	31.5	167.2	413.6
X2G15	54	Bk	20	20	25.77	7.09	286.02	715.05	0.275	281.6	283.0	31.4	167.2	470.8
X2G16	54	Bk	20	80	39.69	10.06	396.82	248.01	0.254	281.6	281.6	34.9	189.2	426.8
X2G16	54	Bk	20	80	39.69	10.06	396.82	248.01	0.254	286.0	283.9	23.1	220.0	444.4
X2G16	54	Bk	20	80	39.69	10.06	396.82	248.01	0.254	312.4	310.7	28.0	224.4	462.0
X2G16	54	Bk	20	80	39.69	10.06	396.82	248.01	0.254	321.2	323.5	29.1	211.2	470.8
X2G16	54	Bk	20	80	39.69	10.06	396.82	248.01	0.254	303.6	302.2	32.8	211.2	448.8
X2G16	54	Bk	20	80	39.69	10.06	396.82	248.01	0.254	338.8	344.3	35.9	242.0	488.4
X2G73	54	Bk	50	20	69.21	18.77	766.11	766.11	0.271	418.0	415.7	37.2	264.0	598.4
X2G73	54	Bk	50	20	69.21	18.77	766.11	766.11	0.271	422.4	425.9	29.7	259.6	624.8
X2G73	54	Bk	50	20	69.21	18.77	766.11	766.11	0.271	435.6	437.6	35.7	268.4	629.2
X2G73	54	Bk	50	20	69.21	18.77	766.11	766.11	0.271	440.0	439.3	38.9	264.0	629.2
X2G73	54	Bk	50	20	69.21	18.77	766.11	766.11	0.271	409.2	409.7	24.3	272.8	624.8

Table A.2: Continued.

Sample ID	G_z [μm]	G_h	DoC [μm]	V_w [$\frac{mm}{sec}$]	F'_N [$\frac{N}{mm}$]	F'_t [$\frac{N}{mm}$]	P'_w [$\frac{W}{mm}$]	E'_g [$\frac{J}{mm^3}$]	C_f	3D 1[μm] [μm]	2D 1[μm] [μm]	2D Std [μm]	3D 3[μm] [μm]	3D 0.25[μm] [μm]
X2G73	54	Bk	50	20	69.21	18.77	766.11	766.11	0.271	426.8	422.7	26.0	308.0	580.8
X2G62	54	Ag	20	80	29.26	8.34	326.84	204.28	0.285	206.8	197.1	16.9	127.6	338.8
X2G62	54	Ag	20	80	29.26	8.34	326.84	204.28	0.285	189.2	184.1	46.8	123.2	369.6
X2G62	54	Ag	20	80	29.26	8.34	326.84	204.28	0.285	220.0	159.8	46.8	123.2	369.6
X2G62	54	Ag	20	80	29.26	8.34	326.84	204.28	0.285	215.6	170.7	61.0	132.0	378.4
X2G62	54	Ag	20	80	29.26	8.34	326.84	204.28	0.285	202.4	195.5	25.5	132.0	365.2
X2G62	54	Ag	20	80	29.26	8.34	326.84	204.28	0.285	193.6	195.7	19.9	114.4	360.8
X2G71	54	Ag	20	20	26.43	7.69	308.14	770.35	0.291	193.6	184.4	19.9	114.4	391.6
X2G71	54	Ag	20	20	26.43	7.69	308.14	770.35	0.291	189.2	185.6	22.3	162.8	378.4
X2G71	54	Ag	20	20	26.43	7.69	308.14	770.35	0.291	184.8	178.6	22.5	114.4	347.6
X2G71	54	Ag	20	20	26.43	7.69	308.14	770.35	0.291	193.6	190.8	20.1	123.2	374.0
X2G71	54	Ag	20	20	26.43	7.69	308.14	770.35	0.291	189.2	174.8	21.2	140.8	299.2
X2G71	54	Ag	20	20	26.43	7.69	308.14	770.35	0.291	198.0	194.5	21.4	127.6	391.6
X2G70	54	Ag	50	20	42.00	11.73	479.34	479.34	0.279	316.8	318.2	24.3	176.0	536.8
X2G70	54	Ag	50	20	42.00	11.73	479.34	479.34	0.279	330.0	327.0	25.2	176.0	545.6
X2G70	54	Ag	50	20	42.00	11.73	479.34	479.34	0.279	360.8	323.6	86.3	233.2	554.4

Table A.2: Continued.

Sample ID	G_z [μm]	G_h	DoC [μm]	V_w [$\frac{mm}{sec}$]	F'_N [$\frac{N}{mm}$]	F'_t [$\frac{N}{mm}$]	P'_w [$\frac{W}{mm}$]	E'_g [$\frac{J}{mm^3}$]	C_f	3D 1[μm] [μm]	2D 1[μm] [μm]	2D Std [μm]	3D 3[μm] [μm]	3D 0.25[μm] [μm]
X2G70	54	Ag	50	20	42.00	11.73	479.34	479.34	0.279	369.6	366.9	29.8	220.0	580.8
X2G70	54	Ag	50	20	42.00	11.73	479.34	479.34	0.279	338.8	354.7	36.7	193.6	550.0
X2G70	54	Ag	50	20	42.00	11.73	479.34	479.34	0.279	360.8	349.4	49.2	198.0	558.8
X2G84	232	Ag	50	20	34.45	7.42	280.80	280.80	0.215	426.8	423.8	31.8	294.8	611.6
X2G84	232	Ag	50	20	34.45	7.42	280.80	280.80	0.215	426.8	430.9	34.6	294.8	611.6
X2G84	232	Ag	50	20	34.45	7.42	280.80	280.80	0.215	457.6	457.0	37.8	325.6	611.6
X2G84	232	Ag	50	20	34.45	7.42	280.80	280.80	0.215	466.4	484.3	47.9	338.8	690.8
X2G84	232	Ag	50	20	34.45	7.42	280.80	280.80	0.215	453.2	462.2	41.9	312.4	629.2
X2G84	232	Ag	50	20	34.45	7.42	280.80	280.80	0.215	462.0	472.8	36.6	312.4	660.0
X2G80	232	Ag	50	80	72.23	16.16	624.44	156.11	0.224	479.6	491.3	44.0	352.0	629.2
X2G80	232	Ag	50	80	72.23	16.16	624.44	156.11	0.224	466.4	481.6	53.8	365.2	655.6
X2G80	232	Ag	50	80	72.23	16.16	624.44	156.11	0.224	457.6	460.3	43.5	321.2	611.6
X2G80	232	Ag	50	80	72.23	16.16	624.44	156.11	0.224	448.8	457.1	39.5	316.8	611.6
X2G80	232	Ag	50	80	72.23	16.16	624.44	156.11	0.224	444.4	460.9	47.8	334.4	629.2
X2G80	232	Ag	50	80	72.23	16.16	624.44	156.11	0.224	475.2	480.5	43.8	321.2	629.2
X2G58	232	Bk	50	80	95.26	16.83	652.17	163.04	0.177	523.6	538.7	54.8	413.6	690.8

Table A.2: Continued.

Sample ID	G_z [μm]	G_h	DoC [μm]	V_w [$\frac{mm}{sec}$]	F'_N [$\frac{N}{mm}$]	F'_t [$\frac{N}{mm}$]	P'_w [$\frac{W}{mm}$]	E'_g [$\frac{J}{mm^3}$]	C_f	3D 1[μm] [μm]	2D 1[μm] [μm]	2D Std [μm]	3D 3[μm] [μm]	3D 0.25[μm] [μm]
X2G58	232	Bk	50	80	95.26	16.83	652.17	163.04	0.177	558.8	572.0	60.0	435.6	704.0
X2G58	232	Bk	50	80	95.26	16.83	652.17	163.04	0.177	558.8	558.5	28.1	440.0	690.8
X2G58	232	Bk	50	80	95.26	16.83	652.17	163.04	0.177	545.6	540.1	57.3	396.0	673.2
X2G58	232	Bk	50	80	95.26	16.83	652.17	163.04	0.177	541.2	547.8	43.3	404.8	668.8
X2G58	232	Bk	50	80	95.26	16.83	652.17	163.04	0.177	580.8	582.5	49.4	431.2	712.8
X2G74	54	Bk	50	80	169.17	30.21	1118.89	279.72	0.179	624.8	636.4	59.4	484.0	734.8
X2G74	54	Bk	50	80	169.17	30.21	1118.89	279.72	0.179	611.6	627.6	57.1	501.6	730.4
X2G74	54	Bk	50	80	169.17	30.21	1118.89	279.72	0.179	554.4	563.7	70.1	404.8	686.4
X2G74	54	Bk	50	80	169.17	30.21	1118.89	279.72	0.179	558.8	583.9	67.0	387.2	690.8
X2G74	54	Bk	50	80	169.17	30.21	1118.89	279.72	0.179	616.0	623.3	56.7	479.6	730.4
X2G74	54	Bk	50	80	169.17	30.21	1118.89	279.72	0.179	589.6	612.2	70.5	444.4	717.2
X2G63	54	Ag	50	80	212.59	32.75	1130.85	282.71	0.154	704.0	702.9	64.1	594.0	774.4
X2G63	54	Ag	50	80	212.59	32.75	1130.85	282.71	0.154	699.6	702.7	50.8	602.8	756.8
X2G63	54	Ag	50	80	212.59	32.75	1130.85	282.71	0.154	633.6	620.7	64.3	501.6	739.2
X2G63	54	Ag	50	80	212.59	32.75	1130.85	282.71	0.154	624.8	611.8	48.4	479.6	712.8
X2G63	54	Ag	50	80	212.59	32.75	1130.85	282.71	0.154	686.4	689.0	59.3	576.4	783.2

Table A.2: Continued.

Sample ID	G_z [μm]	G_h	DoC [μm]	V_w [$\frac{mm}{sec}$]	F'_N [$\frac{N}{mm}$]	F'_t [$\frac{N}{mm}$]	P'_w [$\frac{W}{mm}$]	E'_g [$\frac{J}{mm^3}$]	C_f	3D 1[μm] [μm]	2D 1[μm] [μm]	2D Std [μm]	3D 3[μm] [μm]	3D 0.25[μm] [μm]
X2G63	54	Ag	50	80	212.59	32.75	1130.85	282.71	0.154	651.2	639.5	41.7	514.8	730.4

APPENDIX B

RESIDUAL STRESS MEASUREMENT RESULTS

Table B.1: Tests for determination of the mean value of $d_{\{224\}}$ and its deviation.

Test	φ	Ψ	Ω	χ	2Θ	$d_{[hkl]}$	Std(2Θ)
I.D.	deg	deg	deg	deg	deg	Å	deg
13960	0	0	68.9975	0	137.9949	0.8251	0.0045
13962	0	0	68.9975	0	137.9950	0.8251	0.0054
13961	0	0	68.9962	0	137.9923	0.8251	0.0057
10332	0	0	68.9962	0	137.9923	0.8251	0.0125
13918	0	0	68.9823	0	137.9646	0.8252	0.0034
13917	0	0	68.9811	0	137.9622	0.8252	0.0036
13933	0	0	68.9732	0	137.9464	0.8252	0.0090
10304	0	0	68.9794	0	137.9587	0.8252	0.0122
10331	0	0	68.9734	0	137.9468	0.8252	0.0137
13882	0	0	68.9540	0	137.9079	0.8253	0.0094
10242	0	0	68.9560	0	137.9120	0.8253	0.0140
10303	0	0	68.9692	0	137.9384	0.8253	0.0168
10243	0	0	68.9612	0	137.9224	0.8253	0.0170
13881	0	0	68.9454	0	137.8907	0.8254	0.0078
13866	0	0	68.9376	0	137.8752	0.8254	0.0094
13867	0	0	68.9339	0	137.8677	0.8254	0.0125
10244	0	0	68.9466	0	137.8931	0.8254	0.0213
10258	0	0	68.9270	28.2	137.8540	0.8255	0.0210
10259	0	0	68.9308	28.2	137.8615	0.8255	0.0228
					Average	**0.8253**	
					Std	**1.33E-04**	

Table B.2: Tests for determination of the mean value of $d_{\{422\}}$ and its deviation.

Test	φ	Ψ	Ω	χ	2Θ	$d_{[hkl]}$	Std(2Θ)
I.D.	deg	deg	deg	deg	deg	Å	deg
10258	0	0	70.0571	28.2	140.1141	0.8194	0.0122
13867	0	0	70.0598	0	140.1195	0.8194	0.0058
13866	0	0	70.0608	0	140.1216	0.8194	0.0054
10331	0	0	70.0749	0	140.1497	0.8193	0.0085
10304	0	0	70.0787	0	140.1573	0.8193	0.0087
10244	0	0	70.0849	0	140.1698	0.8193	0.0108
10303	0	0	70.0850	0	140.1699	0.8193	0.0078
13881	0	0	70.0857	0	140.1713	0.8193	0.0111
13961	0	0	70.0877	0	140.1754	0.8193	0.0022
13962	0	0	70.0915	0	140.1830	0.8192	0.0021
13960	0	0	70.0925	0	140.1849	0.8192	0.0019
10332	0	0	70.0942	0	140.1883	0.8192	0.0123
13882	0	0	70.0981	0	140.1961	0.8192	0.0108
10242	0	0	70.0988	0	140.1976	0.8192	0.0075
10243	0	0	70.1011	0	140.2021	0.8192	0.0077
13918	0	0	70.1027	0	140.2053	0.8192	0.0031
					Average	**0.8193**	
					Std	**7.75E-05**	

Table B.3: Extended summary of residual stress measurement results. Measurements on the {224} and {422} planes can be seen.

Sample	Test	Depth	Hydro	Mises	σ_I	σ_{II}	σ_{III}	Std σ_I	Std σ_{II}	Std σ_{III}
I.D.	I.D.	μm	MPa	MPa	MPa	MPa	MPa	MPa	MPa	MPa
			224							
X1G06	13732	0	-282.20	561.10	-910.30	-203.40	265.30	424.10	342.80	404.30
X1G06	13802	76	-86.96	107.41	-148.01	-113.66	0.80	65.39	66.23	65.35
X1G06	10273	254	-8.67	15.75	-26.15	-12.35	12.50	101.86	98.94	55.83
X1G06	10318	318	11.06	17.35	-5.85	9.62	29.42	61.48	59.24	58.16
X1G15	13836	0	-553.54	483.40	-809.96	-692.68	-157.98	70.99	71.45	59.37
X1G15	13883	47	-143.80	49.61	-168.82	-159.31	-103.27	37.08	37.15	36.22
X1G15	13934	117	-6.19	33.56	-33.67	-2.62	17.72	56.46	57.03	56.53
X1G10	13781	124	-69.95	33.38	-100.99	-66.30	-42.57	69.93	54.30	68.52
X1G10	13919	154	-57.74	37.66	-89.36	-70.97	-12.88	113.56	107.24	50.10
X1G10	13926	154	-24.73	97.75	-104.78	-18.14	48.73	51.12	51.81	52.92
X2G08	13711	0	-436.30	454.58	-706.63	-538.68	-63.60	95.45	78.25	48.74
X2G08	13753	72	-97.44	135.07	-208.26	-85.52	1.45	77.76	59.09	71.59
X2G08	10289	122	-6.66	19.38	-22.28	-8.64	10.93	57.06	57.59	60.61
			422							
X1G06	13732	0	-447.86	892.73	-1220.10	-324.53	201.07	526.57	247.93	155.01
X1G06	13802	76	-97.20	112.80	-173.70	-112.70	-5.00	25.70	25.50	25.30
X1G06	13823	76	-26.42	26.30	-48.10	-23.60	-7.40	24.40	24.00	21.50
X1G06	10273	254	7.38	56.20	-38.95	9.76	51.34	36.80	34.66	38.29
X1G15	13836	0	-539.03	524.70	-832.08	-674.64	-110.38	49.78	55.31	38.04
X1G15	13853	17	-75.66	25.44	-94.65	-77.70	-54.63	30.37	32.31	30.92
X1G15	13883	47	-95.22	69.28	-151.83	-90.27	-43.56	26.08	26.00	25.44
X1G10	13781	124	-55.79	51.91	-99.18	-53.05	-15.14	37.29	37.99	38.99
X1G10	13919	154	-73.52	77.87	-137.45	-72.23	-10.86	40.00	34.13	28.40
X1G10	13926	154	-67.10	60.10	-116.30	-64.50	-20.30	20.40	20.90	22.90
X2G08	13711	0	-563.17	565.19	-944.96	-643.64	-100.89	71.45	92.75	48.68
X2G08	13753	72	-72.79	66.58	-113.17	-87.39	-17.82	36.54	32.98	32.43
X2G08	10289	122	18.74	37.79	-12.16	19.57	48.80	24.68	25.28	23.54

Table B.4: Test results for sample X1G06 test 13733 plane {224}. Surface.

Stress [MPa]				Std [MPa]				Strain [-]				Std [-]			
-260.89	-110.18	105.94		330.13	352.27	85.61		-7.13E-04	-8.13E-04	7.82E-04		1.27E-03	2.60E-03	6.32E-04	
-110.18	-708.48	-102.42		352.27	573.77	118.07		-8.13E-04	-4.02E-03	-7.56E-04		2.60E-03	2.81E-03	8.71E-04	
105.94	-102.42	120.85		85.61	118.07	188.30		7.82E-04	-7.56E-04	2.10E-03		6.32E-04	8.71E-04	2.94E-04	
Principal values [MPa]				Std [MPa]											
-910.39	0	0		424.08	0	0									
0	-203.50	0		0	342.80	0									
0	0	265.37		0	0	404.39									
Sample	X1G06														
Plane	{224}														
Depth	0	µm													
Hydro	-282.84	MPa													
Mises	561.18	MPa													
Test	φ	Ψ	Ω	χ	2Θ	$d_{[hkl]}$	Std(2Θ)	StrainLab	Std	Strain Th	Std	StressLab	Std	Weigth	Depth
I.D.	deg	deg	deg	deg	deg	Å	deg	1.E-06	1.E-06	1.E-06	1.E-06	MPa	MPa		µm
13733	0	-42.61	26.6	0	138.4198	0.8239	0.5494	-2188.39	1541.50	25.61	1074.24	-367.65	258.97	6.4	12.0
13734	0	-28.17	40.4	0	137.1430	0.8275	0.4448	1764.21	739.38	819.27	744.90	296.39	124.22	9.8	15.6
13735	0	0.04	68.6	0	137.1161	0.8276	0.1495	2593.91	507.00	2105.76	294.16	435.78	85.18	86.6	18.5
13736	0	27.97	96.8	0	137.6511	0.8261	0.1704	785.66	581.40	2132.08	388.75	131.99	97.68	66.6	15.6
13737	0	41.8	110.6	0	137.6019	0.8262	0.1561	948.39	592.70	1629.99	458.97	159.33	99.57	79.4	12.2
13738	0	55.09	123.6	0	137.0104	0.8279	0.2076	3032.43	672.05	942.80	625.83	509.45	112.90	44.9	7.3
13739	45	-55.41	13.6	0	138.0169	0.8250	0.3343	-666.39	895.17	-1497.00	862.09	-111.95	150.39	17.3	7.3
13741	45	-28.4	40.4	0	137.5992	0.8262	0.2397	1122.44	990.69	896.94	411.07	188.57	166.44	33.7	15.6
13742	45	0.03	68.6	0	137.1328	0.8275	0.1439	2781.00	400.67	2104.22	293.54	467.21	67.31	93.4	18.5
13743	45	27.93	96.8	0	137.7433	0.8258	0.1420	488.25	392.84	960.30	811.84	82.03	66.00	96.0	15.6
13744	45	41.57	110.6	0	138.0519	0.8249	0.3594	-608.14	1595.67	-197.48	1318.62	-102.17	268.07	15.0	12.3
13745	45	54.44	123.6	0	138.3187	0.8242	0.7382	-1869.90	2816.98	-1358.19	1717.44	-314.14	473.25	3.6	7.7
13748	90	-28.45	40.4	0	137.7022	0.8259	0.3329	834.91	1191.12	1344.60	1179.23	140.26	200.11	17.5	15.5
13749	90	-0.11	68.6	0	137.4229	0.8267	0.1141	1391.06	383.15	2107.68	295.71	233.70	64.37	148.6	18.5
13750	90	28.25	96.8	0	137.0949	0.8276	0.1656	2880.83	773.89	99.79	618.93	483.98	130.01	70.6	15.6
13751	90	41.25	110.6	0	138.6949	0.8232	0.5300	-2476.15	1452.08	-1302.35	1083.45	-415.99	243.95	6.9	12.4

Table B.5: Test results for sample X1G06 test 13733 plane {422}. Surface.

Stress [MPa]				Std [MPa]				Strain [-]				Std [-]			
-403.10	191.45	-14.15		220.53	172.39	54.30		-1.06E-03	1.41E-03	-1.04E-04		8.25E-04	1.27E-03	4.01E-04	
191.45	-1128.91	-29.37		172.39	553.88	74.24		1.41E-03	-6.41E-03	-2.17E-04		1.27E-03	2.86E-03	5.48E-04	
-14.15	-29.37	188.43		54.30	74.24	148.66		-1.04E-04	-2.17E-04	3.31E-03		4.01E-04	5.48E-04	2.96E-04	
Principal values [MPa]				Std [MPa]											
-1220.10	0	0		526.57	0	0									
0	-324.53	0		0	247.93	0									
0	0	201.07		0	0	155.01									
Sample	X1G06														
Plane	{422}														
Depth	0	µm													
Hydro	-447.86	MPa													
Mises	892.73	MPa													
Test	φ	Ψ	Ω	χ	2Θ	$d_{[hkl]}$	Std(2Θ)	StrainLab	Std	Strain Th	Std	StressLab	Std	Weigth	Depth
I.D.	deg	deg	deg	deg	deg	Å	deg	1.E-06	1.E-06	1.E-06	1.E-06	MPa	MPa		µm
13733	0	-43.42	26.6	0	140.0426	0.8196	0.4175	628.96	853.58	1353.21	571.35	105.67	143.40	8.8	11.9
13734	0	-29.26	40.4	0	139.3220	0.8215	0.1654	2838.57	672.51	2357.87	411.47	476.88	112.98	56.2	15.5
13735	0	-0.9	68.6	0	138.9961	0.8224	0.1524	3758.46	595.32	3312.94	294.20	631.42	100.01	66.2	18.6
13736	0	27.01	96.8	0	139.5759	0.8208	0.2041	2079.59	654.72	2323.05	377.41	349.37	109.99	36.9	16.0
13737	0	40.86	110.6	0	139.4861	0.8211	0.1972	1990.15	560.48	1340.55	454.70	334.35	94.16	39.5	12.6
13739	45	-56.46	13.6	0	140.1181	0.8194	0.2880	337.22	837.56	-392.05	1091.82	56.65	140.71	18.5	7.2
13740	45	-43.31	26.6	0	139.8268	0.8202	0.6094	784.41	2057.40	876.25	772.26	131.78	345.64	4.1	11.9
13741	45	-29.4	40.4	0	139.5978	0.8208	0.1666	1579.39	589.52	2144.65	468.25	265.34	99.04	55.4	15.5
13742	45	-0.93	68.6	0	139.0535	0.8222	0.1738	3798.52	489.53	3315.86	298.50	638.15	82.24	50.9	18.6
13743	45	26.94	96.8	0	139.7152	0.8205	0.1490	1362.31	423.35	1971.94	522.16	228.87	71.12	69.3	16.0
13744	45	40.53	110.6	0	140.1336	0.8194	0.5063	246.20	1426.40	709.46	860.17	41.36	239.64	6.0	12.7
13748	90	-29.52	40.4	0	139.8361	0.8201	0.3096	982.81	877.03	1131.79	833.99	165.11	147.34	16.0	15.5
13749	90	-1.09	68.6	0	139.3800	0.8213	0.1122	2498.92	305.95	3314.85	302.18	419.82	51.40	122.1	18.6
13750	90	27.15	96.8	0	139.3070	0.8215	0.1320	2689.91	471.57	1110.57	598.80	451.90	79.22	88.2	15.9
13751	90	40.27	110.6	0	140.6679	0.8180	0.5616	-1656.64	1591.18	-952.04	1135.46	-278.31	267.32	4.9	13.1

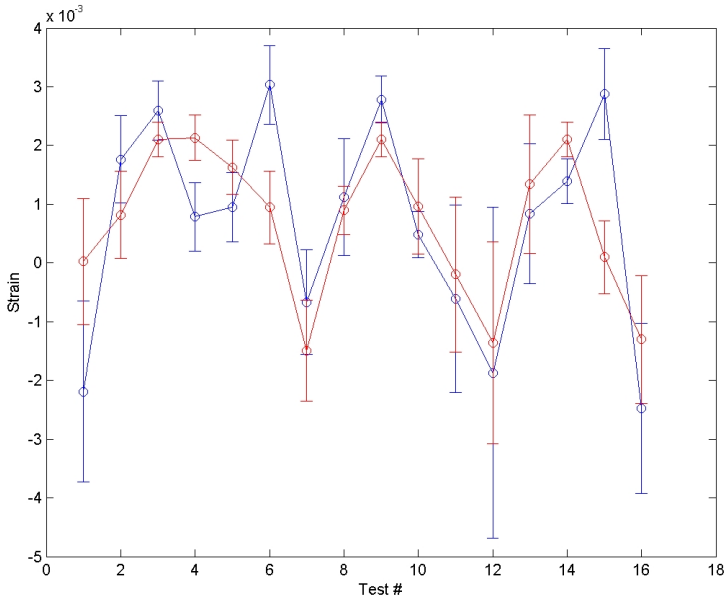

(a) plane{224}

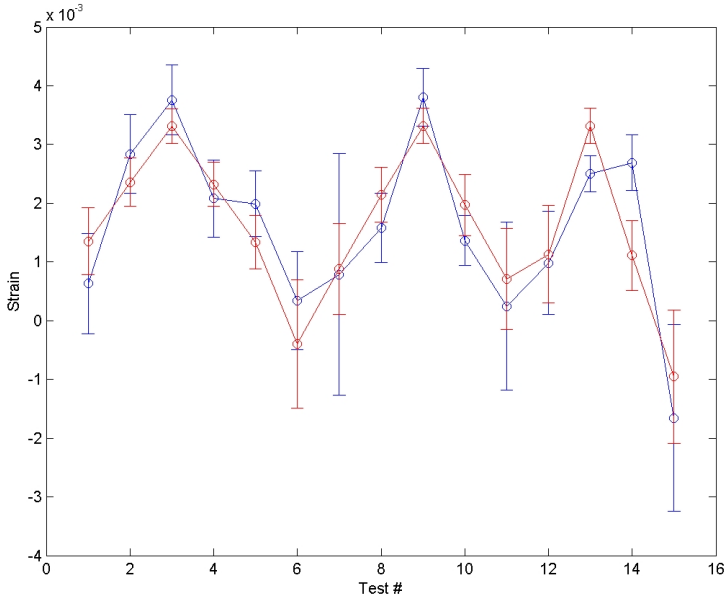

(b) plane{422}

Figure B.1: Comparison of the theoretical strain component ε_{33} (red) with the corresponding measured component ε'_{33} for sample X1G06 test 13733. Surface.

Table B.6: Test results for sample X1G06 test 13802 plane {224}. 76μm subsurface.

Stress [MPa]				Std [MPa]				Strain [-]				Std [-]			
-133.24	-16.55	3.90		64.97	5.50	2.47		-6.11E-04	-1.22E-04	2.90E-05		2.01E-04	4.10E-05	1.80E-05	
-16.55	-128.06	-4.65		5.50	66.47	1.55		-1.22E-04	-5.73E-04	-3.40E-05		4.10E-05	2.12E-04	1.10E-05	
3.90	-4.65	0.42		2.47	1.55	65.38		2.90E-05	-3.40E-05	3.76E-04		1.80E-05	1.10E-05	2.03E-04	
Principal values [MPa]				Std [MPa]											
-148.01	0	0		65.39	0	0									
0	-113.66	0		0	66.23	0									
0	0	0.80		0	0	65.35									
Sample	X1G06														
Plane	{224}														
Depth	76	µm													
Hydro	-86.96	MPa													
Mises	107.41	MPa													

Test	φ	Ψ	Ω	χ	2Θ	$d_{[hkl]}$	Std(2Θ)	StrainLab	Std	Strain Th	Std	StressLab	Std	Weigth	Depth
I.D.	deg	deg	deg	deg	deg	Å	deg	1.E-06	1.E-06	1.E-06	1.E-06	MPa	MPa		µm
13802	0	-55.37	13.6	0	137.9397	0.8252	0.0113	-201.30	186.07	-319.01	198.35	-33.82	31.26	21.9	7.3
13803	0	-42.35	26.6	0	137.9084	0.8253	0.0087	-115.44	217.51	-100.64	198.49	-19.39	36.54	36.9	12.0
13804	0	-28.52	40.4	0	137.8376	0.8255	0.0092	133.43	194.24	126.78	199.49	22.42	32.63	33.0	15.5
13805	0	-0.29	68.6	0	137.7758	0.8257	0.0074	329.49	206.15	375.46	202.99	55.35	34.63	51.0	18.5
13806	0	27.89	96.8	0	137.8265	0.8256	0.0114	163.03	209.15	183.73	204.31	27.39	35.14	21.5	15.7
13807	0	41.66	110.6	0	137.8862	0.8254	0.0159	-40.18	206.23	-31.48	203.95	-6.75	34.65	11.0	12.2
13808	0	54.61	123.6	0	137.9777	0.8251	0.0141	-352.21	210.25	-252.70	203.32	-59.17	35.32	14.0	7.6
13809	45	-55.39	13.6	0	137.9808	0.8251	0.0116	-354.34	197.73	-358.60	199.04	-59.53	33.22	20.7	7.3
13810	45	-42.37	26.6	0	137.9326	0.8253	0.0101	-191.75	202.39	-115.06	198.17	-32.21	34.00	27.4	12.0
13811	45	-28.53	40.4	0	137.8636	0.8255	0.0086	50.86	209.50	130.53	198.72	8.54	35.20	37.7	15.5
13812	45	-0.27	68.6	0	137.7418	0.8258	0.0081	457.87	195.10	375.78	202.97	76.92	32.78	42.5	18.5
13813	45	27.9	96.8	0	137.8019	0.8256	0.0125	258.63	205.77	133.92	207.50	43.45	34.57	17.9	15.7
13814	45	41.66	110.6	0	137.8790	0.8254	0.0146	-7.19	213.79	-109.58	208.76	-1.21	35.92	13.1	12.2
13815	45	54.61	123.6	0	137.9885	0.8251	0.0174	-385.75	212.38	-351.98	209.14	-64.81	35.68	9.2	7.6
13816	90	-55.36	13.6	0	137.9254	0.8253	0.0109	-190.51	207.74	-234.10	203.23	-32.00	34.90	23.5	7.3
13817	90	-42.33	26.6	0	137.8639	0.8255	0.0081	36.43	198.34	-20.09	200.94	6.12	33.32	42.5	12.0
13818	90	-28.52	40.4	0	137.8320	0.8255	0.0104	157.10	198.04	188.48	200.23	26.39	33.27	25.8	15.5
13819	90	-0.27	68.6	0	137.7498	0.8258	0.0070	414.78	209.40	376.08	202.98	69.68	35.18	57.0	18.5
13820	90	27.87	96.8	0	137.8609	0.8255	0.0112	44.08	215.20	140.18	207.85	7.41	36.15	22.3	15.7
13821	90	41.64	110.6	0	137.9224	0.8253	0.0128	-162.45	205.16	-76.96	210.42	-27.29	34.47	17.0	12.2
13822	90	54.62	123.6	0	137.9598	0.8252	0.0137	-270.93	218.66	-287.07	212.44	-45.52	36.73	14.9	7.6

Table B.7: Test results for sample X1G06 test 13802 plane {422}. 76μm subsurface.

Stress [MPa]				Std [MPa]				Strain [-]				Std [-]			
-151.32	-29.97	6.06		26.00	2.66	0.99		-7.00E-04	-2.21E-04	4.50E-05		8.40E-05	2.00E-05	7.00E-06	
-29.97	-133.43	-12.54		2.66	25.23	1.40		-2.21E-04	-5.68E-04	-9.30E-05		2.00E-05	7.80E-05	1.00E-05	
6.06	-12.54	-6.90		0.99	1.40	25.41		4.50E-05	-9.30E-05	3.66E-04		7.00E-06	1.00E-05	7.90E-05	
Principal values [MPa]				Std [MPa]											
-173.79	0	0		25.78	0	0									
0	-112.80	0		0	25.55	0									
0	0	-5.07		0	0	25.35									
Sample	X1G06														
Plane	{422}														
Depth	76	µm													
Hydro	-97.22	MPa													
Mises	112.82	MPa													
Test	φ	Ψ	Ω	χ	2Θ	$d_{[hkl]}$	Std(2Θ)	StrainLab	Std	Strain Th	Std	StressLab	Std	Weigth	Depth
I.D.	deg	deg	deg	deg	deg	Å	deg	1.E-06	1.E-06	1.E-06	1.E-06	MPa	MPa		µm
13802	0	-56.53	13.6	0	140.2645	0.8190	0.0081	-320.79	79.12	-417.25	80.60	-53.89	13.29	17.8	7.2
13803	0	-43.51	26.6	0	140.2228	0.8191	0.0072	-186.29	85.07	-184.28	79.32	-31.30	14.29	22.5	11.9
13804	0	-29.68	40.4	0	140.1620	0.8193	0.0060	6.20	82.60	65.83	78.65	1.04	13.88	32.4	15.5
13805	0	-1.42	68.6	0	140.0355	0.8196	0.0048	408.52	84.71	362.83	78.96	68.63	14.23	50.6	18.6
13806	0	26.74	96.8	0	140.1215	0.8194	0.0079	141.49	83.55	185.86	80.24	23.77	14.04	18.7	16.1
13807	0	40.51	110.6	0	140.1843	0.8192	0.0090	-73.92	83.30	-39.81	81.41	-12.42	13.99	14.4	12.8
13808	0	53.47	123.6	0	140.2660	0.8190	0.0095	-323.40	88.44	-279.69	82.72	-54.33	14.86	12.9	8.5
13809	45	-56.55	13.6	0	140.2949	0.8190	0.0062	-403.84	79.97	-453.25	78.22	-67.85	13.43	30.3	7.2
13810	45	-43.52	26.6	0	140.2449	0.8191	0.0068	-257.79	82.01	-179.65	77.42	-43.31	13.78	25.2	11.9
13811	45	-29.69	40.4	0	140.1718	0.8193	0.0059	-22.72	75.12	95.27	77.27	-3.82	12.62	33.5	15.5
13812	45	-1.42	68.6	0	140.0415	0.8196	0.0068	394.12	81.45	366.62	78.89	66.21	13.68	25.2	18.6
13813	45	26.74	96.8	0	140.1181	0.8194	0.0098	135.39	89.69	91.34	80.99	22.75	15.07	12.1	16.1
13814	45	40.49	110.6	0	140.2154	0.8192	0.0091	-158.20	83.77	-182.57	81.79	-26.58	14.07	14.1	12.8
13815	45	53.45	123.6	0	140.3032	0.8189	0.0073	-435.45	82.44	-454.66	82.25	-73.16	13.85	21.9	8.5
13816	90	-56.49	13.6	0	140.1878	0.8192	0.0082	-65.60	71.76	-198.41	76.10	-11.02	12.06	17.3	7.2
13817	90	-43.49	26.6	0	140.1768	0.8193	0.0051	-42.62	84.87	15.77	76.19	-7.16	14.26	44.8	11.9
13818	90	-29.66	40.4	0	140.1111	0.8194	0.0077	172.08	73.11	216.65	76.73	28.91	12.28	19.7	15.5
13819	90	-1.4	68.6	0	139.9995	0.8197	0.0067	528.59	76.53	369.65	78.89	88.80	12.86	26.0	18.6
13820	90	26.74	96.8	0	140.1285	0.8194	0.0064	111.87	78.25	102.33	80.77	18.79	13.15	28.5	16.1
13821	90	40.48	110.6	0	140.2366	0.8191	0.0082	-230.51	78.64	-119.30	81.06	-38.73	13.21	17.3	12.8
13822	90	53.46	123.6	0	140.2718	0.8190	0.0072	-339.66	89.13	-325.75	80.79	-57.06	14.97	22.5	8.5

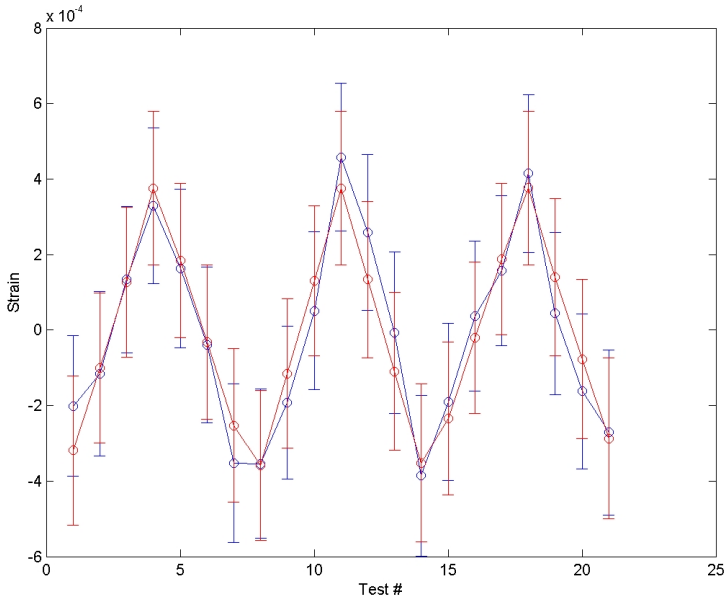

(a) plane{224}

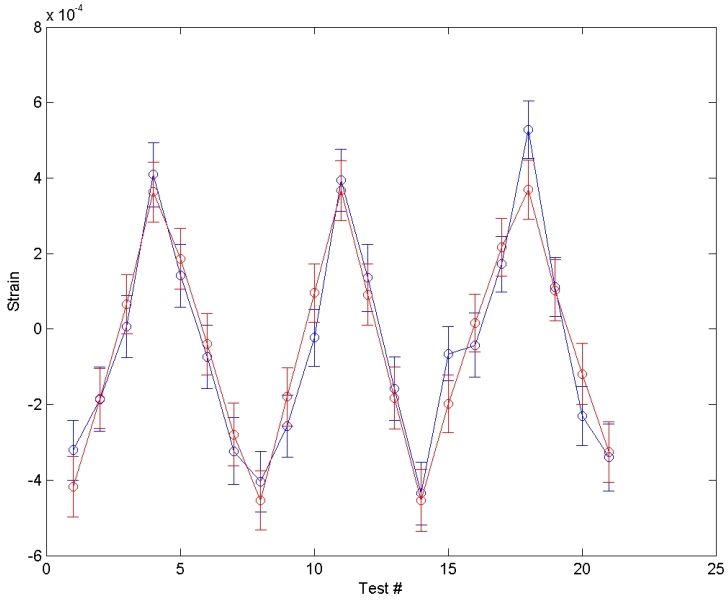

(b) plane{422}

Figure B.2: Comparison of the theoretical strain component ε_{33} (red) with the corresponding measured component ε'_{33} for sample X1G06 test 13802. 76μm subsurface.

Table B.8: Test results for sample X1G06 test 13823 plane {422}. 76μm subsurface.

Stress [MPa]				Std [MPa]				Strain [-]				Std [-]			
-151.32	-29.97	6.06		26.00	2.66	0.99		-7.00E-04	-2.21E-04	4.50E-05		8.40E-05	2.00E-05	7.00E-06	
-29.97	-133.43	-12.54		2.66	25.23	1.40		-2.21E-04	-5.68E-04	-9.30E-05		2.00E-05	7.80E-05	1.00E-05	
6.06	-12.54	-6.90		0.99	1.40	25.41		4.50E-05	-9.30E-05	3.66E-04		7.00E-06	1.00E-05	7.90E-05	
Principal values [MPa]				Std [MPa]											
-173.79	0	0		25.78	0	0									
0	-112.80	0		0	25.55	0									
0	0	-5.07		0	0	25.35									
Sample	X1G06														
Plane	{422}														
Depth	76	µm													
Hydro	-97.22	MPa													
Mises	112.82	MPa													
Test	φ	Ψ	Ω	χ	2Θ	$d_{[hkl]}$	Std(2Θ)	StrainLab	Std	Strain Th	Std	StressLab	Std	Weigth	Depth
I.D.	deg	deg	deg	deg	deg	Å	deg	1.E-06	1.E-06	1.E-06	1.E-06	MPa	MPa		µm
13802	0	-56.53	13.6	0	140.2645	0.8190	0.0081	-320.79	79.12	-417.25	80.60	-53.89	13.29	17.8	7.2
13803	0	-43.51	26.6	0	140.2228	0.8191	0.0072	-186.29	85.07	-184.28	79.32	-31.30	14.29	22.5	11.9
13804	0	-29.68	40.4	0	140.1620	0.8193	0.0060	6.20	82.60	65.83	78.65	1.04	13.88	32.4	15.5
13805	0	-1.42	68.6	0	140.0355	0.8196	0.0048	408.52	84.71	362.83	78.96	68.63	14.23	50.6	18.6
13806	0	26.74	96.8	0	140.1215	0.8194	0.0079	141.49	83.55	185.86	80.24	23.77	14.04	18.7	16.1
13807	0	40.51	110.6	0	140.1843	0.8192	0.0090	-73.92	83.30	-39.81	81.41	-12.42	13.99	14.4	12.8
13808	0	53.47	123.6	0	140.2660	0.8190	0.0095	-323.40	88.44	-279.69	82.72	-54.33	14.86	12.9	8.5
13809	45	-56.55	13.6	0	140.2949	0.8190	0.0062	-403.84	79.97	-453.25	78.22	-67.85	13.43	30.3	7.2
13810	45	-43.52	26.6	0	140.2449	0.8191	0.0068	-257.79	82.01	-179.65	77.42	-43.31	13.78	25.2	11.9
13811	45	-29.69	40.4	0	140.1718	0.8193	0.0059	-22.72	75.12	95.27	77.27	-3.82	12.62	33.5	15.5
13812	45	-1.42	68.6	0	140.0415	0.8196	0.0068	394.12	81.45	366.62	78.89	66.21	13.68	25.2	18.6
13813	45	26.74	96.8	0	140.1181	0.8194	0.0098	135.39	89.69	91.34	80.99	22.75	15.07	12.1	16.1
13814	45	40.49	110.6	0	140.2154	0.8192	0.0091	-158.20	83.77	-182.57	81.79	-26.58	14.07	14.1	12.8
13815	45	53.45	123.6	0	140.3032	0.8189	0.0073	-435.45	82.44	-454.66	82.25	-73.16	13.85	21.9	8.5
13816	90	-56.49	13.6	0	140.1878	0.8192	0.0082	-65.60	71.76	-198.41	76.10	-11.02	12.06	17.3	7.2
13817	90	-43.49	26.6	0	140.1768	0.8193	0.0051	-42.62	84.87	15.77	76.19	-7.16	14.26	44.8	11.9
13818	90	-29.66	40.4	0	140.1111	0.8194	0.0077	172.08	73.11	216.65	76.73	28.91	12.28	19.7	15.5
13819	90	-1.4	68.6	0	139.9995	0.8197	0.0067	528.59	76.53	369.65	78.89	88.80	12.86	26.0	18.6
13820	90	26.74	96.8	0	140.1285	0.8194	0.0064	111.87	78.25	102.33	80.77	18.79	13.15	28.5	16.1
13821	90	40.48	110.6	0	140.2366	0.8191	0.0082	-230.51	78.64	-119.30	81.06	-38.73	13.21	17.3	12.8
13822	90	53.46	123.6	0	140.2718	0.8190	0.0072	-339.66	89.13	-325.75	80.79	-57.06	14.97	22.5	8.5

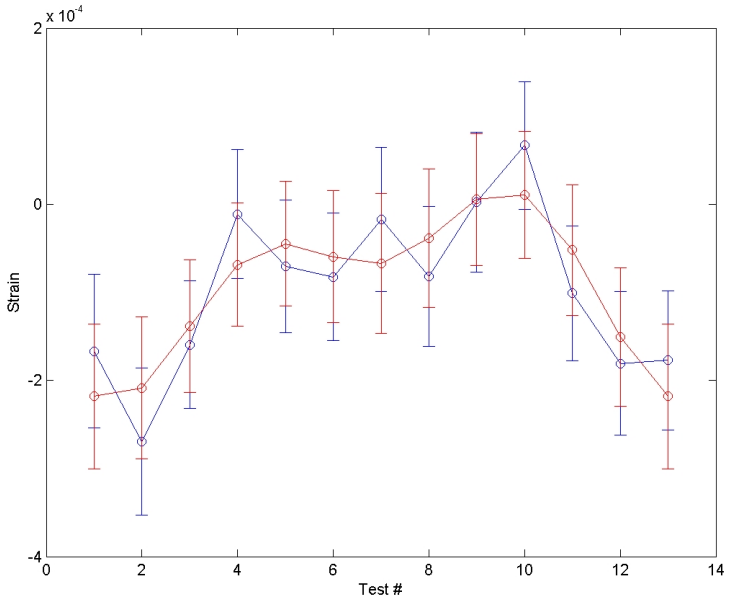

Figure B.3: Comparison of the theoretical strain component ε_{33} (red) with the corresponding measured component ε'_{33} for sample X1G06 test 13823 plane $\{422\}$. 76μm subsurface.

Table B.9: Test results for sample X1G06 test 10273 plane {224}. 254μm subsurface.

Stress [MPa]				Std [MPa]				Strain [-]				Std [-]			
-7.51	1.04	1.78		101.09	6.79	1.79		-1.80E-05	8.00E-06	1.30E-05		4.02E-04	5.00E-05	1.30E-05	
1.04	-21.14	2.87		6.79	102.25	2.11		8.00E-06	-1.19E-04	2.10E-05		5.00E-05	4.11E-04	1.60E-05	
1.78	2.87	2.64		1.79	2.11	54.60		1.30E-05	2.10E-05	5.70E-05		1.30E-05	1.60E-05	2.11E-04	
Principal values [MPa]				Std [MPa]											
-26.15	0	0		101.86	0	0									
0	-12.35	0		0	98.94	0									
0	0	12.50		0	0	55.83									
Sample	X1G06														
Plane	{224}														
Depth	254	µm													
Hydro	-8.67	MPa													
Mises	15.75	MPa													
Test	φ	Ψ	Ω	χ	2Θ	$d_{[hkl]}$	Std(2Θ)	StrainLab	Std	Strain Th	Std	StressLab	Std	Weigth	Depth
I.D.	deg	deg	deg	deg	deg	Å	deg	1.E-06	1.E-06	1.E-06	1.E-06	MPa	MPa		µm
10273	0	-28.56	40.4	0	137.9235	0.8253	0.0062	35.81	163.19	28.52	158.89	6.02	27.42	31.7	15.5
10274	30	-28.57	40.4	0	137.9386	0.8253	0.0070	-10.95	157.91	16.85	157.28	-1.84	26.53	24.9	15.5
10275	60	-28.57	40.4	0	137.9387	0.8253	0.0107	-15.78	163.90	2.85	156.57	-2.65	27.53	10.6	15.5
10276	90	-28.56	40.4	0	137.9170	0.8253	0.0118	58.07	154.61	-1.26	156.52	9.76	25.97	8.7	15.5
10277	120	-28.57	40.4	0	137.9437	0.8252	0.0099	-19.02	155.86	10.83	157.28	-3.19	26.18	12.4	15.5
10278	150	-28.56	40.4	0	137.9290	0.8253	0.0076	21.20	167.06	32.90	160.24	3.56	28.07	21.1	15.5
10279	180	-28.56	40.4	0	137.9187	0.8253	0.0142	49.69	168.86	50.57	164.14	8.35	28.37	6.0	15.5
10280	210	-28.56	40.4	0	137.9137	0.8253	0.0085	77.55	165.19	53.76	166.71	13.03	27.75	16.9	15.5
10281	240	-28.56	40.4	0	137.9227	0.8253	0.0060	40.79	159.90	44.74	167.88	6.85	26.86	33.8	15.5
10282	270	-28.56	40.4	0	137.9261	0.8253	0.0154	20.83	182.49	34.36	167.12	3.50	30.66	5.1	15.5
10283	300	-28.57	40.4	0	137.9324	0.8253	0.0071	17.31	166.79	30.68	164.13	2.91	28.02	24.2	15.5
10284	330	-28.56	40.4	0	137.9206	0.8253	0.0091	60.03	153.77	31.64	161.04	10.09	25.83	14.7	15.5
10285	360	-28.56	40.4	0	137.9290	0.8253	0.0064	29.40	161.00	28.53	158.90	4.94	27.05	29.7	15.5

Table B.10: Test results for sample X1G06 test 10273 plane {422}. 254μm subsurface.

Stress [MPa]				Std [MPa]				Strain [-]				Std [-]			
5.04	44.37	3.58		38.09	6.88	1.85		6.00E-06	3.27E-04	2.60E-05		1.31E-04	5.10E-05	1.40E-05	
44.37	7.56	-2.71		6.88	37.18	1.72		3.27E-04	2.40E-05	-2.00E-05		5.10E-05	1.28E-04	1.30E-05	
3.58	-2.71	9.55		1.85	1.72	34.38		2.60E-05	-2.00E-05	3.90E-05		1.40E-05	1.30E-05	1.07E-04	
Principal values [MPa]				Std [MPa]											
-38.95	0	0		36.80	0	0									
0	9.76	0		0	34.66	0									
0	0	51.34		0	0	38.29									
Sample	X1G06														
Plane	{422}														
Depth	254	µm													
Hydro	7.38	MPa													
Mises	56.2	MPa													
Test	φ	Ψ	Ω	χ	2Θ	$d_{[hkl]}$	Std(2Θ)	StrainLab	Std	Strain Th	Std	StressLab	Std	Weigth	Depth
I.D.	deg	deg	deg	deg	deg	Å	deg	1.E-06	1.E-06	1.E-06	1.E-06	MPa	MPa		µm
10273	0	-29.68	40.4	0	140.1627	0.8193	0.0041	9.61	108.65	7.97	105.84	1.61	18.25	56.6	15.5
10274	30	-29.68	40.4	0	140.1546	0.8193	0.0076	42.10	108.66	90.28	108.08	7.07	18.26	16.5	15.5
10275	60	-29.66	40.4	0	140.1134	0.8194	0.0102	164.08	115.91	107.09	108.50	27.57	19.47	9.1	15.5
10276	90	-29.68	40.4	0	140.1586	0.8193	0.0089	22.84	106.35	52.45	108.79	3.84	17.87	12.0	15.5
10278	150	-29.69	40.4	0	140.1709	0.8193	0.0045	-18.91	112.51	-9.45	109.63	-3.18	18.90	47.0	15.5
10279	180	-29.67	40.4	0	140.1310	0.8194	0.0119	96.08	112.20	53.41	111.31	16.14	18.85	6.7	15.5
10280	210	-29.67	40.4	0	140.1471	0.8193	0.0088	60.44	115.33	112.41	110.49	10.15	19.38	12.3	15.5
10281	240	-29.66	40.4	0	140.1245	0.8194	0.0067	127.46	101.33	100.05	105.12	21.41	17.02	21.2	15.5
10283	300	-29.69	40.4	0	140.1824	0.8192	0.0114	-71.92	110.43	-61.76	100.58	-12.08	18.55	7.3	15.5
10284	330	-29.69	40.4	0	140.1842	0.8192	0.0163	-62.24	106.38	-66.05	102.77	-10.46	17.87	3.6	15.5
10285	360	-29.68	40.4	0	140.1583	0.8193	0.0037	24.66	104.54	7.97	105.84	4.14	17.56	69.5	15.5

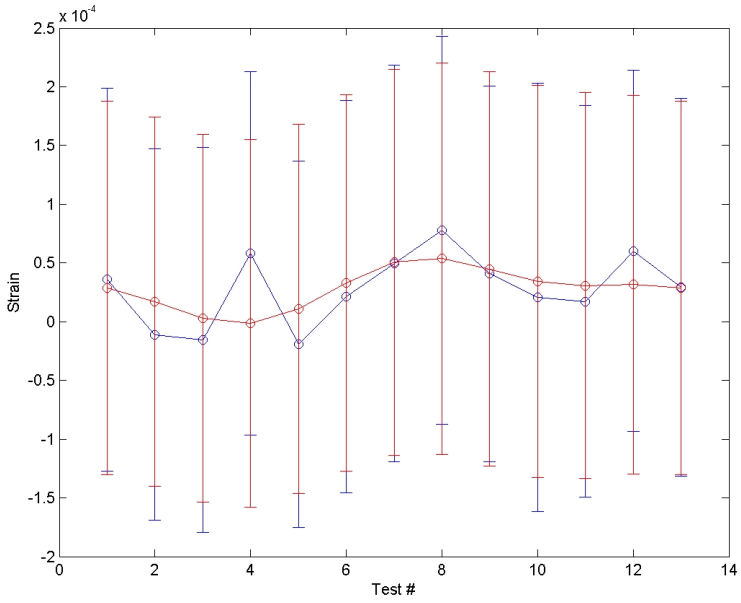

(a) plane{224}

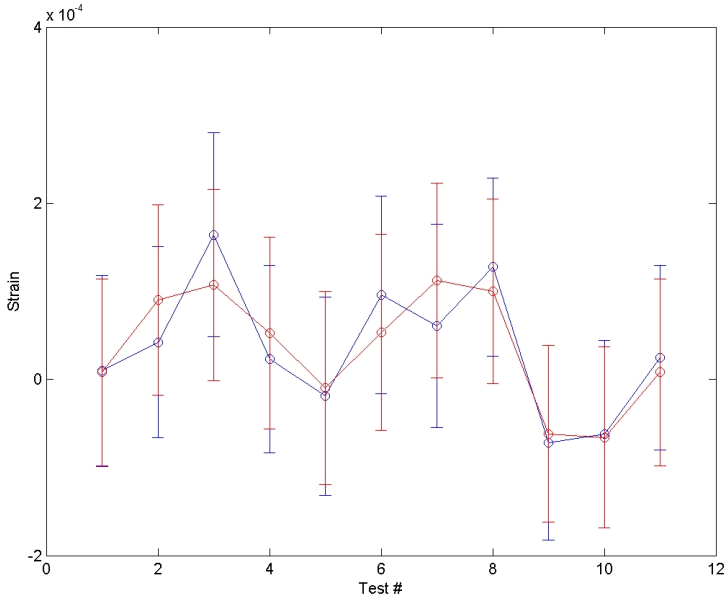

(b) plane{422}

Figure B.4: Comparison of the theoretical strain component ε_{33} (red) with the corresponding measured component ε'_{33} for sample X1G06 test 10273. 254μm subsurface.

Table B.11: Test results for sample X1G06 test 10318 plane {224}. 318μm subsurface.

Stress [MPa]				Std [MPa]				Strain [-]				Std [-]			
16.02	-8.52	1.43		59.51	7.49	2.32		7.10E-05	-6.30E-05	1.10E-05		1.98E-04	5.50E-05	1.70E-05	
-8.52	0.78	-1.92		7.49	60.74	2.94		-6.30E-05	-4.20E-05	-1.40E-05		5.50E-05	2.03E-04	2.20E-05	
1.43	-1.92	16.40		2.32	2.94	60.22		1.10E-05	-1.40E-05	7.40E-05		1.70E-05	2.20E-05	2.15E-04	
Principal values [MPa]				Std [MPa]											
-5.85	0	0		61.48	0	0									
0	9.62	0		0	59.24	0									
0	0	29.42		0	0	58.16									
Sample	X1G06														
Plane	{224}														
Depth	318	µm													
Hydro	11.06	MPa													
Mises	17.35	MPa													
Test	φ	Ψ	Ω	χ	2Θ	$d_{[hkl]}$	Std(2Θ)	StrainLab	Std	Strain Th	Std	StressLab	Std	Weigth	Depth
I.D.	deg	deg	deg	deg	deg	Å	deg	1.E-06	1.E-06	1.E-06	1.E-06	MPa	MPa		µm
10318	0	-28.56	40.4	0	137.9295	0.8253	0.0138	79.66	194.41	64.08	195.58	13.38	32.66	7.5	15.5
10319	30	-28.57	40.4	0	137.9454	0.8252	0.0093	30.59	201.27	52.33	197.78	5.14	33.81	16.5	15.5
10320	60	-28.57	40.4	0	137.9381	0.8253	0.0156	51.75	205.20	47.08	198.79	8.69	34.47	5.9	15.5
10321	90	-28.57	40.4	0	137.9315	0.8253	0.0099	75.23	189.54	59.13	196.82	12.64	31.84	14.6	15.5
10322	120	-28.57	40.4	0	137.9358	0.8253	0.0072	59.71	199.97	80.85	192.90	10.03	33.60	27.5	15.5
10323	150	-28.57	40.4	0	137.9302	0.8253	0.0081	84.40	191.65	92.61	190.40	14.18	32.20	21.7	15.5
10324	180	-28.56	40.4	0	137.9213	0.8253	0.0098	113.30	190.23	81.83	192.62	19.03	31.96	14.9	15.5
10326	240	-28.58	40.4	0	137.9603	0.8252	0.0181	-19.32	205.65	35.34	200.92	-3.25	34.55	4.4	15.5
10327	270	-28.56	40.4	0	137.9274	0.8253	0.0076	94.00	204.63	35.38	200.03	15.79	34.38	24.7	15.5
10328	300	-28.57	40.4	0	137.9400	0.8252	0.0070	44.37	193.45	51.39	197.16	7.45	32.50	29.1	15.5
10329	330	-28.57	40.4	0	137.9425	0.8252	0.0057	29.78	196.83	65.36	195.09	5.00	33.07	43.9	15.5
10330	360	-28.56	40.4	0	137.9269	0.8253	0.0113	85.90	203.08	64.09	195.57	14.43	34.12	11.2	15.5

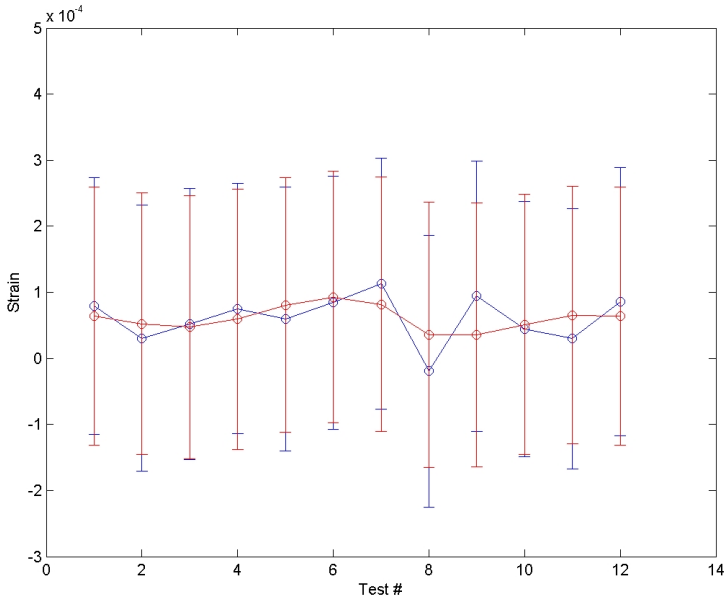

Figure B.5: Comparison of the theoretical strain component ε_{33} (red) with the corresponding measured component ε'_{33} for sample X1G06 test 10318 plane {224}. 318μm subsurface.

Table B.12: Test results for sample X1G15 test 13836 plane {224}. Surface.

Stress [MPa]				Std [MPa]				Strain [-]				Std [-]			
-702.55	-19.76	-44.88		73.03	31.66	16.28		-2.81E-03	-1.46E-04	-3.31E-04		3.02E-04	2.34E-04	1.20E-04	
-19.76	-795.52	-2.29		31.66	71.10	15.36		-1.46E-04	-3.50E-03	-1.70E-05		2.34E-04	2.95E-04	1.13E-04	
-44.88	-2.29	-162.55		16.28	15.36	59.66		-3.31E-04	-1.70E-05	1.17E-03		1.20E-04	1.13E-04	1.94E-04	
Principal values [MPa]				Std [MPa]											
-809.96	0	0		70.99	0	0									
0	-692.68	0		0	71.45	0									
0	0	-157.98		0	0	59.37									
Sample	X1G15														
Plane	{224}														
Depth	0	µm													
Hydro	-553.54	MPa													
Mises	483.40	MPa													
Test	φ	Ψ	Ω	χ	2Θ	$d_{[hkl]}$	Std(2Θ)	StrainLab	Std	Strain Th	Std	StressLab	Std	Weigth	Depth
I.D.	deg	deg	deg	deg	deg	Å	deg	1.E-06	1.E-06	1.E-06	1.E-06	MPa	MPa		µm
13836	0	-42.38	26.6	0	137.9687	0.8252	0.0825	-266.92	334.52	-309.07	221.02	-44.84	56.20	14.8	12.0
13837	30	-42.5	26.6	0	138.1953	0.8245	0.1459	-973.14	469.99	-488.27	247.52	-163.49	78.96	4.7	12.0
13838	60	-42.38	26.6	0	137.9669	0.8252	0.0979	-301.19	312.41	-751.16	231.72	-50.60	52.48	10.5	12.0
13839	90	-42.49	26.6	0	138.1857	0.8246	0.0969	-905.67	329.60	-941.79	211.84	-152.15	55.37	10.8	12.0
13840	120	-42.55	26.6	0	138.3073	0.8242	0.0865	-1256.13	350.23	-977.19	234.25	-211.03	58.84	13.5	12.0
13841	150	-42.49	26.6	0	138.1703	0.8246	0.0780	-907.36	298.98	-943.57	258.23	-152.44	50.23	16.6	12.0
13842	180	-42.47	26.6	0	138.1341	0.8247	0.0560	-772.77	262.45	-974.14	263.89	-129.82	44.09	32.2	12.0
13843	210	-42.54	26.6	0	138.2823	0.8243	0.0800	-1280.86	381.56	-1079.90	264.73	-215.18	64.10	15.8	12.0
13844	240	-42.47	26.6	0	138.1396	0.8247	0.0613	-824.91	258.60	-1116.52	254.62	-138.58	43.45	26.9	12.0
13845	270	-42.56	26.6	0	138.3173	0.8242	0.0698	-1463.63	312.45	-982.28	248.81	-245.89	52.49	20.7	12.0
13846	300	-42.39	26.6	0	137.9716	0.8252	0.0533	-281.17	238.14	-665.23	236.56	-47.24	40.01	35.6	12.0
13847	330	-42.41	26.6	0	138.0247	0.8250	0.0828	-471.16	254.10	-384.35	214.68	-79.16	42.69	14.7	12.0
13848	360	-42.38	26.6	0	137.9510	0.8252	0.1036	-207.34	417.76	-308.55	222.70	-34.83	70.18	9.4	12.0
13849	0	0	68.8	0	137.5749	0.8263	0.0309	1065.38	185.02	1172.60	194.16	178.98	31.08	105.8	18.5
13850	0	0	68.8	0	137.5183	0.8264	0.0290	1269.98	216.51	1172.58	194.10	213.36	36.37	120.1	18.5

Table B.13: Test results for sample X1G15 test 13836 plane {422}. Surface.

Stress [MPa]				Std [MPa]				Strain [-]				Std [-]			
-672.84	1.79	-60.58		57.55	25.71	10.31		-2.66E-03	1.30E-05	-4.47E-04		2.54E-04	1.90E-04	7.60E-05	
1.79	-827.10	-2.42		25.71	49.97	7.64		1.30E-05	-3.80E-03	-1.80E-05		1.90E-04	1.93E-04	5.60E-05	
-60.58	-2.42	-117.16		10.31	7.64	37.39		-4.47E-04	-1.80E-05	1.45E-03		7.60E-05	5.60E-05	1.07E-04	

Principal values [MPa]				Std [MPa]											
-832.08	0	0		49.78	0	0									
0	-674.64	0		0	55.31	0									
0	0	-110.38		0	0	38.04									

Sample	X1G15	
Plane	{422}	
Depth	0	µm
Hydro	-539.03	MPa
Mises	524.70	MPa

Test	φ	Ψ	Ω	χ	2Θ	$d_{[hkl]}$	Std(2Θ)	StrainLab	Std	Strain Th	Std	StressLab	Std	Weigth	Depth
I.D.	deg	deg	deg	deg	deg	Å	deg	1.E-06	1.E-06	1.E-06	1.E-06	MPa	MPa		µm
13836	0	-43.49	26.6	0	140.1742	0.8193	0.0521	-58.45	209.86	-50.96	158.41	-9.82	35.26	16.2	11.9
13837	30	-43.58	26.6	0	140.3520	0.8188	0.0813	-622.75	277.01	-238.01	173.26	-104.62	46.54	6.6	11.9
13838	60	-43.53	26.6	0	140.2647	0.8190	0.0494	-307.53	162.99	-661.16	173.26	-51.66	27.38	18.0	11.9
13839	90	-43.65	26.6	0	140.4967	0.8184	0.0552	-1052.00	205.55	-1033.28	157.58	-176.74	34.53	14.4	11.9
13840	120	-43.69	26.6	0	140.5781	0.8182	0.0629	-1298.40	171.30	-1132.26	163.22	-218.13	28.78	11.1	11.9
13841	150	-43.64	26.6	0	140.4869	0.8185	0.0684	-964.75	291.43	-1026.62	172.48	-162.08	48.96	9.4	11.9
13842	180	-43.63	26.6	0	140.4515	0.8185	0.0608	-882.87	228.52	-953.38	163.86	-148.32	38.39	11.9	11.9
13843	210	-43.68	26.6	0	140.5579	0.8183	0.0723	-1168.70	309.13	-1036.11	163.92	-196.34	51.93	8.4	11.9
13844	240	-43.62	26.6	0	140.4405	0.8186	0.0435	-892.45	144.87	-1146.59	148.74	-149.93	24.34	23.2	11.9
13845	270	-43.7	26.6	0	140.6014	0.8182	0.0443	-1410.22	198.75	-1074.21	135.65	-236.92	33.39	22.4	11.9
13846	300	-43.56	26.6	0	140.3258	0.8189	0.0321	-522.45	178.01	-705.84	154.50	-87.77	29.91	42.6	11.9
13847	330	-43.53	26.6	0	140.2641	0.8190	0.0497	-250.96	224.85	-262.20	163.86	-42.16	37.77	17.8	11.9
13848	360	-43.47	26.6	0	140.1418	0.8193	0.0616	66.23	180.20	-49.51	157.88	11.13	30.27	11.6	11.9
13849	0	0	69.9	0	139.7140	0.8205	0.0197	1440.54	107.27	1445.40	106.75	242.01	18.02	113.1	18.6

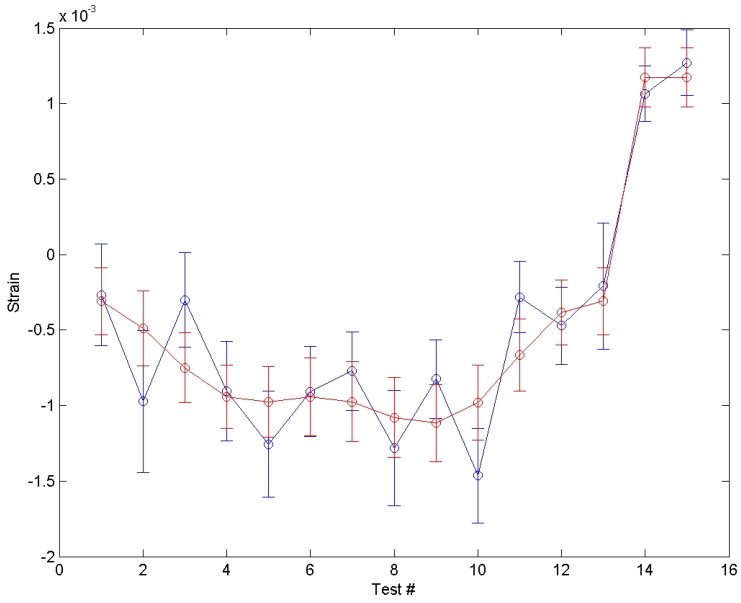

(a) plane{224}

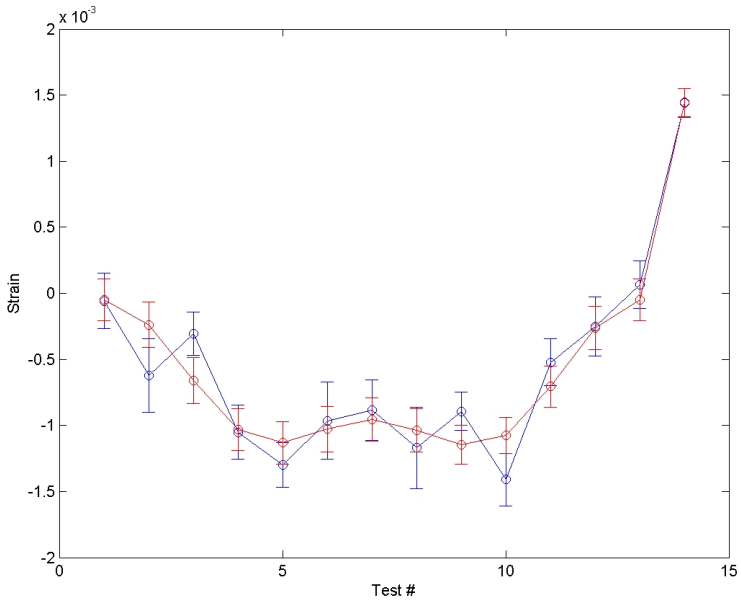

(b) plane{422}

Figure B.6: Comparison of the theoretical strain component ε_{33} (red) with the corresponding measured component ε'_{33} for sample X1G15 test 13836. Surface.

Table B.14: Test results for sample X1G15 test 13853 plane {422}. 17μm subsurface.

Stress [MPa]				Std [MPa]				Strain [-]				Std [-]			
-86.87	11.85	7.04		29.84	2.28	1.38		-3.17E-04	8.70E-05	5.20E-05		8.80E-05	1.70E-05	1.00E-05	
11.85	-59.63	0.29		2.28	30.91	1.07		8.70E-05	-1.16E-04	2.00E-06		1.70E-05	9.60E-05	8.00E-06	
7.04	0.29	-80.47		1.38	1.07	32.90		5.20E-05	2.00E-06	-2.70E-04		1.00E-05	8.00E-06	1.09E-04	
Principal values [MPa]				Std [MPa]											
-94.65	0	0		30.37	0	0									
0	-77.70	0		0	32.31	0									
0	0	-54.63		0	0	30.92									
Sample	X1G15														
Plane	{422}														
Depth	17	µm													
Hydro	-75.66	MPa													
Mises	25.44	MPa													
Test	φ	Ψ	Ω	χ	2Θ	$d_{[hkl]}$	Std(2Θ)	StrainLab	Std	Strain Th	Std	StressLab	Std	Weigth	Depth
I.D.	deg	deg	deg	deg	deg	Å	deg	1.E-06	1.E-06	1.E-06	1.E-06	MPa	MPa		µm
13853	0	-43.53	26.6	0	140.2627	0.8190	0.0052	-318.36	101.96	-343.99	97.39	-53.48	17.13	15.8	11.9
13854	30	-43.53	26.6	0	140.2533	0.8191	0.0063	-295.58	98.68	-278.35	97.82	-49.66	16.58	10.8	11.9
13855	60	-43.52	26.6	0	140.2347	0.8191	0.0044	-235.78	96.68	-212.50	99.58	-39.61	16.24	22.1	11.9
13857	120	-43.51	26.6	0	140.2214	0.8191	0.0072	-193.21	103.29	-232.47	100.23	-32.46	17.35	8.3	11.9
13858	150	-43.53	26.6	0	140.2608	0.8190	0.0076	-314.30	102.16	-260.37	99.81	-52.80	17.16	7.4	11.9
13859	180	-43.51	26.6	0	140.2190	0.8191	0.0076	-186.66	99.86	-240.24	101.17	-31.36	16.78	7.4	11.9
13860	210	-43.52	26.6	0	140.2311	0.8191	0.0076	-223.47	102.79	-186.36	103.27	-37.54	17.27	7.4	11.9
13861	240	-43.51	26.6	0	140.2117	0.8192	0.0050	-164.51	109.86	-156.91	104.47	-27.64	18.46	17.1	11.9
13862	270	-43.5	26.6	0	140.2086	0.8192	0.0056	-156.01	103.98	-194.64	104.29	-26.21	17.47	13.7	11.9
13864	330	-43.55	26.6	0	140.2932	0.8190	0.0055	-418.54	95.86	-348.07	99.33	-70.32	16.10	14.2	11.9
13865	360	-43.53	26.6	0	140.2525	0.8191	0.0055	-291.47	99.51	-343.99	97.39	-48.97	16.72	14.2	11.9

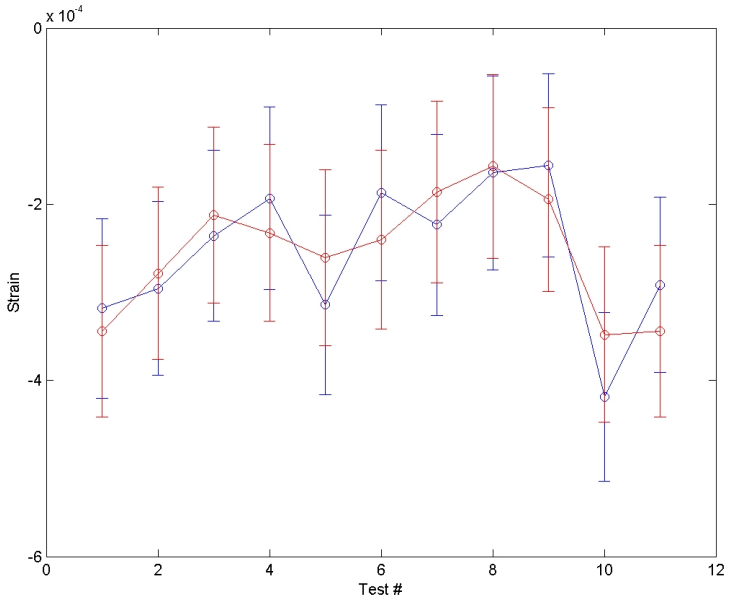

Figure B.7: Comparison of the theoretical strain component ε_{33} (red) with the corresponding measured component ε'_{33} for sample X1G06 test 13853 plane $\{422\}$. 18μm subsurface.

Table B.15: Test results for sample X1G15 test 13883 plane {224}. 47μm subsurface.

Stress [MPa]				Std [MPa]				Strain [-]				Std [-]			
-160.43	2.35	-2.96		37.12	1.47	0.65		-5.68E-04	1.70E-05	-2.20E-05		1.17E-04	1.10E-05	5.00E-06	
2.35	-167.29	3.89		1.47	37.21	0.89		1.70E-05	-6.19E-04	2.90E-05		1.10E-05	1.19E-04	7.00E-06	
-2.96	3.89	-103.67		0.65	0.89	36.18		-2.20E-05	2.90E-05	-1.49E-04		5.00E-06	7.00E-06	1.12E-04	
Principal values [MPa]				Std [MPa]											
-168.82	0	0		37.08	0	0									
0	-159.31	0		0	37.15	0									
0	0	-103.27		0	0	36.22									
Sample	X1G15														
Plane	{224}														
Depth	47	µm													
Hydro	-143.80	MPa													
Mises	49.61	MPa													
Test	φ	Ψ	Ω	χ	2Θ	$d_{[hkl]}$	Std(2Θ)	StrainLab	Std	Strain Th	Std	StressLab	Std	Weigth	Depth
I.D.	deg	deg	deg	deg	deg	Å	deg	1.E-06	1.E-06	1.E-06	1.E-06	MPa	MPa		µm
13883	0	-42.38	26.6	0	137.9638	0.8252	0.0048	-243.16	115.91	-317.48	113.99	-40.85	19.47	10.3	12.0
13884	60	-42.41	26.6	0	138.0166	0.8250	0.0049	-424.37	110.49	-363.78	111.81	-71.29	18.56	9.9	12.0
13885	120	-42.39	26.6	0	137.9733	0.8252	0.0038	-276.93	109.42	-399.07	110.77	-46.52	18.38	16.4	12.0
13886	180	-42.4	26.6	0	138.0065	0.8251	0.0025	-391.67	112.73	-361.20	112.17	-65.80	18.94	37.9	12.0
13887	210	-42.39	26.6	0	137.9890	0.8251	0.0025	-327.75	111.68	-342.83	112.27	-55.06	18.76	37.9	12.0
13888	270	-42.41	26.6	0	138.0152	0.8250	0.0075	-418.11	116.16	-333.88	113.70	-70.24	19.52	4.2	12.0
13889	330	-42.4	26.6	0	137.9972	0.8251	0.0035	-354.34	115.36	-318.81	114.09	-59.53	19.38	19.3	12.0
13890	30	-28.58	40.4	0	137.9669	0.8252	0.0044	-252.92	114.77	-240.41	112.16	-42.49	19.28	12.2	15.5
13891	90	-28.58	40.4	0	137.9662	0.8252	0.0031	-255.05	112.57	-280.54	110.44	-42.85	18.91	24.6	15.5
13892	150	-28.61	40.4	0	138.0204	0.8250	0.0036	-432.35	113.11	-279.33	111.04	-72.64	19.00	18.3	15.5
13893	180	-28.58	40.4	0	137.9648	0.8252	0.0033	-249.12	110.39	-263.18	111.54	-41.85	18.55	21.7	15.5
13894	240	-28.56	40.4	0	137.9227	0.8253	0.0030	-109.27	113.14	-238.21	112.03	-18.36	19.01	26.3	15.5
13895	300	-28.58	40.4	0	137.9565	0.8252	0.0052	-219.65	111.39	-226.82	112.83	-36.90	18.71	8.8	15.5
13896	360	-28.58	40.4	0	137.9617	0.8252	0.0023	-237.24	110.80	-226.41	112.90	-39.86	18.61	44.7	15.5

Table B.16: Test results for sample X1G15 test 13883 plane {422}. 47μm subsurface.

Stress [MPa]				Std [MPa]				Strain [-]				Std [-]			
-95.30	-16.76	-3.98		25.98	1.70	0.51		-2.95E-04	-1.24E-04	-2.90E-05		8.20E-05	1.30E-05	4.00E-06	
-16.76	-145.96	-8.40		1.70	26.06	0.41		-1.24E-04	-6.69E-04	-6.20E-05		1.30E-05	8.20E-05	3.00E-06	
-3.98	-8.40	-44.40		0.51	0.41	25.46		-2.90E-05	-6.20E-05	8.00E-05		4.00E-06	3.00E-06	7.90E-05	
Principal values [MPa]				Std [MPa]											
-151.83	0	0		26.08	0	0									
0	-90.27	0		0	26.00	0									
0	0	-43.56		0	0	25.44									
Sample	X1G15														
Plane	{422}														
Depth	47	µm													
Hydro	-95.22	MPa													
Mises	69.28	MPa													
Test	φ	Ψ	Ω	χ	2Θ	$d_{[hkl]}$	Std(2Θ)	StrainLab	Std	Strain Th	Std	StressLab	Std	Weigth	Depth
I.D.	deg	deg	deg	deg	deg	Å	deg	1.E-06	1.E-06	1.E-06	1.E-06	MPa	MPa		µm
13883	0	-43.49	26.6	0	140.1814	0.8192	0.0026	-59.70	76.54	-68.28	79.37	-10.03	12.86	20.3	11.9
13884	60	-43.51	26.6	0	140.2156	0.8192	0.0046	-169.95	79.79	-213.15	78.54	-28.55	13.40	6.5	11.9
13885	120	-43.49	26.6	0	140.1828	0.8192	0.0026	-66.77	78.53	-140.71	78.14	-11.22	13.19	20.3	11.9
13886	180	-43.53	26.6	0	140.2521	0.8191	0.0035	-280.43	80.29	-127.12	78.78	-47.11	13.49	11.2	11.9
13887	210	-43.5	26.6	0	140.1937	0.8192	0.0027	-96.87	80.03	-249.00	79.44	-16.27	13.44	18.8	11.9
13888	270	-43.57	26.6	0	140.3331	0.8189	0.0014	-537.73	78.85	-337.57	80.38	-90.34	13.25	70.1	11.9
13889	330	-43.48	26.6	0	140.1691	0.8193	0.0036	-19.65	83.32	-96.63	80.19	-3.30	14.00	10.6	11.9
13890	30	-29.69	40.4	0	140.1876	0.8192	0.0027	-79.39	81.32	-12.51	78.27	-13.34	13.66	18.8	15.5
13891	90	-29.7	40.4	0	140.1961	0.8192	0.0037	-101.28	77.72	-50.26	77.63	-17.01	13.06	10.0	15.5
13892	150	-29.67	40.4	0	140.1368	0.8194	0.0036	84.21	77.10	-3.52	77.95	14.15	12.95	10.6	15.5
13893	180	-29.71	40.4	0	140.2134	0.8192	0.0033	-161.52	78.62	-37.15	78.37	-27.14	13.21	12.6	15.5
13894	240	-29.69	40.4	0	140.1720	0.8193	0.0022	-29.43	79.69	-165.63	79.37	-4.94	13.39	28.4	15.5
13895	300	-29.69	40.4	0	140.1704	0.8193	0.0035	-20.33	80.96	-87.81	79.79	-3.42	13.60	11.2	15.5
13896	360	-29.69	40.4	0	140.1743	0.8193	0.0025	-37.20	77.28	13.48	78.81	-6.25	12.98	22.0	15.5

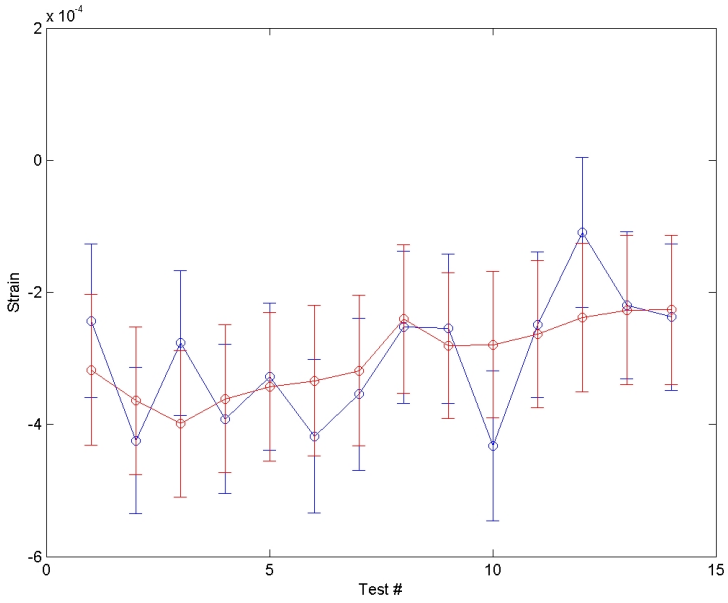

(a) plane{224}

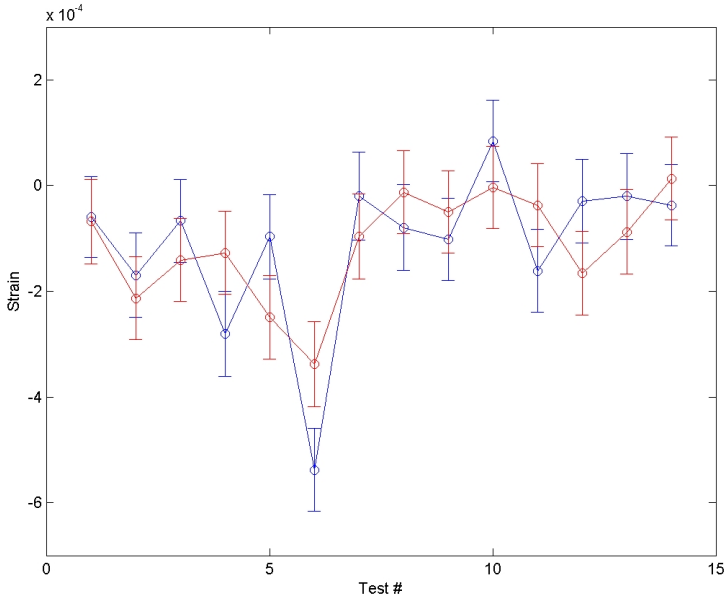

(b) plane{422}

Figure B.8: Comparison of the theoretical strain component ε_{33} (red) with the corresponding measured component ε'_{33} for sample X1G15 test 13883. 47μm subsurface.

Table B.17: Test results for sample X1G15 test 13934 plane {224}. 117μm subsurface.

Stress [MPa]				Std [MPa]				Strain [-]				Std [-]			
11.66	-15.29	-1.08		56.35	1.57	0.66		1.13E-04	-1.13E-04	-8.00E-06		1.74E-04	1.20E-05	5.00E-06	
-15.29	-26.63	7.70		1.57	56.51	0.95		-1.13E-04	-1.70E-04	5.70E-05		1.20E-05	1.75E-04	7.00E-06	
-1.08	7.70	-3.60		0.66	0.95	57.16		-8.00E-06	5.70E-05	0.00E+00		5.00E-06	7.00E-06	1.79E-04	
Principal values [MPa]				Std [MPa]											
-33.67	0	0		56.46	0	0									
0	-2.62	0		0	57.03	0									
0	0	17.72		0	0	56.53									
Sample	X1G15														
Plane	{224}														
Depth	117	µm													
Hydro	-6.19	MPa													
Mises	33.56	MPa													
Test	φ	Ψ	Ω	χ	2Θ	$d_{[hkl]}$	Std(2Θ)	StrainLab	Std	Strain Th	Std	StressLab	Std	Weigth	Depth
I.D.	deg	deg	deg	deg	deg	Å	deg	1.E-06	1.E-06	1.E-06	1.E-06	MPa	MPa		µm
13934	0	-42.39	26.6	0	137.9893	0.8251	0.0047	50.29	175.52	59.08	177.27	8.45	29.49	15.0	12.0
13935	30	-42.41	26.6	0	138.0174	0.8250	0.0025	-42.44	176.92	-46.83	176.63	-7.13	29.72	53.1	12.0
13936	60	-42.41	26.6	0	138.0296	0.8250	0.0034	-84.32	177.70	-134.74	176.77	-14.17	29.85	28.7	12.0
13937	90	-42.42	26.6	0	138.0454	0.8250	0.0077	-139.59	174.39	-134.00	177.26	-23.45	29.30	5.6	12.0
13938	120	-42.42	26.6	0	138.0309	0.8250	0.0043	-89.84	175.91	-53.75	177.24	-15.09	29.55	18.0	12.0
13939	150	-42.4	26.6	0	137.9961	0.8251	0.0072	27.91	183.15	28.32	176.68	4.69	30.77	6.4	12.0
13940	180	-42.39	26.6	0	137.9794	0.8251	0.0020	84.77	176.12	43.25	175.86	14.24	29.59	83.0	12.0
13941	210	-42.4	26.6	0	138.0096	0.8251	0.0043	-18.18	170.92	-3.93	175.29	-3.05	28.72	18.0	12.0
13942	240	-42.41	26.6	0	138.0220	0.8250	0.0032	-59.86	178.29	-44.60	175.68	-10.06	29.95	32.4	12.0
13943	270	-42.41	26.6	0	138.0158	0.8250	0.0047	-36.42	177.52	-20.74	176.80	-6.12	29.82	15.0	12.0
13944	300	-42.39	26.6	0	137.9778	0.8251	0.0020	88.66	177.75	52.20	177.73	14.89	29.86	83.0	12.0
13945	330	-42.39	26.6	0	137.9729	0.8252	0.0021	106.94	178.09	98.60	177.88	17.97	29.92	75.3	12.0
13946	360	-42.4	26.6	0	137.9910	0.8251	0.0036	46.72	179.09	59.08	177.27	7.85	30.09	25.6	12.0
13947	0	-42.4	26.6	0	137.9908	0.8251	0.0040	43.34	176.11	59.09	177.27	7.28	29.59	20.7	12.0
13948	30	-42.41	26.6	0	138.0235	0.8250	0.0025	-62.36	176.85	-46.83	176.63	-10.48	29.71	53.1	12.0
13949	60	-42.42	26.6	0	138.0473	0.8250	0.0080	-136.28	183.16	-134.77	176.77	-22.89	30.77	5.2	12.0

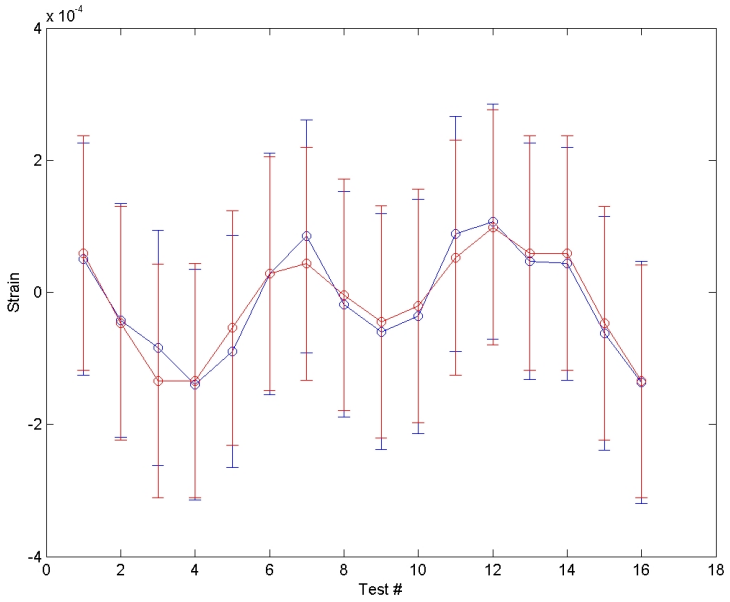

Figure B.9: Comparison of the theoretical strain component ε_{33} (red) with the corresponding measured component ε'_{33} for sample X1G15 test 13934 plane {224}. 117μm subsurface.

Table B.18: Test results for sample X1G10 test 13781 plane {224}. 124μm subsurface.

Stress [MPa]				Std [MPa]				Strain [-]				Std [-]			
-68.47	-8.24	-4.42		70.57	9.06	2.90		-2.06E-04	-6.10E-05	-3.30E-05		2.24E-04	6.70E-05	2.10E-05	
-8.24	-91.98	12.87		9.06	72.79	4.80		-6.10E-05	-3.79E-04	9.50E-05		6.70E-05	2.45E-04	3.50E-05	
-4.42	12.87	-49.40		2.90	4.80	67.35		-3.30E-05	9.50E-05	-6.50E-05		2.10E-05	3.50E-05	2.01E-04	
Principal values [MPa]				Std [MPa]											
-100.99	0	0		69.93	0	0									
0	-66.30	0		0	71.61	0									
0	0	-42.57		0	0	68.52									
Sample	X1G10														
Plane	{224}														
Depth	124	µm													
Hydro	-69.95	MPa													
Mises	33.38	MPa													
Test	φ	Ψ	Ω	χ	2Θ	$d_{[hkl]}$	Std(2Θ)	StrainLab	Std	Strain Th	Std	StressLab	Std	Weigth	Depth
I.D.	deg	deg	deg	deg	deg	Å	deg	1.E-06	1.E-06	1.E-06	1.E-06	MPa	MPa		µm
13781	0	-55.36	13.6	0	137.9211	0.8253	0.0104	-95.67	214.84	-129.61	216.88	-16.07	36.09	84.3	7.3
13782	0	-42.37	26.6	0	137.9322	0.8253	0.0224	-123.01	217.51	-96.27	211.88	-20.67	36.54	18.2	12.0
13783	0	-28.55	40.4	0	137.9021	0.8254	0.0075	-23.92	200.43	-69.61	206.77	-4.02	33.67	162.1	15.5
13784	0	-0.39	68.6	0	137.9725	0.8252	0.0142	-261.64	197.81	-64.43	200.83	-43.96	33.23	45.2	18.5
13785	0	27.85	96.8	0	137.9028	0.8254	0.0117	-48.61	214.30	-122.51	204.94	-8.17	36.00	66.6	15.7
13786	0	41.63	110.6	0	137.9411	0.8252	0.0274	-153.26	204.76	-159.36	210.21	-25.75	34.40	12.1	12.2
13787	0	54.62	123.6	0	137.9609	0.8252	0.0168	-249.50	238.79	-189.19	215.74	-41.92	40.12	32.3	7.6
13788	45	-55.41	13.6	0	138.0150	0.8250	0.0142	-433.44	204.93	-301.50	207.29	-72.82	34.43	45.2	7.3
13789	45	-42.36	26.6	0	137.9282	0.8253	0.0114	-134.74	218.75	-239.72	205.05	-22.64	36.75	70.2	12.0
13790	45	-28.57	40.4	0	137.9307	0.8253	0.0101	-138.20	210.91	-167.85	203.26	-23.22	35.43	89.4	15.5
13791	45	-0.36	68.6	0	137.9166	0.8253	0.0085	-90.72	212.69	-65.42	200.85	-15.24	35.73	126.2	18.5
13792	45	27.84	96.8	0	137.9126	0.8253	0.0120	-67.62	199.06	-91.31	198.87	-11.36	33.44	63.3	15.7
13793	45	41.63	110.6	0	137.9441	0.8252	0.0168	-182.78	222.06	-148.25	199.65	-30.71	37.31	32.3	12.2
13794	45	54.64	123.6	0	137.9276	0.8253	0.0204	-147.20	192.93	-214.91	202.10	-24.73	32.41	21.9	7.6
13795	90	-55.45	13.6	0	138.0907	0.8248	0.0597	-646.38	285.43	-366.81	234.02	-108.59	47.95	2.6	7.3
13796	90	-42.33	26.6	0	137.8541	0.8255	0.0104	119.00	206.21	-301.96	222.40	19.99	34.64	84.3	12.0
13797	90	-28.58	40.4	0	137.9597	0.8252	0.0166	-228.60	213.14	-216.61	211.28	-38.40	35.81	33.1	15.5

Table B.19: Test results for sample X1G10 test 13781 plane {422}. 124μm subsurface.

Stress [MPa]				Std [MPa]				Strain [-]				Std [-]			
-22.96	18.22	1.64		41.50	7.11	3.26		7.00E-05	1.34E-04	1.20E-05		1.54E-04	5.30E-05	2.40E-05	
18.22	-84.99	18.83		7.11	37.22	2.61		1.34E-04	-3.88E-04	1.39E-04		5.30E-05	1.19E-04	1.90E-05	
1.64	18.83	-59.42		3.26	2.61	36.65		1.20E-05	1.39E-04	-1.99E-04		2.40E-05	1.90E-05	1.13E-04	
Principal values [MPa]				Std [MPa]											
-99.18	0	0		37.29	0	0									
0	-53.05	0		0	37.99	0									
0	0	-15.14		0	0	38.99									
Sample	X1G10														
Plane	{422}														
Depth	124	µm													
Hydro	-55.79	MPa													
Mises	51.91	MPa													
Test	φ	Ψ	Ω	χ	2Θ	$d_{[hkl]}$	Std(2Θ)	StrainLab	Std	Strain Th	Std	StressLab	Std	Weigth	Depth
I.D.	deg	deg	deg	deg	deg	Å	deg	1.E-06	1.E-06	1.E-06	1.E-06	MPa	MPa		µm
13781	0	-56.48	13.6	0	140.1603	0.8193	0.0529	26.52	203.95	-23.61	146.24	4.46	34.26	2.3	7.2
13782	0	-43.52	26.6	0	140.2476	0.8191	0.0138	-264.60	127.36	-83.93	134.16	-44.45	21.40	34.4	11.9
13783	0	-29.68	40.4	0	140.1619	0.8193	0.0088	6.36	115.64	-143.89	122.61	1.07	19.43	84.6	15.5
13784	0	-1.54	68.6	0	140.2897	0.8190	0.0116	-386.25	117.92	-199.94	113.31	-64.89	19.81	48.7	18.6
13785	0	26.67	96.8	0	140.2526	0.8191	0.0080	-275.67	110.15	-135.57	110.23	-46.31	18.51	102.3	16.1
13786	0	40.51	110.6	0	140.1729	0.8193	0.0126	-24.23	108.66	-73.99	112.34	-4.07	18.25	41.3	12.8
13787	0	53.52	123.6	0	140.1629	0.8193	0.0194	19.14	115.17	-13.95	120.49	3.22	19.35	17.4	8.4
13788	45	-56.53	13.6	0	140.2620	0.8190	0.0112	-310.78	108.70	-176.21	112.78	-52.21	18.26	52.2	7.2
13789	45	-43.49	26.6	0	140.1817	0.8192	0.0094	-53.26	111.67	-223.40	111.65	-8.95	18.76	74.1	11.9
13790	45	-29.72	40.4	0	140.2342	0.8191	0.0107	-221.61	106.51	-248.52	111.17	-37.23	17.89	57.2	15.5
13791	45	-1.5	68.6	0	140.2008	0.8192	0.0060	-117.84	109.63	-204.96	112.98	-19.80	18.42	181.9	18.6
13792	45	26.71	96.8	0	140.1766	0.8193	0.0056	-36.65	116.19	-78.43	114.85	-6.16	19.52	208.9	16.1
13793	45	40.54	110.6	0	140.1156	0.8194	0.0153	164.04	126.69	-20.18	114.88	27.56	21.28	28.0	12.8
13794	45	53.5	123.6	0	140.1931	0.8192	0.0110	-108.14	120.51	15.51	114.72	-18.17	20.25	54.1	8.4
13795	90	-56.58	13.6	0	140.3663	0.8188	0.0187	-626.21	117.95	-458.72	108.12	-105.20	19.82	18.7	7.2
13796	90	-43.52	26.6	0	140.2305	0.8191	0.0132	-185.63	116.59	-427.71	106.43	-31.19	19.59	37.6	11.9
13797	90	-29.73	40.4	0	140.2548	0.8191	0.0088	-291.00	115.98	-365.57	107.01	-48.89	19.49	84.6	15.5
13798	90	-1.57	68.6	0	140.3379	0.8188	0.0107	-547.67	115.48	-207.23	112.74	-92.01	19.40	57.2	18.6
13799	90	26.74	96.8	0	140.1277	0.8194	0.0153	135.97	129.17	-126.02	119.77	22.84	21.70	28.0	16.1
13800	90	40.5	110.6	0	140.1961	0.8192	0.0213	-117.76	141.15	-141.83	122.58	-19.78	23.71	14.4	12.8
13801	90	53.46	123.6	0	140.2741	0.8190	0.0244	-311.34	120.34	-188.40	124.17	-52.31	20.22	11.0	8.5

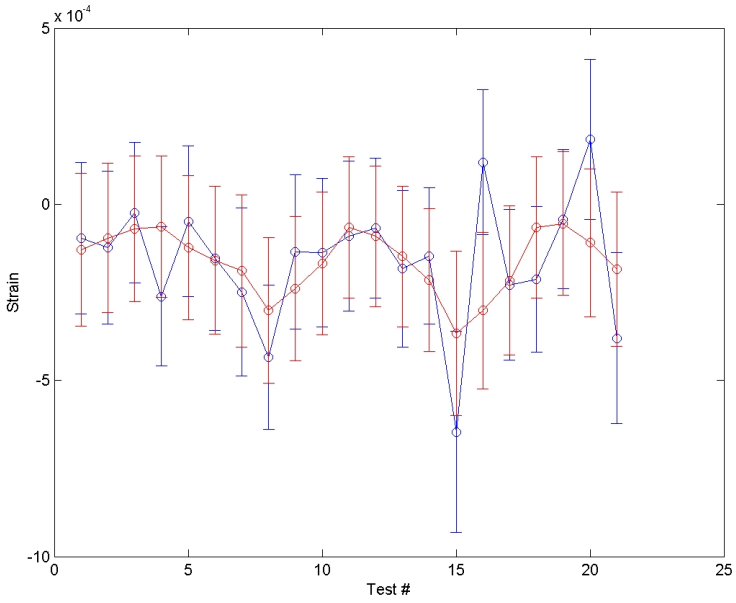

(a) plane{224}

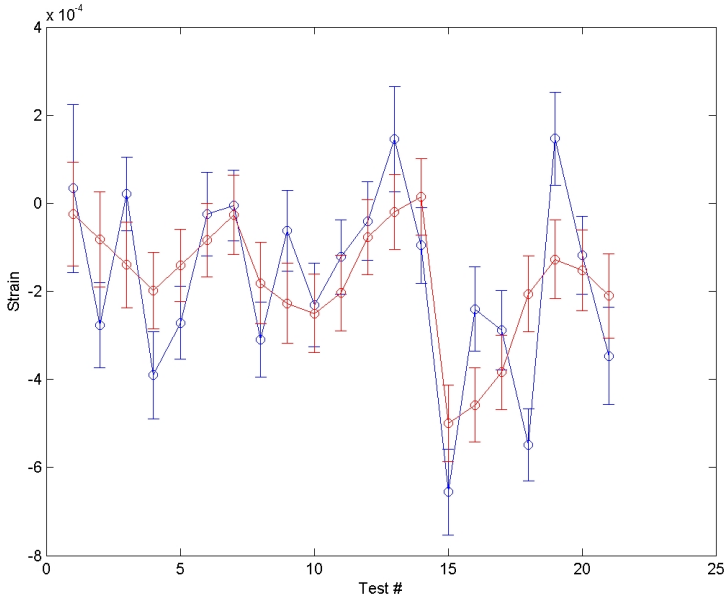

(b) plane{422}

Figure B.10: Comparison of the theoretical strain component ε_{33} (red) with the corresponding measured component ε'_{33} for sample X1G10 test 13781. 124μm subsurface.

Table B.20: Test results for sample X1G10 test 13919 plane {224}. 154μm subsurface.

Stress [MPa]				Std [MPa]				Strain [-]				Std [-]			
-86.07	9.29	-1.10		113.87	2.22	1.34		-3.88E-04	6.90E-05	-8.00E-06		5.53E-04	1.60E-05	1.00E-05	
9.29	-50.90	5.40		2.22	111.86	1.65		6.90E-05	-1.28E-04	4.00E-05		1.60E-05	5.39E-04	1.20E-05	
-1.10	5.40	-36.23		1.34	1.65	55.98		-8.00E-06	4.00E-05	-2.00E-05		1.00E-05	1.20E-05	5.45E-04	
Principal values [MPa]				Std [MPa]											
-89.36	0	0		113.56	0	0									
0	-70.97	0		0	107.24	0									
0	0	-12.88		0	0	50.06									
Sample	X1G10														
Plane	{224}														
Depth	154	µm													
Hydro	-57.74	MPa													
Mises	37.66	MPa													
Test	φ	Ψ	Ω	χ	2Θ	$d_{[hkl]}$	Std(2Θ)	StrainLab	Std	Strain Th	Std	StressLab	Std	Weigth	Depth
I.D.	deg	deg	deg	deg	deg	Å	deg	1.E-06	1.E-06	1.E-06	1.E-06	MPa	MPa		µm
13919	0	-42.36	26.6	0	137.9144	0.8253	0.0062	-117.37	145.52	-178.86	140.48	-19.72	24.45	7.9	12.0
13920	60	-42.35	26.6	0	137.9078	0.8253	0.0047	-99.09	137.11	-101.96	139.87	-16.65	23.03	13.7	12.0
13921	120	-42.37	26.6	0	137.9393	0.8253	0.0054	-202.26	136.53	-164.03	133.28	-33.98	22.94	10.4	12.0
13922	180	-42.35	26.6	0	137.9024	0.8254	0.0066	-77.13	132.26	-195.06	132.52	-12.96	22.22	7.0	12.0
13923	210	-42.38	26.6	0	137.9561	0.8252	0.0055	-251.31	135.12	-117.85	132.57	-42.22	22.70	10.0	12.0
13924	270	-42.33	26.6	0	137.8645	0.8255	0.0104	53.68	136.33	-29.40	133.05	9.02	22.90	2.8	12.0
13925	330	-42.38	26.6	0	137.9543	0.8252	0.0056	-248.94	134.74	-157.73	136.01	-41.82	22.64	9.7	12.0

Table B.21: Test results for sample X1G10 test 13919 plane {422}. 154μm subsurface.

Stress [MPa]				Std [MPa]				Strain [-]				Std [-]			
-41.26	41.18	-10.84		42.13	1.98	0.96		1.10E-05	3.04E-04	-8.00E-05		1.77E-04	1.50E-05	7.00E-06	
41.18	-115.54	-21.37		1.98	40.96	1.54		3.04E-04	-5.38E-04	-1.58E-04		1.50E-05	1.65E-04	1.10E-05	
-10.84	-21.37	-63.75		0.96	1.54	26.61		-8.00E-05	-1.58E-04	-1.55E-04		7.00E-06	1.10E-05	1.36E-04	
Principal values [MPa]				Std [MPa]											
-137.45	0	0		40.00	0	0									
0	-72.23	0		0	34.13	0									
0	0	-10.86		0	0	28.40									
Sample	X1G10														
Plane	{422}														
Depth	154	µm													
Hydro	-73.52	MPa													
Mises	77.87	MPa													
Test	φ	Ψ	Ω	χ	2Θ	$d_{[hkl]}$	Std(2Θ)	StrainLab	Std	Strain Th	Std	StressLab	Std	Weigth	Depth
I.D.	deg	deg	deg	deg	deg	Å	deg	1.E-06	1.E-06	1.E-06	1.E-06	MPa	MPa		µm
13919	0	-43.49	26.6	0	140.1864	0.8192	0.0040	-39.89	84.97	3.10	83.45	-6.70	14.27	12.1	11.9
13920	60	-43.49	26.6	0	140.1709	0.8193	0.0034	6.66	84.09	29.41	85.32	1.12	14.13	16.7	11.9
13921	120	-43.52	26.6	0	140.2485	0.8191	0.0042	-236.90	82.45	-300.14	81.59	-39.80	13.85	10.9	11.9
13922	180	-43.54	26.6	0	140.2728	0.8190	0.0041	-318.09	81.77	-156.64	82.07	-53.44	13.74	11.5	11.9
13923	210	-43.49	26.6	0	140.1713	0.8193	0.0033	7.33	84.49	-165.09	83.85	1.23	14.19	17.7	11.9
13924	270	-43.58	26.6	0	140.3625	0.8188	0.0093	-588.51	87.74	-494.63	87.08	-98.87	14.74	2.2	11.9
13925	330	-43.52	26.6	0	140.2317	0.8191	0.0058	-190.35	82.15	-276.05	82.14	-31.98	13.80	5.7	11.9

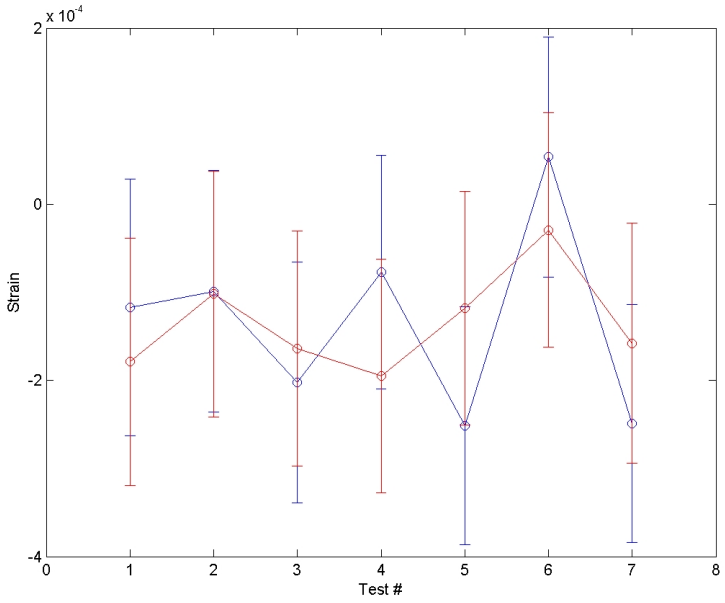

(a) plane{224}

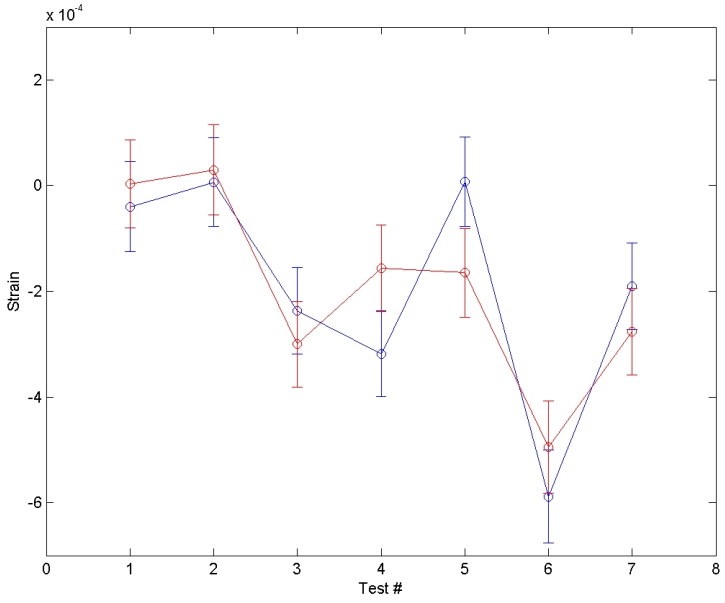

(b) plane{422}

Figure B.11: Comparison of the theoretical strain component ε_{33} (red) with the corresponding measured component ε'_{33} for sample X1G10 test 13919. 154μm subsurface.

Table B.22: Test results for sample X1G10 test 13926 plane {224}. 154μm subsurface.

Stress [MPa]				Std [MPa]				Strain [-]				Std [-]			
36.85	-40.25	4.34		52.00	7.50	1.58		3.78E-04	-2.97E-04	3.20E-05		1.64E-04	5.50E-05	1.20E-05	
-40.25	-92.55	5.50		7.50	51.62	1.38		-2.97E-04	-5.77E-04	4.10E-05		5.50E-05	1.61E-04	1.00E-05	
4.34	5.50	-18.49		1.58	1.38	51.85		3.20E-05	4.10E-05	-3.00E-05		1.20E-05	1.00E-05	1.61E-04	
Principal values [MPa]				Std [MPa]											
-104.78	0	0		51.12	0	0									
0	-18.14	0		0	51.81	0									
0	0	48.73		0	0	52.92									
Sample	X1G10														
Plane	{224}														
Depth	154	µm													
Hydro	-24.73	MPa													
Mises	97.75	MPa													
Test	φ	Ψ	Ω	χ	2Θ	$d_{[hkl]}$	Std(2Θ)	StrainLab	Std	Strain Th	Std	StressLab	Std	Weigth	Depth
I.D.	deg	deg	deg	deg	deg	Å	deg	1.E-06	1.E-06	1.E-06	1.E-06	MPa	MPa		µm
13926	30	-28.58	40.4	0	137.9509	0.8252	0.0040	-66.28	160.10	-90.92	158.22	-11.13	26.90	14.9	15.5
13927	90	-28.59	40.4	0	137.9874	0.8251	0.0019	-187.59	160.61	-189.84	161.87	-31.51	26.98	66.0	15.5
13928	150	-28.56	40.4	0	137.9207	0.8253	0.0082	42.15	168.59	73.37	165.99	7.08	28.32	3.5	15.5
13929	180	-28.55	40.4	0	137.8928	0.8254	0.0039	130.64	161.57	89.71	163.26	21.95	27.14	15.7	15.5
13930	240	-28.59	40.4	0	137.9764	0.8251	0.0065	-145.36	159.52	-116.86	158.88	-24.42	26.80	5.6	15.5
13931	300	-28.57	40.4	0	137.9308	0.8253	0.0067	1.39	161.89	-25.97	161.36	0.23	27.20	5.3	15.5
13932	360	-28.57	40.4	0	137.9305	0.8253	0.0070	0.52	158.76	35.98	159.91	0.09	26.67	4.9	15.5

Table B.23: Test results for sample X1G10 test 13926 plane {422}. 154μm subsurface.

Stress [MPa]				Std [MPa]				Strain [-]				Std [-]			
-79.71	42.83	16.82		21.47	3.51	0.91		-3.01E-04	3.16E-04	1.24E-04		7.30E-05	2.60E-05	7.00E-06	
42.83	-54.11	-2.00		3.51	22.53	1.56		3.16E-04	-1.12E-04	-1.50E-05		2.60E-05	8.00E-05	1.20E-05	
16.82	-2.00	-67.48		0.91	1.56	20.92		1.24E-04	-1.50E-05	-2.10E-04		7.00E-06	1.20E-05	6.30E-05	
Principal values [MPa]				Std [MPa]											
-116.37	0	0		20.48	0	0									
0	-64.60	0		0	20.96	0									
0	0	-20.33		0	0	22.93									
Sample	X1G10														
Plane	{422}														
Depth	154	µm													
Hydro	-67.10	MPa													
Mises	60.03	MPa													
Test	φ	Ψ	Ω	χ	2Θ	$d_{[hkl]}$	Std(2Θ)	StrainLab	Std	Strain Th	Std	StressLab	Std	Weigth	Depth
I.D.	deg	deg	deg	deg	deg	Å	deg	1.E-06	1.E-06	1.E-06	1.E-06	MPa	MPa		µm
13926	30	-29.73	40.4	0	140.2530	0.8191	0.0039	-282.56	62.80	-239.97	65.69	-47.47	10.55	10.6	15.5
13927	90	-29.71	40.4	0	140.2158	0.8192	0.0066	-162.19	69.15	-173.56	65.93	-27.25	11.62	3.7	15.5
13928	150	-29.71	40.4	0	140.2204	0.8191	0.0058	-177.96	60.06	-189.41	62.86	-29.90	10.09	4.8	15.5
13929	180	-29.71	40.4	0	140.2111	0.8192	0.0027	-150.54	66.79	-125.80	64.44	-25.29	11.22	22.1	15.5
13930	240	-29.69	40.4	0	140.1866	0.8192	0.0066	-63.55	68.59	-88.27	68.41	-10.68	11.52	3.7	15.5
13931	300	-29.74	40.4	0	140.2759	0.8190	0.0027	-359.15	62.63	-329.66	63.57	-60.34	10.52	22.1	15.5
13932	360	-29.73	40.4	0	140.2531	0.8191	0.0033	-290.42	67.21	-339.58	64.54	-48.79	11.29	14.8	15.5

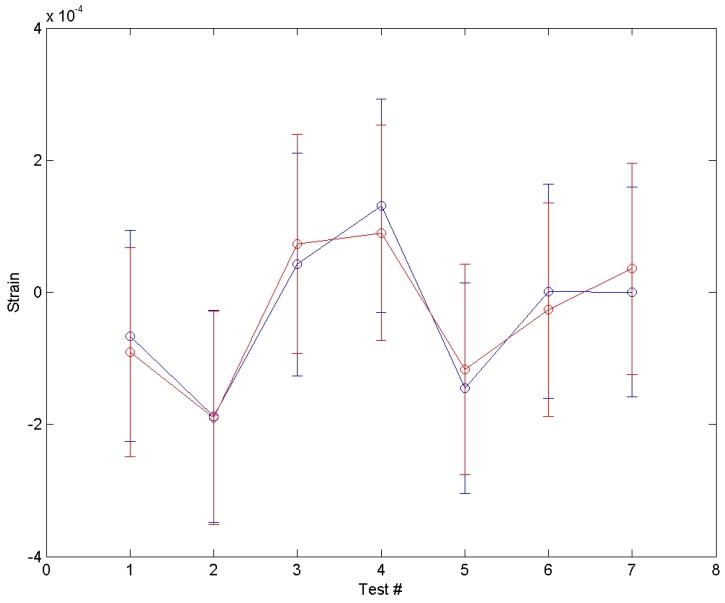

(a) plane{224}

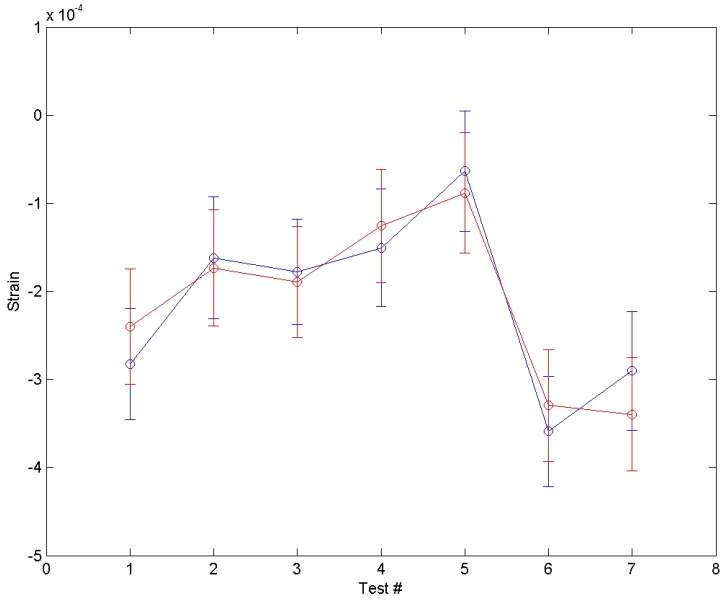

(b) plane{422}

Figure B.12: Comparison of the theoretical strain component ε_{33} (red) with the corresponding measured component ε'_{33} for sample X1G10 test 13926. 154μm subsurface.

Table B.24: Test results for sample X2G08 test 13711 plane {224}. Surface.

Stress [MPa]				Std [MPa]				Strain [-]				Std [-]			
-554.10	12.26	-55.61		79.56	51.22	19.72		-2.22E-03	9.00E-05	-4.10E-04		3.76E-04	3.78E-04	1.46E-04	
12.26	-683.32	-2.81		51.22	104.21	16.64		9.00E-05	-3.17E-03	-2.10E-05		3.78E-04	5.55E-04	1.23E-04	
-55.61	-2.81	-71.49		19.72	16.64	47.40		-4.10E-04	-2.10E-05	1.34E-03		1.46E-04	1.23E-04	2.24E-04	
Principal values [MPa]				Std [MPa]											
-706.63	0	0		95.45	0	0									
0	-538.68	0		0	78.25	0									
0	0	-63.60		0	0	48.74									
Sample	X2G08														
Plane	{224}														
Depth	0	µm													
Hydro	-436.30	MPa													
Mises	454.58	MPa													
Test	φ	Ψ	Ω	χ	2Θ	$d_{[hkl]}$	Std(2Θ)	StrainLab	Std	Strain Th	Std	StressLab	Std	Weigth	Depth
I.D.	deg	deg	deg	deg	deg	Å	deg	1.E-06	1.E-06	1.E-06	1.E-06	MPa	MPa		µm
13711	0	-55.44	13.6	0	138.0832	0.8249	0.2042	-461.26	575.04	-689.96	325.55	-77.49	96.61	6.0	7.3
13712	0	-42.38	26.6	0	137.9572	0.8252	0.0363	-92.95	170.69	132.63	271.52	-15.61	28.68	190.1	12.0
13713	0	-28.46	40.4	0	137.7239	0.8258	0.0869	739.12	296.21	877.44	228.86	124.17	49.76	33.2	15.5
13714	0	-0.1	68.6	0	137.3903	0.8268	0.0706	1874.77	326.49	1343.44	223.37	314.96	54.85	50.3	18.5
13715	0	27.89	96.8	0	137.8124	0.8256	0.0465	460.79	242.38	222.51	244.85	77.41	40.72	115.9	15.7
13716	0	41.6	110.6	0	137.9933	0.8251	0.1562	-117.88	626.83	-636.58	256.73	-19.80	105.31	10.3	12.3
13717	0	54.33	123.6	0	138.5308	0.8236	0.1190	-1857.06	366.28	-1398.81	287.04	-311.99	61.53	17.7	7.8
13718	45	-55.41	13.6	0	138.0101	0.8251	0.0500	-362.26	193.21	-1049.39	198.61	-60.86	32.46	100.2	7.3
13719	45	-42.45	26.6	0	138.0919	0.8248	0.0544	-551.86	251.21	-152.68	208.42	-92.71	42.20	84.7	12.0
13720	45	-28.45	40.4	0	137.7024	0.8259	0.0476	765.05	228.03	701.49	217.69	128.53	38.31	110.6	15.5
13721	45	-0.17	68.6	0	137.5347	0.8264	0.0479	1356.79	227.62	1343.87	223.65	227.94	38.24	109.2	18.5
13722	45	27.89	96.8	0	137.8292	0.8256	0.0639	340.15	311.55	226.34	206.92	57.14	52.34	61.4	15.7
13723	45	41.57	110.6	0	138.0670	0.8249	0.0786	-428.50	317.94	-699.09	198.57	-71.99	53.41	40.6	12.3
13724	45	54.3	123.6	0	138.5907	0.8235	0.0459	-2221.74	198.47	-1550.77	194.64	-373.25	33.34	118.9	7.8
13725	90	-55.61	13.6	0	138.4195	0.8239	0.1107	-1724.92	326.78	-1714.97	290.65	-289.79	54.90	20.4	7.3
13726	90	-42.52	26.6	0	138.2481	0.8244	0.1098	-1129.31	354.60	-701.24	179.70	-189.72	59.57	20.8	12.0
13727	90	-28.51	40.4	0	137.8202	0.8256	0.0433	419.01	204.09	331.23	167.50	70.39	34.29	133.6	15.5
13728	90	-0.23	68.6	0	137.6527	0.8260	0.0396	915.65	217.47	1342.30	223.91	153.83	36.54	159.8	18.5
13729	90	27.84	96.8	0	137.9263	0.8253	0.0459	2.32	175.74	340.54	192.24	0.39	29.52	118.9	15.7
13730	90	41.52	110.6	0	138.1659	0.8246	0.0650	-791.81	250.88	-662.40	290.46	-133.02	42.15	59.3	12.3
13731	90	54.52	123.6	0	138.1615	0.8246	0.3127	-1194.24	832.38	-1666.03	406.01	-200.63	139.84	2.6	7.7

Table B.25: Test results for sample X2G08 test 13711 plane {422}. Surface.

Stress [MPa]				Std [MPa]				Strain [-]				Std [-]			
-663.87	74.62	-63.26		107.09	32.05	25.07		-2.49E-03	5.51E-04	-4.67E-04		5.20E-04	2.37E-04	1.85E-04	
74.62	-916.76	14.87		32.05	56.51	15.08		5.51E-04	-4.35E-03	1.10E-04		2.37E-04	2.31E-04	1.11E-04	
-63.26	14.87	-108.86		25.07	15.08	51.99		-4.67E-04	1.10E-04	1.61E-03		1.85E-04	1.11E-04	1.30E-04	
Principal values [MPa]				Std [MPa]											
-944.96	0	0		71.45	0	0									
0	-643.64	0		0	92.75	0									
0	0	-100.89		0	0	48.68									
Sample	X2G08														
Plane	{422}														
Depth	0	µm													
Hydro	-563.17	MPa													
Mises	565.19	MPa													
Test	φ	Ψ	Ω	χ	2Θ	$d_{[hkl]}$	Std(2Θ)	StrainLab	Std	Strain Th	Std	StressLab	Std	Weigth	Depth
I.D.	deg	deg	deg	deg	deg	Å	deg	1.E-06	1.E-06	1.E-06	1.E-06	MPa	MPa		µm
13711	0	-56.56	13.6	0	140.3176	0.8189	0.1099	-492.81	270.43	-813.30	258.43	-82.79	45.43	12.8	7.2
13712	0	-43.46	26.6	0	140.1230	0.8194	0.0394	116.04	152.05	137.78	168.83	19.49	25.54	99.9	11.9
13713	0	-29.52	40.4	0	139.8488	0.8201	0.0442	985.99	205.74	1015.48	126.28	165.65	34.56	79.4	15.5
13714	0	-1.19	68.6	0	139.5753	0.8208	0.0590	1894.52	219.70	1627.60	126.89	318.28	36.91	44.6	18.6
13715	0	26.8	96.8	0	139.9966	0.8197	0.0411	509.36	186.48	401.61	309.45	85.57	31.33	91.8	16.1
13716	0	40.55	110.6	0	140.0938	0.8195	0.2771	-137.72	1017.88	-577.55	421.00	-23.14	171.00	2.0	12.8
13717	0	53.2	123.6	0	140.7993	0.8177	0.1416	-2110.76	557.18	-1462.81	515.32	-354.61	93.61	7.7	8.6
13718	45	-56.66	13.6	0	140.5298	0.8183	0.0252	-1175.41	117.43	-1284.84	130.58	-197.47	19.73	244.2	7.2
13719	45	-43.6	26.6	0	140.3965	0.8187	0.0298	-739.73	124.77	-267.85	114.46	-124.27	20.96	174.6	11.9
13720	45	-29.57	40.4	0	139.9334	0.8199	0.0335	722.13	156.18	736.11	109.39	121.32	26.24	138.2	15.5
13721	45	-1.23	68.6	0	139.6673	0.8206	0.0347	1636.94	177.21	1618.82	128.75	275.01	29.77	128.8	18.6
13722	45	26.77	96.8	0	140.0522	0.8196	0.0433	325.85	207.24	498.37	162.18	54.74	34.82	82.7	16.1
13723	45	40.42	110.6	0	140.3600	0.8188	0.0538	-560.75	255.34	-522.86	177.07	-94.21	42.90	53.6	12.9
13724	45	53.33	123.6	0	140.5448	0.8183	0.0200	-1198.70	157.04	-1513.16	188.65	-201.38	26.38	387.7	8.5
13725	90	-56.9	13.6	0	140.9962	0.8172	0.0687	-2586.32	235.43	-2674.82	176.22	-434.50	39.55	32.9	7.2
13726	90	-43.7	26.6	0	140.5951	0.8182	0.0644	-1355.62	211.61	-1345.78	164.62	-227.74	35.55	37.4	11.9
13727	90	-29.64	40.4	0	140.0881	0.8195	0.0288	235.46	142.93	56.72	157.89	39.56	24.01	187.0	15.5
13728	90	-1.28	68.6	0	139.7540	0.8204	0.0252	1317.26	115.34	1602.20	131.76	221.30	19.38	244.2	18.6
13729	90	26.79	96.8	0	140.0114	0.8197	0.0217	481.89	133.11	486.71	131.76	80.96	22.36	329.3	16.1
13730	90	40.39	110.6	0	140.4127	0.8186	0.0441	-765.17	131.88	-785.95	166.84	-128.55	22.16	79.7	12.9
13731	90	53.12	123.6	0	140.9517	0.8173	0.1254	-2273.11	385.95	-2103.13	198.82	-381.88	64.84	9.9	8.7

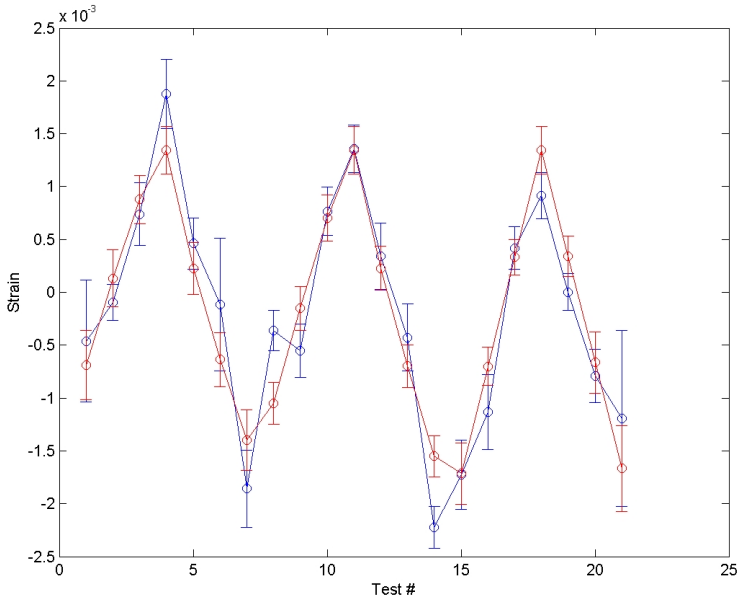

(a) plane{224}

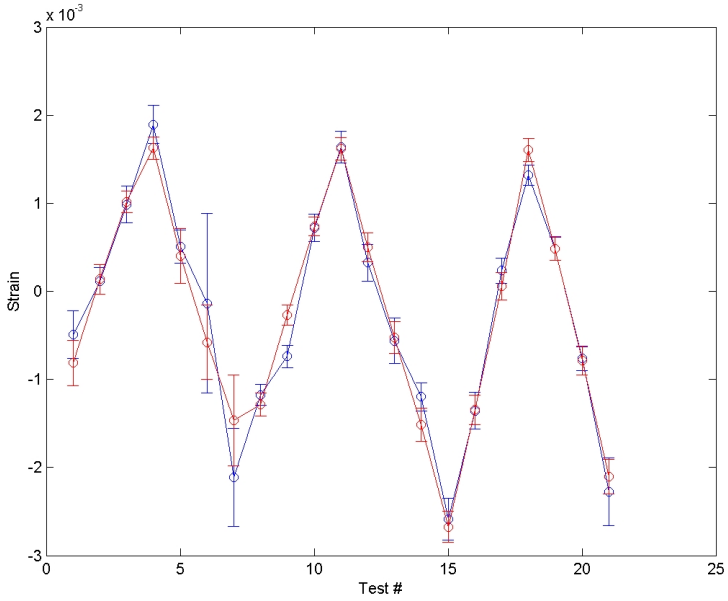

(b) plane{422}

Figure B.13: Comparison of the theoretical strain component ε_{33} (red) with the corresponding measured component ε'_{33} for sample X2G08 test 13711. Surface.

Table B.26: Test results for sample X2G08 test 13753 plane {224}. 72μm subsurface.

Stress [MPa]				Std [MPa]				Strain [-]				Std [-]			
-88.25	-103.02	-2.95		65.37	39.03	7.50		-2.34E-04	-7.60E-04	-2.20E-05		2.19E-04	2.88E-04	5.50E-05	
-103.02	-118.87	0.57		39.03	63.02	4.31		-7.60E-04	-4.60E-04	4.00E-06		2.88E-04	2.00E-04	3.20E-05	
-2.95	0.57	-85.21		7.50	4.31	59.16		-2.20E-05	4.00E-06	-2.11E-04		5.50E-05	3.20E-05	1.75E-04	
Principal values [MPa]				Std [MPa]											
-208.26	0	0		77.76	0	0									
0	-85.52	0		0	59.09	0									
0	0	1.45		0	0	71.59									
Sample	X2G08														
Plane	{224}														
Depth	72	µm													
Hydro	-97.44	MPa													
Mises	135.07	MPa													

Test	φ	Ψ	Ω	χ	2Θ	$d_{[hkl]}$	Std(2Θ)	StrainLab	Std	Strain Th	Std	StressLab	Std	Weigth	Depth
I.D.	deg	deg	deg	deg	deg	Å	deg	1.E-06	1.E-06	1.E-06	1.E-06	MPa	MPa		µm
13753	0	-55.43	13.6	0	138.0531	0.8249	0.0301	-348.15	204.61	-206.17	216.65	-58.49	34.38	27.7	7.3
13754	0	-42.38	26.6	0	137.9530	0.8252	0.0337	-95.38	246.88	-199.83	207.71	-16.02	41.48	22.1	12.0
13755	0	-28.63	40.4	0	138.0652	0.8249	0.0478	-424.31	282.31	-198.17	195.63	-71.28	47.43	11.0	15.5
13756	0	-0.46	68.6	0	138.1147	0.8248	0.0395	-585.30	183.52	-210.98	175.32	-98.33	30.83	16.1	18.5
13757	0	27.81	96.8	0	137.9714	0.8252	0.0395	-157.24	203.79	-234.15	176.70	-26.42	34.24	16.1	15.7
13759	0	54.62	123.6	0	137.9631	0.8252	0.0144	-120.34	195.38	-246.76	194.62	-20.22	32.82	121.2	7.6
13761	45	-42.45	26.6	0	138.0917	0.8248	0.0087	-557.77	188.99	-607.01	220.71	-93.71	31.75	332.1	12.0
13762	45	-28.59	40.4	0	137.9764	0.8251	0.0084	-166.18	187.82	-406.01	189.80	-27.92	31.55	356.3	15.5
13763	45	-0.34	68.6	0	137.8709	0.8254	0.0545	202.68	239.62	-211.19	175.18	34.05	40.26	8.5	18.5
13764	45	27.71	96.8	0	138.1859	0.8246	0.0448	-852.67	236.49	-415.15	203.47	-143.25	39.73	12.5	15.7
13765	45	41.53	110.6	0	138.1440	0.8247	0.1059	-578.58	339.03	-617.53	252.05	-97.20	56.96	2.2	12.3
13767	90	-55.44	13.6	0	138.0795	0.8249	0.0095	-521.32	188.38	-383.79	182.44	-87.58	31.65	278.5	7.3
13768	90	-42.41	26.6	0	138.0235	0.8250	0.0083	-327.49	172.98	-328.56	176.54	-55.02	29.06	364.9	12.0
13769	90	-28.62	40.4	0	138.0439	0.8250	0.0091	-395.00	186.15	-271.89	173.12	-66.36	31.27	303.6	15.5
13770	90	-0.36	68.6	0	137.9295	0.8253	0.0067	-19.30	193.11	-211.38	175.06	-3.24	32.44	560.0	18.5
13771	90	27.81	96.8	0	137.9897	0.8251	0.0255	-216.69	219.42	-261.87	185.87	-36.40	36.86	38.7	15.7
13772	90	41.58	110.6	0	138.0373	0.8250	0.0125	-360.14	188.34	-316.55	192.83	-60.50	31.64	160.9	12.2
13773	90	54.61	123.6	0	137.9779	0.8251	0.0072	-176.24	182.35	-372.44	198.70	-29.61	30.63	484.9	7.6

Table B.27: Test results for sample X2G08 test 13753 plane {422}. 72μm subsurface.

Stress [MPa]				Std [MPa]				Strain [-]				Std [-]			
-71.83	-15.09	-28.91		36.50	5.69	2.16		-2.18E-04	-1.11E-04	-2.13E-04		1.31E-04	4.20E-05	1.60E-05	
-15.09	-106.18	14.75		5.69	35.93	1.23		-1.11E-04	-4.72E-04	1.09E-04		4.20E-05	1.24E-04	9.00E-06	
-28.91	14.75	-40.37		2.16	1.23	30.32		-2.13E-04	1.09E-04	1.40E-05		1.60E-05	9.00E-06	9.50E-05	
Principal values [MPa]				Std [MPa]											
-113.17	0	0		36.54	0	0									
0	-87.39	0		0	32.98	0									
0	0	-17.82		0	0	32.43									
Sample	X2G08														
Plane	{422}														
Depth	72	µm													
Hydro	-72.79	MPa													
Mises	66.58	MPa													
Test	φ	Ψ	Ω	χ	2Θ	$d_{[hkl]}$	Std(2Θ)	StrainLab	Std	Strain Th	Std	StressLab	Std	Weigth	Depth
I.D.	deg	deg	deg	deg	deg	Å	deg	1.E-06	1.E-06	1.E-06	1.E-06	MPa	MPa		µm
13754	0	-43.44	26.6	0	140.0873	0.8195	0.0236	250.96	112.68	117.24	102.82	42.16	18.93	11.1	11.9
13755	0	-29.7	40.4	0	140.1980	0.8192	0.0033	-105.88	99.16	140.65	96.62	-17.79	16.66	569.8	15.5
13756	0	-1.49	68.6	0	140.1874	0.8192	0.0183	-55.73	105.75	24.96	95.15	-9.36	17.77	18.5	18.6
13757	0	26.71	96.8	0	140.1830	0.8192	0.0027	-59.24	98.20	-204.21	88.66	-9.95	16.50	851.3	16.1
13759	0	53.46	123.6	0	140.2892	0.8190	0.0072	-389.50	94.54	-340.00	100.88	-65.44	15.88	119.7	8.5
13761	45	-43.47	26.6	0	140.1431	0.8193	0.0104	79.94	99.19	-134.82	98.15	13.43	16.66	57.4	11.9
13762	45	-29.7	40.4	0	140.2012	0.8192	0.0021	-115.64	92.13	-37.85	91.45	-19.43	15.48	1407.2	15.5
13763	45	-1.48	68.6	0	140.1698	0.8193	0.0692	-16.73	246.02	17.53	94.96	-2.81	41.33	1.3	18.6
13764	45	26.75	96.8	0	140.0909	0.8195	0.0054	238.54	94.67	-140.70	91.75	40.07	15.90	212.8	16.1
13765	45	40.42	110.6	0	140.3673	0.8188	0.0042	-635.78	92.34	-256.62	98.57	-106.81	15.51	351.8	12.9
13767	90	-56.55	13.6	0	140.3092	0.8189	0.0030	-457.05	93.90	-424.33	101.16	-76.78	15.78	689.5	7.2
13768	90	-43.5	26.6	0	140.1995	0.8192	0.0016	-112.10	95.71	-324.87	92.60	-18.83	16.08	2424.1	11.9
13769	90	-29.74	40.4	0	140.2891	0.8190	0.0050	-395.31	99.10	-199.35	89.97	-66.41	16.65	248.2	15.5
13770	90	-1.51	68.6	0	140.2226	0.8191	0.0017	-183.85	96.33	7.94	94.82	-30.89	16.18	2147.3	18.6
13771	90	26.76	96.8	0	140.0737	0.8195	0.0075	288.36	110.04	3.07	96.26	48.44	18.49	110.3	16.1
13772	90	40.53	110.6	0	140.1458	0.8193	0.0138	70.53	119.66	-83.56	100.94	11.85	20.10	32.6	12.8
13773	90	53.45	123.6	0	140.3015	0.8189	0.0031	-431.75	97.17	-195.29	109.29	-72.53	16.32	645.7	8.5

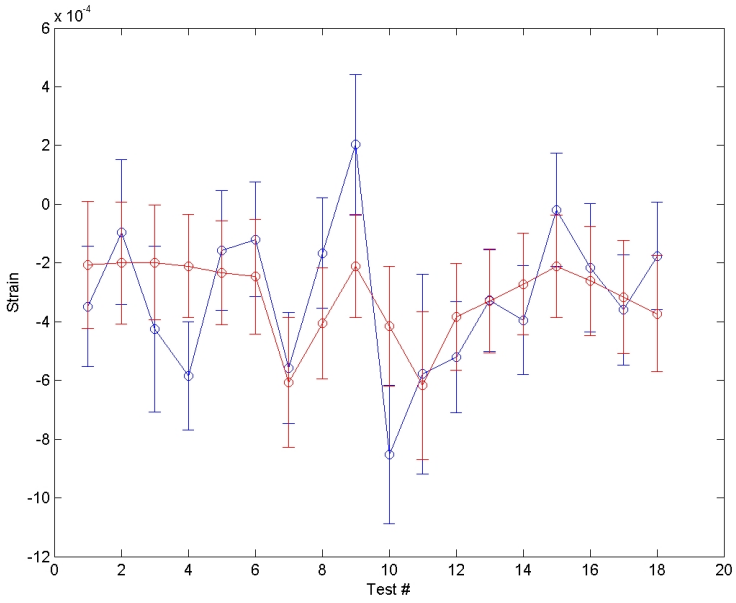

(a) plane{224}

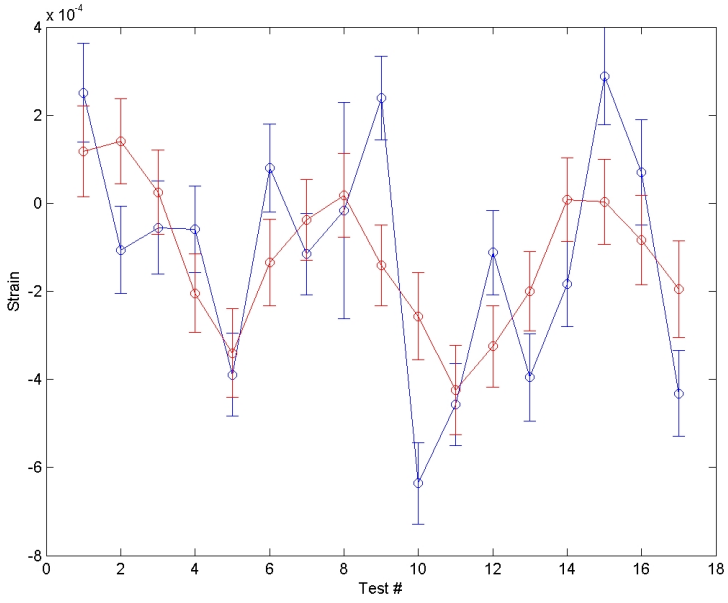

(b) plane{422}

Figure B.14: Comparison of the theoretical strain component ε_{33} (red) with the corresponding measured component ε'_{33} for sample X2G08 test 13753. 72μm subsurface.

Table B.28: Test results for sample X2G08 test 10289 plane {224}. 122μm subsurface.

Stress [MPa]				Std [MPa]				Strain [-]				Std [-]			
2.29	6.92	6.55		58.15	6.14	1.89		4.50E-05	5.10E-05	4.80E-05		1.82E-04	4.50E-05	1.40E-05	
6.92	-6.73	6.25		6.14	63.43	2.18		5.10E-05	-2.10E-05	4.60E-05		4.50E-05	2.20E-04	1.60E-05	
6.55	6.25	-15.54		1.89	2.18	53.81		4.80E-05	4.60E-05	-8.60E-05		1.40E-05	1.60E-05	1.51E-04	
Principal values [MPa]				Std [MPa]											
-22.28	0	0		57.06	0	0									
0	-8.64	0		0	57.59	0									
0	0	10.93		0	0	60.61									
Sample	X2G08														
Plane	{224}														
Depth	122	µm													
Hydro	-6.66	MPa													
Mises	19.38	MPa													
Test	φ	Ψ	Ω	χ	2Θ	$d_{[hkl]}$	Std(2Θ)	StrainLab	Std	Strain Th	Std	StressLab	Std	Weigth	Depth
I.D.	deg	deg	deg	deg	deg	Å	deg	1.E-06	1.E-06	1.E-06	1.E-06	MPa	MPa		µm
10289	0	-42.4	26.6	0	138.0065	0.8251	0.0107	-146.05	165.93	-74.42	161.24	-24.54	27.88	16.0	12.0
10290	60	-42.4	26.6	0	137.9933	0.8251	0.0103	-94.94	192.76	-92.75	191.25	-15.95	32.38	17.2	12.0
10291	120	-42.39	26.6	0	137.9800	0.8251	0.0059	-53.56	173.54	-84.87	175.72	-9.00	29.15	52.5	12.0
10292	180	-42.38	26.6	0	137.9667	0.8252	0.0077	-6.39	170.18	21.77	162.16	-1.07	28.59	30.8	12.0
10293	210	-42.36	26.6	0	137.9188	0.8253	0.0112	156.72	172.45	50.76	169.83	26.33	28.97	14.6	12.0
10294	270	-42.39	26.6	0	137.9786	0.8251	0.0048	-54.62	173.32	-10.66	170.35	-9.18	29.12	79.4	12.0
10295	330	-42.39	26.6	0	137.9847	0.8251	0.0118	-63.49	150.99	-72.72	154.86	-10.67	25.37	13.1	12.0
10296	30	-28.59	40.4	0	137.9806	0.8251	0.0168	-86.55	165.92	-104.22	165.19	-14.54	27.88	6.5	15.5
10297	90	-28.6	40.4	0	138.0035	0.8251	0.0094	-125.48	175.34	-110.01	172.87	-21.08	29.46	20.7	15.5
10298	150	-28.59	40.4	0	137.9820	0.8251	0.0075	-66.15	162.55	-54.16	158.64	-11.11	27.31	32.5	15.5
10299	180	-28.59	40.4	0	137.9719	0.8252	0.0142	-45.14	154.00	-15.39	156.35	-7.58	25.87	9.1	15.5
10300	240	-28.59	40.4	0	137.9875	0.8251	0.0144	-80.26	163.42	-3.41	159.63	-13.48	27.45	8.8	15.5
10301	300	-28.58	40.4	0	137.9641	0.8252	0.0166	13.83	162.55	-64.31	151.74	2.32	27.31	6.6	15.5
10302	360	-28.59	40.4	0	137.9821	0.8251	0.0107	-58.92	170.57	-96.60	154.88	-9.90	28.66	16.0	15.5

Table B.29: Test results for sample X2G08 test 10289 plane {422}. 122μm subsurface.

Stress [MPa]				Std [MPa]				Strain [-]				Std [-]			
47.80	4.69	1.92		23.69	1.71	0.86		2.73E-04	3.50E-05	1.40E-05		7.20E-05	1.30E-05	6.00E-06	
4.69	19.58	5.41		1.71	25.16	1.15		3.50E-05	6.40E-05	4.00E-05		1.30E-05	8.40E-05	8.00E-06	
1.92	5.41	-11.17		0.86	1.15	24.66		1.40E-05	4.00E-05	-1.63E-04		6.00E-06	8.00E-06	8.00E-05	
Principal values [MPa]				Std [MPa]											
-12.16	0	0		24.68	0	0									
0	19.57	0		0	25.28	0									
0	0	48.80		0	0	23.54									
Sample	X2G08														
Plane	{422}														
Depth	122	µm													
Hydro	18.74	MPa													
Mises	37.79	MPa													
Test	φ	Ψ	Ω	χ	2Θ	$d_{[hkl]}$	Std(2Θ)	StrainLab	Std	Strain Th	Std	StressLab	Std	Weigth	Depth
I.D.	deg	deg	deg	deg	deg	Å	deg	1.E-06	1.E-06	1.E-06	1.E-06	MPa	MPa		µm
10289	0	-43.49	26.6	0	140.1718	0.8193	0.0043	-22.01	75.44	29.27	76.43	-3.70	12.67	30.9	11.9
10290	60	-43.49	26.6	0	140.1857	0.8192	0.0035	-57.86	76.85	-57.93	77.07	-9.72	12.91	46.7	11.9
10291	120	-43.49	26.6	0	140.1893	0.8192	0.0041	-67.35	81.46	-72.23	77.79	-11.32	13.69	34.0	11.9
10292	180	-43.47	26.6	0	140.1331	0.8194	0.0051	112.01	71.83	57.35	72.59	18.82	12.07	22.0	11.9
10293	210	-43.48	26.6	0	140.1645	0.8193	0.0054	16.63	74.88	65.05	72.07	2.79	12.58	19.6	11.9
10294	270	-43.46	26.6	0	140.1267	0.8194	0.0078	124.59	79.05	-15.52	79.43	20.93	13.28	9.4	11.9
10295	330	-43.5	26.6	0	140.1957	0.8192	0.0097	-87.23	81.08	12.27	78.42	-14.65	13.62	6.1	11.9
10296	30	-29.68	40.4	0	140.1587	0.8193	0.0076	24.33	81.83	-89.15	78.30	4.09	13.75	9.9	15.5
10297	90	-29.73	40.4	0	140.2578	0.8190	0.0043	-281.52	76.08	-141.31	78.94	-47.30	12.78	30.9	15.5
10298	150	-29.69	40.4	0	140.1746	0.8193	0.0035	-21.89	74.97	-82.76	76.56	-3.68	12.59	46.7	15.5
10299	180	-29.69	40.4	0	140.1714	0.8193	0.0110	-19.52	78.71	-43.83	75.05	-3.28	13.22	4.7	15.5
10300	240	-29.72	40.4	0	140.2302	0.8191	0.0046	-194.03	78.57	-51.00	76.47	-32.60	13.20	27.0	15.5
10301	300	-29.7	40.4	0	140.1922	0.8192	0.0066	-79.21	82.52	-77.99	79.81	-13.31	13.86	13.1	15.5
10302	360	-29.68	40.4	0	140.1603	0.8193	0.0063	17.01	81.07	-68.20	78.56	2.86	13.62	14.4	15.5

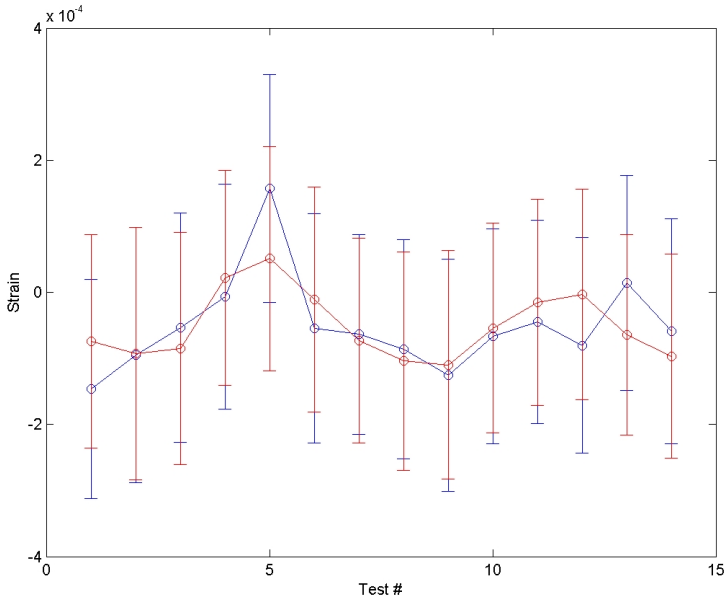

(a) plane{224}

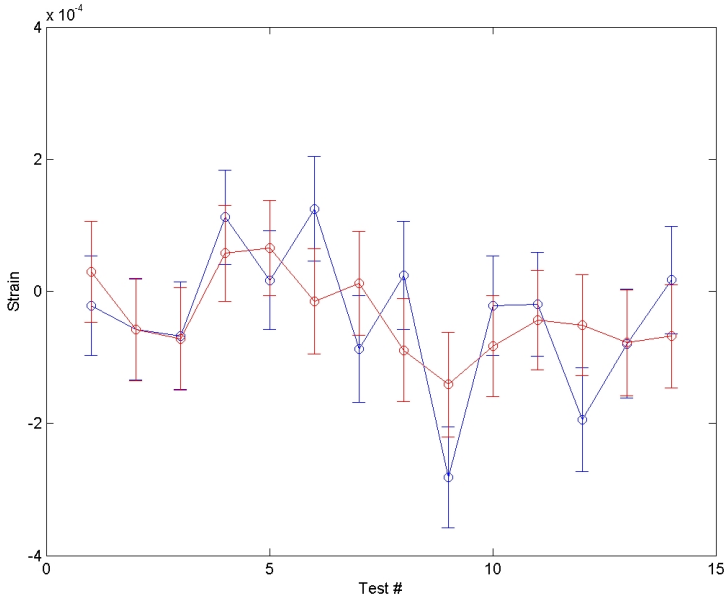

(b) plane{422}

Figure B.15: Comparison of the theoretical strain component ε_{33} (red) with the corresponding measured component ε'_{33} for sample X2G08 test 10289. 122μm subsurface.

REFERENCES

Abaqus. *Abaqus Explicit User's manual*, volume I. Hibbit, Karlsson, & Sorensen, INC., 2001. 8

Appel, F. and Wagner, R. "Microstructure and deformation of two-phase gamma-titanium aluminides". *Materials Science and Engineering: R: Reports*, 22(5):187–268, 1998. 1.2.3, 1.5

Asaro, R. "Crystal plasticity". *Transactions of the ASME. Journal of Applied Mechanics*, 50 (4B):921–934, 1983a. 8.2

Asaro, R. "Micromechanics of crystals and polycrystals". *Advances in Applied Mechanics*, 23: 1–115, 1983b. 8.2

Aurora, A., Marshall, D., Lawn, B., and Swain, M. "Indentation deformation/fracture of normal and anomalous glasses". *Journal of Non-Crystalline Solids*, 31(3):415–428, 1979. 2.1, 7, 7.1, 7.1, 7.5, 9.2, 9.4.5, 10.1.4

Austin, C., Kelly, T., McAllister, K., and Chesnutt, J. "Aircraft engine applications for gamma titanium aluminides". In *Proceedings of the Second International Symposium on Structural Intermetallics*, pages 413–425. The Minerals, Metals & Materials Soc (TMS), Warrendale, PA, USA, 1997. 1.1

Badger, J. and Torrance, A. "A comparison of two models to predict grinding forces from wheel surface topography". *International Journal of Machine Tools and Manufacture*, 40(8): 1099–1120, 2000. 1.3

Balart, M., Bouzina, A., Edwards, L., and Fitzpatrick, M. "The onset of tensile residual stresses in grinding of hardened steels". *Materials Science and Engineering A*, 367(1-2):132–142, 2004. 1.4

Begley, M. and Hutchinson, J. "The mechanics of size-dependent indentation". *Journal of the Mechanics and Physics of Solids*, 46(10):2049–2068, 1998. 1.3

Behnken, H. and Hauk, V. "Determination of steep stress gradients by x-ray diffraction – results of a joint investigation". *Materials Science and Engineering A*, 300(1-2):41–51, 2001. 6.6, 10.2

Bentley, S., Goh, N., and Aspinwall, D. "Reciprocating surface grinding of a gamma titanium aluminide intermetallic alloy". *Journal of Materials Processing Technology*, 118(1-3):22–28, 2001. 1.4, 2.1

Bentley, S., Mantle, A., and Aspinwall, D. "The effect of machining on the fatigue strength of a gamma titanium aluminide intertmetallic alloy". *Intermetallics*, 7(8):967–969, 1999. 1.4, 1.5.1, 2.1, 4.1

Blunt, L. and Ebdon, S. "The application of three-dimensional surface measurement techniques to characterizing grinding wheel topography". *International Journal of Machine Tools and Manufacture*, 36(11):1207–1226, 1996. 7.3

Bowden, F. and Tabor, D. *The friction and lubrication of solids*. Oxford University Press, 1950. 7.1

Brady, M., Brindley, W., Smialek, J., and Locci, I. "Oxidation and protection of gamma titanium aluminides". *JOM*, 48(11):46–50, 1996. 1.2

Brinksmeier, E. "State-of-the-art of non-destructive measurement of sub-surface material properties and damages". *Precision Engineering*, 11(4):211–224, 1989. 1.5

Briscoe, B., Biswas, S., and Panesar, S. "Scratch hardness and friction of a soft rigid-plastic solid". *Wear of Materials: International Conference on Wear of Materials*, 1:451–456, 1991. 1.3

Brockman, R. "Analysis of elastic-plastic deformation in tial polycrystals". *International Journal of Plasticity*, 19(10):1749–1772, 2003. 2.3, 3.2

Butler, D., Blunt, L., See, B., Webster, J., and Stout, K. "The characterisation of grinding wheels using 3d surface measurement techniques". *Journal of Materials Processing Technology*, 127(2):234–237, 2002. 7.3

Cao, G., Fu, L., Lin, J., Zhang, Y., and Chen, C. "The relationships of microstructure and properties of a fully lamellar tial alloy". *Intermetallics*, 8(5-6):647–653, 2000. 1.2.2

Chatterjee, A., Dehm, G., Scheu, C., and Clemens, H. "Onset of microstructural instability in a fully lamellar ti-46.5 at.% al-4 at.% (cr,nb,ta,b) alloy during short-term creep". *Zeitschrift fuer Metallkunde/Materials Research and Advanced Techniques*, 91(9):755–760, 2000. 1.2

Chen, X., Rowe, W., and Cai, R. "Precision grinding using cbn wheels". *International Journal of Machine Tools and Manufacture*, 42(5):585–593, 2002. 1.7

Clemens, H. and Kestler, H. "Processing and applications of intermetallic gamma-tial-based alloys". *Advanced Engineering Materials*, 2(9):551–570, 2000. 1.2, 1.2.2

Clemens, H., Lorich, A., Eberhardt, N., Glatz, W., Knabl, W., and Kestler, H. "Technology, properties and applications of intermetallic gamma-tial based alloys". *Zeitschrift fur Metallkunde*, 90(8):569–580, 1999. 1.2

Cuitio, A. and Ortiz, M. "Computational modeling of single crystals". *Modeling and Simulation in Materials Science and Engineering*, 1(3):225–263, 1992. 8.2

Darolia, R. and Walston, W. "Effect of specimen surface preparation on room temperature tensile ductility of an fe-containing nial single crystal alloy". *Intermetallics*, 4(7):505–516, 1996. 1.4

Dimiduk, D., Miracle, D., and Ward, C. "Development of intermetallic materials for aerospace systems". *Materials Science and Technology*, 8:367–375, 1992. 1.1

Dimiduk, D., Parthasarathy, T., and Hazzledine, P. "Design-tool representations of strain compatibility and stress-strain relationships for lamellar gamma titanium aluminides". *Intermetallics*, 9(10-11):875–882, 2001. 2.3

Dölle, H. and Hauk, V. "X-ray stress evaluation of residual stress systems having general orientation". *Harterei-Techn. Mitt.*, 31:165, 1976. 6.4, 6.6

Dölle, H. and Hauk, V. "System for possible lattice strain distributions for mechanically stressed metallic materials". *Zeitschrift fur metallkunde*, 68(11):725–728, 1977. 6.4, 6.6

Ebbrell, S., Woolley, N., Tridimas, Y., Allanson, D., and Rowe, W. "The effects of cutting fluid application methods on the grinding process". *International Journal of Machine Tools and Manufacture*, 40(2):209–223, 2000. 5.4.3

Eda, H., Kishi, K., and Ueno, H. "Cracking and fracture of matrix structure and carbide particles produced by the grinding process". *Precision Engineering*, 5(2):73–76, 1983. 1.4

Ely, T., Predecki, P., and Noyan, I. "A method for obtaining stress-depth profiles by absorption constrained profile fitting of diffraction peaks". *Advances in X-Ray Analysis*, 43, 1999. 6.3, 6.6, 10.2

Engineer, F., Guo, C., and Malkin, S. "Experimental measurement of fluid flow through the grinding zone". *Journal of Engineering for Industry, Transactions of the ASME*, 114(1):61–66, 1992. 5.4.3

Feng, C., Michel, D., and Crowe, C. "Twinning in tial". *Scripta Metallurgica*, 23(7):1135–1140, 1989. 1.2.1

Field, M. "Surface integrity in grinding". In Shaw, M., editor, *Proceedings of the Int. Grinding Conference*, New Developments in Grinding, Pittsburgh, PN, 1972. Carnegie Press. 1.4, 1.8

Field, M., Kahles, J., and Cammett, J. "A review of measuring methods for surface integrity". *Annals of CIRP*, 21(2):219–238, 1972. 1.5, 1.5.1, 4.1

Forman, P. "Zygo interferometer system". In *Proceedings of the SPIE 192*, 1979. 2.1, 4.3

Frank, G., Olson, S., and Brockman, R. "Numerical models of orthotropic and lamellar grain structures". *Intermetallics*, 11(4):331–340, 2003. 3.2

Furutani, K., Ohguro, N., Nguyen, T., and Nakamura, T. "In-process measurement of topography change of grinding wheel by using hydrodynamic pressure". *International Journal of Machine Tools and Manufacture*, 42(13):1447–1453, 2002. 5.4.4

Furutani, K., Ohguro, N., Nguyen, T., and Nakamura, T. "Automatic compensation for grinding wheel wear by pressure based in-process measurement in wet grinding". *Precision Engineering*, 27(1):9–13, 2003. 5.4.4

GE. "Diamond characterization". Technical Report GES 1278 E, 2000. 5.3

Gillespie, L. *Deburring and edge finishing handbook*. 1977. 4.1

Goh, C. *Crystallographic Plasticity in Fretting of Ti-6Al-4V*. Doctoral dissertation, Georgia Institute of Technology, 2003. 8.3.2

Grum, J. "A review of the influence of grinding conditions on resulting residual stresses after induction surface hardening and grinding". *Journal of Materials Processing Technology*, 114(3): 212–226, 2001. 1.4

Guo, C. and Malkin, S. "Analysis of fluid flow through the grinding zone". *Journal of Engineering for Industry, Transactions of the ASME*, 114(4):427–434, 1992. 5.4.3

Hahn, R. and Lindsay, R. "Principles of grinding. part i: Basic relationships in precision machining". In Bhateja, C. and Lindsay, R., editors, *Grinding Theory Techniques and Troubleshooting*. SME, 1982a. 1.1, 7.1

Hahn, R. and Lindsay, R. "Principles of grinding. part ii: The metal removal parameter". In Bhateja, C. and Lindsay, R., editors, *Grinding Theory Techniques and Troubleshooting*, pages 11–17. SME, 1982b. 1.1, 7.1

Hahn, R. and Lindsay, R. "Principles of grinding. part iii: The wheel removal parameter". In Bhateja, C. and Lindsay, R., editors, *Grinding Theory Techniques and Trouble Shooting*, page 1824. SME, 1982c. 1.1

Hahn, R. and Lindsay, R. "Principles of grinding. part iv: Surface finish, geometry, and integrity". In Bhateja, C. and Lindsay, R., editors, *Grinding Theory Techniques and Trouble Shooting*. SME, 1982d. 1.1

Hall, E. and Huang, S.-C. "Deformation mechanisms in gamma titanium aluminides. a review". In *Proceedings of the Symposium of Microstructure-Properties Relationship for Titanium Aluminides Alloys*, pages 47–64. The Minerals, Metals & Materials Soc (TMS), Warrendale, PA, USA, 1991. 1.2.2

Hao, Y., Xu, D., Cui, Y., Yang, R., and Li, D. "The site occupancies of alloying elements in tial and ti3al alloys". *Acta Materialia*, 47(4):1129–1139, 1999. 1.2.2, 3.1

Hecker, R. *Part surface roughness modeling and process optimal control of cylindrical grinding*. Doctoral dissertation, Georgia Institute of Technology, 2002. 2.3, 7, 7.1, 7.1, 7.3

Hono, K., Abe, E., Kumagai, T., and Harada, H. "Chemical compositions of ultrafine lamellae in the water-quenched $ti-48al$ alloy". *Scripta Materialia*, 35(4):495–499, 1996. 1.2.2, 1.3

Hutchings, I. *Tribology*. CRC Press, 1992. 1.3

Hwang, T., Evans, C., and Malkin, S. "Size effect for specific energy in grinding of silicon nitride". *Wear*, 225-229(Part 2):862–867, 1999. 1.3

Inui, H., Nakamura, A., Oh, M., and Yamaguchi, M. "Deformation structures in ti-rich tial polysynthetically twinned crystals". *Philosophical Magazine A (Physics of Condensed Matter, Defects and Mechanical Properties)*, 66(4):557–573, 1992a. 1.2.3

Inui, H., Oh, M., Nakamura, A., and Yamaguchi, M. "Ordered domains in tial coexisting with ti3al in the lamellar structure of ti-rich tial compounds". *Philosophical Magazine A (Physics of Condensed Matter, Defects and Mechanical Properties)*, 66(4):539–555, 1992b. 1.2.1

Jones, P. *Effects of conventional machining on high cycle fatigue behavior of the intermetallic alloy $Ti-47Al-2Nb-2Cr$ (at.%)*. Doctoral dissertation, University of Dayton, 1997. 2.1, 9.4.1, 9.4.2, 9.4, 9.5

Jones, P. and Eylon, D. "Effects of conventional machining on high cycle fatigue behavior of the intermetallic alloy $ti-47al-2nb-2cr$ (at.%)". *Materials Science and Engineering A*, 263 (2):296–304, 1999. 1.4, 1.5.1, 2.1, 4.1, 9.4.2

Kad, B., Dao, M., and Asaro, R. "Numerical simulations of stress-strain behavior in two-phase $\alpha_2+\gamma$ lamellar tial alloys". *Materials Science and Engineering A*, 192-193(Part 1):97–103, 1995. 2.3, 8.2, 8.3.2

Kagiwada, T. and Kanauchi, T. "Three-dimensional thermal deformation and thermal stress in workpieces under surface grinding". *Journal of Thermal Stresses*, 8(3):305–318, 1985. 1.4

Kattner, U., Lin, J.-C., and Chang, Y. "Thermodynamic assessment and calculation of the ti-al system". *Metallurgical Transactions A (Physical Metallurgy and Materials Science)*, 23A (8):2081–2090, 1992. 1.2.1, 1.1, 1.2.2, 3.1

Kawabata, T., Tamura, T., and Izumi, O. "Parameters for ductility improvement in tial". In Liu, C., editor, *High Temperature Ordered Intermetallic Alloys III*, pages 329–334. MRS, Pittsburgh, PA, 1989. 1.2.2, 3.1

Kim, H., Theodore, N., Gadre, K., Mayer, J., and Alford, T. "Investigation of thermal stability, phase formation, electrical, and microstructural properties of sputter-deposited titanium aluminide thin films". *Thin Solid Films*, 460(1-2):17–24, 2004. 1.2

Kim, Y.-W. "Intermetallic alloys based on gamma titanium aluminide". *JOM*, 41(7):24–30, 1989. 1.2, 1.2.2

Kim, Y.-W. "Ordered intermetallic alloys. part iii: gamma titanium aluminides". *Journal of Metals*, 46(7):30–39, 1994. 1.2.2

Kim, Y.-W. "Trends in the development of $\gamma - tial$ alloys". In *Gamma Titanium Aluminides I.* The Minerals, Metals & Materials Soc (TMS), Warrendale, PA, USA, 1995. 1.1

Kim, Y.-W. and Dimiduk, D. "Progress in the understanding of gamma titanium aluminides". *JOM*, 43(8):40–47, 1991. 1.2

Knippscheer, S. and Frommeyer, G. "Intermetallic tial(cr,mo,si) alloys for lightweight engine parts. structure, properties, and applications". *Advanced Engineering Materials*, 1(3-4):187–191, 1999. 1.2

Kondoh, T., Goto, T., Sasaki, T., and Hirose, Y. "X-ray stress measurement for titanium aluminide intermetallic compound.". *Advances in X-Ray Analysis*, 43, 1999. 1.4

König, W. and Lortz, W. "Properties of cutting edges related to chip formation in grinding". *Annals of CIRP*, 24(1):231–235, 1975. 7.2

Kumar, K. "Superabrasive grinding of titanium alloys. paper mr90-505". In *4th International Grinding Conference*, Dearborn, Michigan, 1990. 5.3

Kumar, K. "Superabrasive grinding of aerospace materials, diamond & cbn ultrahard materials". In *Symposium '93*, Windson, Ontario, Canada, 1993. 5.3

Larsen, J., Worth, B., Balsone, S., and Rosenberger, A. "Reliability issues affecting the implementation of gamma titanium aluminides in turbine engine applications". In Blenkinsop, P., Evans, W., and Flower, H., editors, *Titanium 95*, volume 1, page 113120. The Institute of Materials, London, UK, 1996. 1.1

Lawn, B. and Wilshaw, T. "Indentation fracture: Principles and applications". *Journal of Materials Science*, 10:1049–1081, 1975. 2.1, 7, 7.1, 7.1, 7.5, 9.2, 9.4.5, 10.1.4

Lee, E. "Elastic-plastic deformation at finite strains". *Journal of Applied Mechanics*, 36:1–6, 1969. 8.2

Liu, Z., Sun, J., and Shen, W. "Study of plowing and friction at the surfaces of plastic deformed metals". *Tribology International*, 35(8):511–522, 2002. 1.5.1

Ludema, K. "Mechanism-based modeling of friction and wear". *Wear*, 200(1-2):1–7, 1996. 1.3

Mahdi, M. and Zhang, L. "Applied mechanics in grinding–v. thermal residual stresses". *International Journal of Machine Tools and Manufacture*, 37(5):619–633, 1997. 1.4

Malkin, S. *Grinding Technology. Theory and Applications of Machining with Abrasives.* Ellis Horwood Limited, New York, 1989. 1.1, 7.4.1

Mantle, A. and Aspinwall, D. "Surface integrity of a high speed milled gamma titanium aluminide". *Journal of Materials Processing Technology*, 118(1-3):143–150, 2001. 2.1

Marketz, W., Fischer, F., and Clemens, H. "Deformation mechanisms in tial intermetallics–experiments and modeling". *International Journal of Plasticity*, 19(3):281–321, 2003. 1.2.2

Matsuno, Y., Yamada, H., Harada, M., and Kobayashi, A. "Microtopography of the grinding wheel surface with sem". *Annals of CIRP*, 24(1):237–242, 1975. 7.3

McGinty, R. *Multiscale Representation of Polycrystalline Inelasticity.* Doctoral dissertation, Georgia Institute of Technology, 2001. 2.3, 8.2

McGinty, R. and McDowell, D. "Multiscale polycrystal plasticity". *Journal of Engineering Materials and Technology*, 121:203–209, 1999. 8.2

McQuay, P., Simpkins, R., Seo, D., and Bieler, T. "Alloy and process improvements for cast gamma tial alloy applications". In Kim, Y.-W., Dimiduk, D., and Loretto, M., editors, *Gamma Titanium Aluminides*, pages 197–207. The Minerals, Metals & Materials Soc (TMS), Warrendale, PA, USA, 1999. 1.2.2, 3.1

Meng, H. and Ludema, K. "Wear models and predictive equations: their form and content". *Wear*, 181-183(2):443–457, 1995. 1.3, 9.1

Nakayama, K., Brecker, J., and Shaw, M. "Grinding wheel elasticity". *Journal of Engineering for Industry, Transactions of the ASME*, 93:609, 1971. 7.2

Nelson, L. *Subsurface damage in the abrasive machining of Titanium Aluminide.* PhD thesis, Georgia Institute of Technology, 1997. 1.5.1, 2.1, 2.3, 4.2, 7, 7.1, 7.1, 9.2, 9.4.4

Newby, J. *ASM Handbook: Mechanical Testing*, volume 8. American Society of Metals International, 1989. 1.5.1

Noda, T., Okabe, M., Isobe, S., and Sayashi, M. "Silicide precipitation strengthened tial". *Materials Science and Engineering A*, 192-193(Part 2):774–779, 1995. 1.2.2

Novovic, D., Dewes, R., Aspinwall, D., Voice, W., and Bowen, P. "The effect of machined topography and integrity on fatigue life". *International Journal of Machine Tools and Manufacture*, 44(2-3):125–134, 2004. 1.4, 2.1

Noyan, I. and Cohen, J. *Residual stress, measurement by diffraction and interpretation.* Springer-Verlag, New York, 1987. 6.3

Ohmori, H., Takahashi, I., and Bandyopadhyay, B. P. "Ultra-precision grinding of structural ceramics by electrolytic in-process dressing (elid) grinding". *Journal of Materials Processing Technology*, 57(3-4):272–277, 1996. 5.4.1

Ohnuma, I., Fujita, Y., Mitsui, H., Ishikawa, K., Kainuma, R., and Ishida, K. "Phase equilibria in the ti-al binary system". *Acta Materialia*, 48(12):3113–3123, 2000. 1.2.1, 1.1, 3.1

Pagano, N. "Exact moduli of anisotropic laminates". In Sendeckyj, G., editor, *Mechanics of composite materials*. Academic Press, New York, 1974. 3.2

Perez, P., Jimenez, J., Frommeyer, G., and Adeva, P. "Oxidation behaviour of a ti-46al-1mo-0.2si alloy: the effect of mo addition and alloy microstructure". *Materials Science and Engineering A*, 284(1-2):138–147, 2000. 1.2.2

Razavi, H. *Identification and Control of Grinding Processes for Intermetalic [sic] Compunds [sic].* Doctoral dissertation, Georgia Institute of Technology, 2000. 1.5.1, 2.1, 4.2, 7, 7.1, 9.2

Razavi, H., Kurfess, T., and Danyluk, S. "Force control grinding of gamma titanium aluminide". *International Journal of Machine Tools and Manufacture*, 43:185–191, 2003. 4.2

Richter, H. and Hofmann, F. "Residual stress measurements on machined specimens of gamma titanium aluminine material.". *Mat.-wiss. u. Werkstofftech*, 33:24–32, 2002. 1.4, 2.3

Robinson, P. and Bradbury, S. *Qualitative Polarized-Light Microscopy.* Royal Microscopy Society, Oxford University Press, Oxford, 1992. 1.5.1, 4.1

Rowe, W., Morgan, M., Qi, H., and Zheng, H. "The effect of deformation on the contact area in grinding". *Annals of CIRP*, 42(1):409–412, 1993. 7.2

Schneibel, J., Agnew, S., and Carmichael, C. "Surface preparation and bend ductility of nial". *Metallurgical Transactions A (Physical Metallurgy and Materials Science)*, 24A(11):2593–2596, 1993. 1.4

Seo, D., Saari, H., Beddoes, J., and Zhao, L. "The creep behaviour of tial+w as a function of the fully lamellar morphology". In Hemker, K., Dimiduk, D., Clemens, H., Darolia, R., Inui, H., Larsen, J., Sikka, V., Thomas, M., and Whittenberger, J., editors, *Structural Intermetallics 2001*, pages 653–662. TMS Warrendale, PA, USA, 2001. 1.2.2

Sharman, A., Aspinwall, D., Dewes, R., and Bowen, P. "Workpiece surface integrity considerations when finish turning gamma titanium aluminide". *Wear*, 249(5-6):473–481, 2001a. 2.1

Sharman, A., Aspinwall, D., Dewes, R., Clifton, D., and Bowen, P. "The effects of machined workpiece surface integrity on the fatigue life of gamma-titanium aluminide". *International Journal of Machine Tools and Manufacture*, 41(11):1681–1685, 2001b. 1.4, 2.1

Shaw, M. *New Developments in Grinding.* Carnegie Press, 1972. 1.1, 1.3, 1.3, 7.3

Shemet, V., Yurechko, M., Tyagi, A., Quadakkers, W., and Singheiser, L. "The influence of nb and zr additions on the high temperature oxidation mechanisms of tial alloys in ar/o2". In Kim, Y.-W., Dimiduk, D., and Loretto, M., editors, *Gamma Titanium Aluminides*, pages 783–790. The Minerals, Metals & Materials Soc (TMS), Warrendale, PA, 1999. 1.2.2, 3.1

Stone, W. *Thermal effects on subsurface damage during the surface grinding of Titanium Aluminide.* Doctoral dissertation, Georgia Institute of Technology, 2003. 1.5.1, 2.1, 4.2, 7, 7.1, 9.2

Subhash, G., Koeppel, B., and Chandra, A. "Dynamic indentation hardness and rate sensitivity in metals". *Journal of Engineering Materials and Technology*, 121(3):257–263, 1999. 1.3

Suominen, L. and Carr, D. "Selected methods of evaluating residual stress gradients measured by x-ray diffraction. traditional, full tensor, and wavelet.". *Advances in X-Ray Analysis*, 43: 21–30, 1999. 6.6, 10.2

Tetsui, T. "Effects of high niobium addition on the mechanical properties and high-temperature deformability of gamma tial alloy". *Intermetallics*, 10(3):239–245, 2002. 1.2.2, 3.1

Tlusty, G. *Manufacturing Process and Equipment*. Prentice Hall, 1999. 1.3, 1.3

Trail, S. and Bowen, P. "Effects of stress concentrations on the fatigue life of a gamma-based titanium aluminide". *Materials Science and Engineering A*, 192-193(Part 1):427–434, 1995. 1.4, 2.1

Umakoshi, Y., Nakano, T., Sumimoto, K., and Maeda, Y. "Plastic anisotropy of ti_3al single crystals". *Materials Research Society Symposium Proceedings*, 288:441–446, 1993. 1.2.3

Underwood, E. *Quantitative stereology*. Addison-Wesley Publishing Company, 1970. 7.3

Verkerk, J. and Peters, J. "Final report concerning cirp cooperative work on the characterization of grinding wheel topography". *Annals of CIRP*, 26(2):385–395, 1977. 1.3, 7.2

Viswanathan, G., Kim, Y.-W., and Mills, M. "On the role of precipitation strengthening in lamellar ti-46al alloy with c and si addition". In Kim, Y.-W., Dimiduk, D., and Loretto, M., editors, *Gamma Titanium Aluminides 1999*, pages 653–660. TMS, Warrendale, PA, 1999. 1.2.2

Wagner, C., Boldrick, M., and Perez-Mendez, V. "A phi-psi-diffractometer for residual stress measurements". *Advances in X-Ray Analysis*, 26:275–282, 1983. 2.3

Wang, H. and Subhash, G. "Mechanics of mixed-mode ductile material removal with a conical tool and the size dependence of the specific energy". *Journal of the Mechanics and Physics of Solids*, 50(6):1269–1296, 2002. 1.3, 1.3

Wern, H. "Evaluation of residual stress gradients by diffraction methods with wavelets; a neural network approach.". *Advances in X-Ray Analysis*, 43:11–20, 1999. 6.6, 10.2

Williams, J. "Wear modelling: analytical, computational and mapping: a continuum mechanics approach". *Wear*, 225-229(Part 1):1–17, 1999. 1.3

Winholtz, R. and Cohen, J. "Generalized least-squares determination of triaxial stress states by x-ray diffraction and the associated errors". *Australian Journal of Applied Physics*, 41:189–99, 1988. 2.3, 6.4, 6.6

Woodbury, R. *History of the Grinding Machine*. 1959. 1.1

Xu, H. and Jahanmir, S. "Simple technique for observing subsurface damage in machining ceramics". *Journal of American Ceramics Society*, 77(5):1388–1390, 1994. 1.5.1, 2.3, 4.2

Yamabe, Y., Takeyama, M., and Kikuchi, M. "Determination of α $(a3) \rightarrow \alpha_2$ $(d0_{19})$ transition temperatures in ti-(40 45)at.%al alloys". *Scripta Metallurgica et Materialia*, 30(5):553–557, 1994. T. 1.2.1, 3.2

Yamabe, Y., Takeyama, M., and Kikuchi, M. "Microstructure evolution through solid-solid phase transformation in gamma titanium aluminides". In *Proceedings of the Symposium on TMS Annual Meeting on Gamma Titanium Aluminides*, pages 111–129. The Minerals, Metals & Materials Soc (TMS), Warrendale, PA, USA, 1995. 1.2.2

Yamaguchi, M. and Inui, H. "Tial compounds for structural applications". pages 127–142, 1993. 1.2.1

Yamaguchi, M., Inui, H., and Ito, K. "High-temperature structural intermetallics". *Acta Materialia*, 48(1):307–322, 2000. 1.2.1

Yamaguchi, M. and Umakoshi, Y. "The deformation behaviour of intermetallic superlattice compounds". *Progress in Materials Science*, 34(1):1–148, 1990. 1.2.2, 1.2.3

Yoo, M. and Fu, C. "Physical constants, deformation twinning, and microcracking of titanium aluminides". *Metallurgical and Materials Transactions A: Physical Metallurgy and Materials Science*, 29A(1):49–63, 1998. 3.2

Younis, M. and Alawi, H. "Probabilistic analysis of the surface grinding process". *Transactions of the CSME*, 8(4):208–213, 1984. 7.2

Zhang, W.-J., Lorenz, U., and Appel, F. "Recovery, recrystallization and phase transformations during thermomechanical processing and treatment of tial-based alloys". *Acta Materialia*, 48(11):2803–2813, 2000. 1.2.2

Zhang, W. and Deevi, S. "An analysis of the lamellar transformation in tial alloys containing boron". *Materials Science and Engineering A*, 337(1-2):17–20, 2002. 1.2.2, 3.1

Zhu, X., Ballard, B., and Predecki, P. "Determination of z-profiles of diffraction data from tau- profiles using a numerical linear inversion method,". *Advances in X-Ray Analysis*, 38, 1995. 6.6, 10.2

VITA

Gregorio Murtagian is a graduate from Escuelas Técnicas Municipales Raggio (Argentina) high school, and he received his Mechanical Engineering Degree at Universidad Technológical Nacional, Facultad Regional Buenos Aires in 1994. He completed a Materials Science and Technology Master's in 1997 working in the area of dynamic fracture. During the period of 1995-1999 he worked as a researcher at the Center for Industrial Research CINI-TENARIS. He started his PhD program at Georgia Institute of Technology on Fall 1999.